ANALYSIS OF NON-SYMMETRICAL FLAPPING AIRFOILS AND THEIR CONFIGURATIONS

TAY WEE BENG

(B. Eng. (Hons.), M. Eng., NUS)

A THESIS SUBMITTED

FOR THE DEGREE OF DOCTOR OF PHILOSOPHY

DEPARTMENT OF MECHANICAL ENGINEERING

NATIONAL UNIVERSITY OF SINGAPORE

2009

Summary

The objective of this project is to improve the performance of the efficiency, thrust and lift of flapping wing. The first phase of study investigates the effects of different flapping parameters (reduced frequency, Strouhal number, pitch amplitude and phase angle) and the airfoil's shape on its efficiency, average thrust and lift coefficients ($\eta, \overline{C}_t$ and $\overline{C}_l$). Interactions between the parameters are also studied using the Design of Experiment (DOE) methodology. The next phase of the research aims to investigate the effect of active chordwise flexing. A total of five flapping configurations are selected and the objective is to see if flexing can help to further improve these cases. Moreover, the effect of center of flexure, leading/trailing edge flexing, a form of single-sided flexing and the use of non-symmetrical airfoil are also investigated. The last phase of the research investigates the effect of the arrangement of the airfoils in tandem on the performance of the airfoils by varying the phase difference and distance between the two airfoils.

Results from the DOE show that both the variables and shape of the airfoil have a profound effect on the η, $\overline{C}_t$ and $\overline{C}_l$. By using non-symmetrical airfoils, average lift coefficient as high as 2.23 can be obtained. The average thrust coefficient and efficiency also reach high values of 2.53 and 0.61 respectively. The C_l is highly dependent on the airfoil's shape while C_t is influenced more heavily by the variables. Efficiency falls somewhere in between. Two-factor interactions are found to exist among the variables. This shows that it is not sufficient to analyze each variable individually.

The chordwise flexing results show that flexing is not necessarily beneficial for the performance of the airfoils. However, with the correct parameters, efficiency is as high as 0.76

by placing the flexing center at the trailing edge. Average thrust coefficient is more than twice as high from 1.63 to 3.57 if flapping and flexing occur under the right conditions. Moreover, the single-sided flexing also gives an average lift coefficient as high as 4.61 for the S1020 airfoil. The shape of the airfoil does alter the effect of flexing too. It has also been found that in non-optimized flapping configuration, flexing is more likely to improve the efficiency of the airfoil.

For the tandem airfoil arrangement simulations, all the different flapping configurations show improvement in the η, $\overline{C}_t$ or $\overline{C}_l$ when the distance between the two airfoils and the phase angle between the heaving positions of the two airfoils are optimal. The average thrust coefficient of the tandem arrangement managed to attain more than twice that of the single one (4.84 vs. 2.05). On the other hand, the average lift coefficient of the tandem arrangement also increased to 4.59, as compared to the original single airfoil value of 3.04.

The research data obtained from the studies of DOE, airfoil's flexing and tandem configuration will enable the design of a better performing ornithopter in terms of efficiency, thrust and lift production.

Acknowledgements

The author wishes to express sincere appreciation of the assistance and suggestions given by the Supervisor, Assoc. Prof Lim Kah Bin

The author would also like to thank post doctorate research fellow Dr. Hu Yu and Masters student Mr Nguyen Duc for their ideas and contribution.

The author wishes to thank Dr. Tsai Her Mann for a brief but rewarding advice.

The author is grateful to the technologists Mrs Ooi, Ms Tshin, Mr Zhang, Ms Hamida, Mdm Liaw and Mrs Too in Control Lab 1 and 2, for providing excellent computing facilities to carry out the project.

Furthermore, the author wishes to thank the systems engineers Mr. Wang Junhong and Neo Eng Hee for the technical help they have provided at Supercomputers and Visualisation Unit (SVU).

Lastly, the author would like to thank his family members and friends who have given him many useful suggestions and moral support.

Table of Contents

List of Figures

List of Tables

Nomenclature

a_f	Flexing amplitude
a_{lf}	Leading edge flexing amplitude
a_{tf}	Trailing edge flexing amplitude
$\overline{a}_f$	Nominal flexing amplitude
c	Aerofoil chord
c_{rot}	Center of rotation
C_d	Drag coefficient
C_l	Lift coefficient
$\overline{C}_l$	Average lift coefficient
$\overline{C}_{l,o}$	Overall average lift coefficient for tandem configuration
C_p	Pressure coefficient
C_t	Thrust coefficient
$\overline{C}_t$	Average thrust coefficient
$\overline{C}_{t,o}$	Overall average thrust coefficient for tandem configuration
d_{12}	Distance between the 2 airfoils in tandem arrangement, from leading edge of first airfoil to leading edge of second airfoil nondimensionalized by airfoil chord
dl	Vortex segment
f	Frequency, Hz
h	Instantaneous heaving position
h_0	Heaving amplitude, nondimensionalized by airfoil chord
h_{lf}	Leading edge flexed length, perpendicular to airfoil's chord line , nondimensionalized by airfoil chord

h_{tf}	Trailing edge flexed length, perpendicular to airfoil's chord line , nondimensionalized by airfoil chord
k	Reduced frequency fc/U_∞
$\overline{n}$	Unit normal
P	Power input
p	Pressure
p_s	Value calculated by Minitab to determine its significance
r	Distance from arbitrary point to vortex
Re	Reynolds number
$\overline{r}$	Position vector of the body fixed frame in the inertial frame
St	Strouhal number fh_0/U_∞
u	Velocity
U_∞	Freestream velocity
t	Nondimensionalized time $t U_\infty/c$
t_0	Time when flapping starts
$\overline{V}_0$	Velocity of the body frame in the inertial frame
$\overline{v}_{rel}$	Velocity of the wing in the body fixed frame
x_{fc}	Flexing center location, as measured from the leading edge
x_{lf}	Distance from point of flexing to flex center, nearer the leading edge
x_{tf}	Distance from point of flexing to flex center, nearer the trailing edge
β_{lf}	Angle rotated due to leading edge flexing, in degrees
β_{lf}	Angle rotated due to trailing edge flexing, in degrees
θ	Instantaneous pitch angle, in degrees
θ_0	Pitch amplitude, in degrees
θ_v	Angle covered by the vortex, in radians
ψ	Phase difference between rowing and heaving, in degrees

ψ_f	Phase angle between plunging and flexing of airfoil, in degrees
ϕ	Phase difference between pitching and heaving, in degrees
ϕ_{12}	Phase difference between heaving position of first and second airfoils, in degrees
η	Propulsive efficiency
η_o	Overall propulsive efficiency for tandem configuration
Φ	Velocity potential
$\nabla\Phi$	Velocity induced by all singularity elements on the wing surface
$\bar{\Omega}$	Angular velocity of the body fixed frame in the inertial frame
Γ	Circulation
Δq	Induced velocity

1 Introduction

The objective of this research is to enhance the understanding of flapping-wing mode of flying. The ultimate aim is really to improve the performance of the efficiency, thrust and lift of flapping wing aircraft.

In recent years, Micro Aerial Vehicles (MAVs) are becoming increasingly important, especially in the area of military surveillance (Shyy et al. 2008). MAVs are classified into fixed wing or flapping wing MAVs, with wingspan less than 15 cm, as initially defined by the Defense Advance Research Projects Agency (DARPA, United States of America). At the low range of Reynolds numbers, flapping wing MAVs are more efficient and maneuverable compared to fixed wing.

Throughout history, human efforts toward flapping-wing flight have a reputation for futility. However all processes in nature obey the same physical laws as machines since ornithopters have been flown successfully throughout the entire size range of flying vertebrates in nature (Delaurier 1993; Pornsin-Sirirak et al. 2000; Tay 2001). But the conventional aerodynamics that we are familiar with concerns largely with the gliding of planes and birds. The flow of air in such flights is relatively steady. A different class of aerodynamics is in evident in the flights of the insects and birds. The airflow around these flyers is highly unsteady. The principles and theories of conventional steady and quasi-steady aerodynamics are no longer a good guide to the understanding of such flights.

The knowledge of the aerodynamics of flapping flight is now expanding rapidly. Many research groups and universities are conducting experimental as well as computational study on flapping wings (Shyy, Berg et al. 1999; Rozhdestvensky and Ryzhov 2003; Ansari, Zbikowski et al. 2006). Some flow visualisations have revealed complex systems of unsteady

vortices. Analysis of these results is therefore not easy. Moreover, besides investigating the different flapping configuration, research has also branched into other areas to further improve the performance of flapping wing configurations. These include

1. Active chordwise flexing (Miao and Ho 2006)
2. Passive chordwise flexing (Pederzani and Haj-Hariri 2006; Tang et al. 2007; Zhu 2007)
3. Passive spanwise flexing (Heathcote and Gursul 2007; Zhu 2007)
4. Biplane airfoil arrangement (Jones et al. 2003)
5. Tandem airfoil arrangement (Akhtar, Mittal et al. 2007)
6. Non-sinusoidally heaving motion (Sarkar and Venkatraman 2005)

Some of the above ideas such as active flexing were not possible in the past. However, with the advent of smart materials such as shape memory alloy (Jardine et al. 1996), it is now possible.

Despite the numerous work done on flapping wing research, there are still many areas which can be improved. Many researchers had used symmetrical NACA airfoils to do similar forms of investigations. Their studies had concentrated only on thrust and propulsive efficiency. Due to the airfoil's symmetry, the average lift generated was usually not favourable. However, in the design of a Micro Aerial Vehicles (MAV)'s wing, consideration of the lift is equally important. Most designers of ornithopters (such as Pornsin et al. (2000) and Delfly[*]) uses membrane-based wing, which is simple to design and build. The wing can generate reasonable amount of thrust but very small amount of lift. To get around the low lift problem, the stoke angle must be changed to produce more lift. Part of the original thrust is vectored to give lift, resulting in a smaller final thrust. The flight efficiency is rather low, as given by model aviation records (DeLaurier 1994).

[*] Delfly website: http://www.delfly.nl

In the past, the factors affecting the performance of flapping airfoils (such as Strouhal number, reduced frequency) were usually analyzed individually. This prevents interactions between different factors to be investigated. If interactions do exist (which will be shown later), then it will be erroneous to believe that one can predict the resulting efficiency, thrust or lift simply changing one parameter. Moreover, as mentioned earlier, research in flexible and tandem airfoil arrangement are still in their preliminary stage and they have shown a lot of potential in improving the airfoil's performance further.

Hence, the objective of the thesis is as follows. The first phase of study concentrates on investigating the effects of different flapping parameters on the efficiency, thrust and lift of the flapping airfoil. This study therefore attempts to investigate flapping configurations which not only give high efficiency and thrust, but also high lift through the use of non-symmetrical airfoils. This method of generating lift is much more advantageous than changing the stroke angle to produce thrust/lift through force vectoring, assuming the same flapping parameters are used. In this study phase, a total of four other non-symmetrical airfoils are used. The airfoils chosen include NACA4404, S1020, NACA6302, and one which we named as "birdy". The NACA0012 airfoil is also included in the study as a form of comparison. We believe that the use of non-symmetrical airfoils will produce much higher lift. There is also the possibility of two-factor interactions. Thus, in order to analyze two-factor interactions, the Design of Experiment (DOE) methodology is employed. (Mathews 2005).

The next phase of the research aims to investigate the effect of active chordwise flexing. Besides the pure heaving case, three other flapping configurations are also selected. They correspond to the flapping parameters which give the highest efficiency, average thrust and lift coefficients in the first phase of the research. The objective is to see if flexing can help to further improve these optimum cases. It is similar to Miao and Ho (2006) in that different flexure amplitudes are tested. Moreover, the effect of center of flexure, leading/trailing edge flexing and the use of non-symmetrical airfoil are also investigated. Hence, the parameter

space is now much larger.

The last phase of the research investigates the effect of the arrangement of the airfoils in tandem. Through simulations, one hopes to find out how the phase difference and distance between the airfoils affect the efficiency, average thrust and lift coefficients of the airfoils. The results obtained from these simulations will help in the design of a better ornithopter wing.

2 Literature Review

The literature review is divided into four sections. The first section investigates on the types of solvers and algorithms suitable for simulating flapping wings. The second section studies the kinematics of different flapping configurations while the next section discusses the effect of flexing of the airfoil on its performance. Lastly, research involving flapping wings in biplane/tandem will be discussed. Both computational as well as experimental studies are reviewed.

2.1 Solvers for flapping wing simulation

Most computational fluid dynamics (CFD) simulations for MAV studies are now run based on the full Navier Stokes equations. There are a number of reasons for this. First of all, the advancement in computational resources manages to reduce the time taken in most simulations which used to take a few weeks to a few days or hours. Another reason is that the ***Re*** involved in MAV studies is not too high (typically less than 200,000[†]). Moreover, using the full Navier Stokes equation, one is able to simulate all the effects such as flow separation. No special assumption is required. However, there are still studies done using some other theories such as panel methods. This is because they are much faster compared to using the full Navier Stokes equations and they are able to produce acceptable results for the cases studied. This is especially true for the three dimensional (3D) simulations. However, assumptions usually have to be made.

[†] Micro Aerial Vehicle Research, http://www.nd.edu/~mav/research.htm

In the book by Katz and Plotkin (2001), the authors used the unsteady panel method to simulate a moving wing (3D). The greatest advantage compared to using the full Navier Stokes equation is the large decrease in the amount of time required. Simulations in 3D based on the Navier Stokes equation which required weeks to run took only a few hours when using the panel method. However, the panel method is based on potential flow and hence it is non-viscous and cannot handle flow separation. Therefore, one has to analyze carefully if this method is suitable for flapping wing simulations.

Kim and Choi (2000) devised a new second-order time-accurate fractional-step method for solving unsteady incompressible Navier Stokes equations on hybrid unstructured grids. It is a non-staggered method. In other words, the velocity and the pressure are defined at the center of the cell. Moreover, there is another velocity, which is defined at the face center of the cell face. Being a non-staggered method, it is much easier to code and visualise on structured and un-structured grids. Extension to 3D is also much easier. In addition, it is a fully implicit scheme which is more robust compared to semi-implicit ones such as the Adams–Bashforth method. However, the current method is applied on non-moving grids. Modifications will be required to make it work on moving grids.

One of the simplest ways to transform a non-moving grid to a moving one is to use the Arbitrary Lagrangian–Eulerian (ALE) formulation (Hirt et al. 1997). It is basically a coupling approach between Lagrangian points and Eulerian points. Hence, it is possible to apply it to the fractional method of Kim and Choi (2000) to enable the simulation of a moving body. Simulating a moving body can be done by moving the entire grid or only deform the grid around the airfoil region. It is much easier and faster to move the entire grid because there is no need to re-compute some of the matrices. However, this may not be possible in some cases when the airfoil's shape changes. In these cases, there are a number of alternatives. Batina's (1990) dynamic mesh algorithm made use of spring to model each edge of the cell. The grid is shifted to its new position by the extension or contraction of the spring. It can be used for

structured or unstructured grids. However, it is not able to produce good grid quality when the deformation is high. Alternatively, one can use the arc-length-based transfinite interpolation (TFI) (Jones and Samareh-abolhassani 1995). Compared to the spring based algorithm of Batina (1990), the arc-length-based transfinite interpolation is much faster and gives better grid quality. However, it is only applicable for structured grids.

The simulation of different bodies moving independently, such as airfoils in tandem arrangement, proves to be much more complicated. This is because the earlier method of the ALE formulation cannot be applied directly. There are currently a few ways to solve the problem. One of them is the overset method (Tuncer 1996; Cai et al. 2006). In this method, there is usually a background Cartesian grid which is fixed. The moving bodies are usually in structured C or O-type grids which can move freely on the background Cartesian grid. The intricate part is the interpolations between the moving and fixed grids. If not done properly, stability and conservation problems will result in erroneous values.

Another way to solve the moving bodies' problem is to use mesh-free method (Chew et al. 2006). In this method, each body of interest is surrounded by a cloud of mesh-free nodes. The cloud of nodes moves together with the body with a Cartesian grid in the background. For the discretizations of the Navier–Stokes equations, the generalized finite-difference (GFD) method with weighted least squares (WLS) approximation is used at the mesh-free nodes while standard finite-difference approximations are applied elsewhere. This scheme has been demonstrated its ability to solve a variety of moving bodies' problems. However the author also mentioned that the distribution of the nodes in the cloud can have a serious effect on the discretization errors.

A newer alternative is the immersed boundary (IB) method (Mittal and Iaccarino 2005). In this method, the Cartesian grid is used. The bodies' or airfoils' outlines simply cut through the grid. Therefore, simulating complicated body is not a problem. Moving body can also be handled

more easily compared to conformal grids because there is no need to move or deform the grid. However, since the grid does not conform to the outlines, the boundary conditions around the grid require special modifications. In fact, it is the different modifications used by the various research groups that distinguish them. Another problem is that the size of the Cartesian grid has to increase much faster compared to structured grids when the *Re* increases. This is due to the non-conformal nature of the Cartesian grid.

Tseng (2003) used a ghost cell approach whereby the cells just inside the body are represented by ghost cells. Equations involving the ghost cells and the normal cells are formed and substituted into the system of linear equations to be solved. It can be directly applied onto the fractional scheme of Kim and Choi (2000). However, the current formulation is meant only for complicated but fixed bodies. Hence, additional modifications are required to make it work with moving bodies. Ye's (1999) IB approach is based on the cut cell methodology. In other words, the Cartesian cells are cut by the immersed bodies or boundaries. The advantage of this method is that the cut boundary is clearly defined but it also means that the algorithm is much more complicated and therefore the speed of the solver is much slower. An extension of the method by Udaykumar (2001) for moving bodies has also been tested. However, special steps must be performed on some cells due to the movement. These so called "freshly cleared" cells appear because they belong to the solid body at one time, but change to fluid cells because of the movement of the body. This will take up additional computational resources. Moreover, its extension to 3D, although theoretically possible, will be difficult because of the complicated geometry. Ravoux et al. (2003) proposed another type of algorithm which makes use of both IB and volume of fluid (VOF). In this method, the system consists of a "binary" fluid, one phase representing the fluid, while the other representing the solid body. For cells which contain both solid and fluid, a volume fraction is defined. The advantage of this method is that it is easy to implement and it can be used to simulate moving bodies with only a small amount of modifications. However, it has to be used on staggered grids.

2.2 Kinematics of Flapping Configuration

In experimental studies, Koochesfahani (1989) measured the thrust force produced by a rectangle wing, fitted with endplates, pitching at θ_0 = 2° and 4°. The experiments were conducted in a water tunnel at a *Re* of 1.2×10^4 and it was found that the structure of the wake was heavily dependent on the frequency, amplitude and shape of the oscillation waveform. This result showed that by carefully selecting the above mentioned parameters, one could improve and optimise the performance of the wing. Triantafyllou et al. (1993) also used a water tunnel to measure the efficiency of a NACA0012 airfoil flapping with a combination of heave and pitch. Maximum efficiency was achieved at *St* in the range of 0.25 to 0.35. Moreover, large amount of data from observations of fish and cetaceans also found that optimal fish propulsion had approximately the same *St* range. This optimal *St* for high efficiency turned out to be similar for birds and insects during cruising as well (Taylor et al. 2003). It seems that in nature, there is a preferred *St* for all oscillatory lift-based propulsion. Hence, one wonders if we can make use of this principle to design flapping wing with high propulsive efficiency.

Ellington et al. (1996) built a large mechanical model of the hawkmoth *Manduca sexta* to visualize the flow field around its wing since it was difficult to obtain a good visualization with the actual tethered insect. The leading edge vortex (LEV) during the downstroke was found to be the reason for the high lift generated by the wings. The leading edge vortex remains attached during most part of the downstroke. The stability of the vortex was made possible due to the spanwise flow. The experiment was conducted at a *Re* of 10^3. However, it remained to be seen if the same leading edge vortex feature could be found at higher *Re* of the order 10^4. Read et al.'s (2003) experiments, besides testing the standard parameters such as Strouhal number, also investigated higher harmonics in the heave motion, superposed pitch bias and impulsively moving foil in still water. Large side force and instantaneous lift coefficients were recorded. It was also found that a phase angle of 90° to 100° between pitch and heave produced the highest

amount of thrust coefficient. This information will be useful as a guide for the choice of phase angle used in the DOE simulation.

Hover et al. (2004), on the other hand, investigated on the effects of different angle of attack profiles. Both the sawtooth and cosine profiles showed improvement in thrust coefficient or efficiency over the standard sinusoidal profile. This showed that besides the selection of certain parameters as mentioned earlier, different types of flapping profiles such as sawtooth also influenced the performance of the airfoils. Schouveiler et al. (2005) studied experimentally the performance of an aquatic propulsion system inspired from the thunniform (a family of swimmers which propel themselves by flapping at the tail, for example, the whales and tunas) swimming mode. The variables studied included Strouhal number and maximum angle of attack. Systematic measurements of the fluid loading showed a peak efficiency of more than 70% for optimal combinations of the parameters. Moreover, a parameter range was identified where efficiency and high thrust conditions were achieved together, as required for use as a propulsion system. This once again showed that by careful selection of parameters, high efficiency or thrust could be obtained.

On the computational aspect, Streitlien and Triantafyllou (1998) used two simplified models derived from the theory of the von Kármán vortex street and linear nonuniform aerofoil to estimate the thrust and wake. It was found that the von Kármán vortex street theory predicted thrust accurately, while the linear nonuniform aerofoil theory predicted thrust well for all cases except the highest Strouhal number. This showed that these simplified models could be used as an initial estimate of the performance of the airfoil for certain cases. However, it must be stressed that the models were not able to account for features such as flow separations. As a result, the Navier Stokes solver still had to be used to confirm the results.

Smith et al. (1996) used the unsteady panel method to simulate the 3D flapping motion of a tethered sphingid moth and compared their results with the quasi-steady and the experimental

ones. It was found that their result was much more accurate than the quasi-steady one and closer to the experimental values. It was mentioned that the unsteady panel method is valid for flow with ***Re*** of the order 10^4. However, it seems plausible because the panel method is based on potential flow theory which assumes non-viscous flow. As a result, it is not able to account for flow separation which may occur at this ***Re***. Similarly, Fritz and Long (2004) used the unsteady panel method to predict the unsteady flapping flight of small birds and insects. The main difference between this simulation and that of Smith et al. (1996) is that the model is implemented using object orientated C++ which made the code easier to read and modify. However, it suffers from the same problem as the simulation done by Smith et al. (1996) because it is not able to account for flow separation.

Lu et al. (2003) used the Navier Stokes equation in the vorticity and stream-function formulation to numerically simulate a foil in plunging and pitching motion. Based on the presented extensive calculation for a wide range of parameters, three types of the leading-edge vortex shedding evolution were identified and they had an effective influence on the vortex shedding and vortex structures in the wake of the foil. Lu et al. (2003) varied the parameter one at a time during their analysis. Hence, it was not able to investigate any two-factor interaction.

Ramamurti and Sandberg (1999) used a two dimensional (2D) finite element flow solver to study viscous flow past a NACA0012 airfoil at various pitching frequencies. He found that the Strouhal number was the critical parameter for thrust generation. The reduced frequency did not affect thrust generation greatly. Akbari and Price (2000) investigated the effect of reduced frequency, mean angle of attack, thickness and pitch-axis on the performance of the flapping airfoil. They found that the above mentioned factors affected wake structures significantly. Hence, the results of Ramamurti and Sandberg (1999) and Akbari and Price (2000) seemed to contradict one another regarding the effect of reduced frequency. Therefore, more experiments are required to verify about the effect of reduced frequency on thrust. Wu and Sun (2005)

studied the effect of wake on the aerodynamics forces. It was found that at the start of the half-stroke, the wake might either increase or decrease the lift and drag. It depended on the kinematics of the wing at stroke reversal. For the rest of the half-stroke, wake reduced the lift while increased the drag. This showed that it is very important how the wake is shed, which is affected mainly by the flapping configuration. It can either be beneficial or detrimental to the performance of the airfoil.

Three dimensional Navier Stokes simulations are less common due to the expensive computational requirement as well as the complicated analysis involved. Aono et al. (2008) managed to do a 3D simulation of a hovering fruit fly and a hawkmoth. The results exhibited horseshoe-shaped vortex around the wings in the early up and downstroke. It then grew into a doughnut shaped vortex and broke down into 2 circular vortex rings downstream. It was also found that the LEV's position and axial flow intensity are very different for the two insects. The reason is attributed to the different ***Re*** of the two insects (100-250 for fruit fly, >6000 for hawkmoth). In other words, the ***Re*** value is a very important factor affecting the flow fields.

Optimization studies had been conducted by Pedro et al. (2003) and Tuncer and Kaya (2005). Pedro et al. (2003) tried to find an optimal thrust coefficient and propulsive efficiency for a NACA0012 airfoil operating at a ***Re*** of 1.1×10^3 by varying the heaving, pitching, phase and frequency. Both Pedro et al. (2003) and Tuncer and Kaya (2005) showed that the CFD based method is a much better alternative to experimental method for optimization studies. Many different cases could be simulated at a fraction of the time required for the experimental method. However, the variables are studied by varying the variables one at a time. This method of analysis prevented the effect of two-factor interaction to be studied. Moreover, it was not able to obtain a true optimised value by changing the value of one variable at a time. Similarly, Tuncer and Kaya (2005) used a gradient based numerical optimization method to get the optimum output for a NACA0012 airfoil operating at ***Re*** of 1.0×10^4. The gradient based optimization was a more accurate way of getting the optimized value but it depended on the

starting values of the variables chosen. Different sets of starting values could lead to different sets of optimized values. Nevertheless, very high efficiency (η = 67.5%) and average thrust coefficient ($\overline{C}_t$ = 2.64) were obtained.

Another recent study which investigated on the airfoil shape was the research conducted by Takahashi et al. (2007). However, the *Re* used was 5.0×10^6. It was found that at this *Re* number, the airfoil shape became an important factor at influencing the efficiency of an airfoil. But there is currently no similar investigation for simulations conducted at the *Re* of 1.0×10^4, which is the flow regime for that of MAVs. Hence, it will be interesting to see if the above relationship is true also for *Re* at 1.0×10^4.

2.3 Airfoil flexing

Initially, most research works were carried out using rigid airfoils or wings. Recently, more and more studies have been conducted using flexible airfoils or wings. This is because in nature, the fins of fishes and wings of birds or insects are flexible. Hence, it is speculated that there must be some advantages compared to their rigid counterparts. Indeed, several researches had shown an increase in efficiency or thrust when the airfoils or wings exhibit some degree of active or passive flexibility. Moreover, with the advent of smart materials such as shape memory alloy (Jardine et al. 1996), one can actively control the deformation of a wing. This enables an aircraft to deform its wings according to the flight requirements to improve the aircraft's performance.

Tang et al. (2007) found from their numerical study that as the airfoil became more flexible, higher thrust coefficient and smaller lift coefficient were generated. The passive deformation of the airfoil due to its flexibility created a phase difference relative to its pitching motion. Another interesting result was that the detailed airfoil shape was of secondary importance

compared to the equivalent angle of attack. In other words, a rigid and a flexible airfoil could give the same performance as long as both their pitching angles are equivalent throughout the flapping cycle. However, it must be emphasised that the shape of the airfoil used was a flat plate with rounded edges and the *Re* used was 100. It still remains to be seen what will happen if the airfoil shape is more complicated, for example, a NACA4404 airfoil. Miao and Ho (2006) investigated the influence of flexure amplitude on the aerodynamic performance of the flapping airfoil using Fluent (a commercial CFD code). They experimented with different flexure amplitudes, a_f ranging from 0.0 to 0.7 and found that at $Re = 10^4$, $k = 2$ and $h_0 = 0.4$, a flexure amplitude of 0.3 resulted in the highest propulsive efficiency. The result showed that there is a particular amount for flexing which could give optimal efficiency. Moreover, an excessive amount of flexing was actually detrimental to the efficiency. Miao and Ho's (2006) simulation also had only two parameters, namely the flexing amplitude (a_f) and flexing phase angle (ψ_f). There are still many more parameters such as the location of flexing which are not investigated. The airfoil used is a NACA0014 and other types of airfoil shape may also be used. Figure 2.1 gives a graphical representation of the airfoil flexing; here a_f and x represent the maximum flapping amplitude and distance from point of flexing to the leading edge respectively.

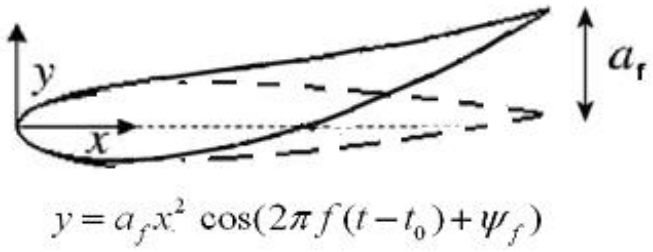

Figure 2.1: A representation of the airfoil flexing by Miao and Ho (2006)

Zhu (2007) carried out a fully-coupled fluid-structure interaction study to investigate the effect of chordwise and spanwise flexing on a flapping foil. The foil was simulated to be immersed in two different types of fluids of high and low density. It was found that in low density fluid, the chordwise flexibility reduced both the thrust and efficiency, while the spanwise flexibility

increased the thrust without reducing efficiency within a small range of structural parameters. On the other hand, in high density fluid, chordwise flexibility increased the efficiency while spanwise flexibility reduced the thrust and efficiency. Hence, depending on the type of application, that is, in the air or underwater, the relevant type of flexing could be employed.

Pederzani and Haj-Hariri (2006) modelled an airfoil partially with membrane to allow flexing. The numerical study showed that this type of airfoil was more flexible. Moreover, another interesting result was that heavier airfoils were even more efficient than lighter ones. Unfortunately, using heavier wings would increase the overall weight of an airplane. Hence it might not be too beneficial. One had to weigh the benefit of using a heavier wing to improving efficiency.

Heathcote and Gursul (2008) used a water tunnel to investigate the effect of chordwise flexibility on a plunging airfoil at *Re* of 0 to 27,000. Thrust coefficient increased for airfoil of intermediate flexibility. This further confirmed the earlier simulation result by Miao and Ho (2006) that there is an optimal amount of flexing for maximum efficiency. Another water tunnel experiment by Heathcote et al. (2008) studied the effect of spanwise flexibility on the thrust, lift and propulsive efficiency of a heaving rectangular wing. For $St > 0.2$, a degree of spanwise flexibility was found to increase the thrust and efficiency. However, a far greater degree of flexibility was found to be detrimental. Therefore, similar to chordwise flexing, there is also an optimal amount of flexing amplitude for spanwise flexing.

2.4 Biplane/Tandem Airfoil Arrangement

Some researchers have also been trying other ways to improve the performance of the flapping wing configuration. Jones et al. (2003) designed a flapping wing aircraft which flew by arranging two flapping airfoils in a biplane configuration. The flight tests showed that this type

of aircraft was very suitable for low speed flight because flow separation did not occur easily. This is an interesting alternative concept to flapping wing motion. However, it is only effective in producing thrust. In order to generate lift, the stroke angle has to be angled. This will therefore result in lower thrust.

Another way to increase the performance of an airfoil is through the addition of another airfoil in tandem. A very good example of this arrangement in nature is the wings of the dragonfly. Numerous experimental and numerical studies had been conducted. Lan and Sun (2001) used an overset solver to study the aerodynamic force and flow structures of flapping airfoils in tandem arrangements. They found that the interaction between the two airfoils could either increase or decrease the horizontal and vertical forces, depending on the phase difference between the two airfoils. The vertical force was largest when the phase difference is 0^o. On the other hand, the horizontal force was largest when the phase difference is 90^o. However, it will be interesting to find out if this result is also true for all types of flapping configurations and airfoils. Isogai et al. (2004) did a 3D Navier Stokes simulation of the flow around the tandem wings of the *Anax parthenope julius*, a typical dragonfly. The lift and power predicted by the simulation were very similar to the experimental data of the actual dragonfly by Azuma and Watanabe (1988). Moreover, it also compared well with the results obtained from a mechanical robot model. Since the two wings in tandem flapped independently, a multiblock method was used. The physical space also had to be mapped to the computational space. Hence, this method of simulating wings in tandem is very complicated. One also had to be careful about interpolation errors at the interface between different blocks. Wang and Russell (2007) filmed the wing motion of a tethered dragonfly and computed the aerodynamic force and power as a function of the phase numerically. It was found that the out-of-phase motion as seen in steady hovering used nearly minimal power to generate the required force to balance the weight. On the other hand, the in-phase motion seen in takeoffs provided an additional force to accelerate. This seems to contradict the earlier findings of Lan and Sun (2001), who found that horizontal force was largest when the phase difference is 90^o. Therefore, more experiments or simulations

must be conducted to find out the relationship between the performance and phase angle of the airfoils. Akhtar et al. (2007) attempted to model the dorsal–tail fin interaction observed in a swimming bluegill sunfish numerically using an immersed boundary (IB) solver. Results showed that vortex shedding from the upstream (dorsal) fin was indeed capable of increasing the thrust coefficient of the downstream (tail) fin significantly. Hence, the tandem airfoil arrangement is indeed better than the single airfoil. Moreover, the phase difference played an important role in the thrust augmentation in this case too. Thrust coefficient reached a maximum when the phase angle between the airfoils was 48^{o}, which is again different from the earlier mentioned cases.

3 Code Development and Validation

3.1 Unsteady Lattice Vortex Method (UVLM)

A software based on the UVLM is developed by Dr Hu Yu, Vinh (2005) and the author. It is intended to simulate the arbitrary motion of the airfoil in different applications like ornithopter or cyclogyro (Hu, Lim et al. 2006; Hu, Tay et al. 2006) design. This code is initially chosen because it has been proven to be able to simulate the aerodynamic forces on rigid flapping wings using minimal computational resources (Smith et al. 1996; Fritz and Long 2004). It is written in both Fortran90 and C++.

3.1.1 Code Development Summary

The vortex lattice method (VLM) is based on the potential flow theory which assumes non-viscous and irrotational flow. It is a boundary element (integral) method where the dependent variable is the potential function. The vortex rings are selected as singular element and the wing thickness is neglected for the UVLM. The vortex rings are deployed on the wing surfaces and wake sheets. Wake sheet is shed from the trailing segment of the wing trailing edge vortex rings. A new wake line is added at each time step. Since the wake does not carry loads, the wake sheet rolls up with the local fluid velocity. The Neumann boundary condition is applied on each collocation point and a system of linear equations are formed. The circulation distribution on each panel can be obtained by solving these equations. The velocity distribution can then be obtained. Then the Bernoulli function is used to calculate the forces on the wing and hence the lift, drag and torque required to drive the wing can be obtained. The next section will explain in more details about the solver.

3.1.2 Theory of the UVLM

3.1.2.1 Basic formulation

The basic governing equation of the unsteady vortex-lattice method is the Laplace equation. Assuming a thin wing, singularity elements are distributed evenly on the wing surface and the objective is to find the strength of these singularity elements subject to several boundary conditions. For the unsteady case, the Newman boundary condition states that the resultant normal velocity (which must include the velocity induced by the movement of the wing) induced by all the singularity elements on the wing surface shall be zero. The boundary condition, computed in the body fixed frame, is given as:

$$(\nabla\Phi - \bar{V}_0 - \bar{v}_{rel} - \bar{\Omega}\times\bar{r})\cdot\bar{n} = 0 \tag{3.1}$$

Where $\nabla\Phi$ is the velocity induced by all singularity elements on the wing surface,

$\bar{V}_0$ is the velocity of the body frame in the inertial frame

$\bar{v}_{rel}$ is the velocity of the wing in the body fixed frame

$\bar{\Omega}$ is the angular velocity of the body fixed frame in the inertial frame

$\bar{r}$ is the position vector of the body fixed frame in the inertial frame

$\bar{n}$ is the unit normal vector

In other words, the requirement is that the linear combination of the fundamental solutions (distributed on the surface panels) satisfies the boundary condition in Eqn (3.1). Since the wing is divided into a number of small panels, Eqn (3.1) is applied to each panel on the wing surface. For 3D thin lifting surface problems, the vortex ring elements are used. The ring is in the form of a rectangle with constant vortex distributed on its four edges. The main advantage of using this element is that it is simple to programme. Moreover, the exact boundary conditions will be satisfied on the cambered wing surface. A picture with nomenclature for some typical vortex ring elements is shown in Figure 3.1.

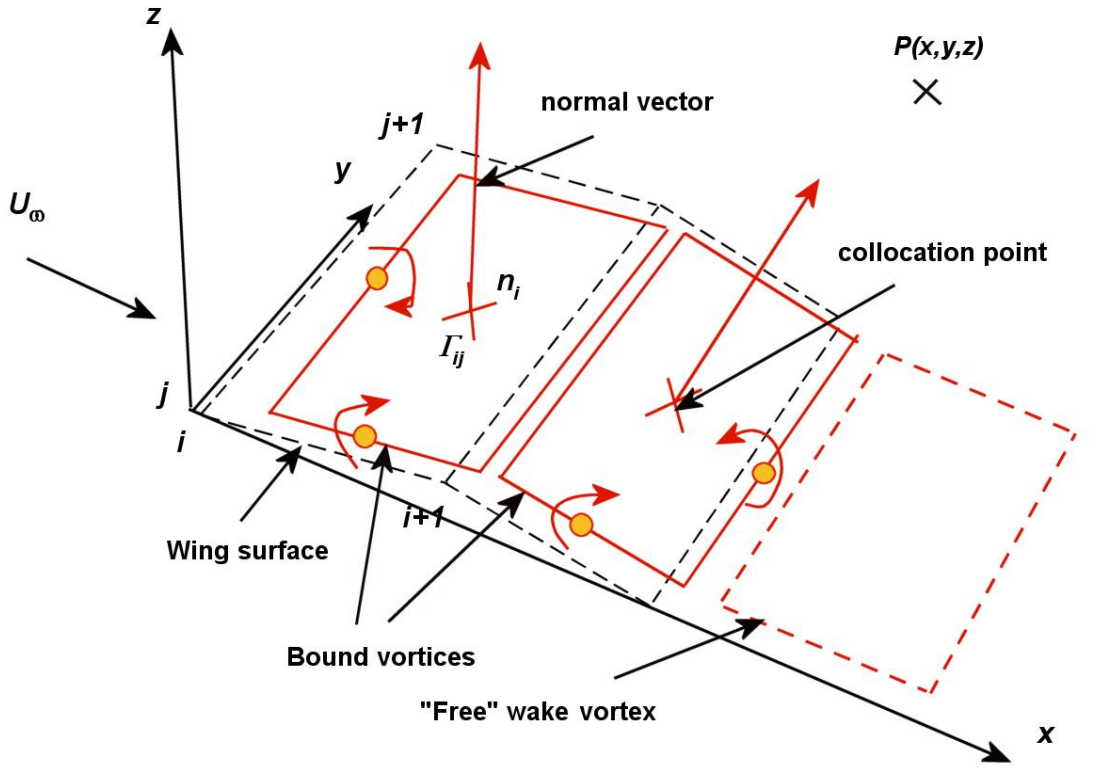

Figure 3.1: Nomenclature for the vortex ring elements for a thin-lifting surface. P refers to an arbitrary point.

The leading segment of the vortex ring is placed on the panel quarter-chord line and the collocation point is placed at the center of the three quarter-chord line. The normal vector $\vec{n}$ is defined at this point too. By placing the leading edge segment of the vortex ring at the quarter-chord line and the collocation point at the three quarter-chord line of the panel, the Kutta condition is satisfied along the chord. A positive circulation Γ is defined here according to the right-hand rule as shown in the Figure 3.1.

The velocity potential of a point vortex is given by:

$$\Phi = -\frac{\Gamma}{2\pi}\theta_v \tag{3.2}$$

Where Φ and θ_v are the velocity potential and angle covered by the vortex in radians respectively.

The velocity induced Δq at an arbitrary point *P(x,y,z)* by a typical vortex segment *dl* with

constant circulation Γ which is originally computed based on the Biot-Savart's law:

$$\Delta q = \frac{\Gamma}{4\pi}\frac{dl \times r}{r^3} \tag{3.3}$$

However, the formula is later replaced with the Scully vortex model (Scully 1968):

$$\Delta q = \frac{\Gamma}{4\pi}\frac{\vec{r}_1 \times \vec{r}_2}{r_1^2 r_2^2 - (\vec{r}_1.\vec{r}_2)^2 + r_c^2(r_1^2 + r_2^2 - 2\vec{r}_1.\vec{r}_2)}(r_1 + r_2)(1 - \vec{r}_1.\vec{r}_2 / r_1 r_2) \tag{3.4}$$

where r_c is the core radius

r_1 and r_2 are the lengths as defined in Figure 3.2

This is an improvement to the original model by Biot-Savart because unlike the original model, as r approaches zero, Δq does not approach infinity. More details about the modification to improve the stability of accuracy of the code will be presented in the later sections.

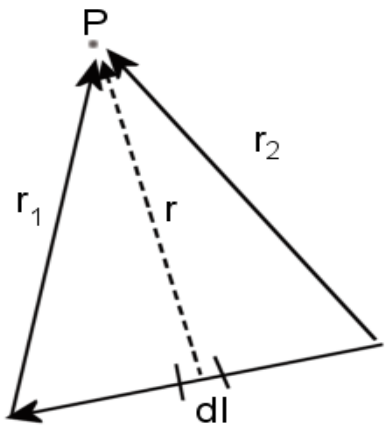

Figure 3.2: Induced velocity due to a finite length vortex segment when using the Scully model

It will be convenient to group the numerical computation of the induced velocity into a subroutine called:

$$(u, v, w) = VORTXL(x, y, z, x_1, y_1, z_1, x_2, v_2, w_2, \Gamma) \tag{3.5}$$

As the wing is divided into panels containing vortex ring elements as shown in Figure 3.1, from the numerical point of view these vortex ring elements can be stored in rectangular patches with indices as shown in Figure 3.1. The induced velocity at an arbitrary point by a typical vortex ring at a location can be computed by applying the vortex line routine in Eqn (3.5) to the rings' four segments:

$$(u_1, v_1, w_1) = VORTXL(x, y, z, x_{i,j}, y_{i,j}, z_{i,j}, x_{i,j+1}, v_{i,j+1}, w_{i,j+1}, \Gamma_{i,j}) \tag{3.6}$$

$$(u_2, v_2, w_2) = VORTXL(x, y, z, x_{i,j+1}, y_{i,j+1}, z_{i,j+1}, x_{i+1,j+1}, v_{i+1,j+1}, w_{i+1,j+1}, \Gamma_{i,j})$$

$$(u_3, v_3, w_3) = VORTXL(x, y, z, x_{i+1,j+1}, y_{i+1,j+1}, z_{i+1,j+1}, x_{i+1,j}, v_{i+1,j}, w_{i+1,j}, \Gamma_{i,j})$$

$$(u_4, v_4, w_4) = VORTXL(x, y, z, x_{i+1,j}, y_{i+1,j}, z_{i+1,j}, x_{i,j}, v_{i,j}, w_{i,j}, \Gamma_{i,j})$$

The total velocity induced by the four vortex segments is then:

$$(u, v, w) = \sum_{i=1}^{4} (u_i, v_i, w_i) \tag{3.7}$$

Eqn (3.7) will be formulated into a subroutine called:

$$(u, v, w) = VORING(x, y, z, i, j, \Gamma) \tag{3.8}$$

For pressure distribution calculations, the local circulation is needed, which for the leading edge panel is equal to Γ_i but for all the elements behind it is equal to the difference Γ_I - Γ_{i-1} .

3.1.2.2 Defining the kinematics of the wing

Consider an inertial frame *X,Y, Z* which is stationary and a body frame *x, y, z* which moves to the left of the page as shown in Figure 3.3. The flight path of the origin and orientation of the *x, y, z* system is assumed to be known and is prescribed as:

$$X_0 = X_0(t),\ Y_0 = Y_0(t),\ Z_0 = Z_0(t) \tag{3.9}$$

$$\phi = \phi(t),\ \theta = \theta(t),\ \psi = \psi(t) \tag{3.10}$$

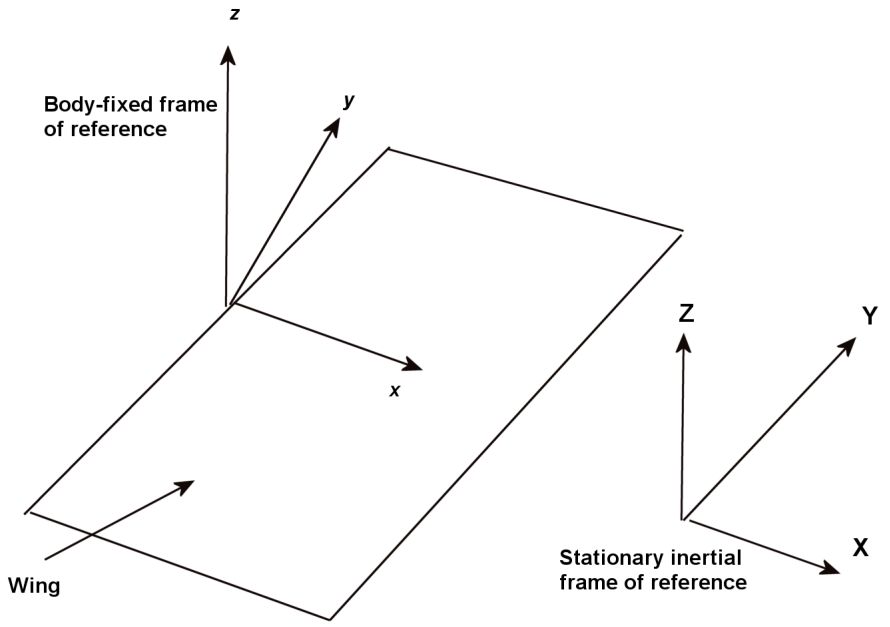

Figure 3.3: Inertial and body coordinates used to describe the motion of the body.

The time-dependent kinematic velocity components *U(t), V(t), W(t)* in the *x, y, z* frame due to the translation velocity and rotation of the body frame of reference can be computed as follows:

$$\begin{bmatrix} U_t \\ V_t \\ W_t \end{bmatrix} = \begin{bmatrix} U_3 \\ V_3 \\ W_3 \end{bmatrix} + \begin{bmatrix} -qz + ry \\ -ry + pz \\ -py + qx - \dfrac{\partial n}{\partial t} \end{bmatrix} \tag{3.11}$$

Where $\begin{bmatrix} U_3 & V_3 & W_3 \end{bmatrix}^T$ is the translational velocity components observed in the body fixed frame; and

$(p,q,r) = (\dot{\phi}(t), \dot{\theta}(t), \dot{\psi}(t))$ is the angular speed of the body fixed frame with respect to the inertial frame

η is the function that defines the geometry of the wing surface and $\eta = \eta(x, y, t)$.

The velocity with reference to the body fixed frame can be calculated by taking a transformation between the two coordinates and may be computed as follow:

$$\begin{bmatrix} U_3 \\ V_3 \\ W_3 \end{bmatrix} = \begin{bmatrix} 1 & 0 & 0 \\ 0 & \cos\phi_t & \sin\phi_t \\ 0 & -\sin\phi_t & \cos\phi_t \end{bmatrix} \begin{bmatrix} \cos\theta_t & 0 & -\sin\theta_t \\ 0 & 1 & 0 \\ \sin\theta_t & 0 & \cos\theta_t \end{bmatrix} \begin{bmatrix} \cos\psi_t & \sin\psi_t & 0 \\ -\sin\psi_t & \cos\psi_t & 0 \\ 0 & 0 & 1 \end{bmatrix} \begin{bmatrix} -X_0 \\ -Y_0 \\ -Z_0 \end{bmatrix} \quad (3.12)$$

$(\phi_t, \theta_t, \psi_t)$ are Euler angles of the body fixed frame around three main principal axes *X, Y, Z* of the inertial frame. To define such a 3D transformation uniquely, it is important to follow to the order of Euler sequence in Eqn (3.12).

3.1.2.3 The wake shedding and roll-up procedure

The wake vortex ring corner points will be created at each time step. During the first time step, only two corner points of the wake are created. These two points are coincident with the trailing segment of the trailing edge vortex ring and they play the role of the starting vortex. Therefore, during the first time step, no wake vortex ring exists. In the second time step, the wing trailing points of the trailing edge vortex ring advances. The free wake vortex rings are created using the two corner points of the trailing edge vortex ring and the two points which are created in the previous time step. This shedding procedure is repeated at each time step and a set of new trailing edge wake vortex rings is created. An example of the wake ("free" wake vortex) created in subsequent steps is shown in Figure 3.1. The strength of the most recently shed wake vortex ring is set to be equal to the strength of the shedding vortex in the previous time step. Once the wake is shed, its strength is unchanged and the wake carries no load and moves with the local velocity. This is the original formulation. However, to improve the accuracy and stability, the wake's strength is allowed to change in the later revision of the code. More details are given in the later section.

Due to the force-free nature of the vortex wake, every vortex moves with the local stream velocity. This local velocity is due to the velocity components induced by the wing and wake. It is usually measured in the inertial frame of reference *(X, Y, Z)*, at each vortex ring corner

point. To obtain the vortex wake roll up, at each time step the induced velocity $(u, v, w)_I$ is calculated and then the vortex elements are moved by:

$$(\Delta x, \Delta y, \Delta z) = (u, v, w)_I \Delta t \tag{3.13}$$

The velocity induced at the wake vortex point is due to a combination of the wing and the wake influence. It can be obtained by using the same influence routine (Eqn (3.8)):

3.1.2.4 The influence coefficients

The influence coefficient is the normal velocity induced at the collocation point of the i^{th} vortex panel by the other vortex panels with unit strength circulation. According to the Newman boundary condition derived in Eqn (3.1), the normal components of the singularity-induced velocity plus the normal components of wing-wake motion induced must be zero. This boundary condition can be expressed in term of influence coefficients as follows:

$$a_{i1}\Gamma_1 + a_{i2}\Gamma_2 + ... + a_{ik}\Gamma_k + ... + a_{im}\Gamma_m + \left[U_t + u_w, V_t + v_w, W_t + w_w\right]_i . \mathbf{n}_i = 0 \tag{3.14}$$

Where $\mathbf{n}_i$ is the normal vector of the i^{th} vortex panel at its collocation point;

Γ_k is the vortex strength of panel *k;*

(U_t, V_t, W_t) are the time-dependent kinematics velocity components due to the motion of the wing and can be calculated using Eqn (3.11);

(u_w, v_w, w_w) are the velocity components induced by the wake vortex rings and can be computed from the strength of wake vortex rings in the previous time step;

a_{ik} is the normal velocity at collocation point *i* induced by unit vortex ring of panel *k*; and

m is MxN

This coefficient can be calculated by:

$$a_{ik} = \begin{bmatrix} u \\ v \\ w \end{bmatrix}_{i,k} . \mathbf{n}_i \tag{3.15}$$

and $(u, v, w)_{i,k}$ is the velocity at collocation point *i* induced by unit vortex ring of panel *k* and

it can be calculated using the subroutine given in Eqn (3.7). The above influence coefficients are calculated in the body fixed frame.

3.1.2.5 The linear set of equations of Newman boundary condition

For each collocation point, an equation can be obtained. The Newman boundary condition must be satisfied on the whole wing surface and hence a system of linear equations is formed. It can be written as:

$$\begin{bmatrix} a_{11} & a_{12} & \dots & a_{1N} \\ a_{21} & a_{22} & \dots & a_{2N} \\ \dots & \dots & \dots & \dots \\ a_{M1} & a_{M2} & \dots & a_{MN} \end{bmatrix} \begin{bmatrix} \Gamma_1 \\ \Gamma_2 \\ \Gamma_3 \\ \Gamma_4 \end{bmatrix} = \begin{bmatrix} -[U_t + u_w, V_t + v_w, W_t + w_w]_1 . \vec{n}_1 \\ -[U_t + u_w, V_t + v_w, W_t + w_w]_2 . \vec{n}_2 \\ \\ -[U_t + u_w, V_t + v_w, W_t + w_w]_M . \vec{n}_M \end{bmatrix} \tag{3.16}$$

Or:

$$[A]_{M\times N}[\Gamma]_{M\times 1} = [RHS]_{M\times 1} \tag{3.17}$$

The unknown vortex strength of all the vortices can be obtained by solving this system of equations using the subroutine LSLRG. It is a linear equation solver from the IMSL numerical libraries by Visual Numerics[‡].

3.1.2.6 Pressure, velocity and load computations

Once all the vortex strengths are known, other flow field parameters can be calculated. Pressure distribution over the wing surface can be computed using the unsteady form of Bernoulli's equation. The pressure difference across a vortex panel (Katz and Plotkin 2001) can be derived from this unsteady form as follows:

[‡] Visual Numerics website: www.vni.com

$$\Delta p = \rho \left(\begin{bmatrix} U_t + u_w \\ V_t + v_w \\ W_t + w_w \end{bmatrix}_{i,j} . \vec{\tau}_i \frac{\Gamma_{i,j} - \Gamma_{i-1,j}}{\Delta c_{i,j}} + \begin{bmatrix} U_t + u_w \\ V_t + v_w \\ W_t + w_w \end{bmatrix}_{i,j} . \vec{\tau}_j \frac{\Gamma_{i,j} - \Gamma_{i,j-1}}{\Delta b_{i,j}} + \frac{\partial \Gamma_{i,j}}{\partial t} \right) \quad (3.18)$$

where $\Delta c_{i,j}$, $\Delta b_{i,j}$ are the chord length and spanwise length of the vortex panel located at point ***(i,j)*** in the array of panels respectively;

$\vec{\tau}_i$ is the chordwise tangential vector of vortex panel at its collocation point;

$\vec{\tau}_j$ is the spanwise tangential vector of vortex panel at its collocation point;

When the pressure difference is known, the force acting on the wing surface due to this pressure difference can be calculated by:

$$\Delta \vec{F}_{i,j} = -(\Delta p \Delta S)_{i,j} . \vec{n}_{i,j} \quad (3.19)$$

Where ΔS is the area the force is acting on. The total force acting on the whole wing surface can be obtained by summing the force on each panel. The force acting on each panel are located at the panel collocation point.

3.1.2.7 Code implementation

The implementation of our ULVM code using the unsteady vortex-lattice algorithm above is depicted in Figure 3.4. To facilitate the coding process, the code is divided into three main modules: pre-processor module, computation model and postprocessor module. The role of each module is clearly shown in the Figure 3.4. The discretization and grid generation are computed in the pre-processor module. Influence coefficients and vortex strengths of all lattices are computed in the computational module. Pressure distribution and other flight parameters are computed in the postprocessor module. Additional information can also be found in Vinh (2005) and Katz and Plotkin (2001).

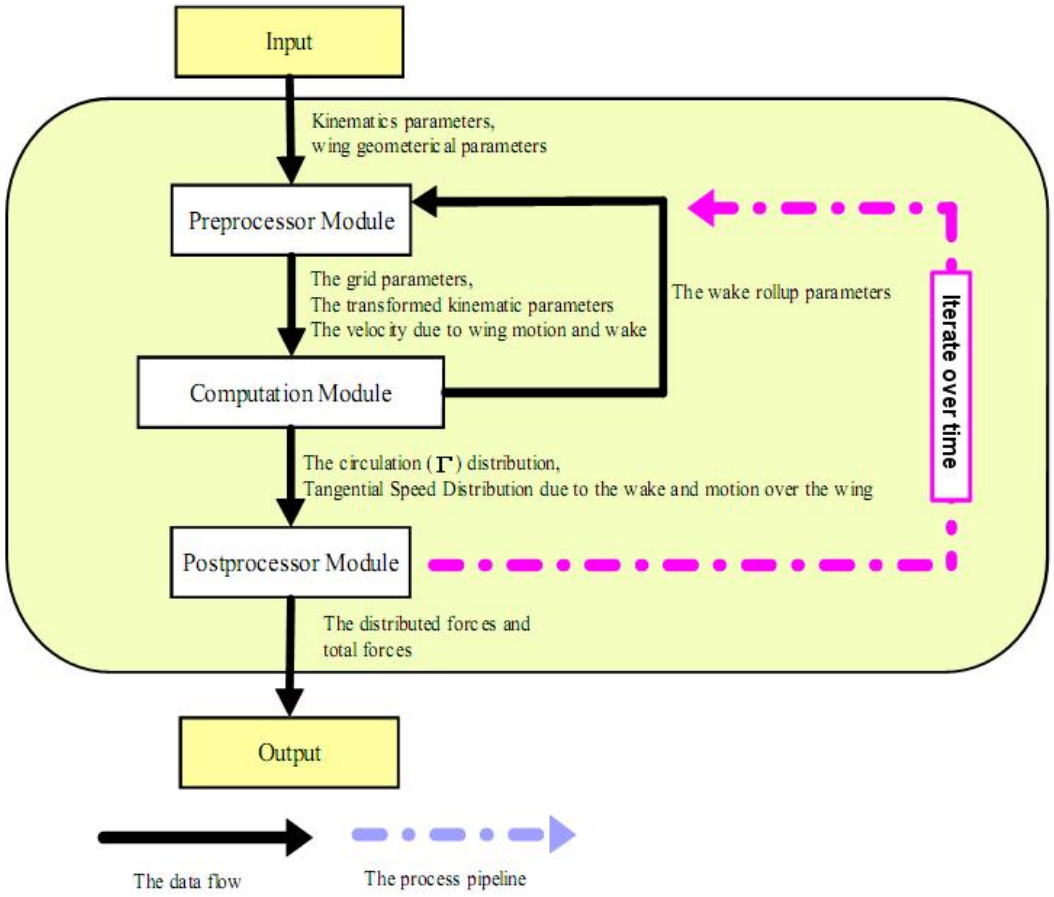

Figure 3.4: Flow chart of the UVLM code. This picture is taken from Vinh (2005)

3.1.3 Modifications and improvements to code

The ULVM code had been developed based on the sample code by Katz and Plotkin (2001). The code was modified to solve for cambered wing moving in any arbitrary motion. Details of this modification and improvements are given below.

3.1.3.1 Geometry model

Along the spanwise direction, the wing surface is divided into some major panels. These panels are modelled using four corner points, root cambered line and rear cambered line. Each major panel is then divided into small minor panels based on the given number of rows and columns. The discretization procedure described above allows one to model wing with

camber and spanwise chord variation.

3.1.3.2 Movement of the wing

The movement of the wing is a prescribed motion. This prescribed motion is a combination of two separated movement of the wing frame and the body frame in the inertial frame. Using the kinematic model above, any prescribed motion can be used for UVLM code. This feature allows one to use the UVLM code not only for flapping wing problems but also for other complex wing movement such as the cyclogyro (Hu et al. 2006).

3.1.3.3 Graphic user interface and vortex visualization

To facilitate the user input, a friendly graphic user interface (Figure 3.5) is provided to simplify the execution of the program. It enables us to visualise the movement of the wings and shedding of the wake, as shown in Figure 3.6. Computed forces are presented in the chart and can be exported to Excel format file for verification purposes, as shown in Figure 3.7.

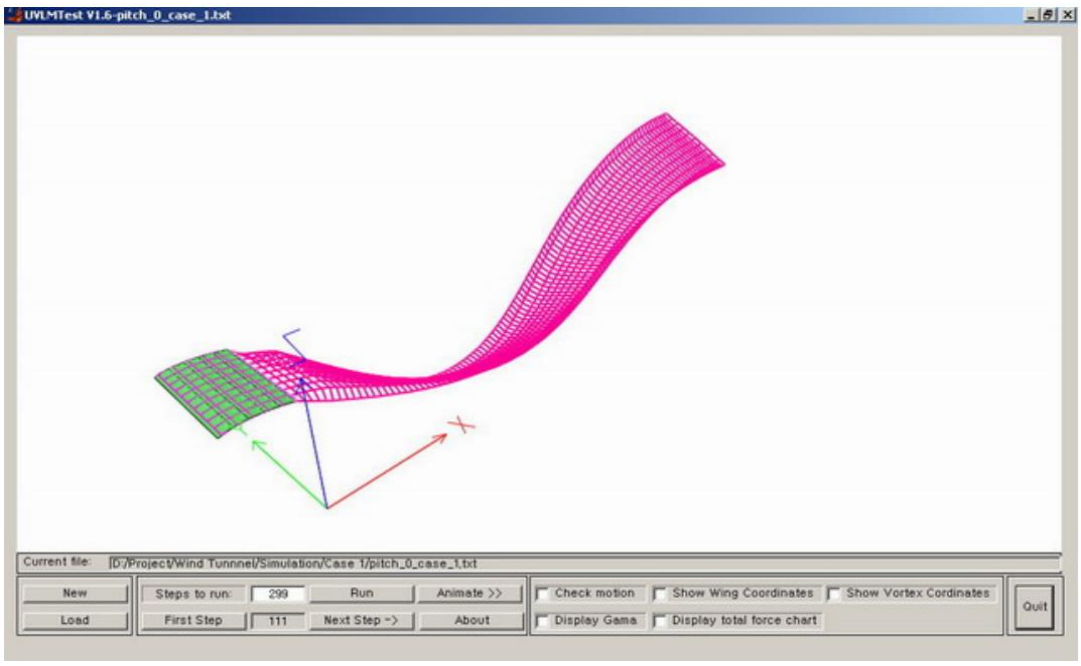

Figure 3.5: Graphic user interface of the UVLM code

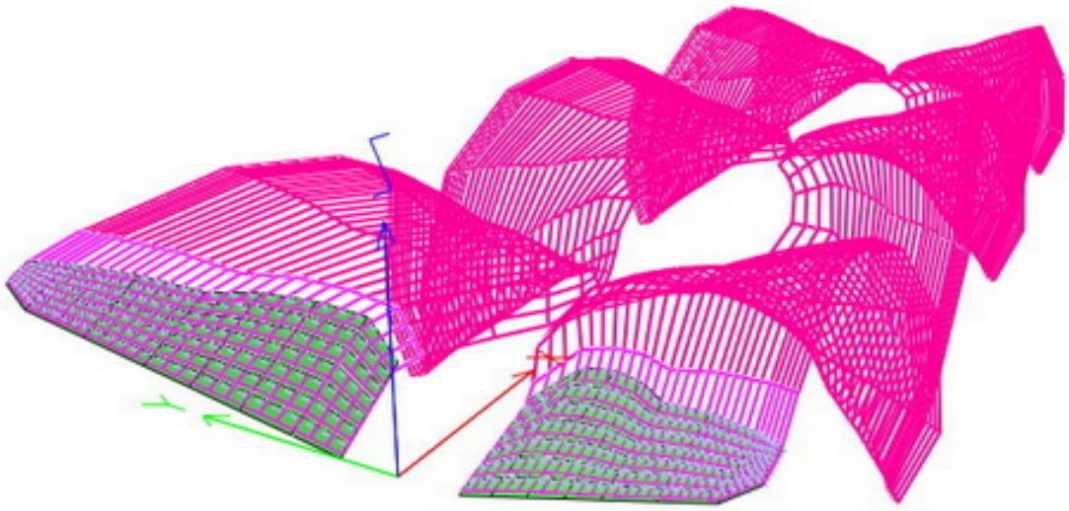

Figure 3.6: Wake rollup produced by a moth wing after some time steps

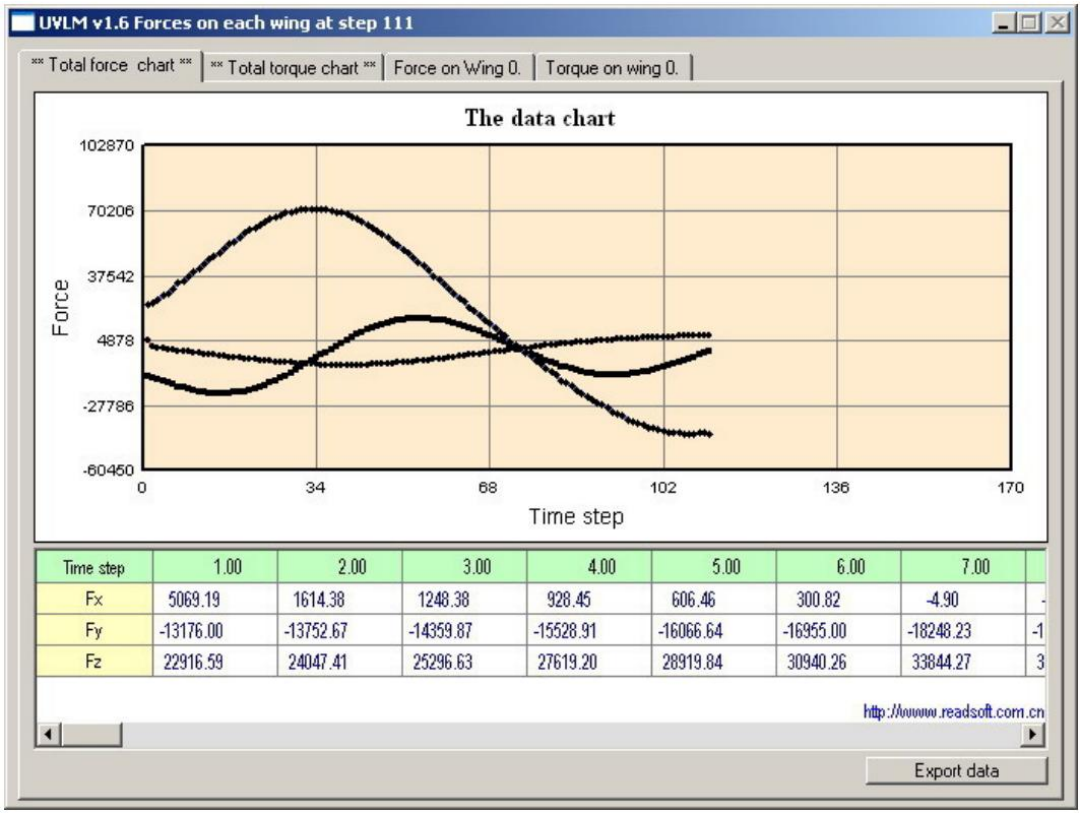

Figure 3.7: An example of pop-up dialog of computed force

3.1.3.4 Vortex blob modifications

The Biot-Savart's Law used to evaluate the induced velocity at a point due to a line vortex

goes to infinity as the distance approaches zero. This results in the instability of the program and it is especially severe in the case when the vortex wakes are very close to the point of evaluation. It usually happens in the hovering case because the aircraft is stationary and hence the wake left by the wing will intersect the same wing after several revolutions. The radius r in Eqn (3.3) becomes very small and the induced velocity becomes very large, resulting in spikes. Figure 3.8 and Figure 3.9 show the spikes appearing in the wake and the aerodynamic forces' graph respectively.

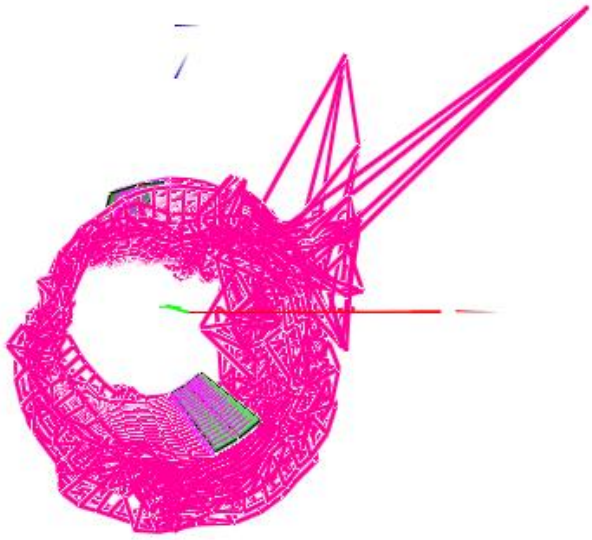

Figure 3.8: Spikes appearing during the computation of the wake

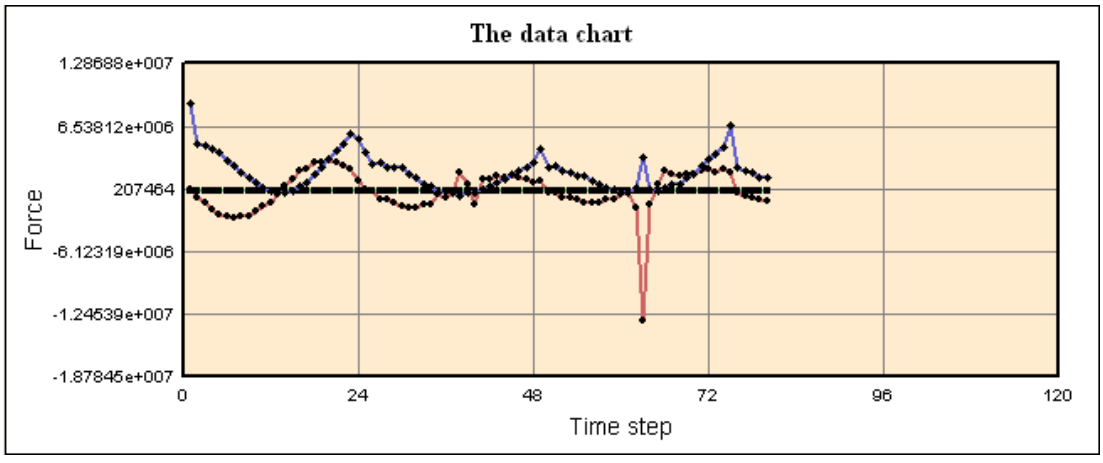

Figure 3.9: Forces with spikes showing irregularities (red and blue represent forces in the x and y directions respectively)

One of the popular methods is to replace the line vortex by a vortex "blob", which is a vortex

with an invariable (Szymendera 2002) or variable (Gandhi and Tauszig 2000) core size. There are different models of the vortex "blob". The common ones include the "Rankine", "Lamb", "Scully" and "Vatistas" models. Figure 3.10 shows a comparison of the different models.

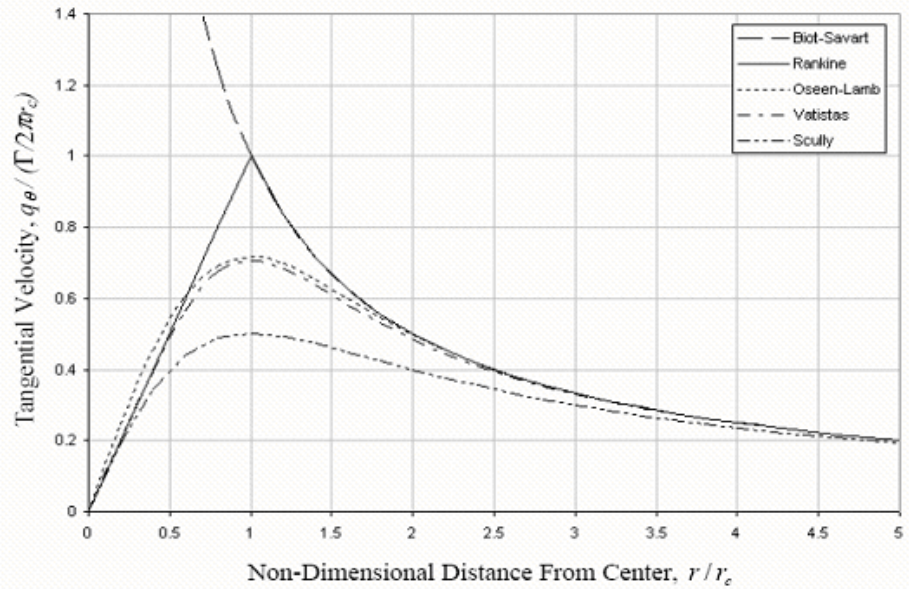

Figure 3.10: Comparison of different vortex models

Besides different models, one also has to select the size of the core and the conditions to switch between the original Biot-Savart law and the new model. Since the choice of these three variables often depends on specific problems, some trial and error processes might be necessary.

In the first modification, the core size is kept fixed. Results show that the Scully vortex model (Scully 1968), whose formulation is given earlier, is the best among the different models. After some trial and error, it is found that a core radius of $r_c = 0.2*dl$ gives the best result. The new improved wake model has much less "spikes" than the original program. However, there are still some remaining "spikes" appearing during the visualization of the wake vortex and in the graphs of lift and thrust forces.

In the second modifications, the vortex core is no longer fixed. Instead, the core is allowed to increase its size, starting from a radius of zero. This model more closely reproduces the actual

physical effect. This is because in reality, viscosity will cause the vortex to expand and reduce its effect as time progresses. After some time, the effect of the wake vortex will be reduced to zero.

The formula of the core radius r_c is given by:

$$r_c(t) = 2.24\sqrt{\upsilon\delta t} \tag{3.20}$$

where ν is the kinematic viscosity of air, t is the time and δ is the turbulent viscosity coefficient. It is given by the expression

$$\delta = 1 + a_1 \frac{\Gamma}{\upsilon} \tag{3.21}$$

where a_1 is the empirical coefficient, which has a nominal value of 10^{-1}, as recommended by Gandhi and Tauszig (2000).

Similar to the first modification, the Scully vortex model gives the best results. Figure 3.11 and Figure 3.12 show the results for the fixed and variable core diffusion method respectively. Comparing between the circled regions, the second modification gives a much smoother graph.

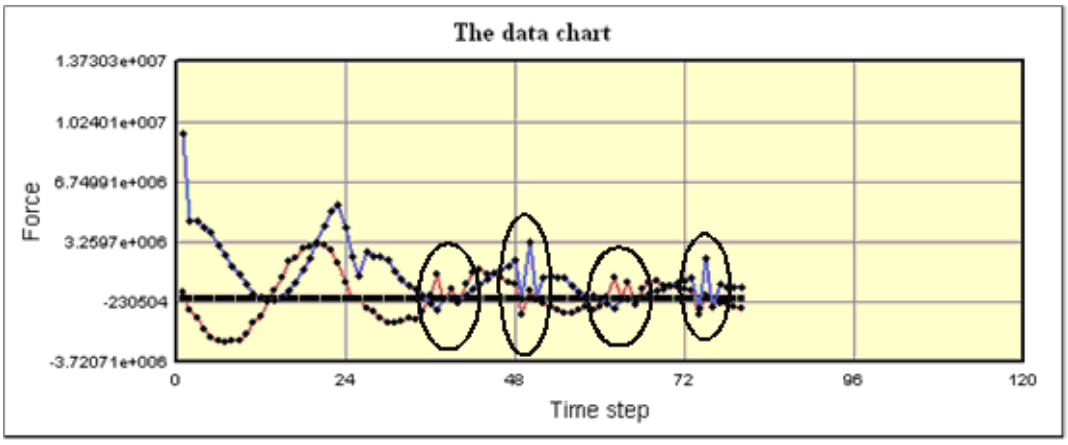

Figure 3.11: First modification, with fixed core size

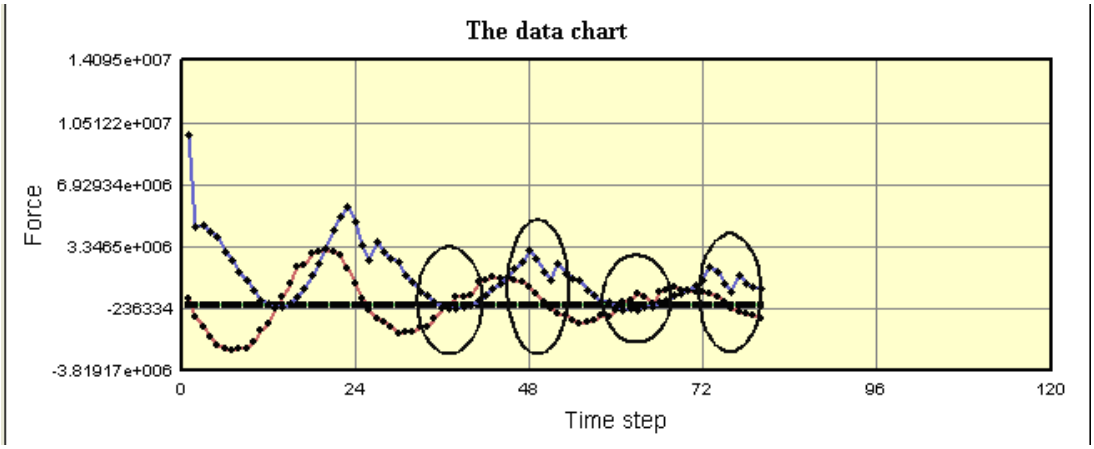

Figure 3.12: Second modification, with variable core size

3.1.4 Verification of the UVLM

The UVLM is an inviscid solver and it is meaningless to specify a *Re* for the solver. However, it is important to determine if the solver is appropriate for low Re flow study. The accuracy of the UVLM is verified using two sets of experiments. The first test is a comparison with the experimental result of the Cyclogyro (Hu et al. 2006). A test model, shown in Figure 3.13, is equipped with 3 blades of chord length 33mm and blade span 130mm. The *Re* for the test case ranges from 8.984×10^3 to 2.326×10^4. The graphs in Figure 3.14 show that the simulation based on UVLM can give acceptable results. However, the UVLM tends to underestimate the total lift forces in both cases of NACA0012 and flat plate airfoil. The reason is because the blade AOA changes very fast and it seems that the solver is not able to handle high frequency rotation well. More details is given in the later part of this section.

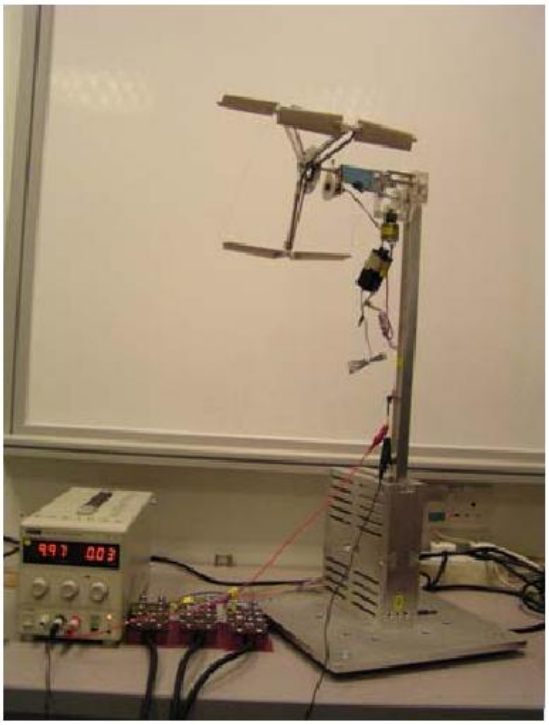

Figure 3.13: The force balance with the cycloidal propeller test model installed

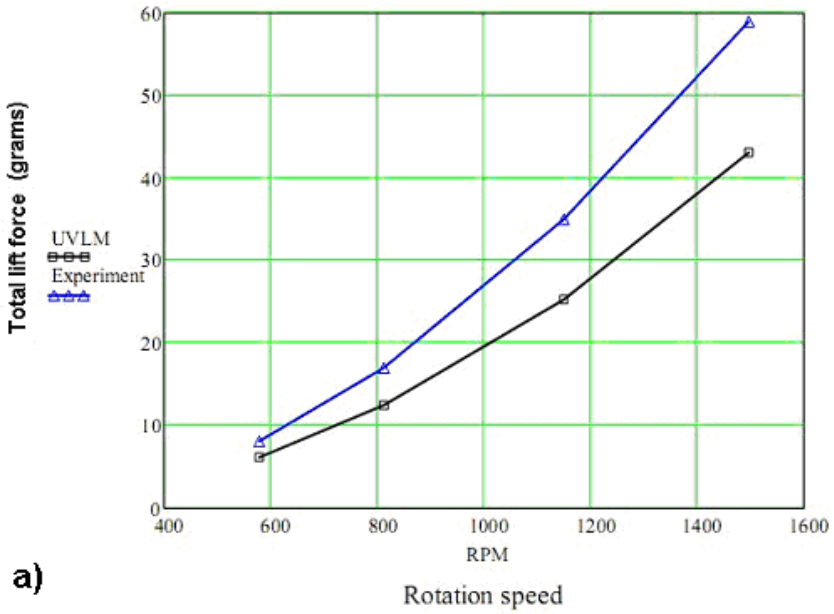

Figure 3.14: Lift force comparison of the cycloidal propeller with (a) 70mm radius, NACA 0012 airfoil (b) 150mm radius and flat plate airfoil (continue on next page)

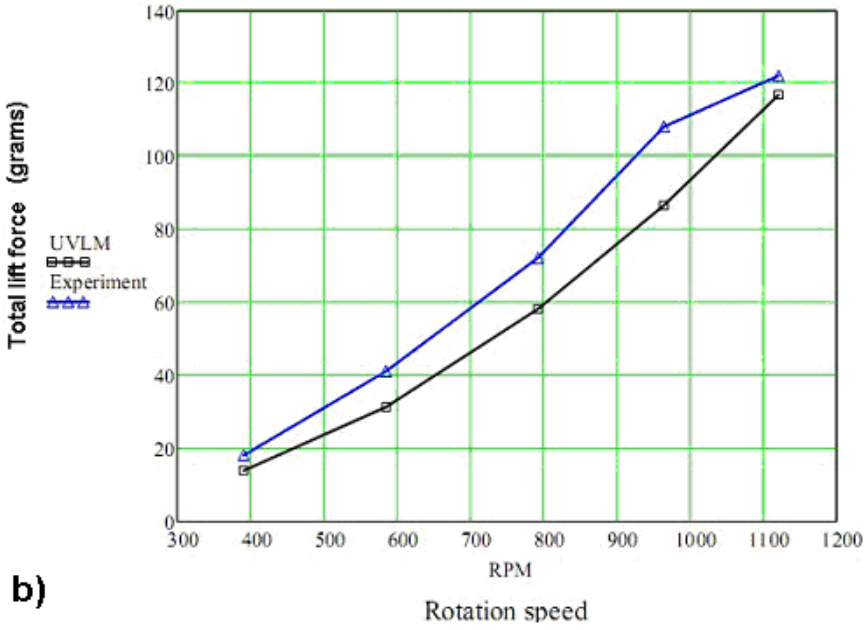

The second experiment is a comparison of the simulation results with that of the experimental ones of a rectangle rigid flapping wing. Two cases at Re = 2.2x10^4, k = 0.0127 and Re = 0.8x10^4, k = 0.159 are tested. This comparison was done by Vinh (2005) and more details can be found in his thesis. Due to the limitation of the apparatus, it is only possible to measure the lift force generated by the wing. The thrust force generated is too small and the apparatus is not sensitive enough.

The simulation was done using UVLM with 722 panels to model the wing. A total of 300 time steps are required for two flapping cycles. It is found that the UVLM under predicts the lift force for both cases. Averaging over one cycle, the computed forces are 1/10 and 1/3 of the measured ones at Re = 0.8x10^4 and 2.2x10^4 respectively. Figure 3.15 shows the lift force graphs of the two cases.

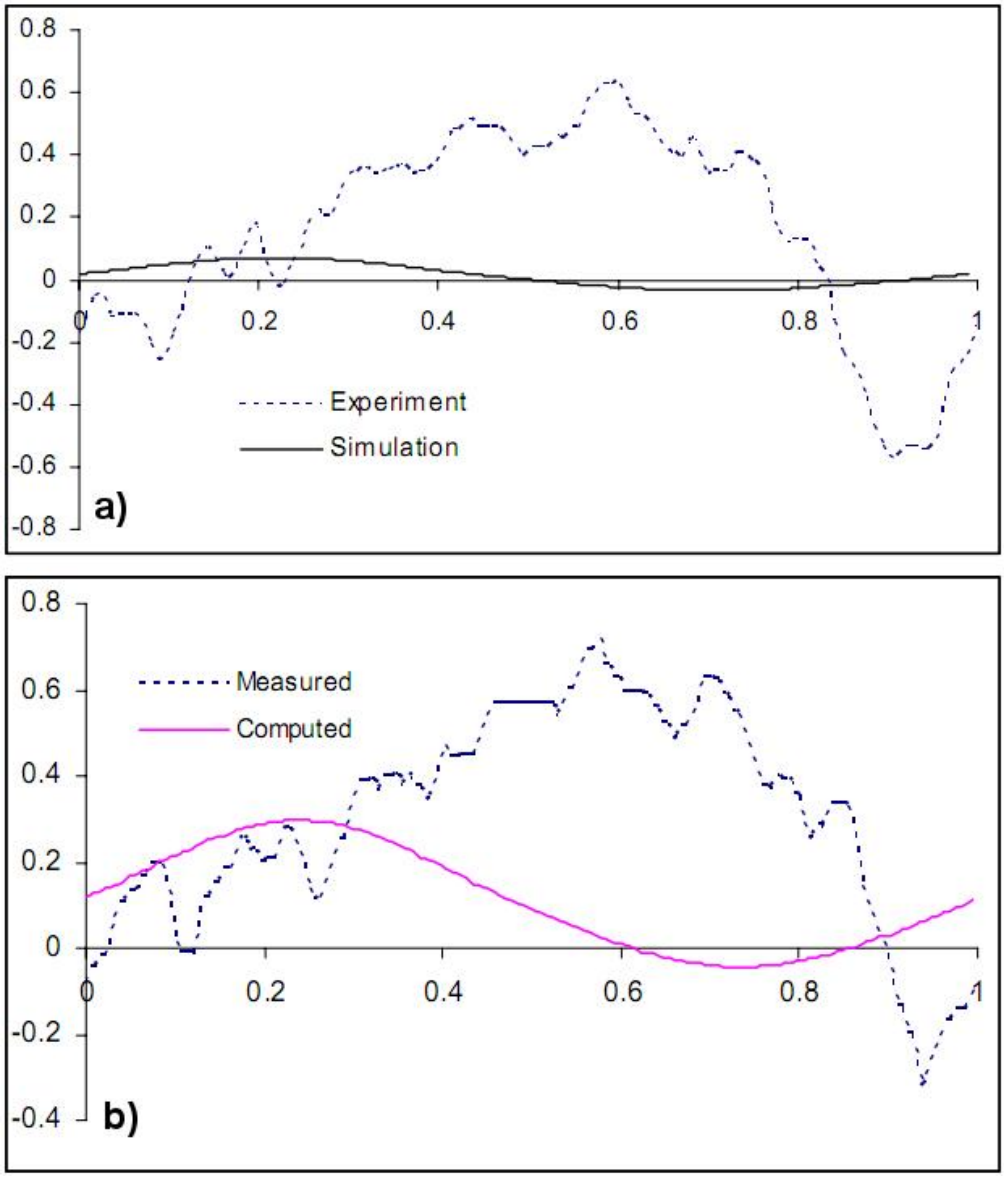

Figure 3.15: Simulated and experimental results of the lift force of the Re = a) 2.2×10^4 and b) 0.8×10^4 cases

Ames et al. (2002) also did similar experiments and compared with their own panel code. In their studies, they also had two cases. The first case had a flapping frequency of 1 Hz and freestream velocity of 18.29 m/s while the second one had f = 1 Hz and U_∞ = 3.05 m/s. The first case represented a scenario of high reduced frequency and low *Re* while the second case represented one of low *k* and low *Re*. The results showed that their panel code greatly underpredicted the force variation for the first case. On the other hand, the panel code overpredicted the force slightly for the second case. According to Ames et al. (2002), at the limit of high reduced frequency and low *Re*, the flow field is dominated by large instantaneous

angle of attack, separated flows, smeared distributed regions of vorticity and shear layers with discrete vertical structures. None of the above factors is expected to be captured in the panel code. However, these factors are less substantial at higher *Re* and low reduced frequency and so the experimental results compared reasonably well. This may be why the first set of tests which uses the Cyclogyro gives acceptable but underestimated results.

Jones et al. (2002) experimental results showed that for $Re \geq 4x10^4$, their inviscid panel code is an acceptable model. Zhu (2007) also compared his results obtained from the panel method with the experimental results of Anderson et al. (1998) and found that their results were similar up to $St = 0.3$. At $St > 0.3$, leading edge separation occurs. Thus, the UVLM can still be useful as a preliminary tool to give a rough estimate of the lift and thrust force due to its low computational requirement. A full Navier Stokes solver still has to be used to confirm the results.

3.2 Structured Collated Navier Stokes Solver (SCNSS)

The UVLM software presented in the previous section is only able to simulate a subset of situations for the flapping wings. Hence a more robust solver must be used. Due to the low *Re* requirement, a Navier Stokes solver must be used.

3.2.1 Algorithm of the SCNSS

3.2.1.1 Fractional step method

The viscous flow around the flapping airfoil is computed using the incompressible Navier Stokes equations in the Arbitrary-Lagrangian-Eulerian (ALE) (Hirt et al. 1997) formulation, as shown in Eqns (3.22) and (3.23). The equations are solved using the fractional step method on

structured C-grids and it is based on the method by Kim and Choi (2000). As mentioned in the literature review in section 2.1, it is easier to code on structured grids since it is a non-staggered method. Moreover, future extension to 3D is also possible compared to a vorticity-stream function solver. However, there are a number of differences between the current solver and that of Kim. The ALE formulation is used instead of the original formulation in order to accommodate the flapping airfoil. Thus, the grid in the current solver also needs to move and morph according to the motion and flexibility of the airfoil. More details about this modification are given in the next section. Due to the collocated or nonstaggered grid system, an additional variable known as the face normal velocity must be defined to prevent pressure oscillations. Figure 3.16 shows part of the nonstaggered C-grid. U_N, U_S, U_E, U_W represent the normal north south, east, west face velocity respectively.

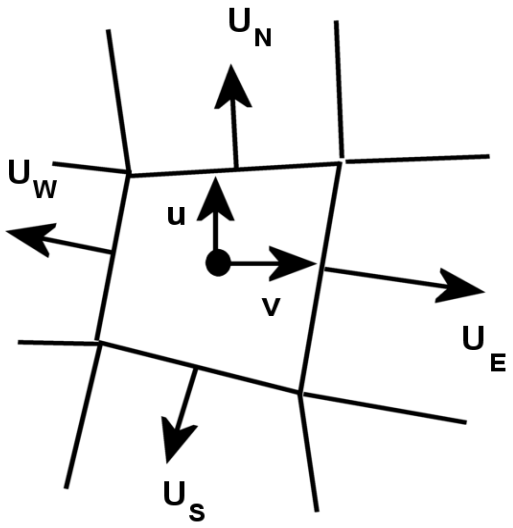

Figure 3.16: Part of the present nonstaggered structured grid

$$\frac{\partial u_i}{\partial t} + \frac{\partial}{\partial x_j}(u_i(u-u_b)_j) = \frac{\partial p}{\partial x_i} + \frac{1}{\mathrm{Re}}\frac{\partial}{\partial x_j}\frac{\partial}{\partial x_j}u_i \tag{3.22}$$

$$\frac{\partial u_i}{\partial x_i} = 0 \tag{3.23}$$

Where x_i are the Cartesian coordinates and u_i are the corresponding velocity components. u_b refers to the grid velocity.

Eqns (3.22) and (3.23) are discretized by using the Crank Nicolson scheme for both the convective and viscous terms to obtain a second order fully implicit time advancement scheme below:

$$\frac{u_i^{n+1}-u_i^n}{\Delta t}+\frac{1}{2}\frac{\partial}{\partial x_j}(u_i^{n+1}(u-u_b)_j^n+u_i^n(u-u_b)_j^{n+1})= \\ -\frac{\partial p^{n+1}}{\partial x_i}+\frac{1}{2}\frac{1}{\mathrm{Re}}\frac{\partial}{\partial x_j}\frac{\partial}{\partial x_j}(u_i^{n+1}+u_i^n) \tag{3.24}$$

$$\frac{\partial u_i^{n+1}}{\partial x_i}=0 \tag{3.25}$$

A fully implicit scheme is preferred because it is more stable compared to semi-implicit schemes such as the Adams-Bashforth method. Next, the fractional method is applied to Eqns (3.24) and (3.25) to give:

$$\frac{\hat{u}_i-u_i^n}{\Delta t}+\frac{1}{2}\frac{\partial}{\partial x_j}(\hat{u}_i(u-u_b)_j^n+u_i^n(\hat{u}-u_b)_j)=-\frac{\partial p^n}{\partial x_i}+\frac{1}{2}\frac{1}{\mathrm{Re}}\frac{\partial}{\partial x_j}\frac{\partial}{\partial x_j}(\hat{u}_i+u_i^n) \tag{3.26}$$

$$\frac{u_i^*-\hat{u}_i}{\Delta t}=\frac{\partial p^n}{\partial x_i} \tag{3.27}$$

$$\frac{\partial}{\partial x_i}\frac{\partial p^{n+1}}{\partial x_i}=\frac{1}{\Delta t}\frac{\partial u_i^*}{\partial x_i} \tag{3.28}$$

$$\frac{u_i^{n+1}-u_i^*}{\Delta t}=-\frac{\partial p^{n+1}}{\partial x_i} \tag{3.29}$$

Where $\hat{u}_i$ and u_i^* are the intermediate velocities. Eqns (3.26) to (3.29) are integrated over each cell area *A* and after the divergence theorem is applied, one can get:

$$\frac{\delta\hat{u}_i}{\Delta t}A+\frac{1}{2}\sum_f F_f^c(\delta\hat{u}_i,(U^n-U_b^n))+F_f^c(u_i^n,\overline{\delta\hat{u}_j}n_j)+\frac{1}{2}\sum_f F_f^d(\delta\hat{u}_i) \\ =-\sum_f\overline{p^n}n_i\Delta l-\sum_f F_f^c(u_i^n,(U^n-0.5U_b^n-0.5U_b^{n+1}))-\sum_f F_f^d(u_i^n) \tag{3.30}$$

$$u_i^*-\hat{u}_i=\frac{\Delta t}{A}\sum_f\overline{p^n}n_i\Delta l \tag{3.31}$$

$$\sum_f \frac{\partial p^{n+1}}{\partial x_i} n_i \Delta l = \frac{1}{\Delta t} \sum_f U^* \Delta l \tag{3.32}$$

$$u_i^{n+1} - u_i^* = -\frac{\Delta t}{A} \sum_f \overline{p^{n+1}} n_i \Delta l \tag{3.33}$$

$$U^{n+1} - U^* = -\Delta t \frac{\partial p^{n+1}}{\partial x_i} n_i \tag{3.34}$$

Where $\delta \hat{u}_i = \hat{u}_i - u_i^n$, $U = (u_i)_{face} n_i$, $(u_i)_{face}$ and n_i are the Cartesian velocities and outward normal unit vector on the cell edge respectively, $U^* = \overline{u_i^*} n_i$, superscript $\bar{}$ indicates interpolation, subscript *b* indicates grid velocity, and Δl is the length of the edge of the cell

Note that the face normal velocity U^{n+1} is divergence-free and $\oint_l U^{n+1} dl = 0$

$F_f^d(u) = -\frac{1}{\mathrm{Re}}(\nabla u \cdot \hat{n}) \Delta l$ is the viscous flux of *x*-momentum through face of length Δl with unit normal $\hat{n}$.

$F_f^c(u) = U^n \overline{u_f} \Delta l$ is the convective flux of *x*-momentum through face of length Δl.

During the evaluation of Eqns (3.30) to (3.34), Φ and $\frac{\partial \Phi}{\partial n}$ at the mid-point on each cell face will be required, where Φ is an arbitrary flow variable. The interpolation scheme used follows the scheme recommended by Kim and Choi (2000). The system of linear equations obtained from the momentum and Poisson equations are solved using PETSc (Balay et al. 2004), a linear equation solver and hypre (Falgout et al. 2006), a multigrid solver respectively. The code is developed entirely in this work using Fortran90 by the author. The reader can refer to the paper by Kim and Choi (2000) for more details about the solver.

3.2.1.2 C-grid and grid motion

The C-grids for the simulation are generated using the software Pointwise Gridgen. Figure 3.17 shows an example of the grid. The domain size for the airfoil is such that the distances of

the top/bottom, inflow, and farfield boundary to the airfoil are 8.0, 7.0, and 15.0 units respectively.

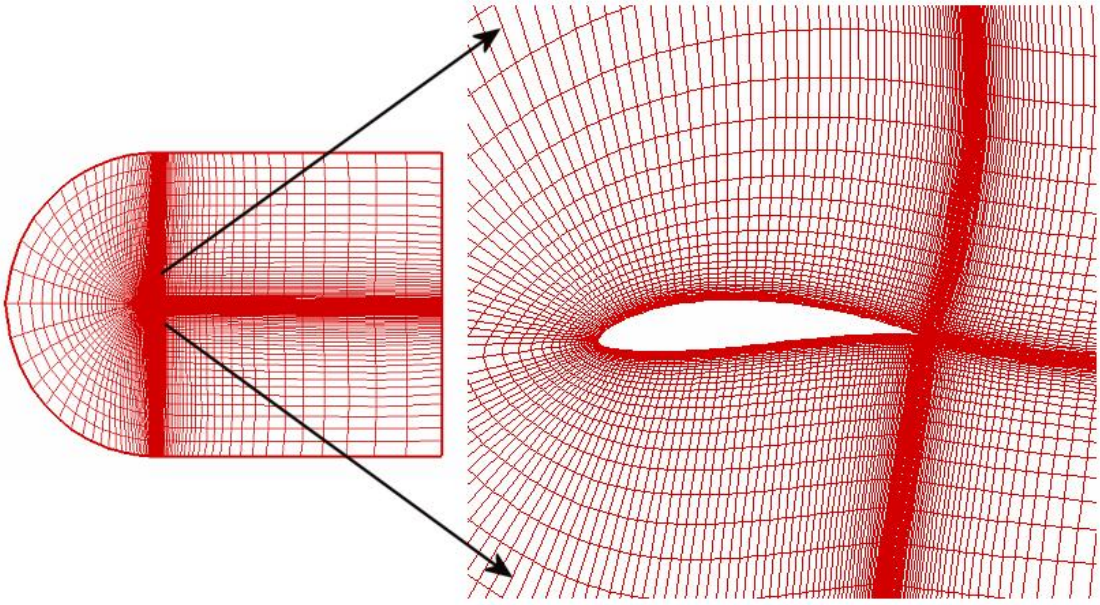

Figure 3.17: An example of the 240x80 C-grid for the SCNSS and its magnification

In the original algorithm given by Kim and Choi (2000), the body of interest is not moving and hence the grid is fixed. Now, in order to simulate the flapping and flexing airfoil, the grid needs to move or deformed. If the airfoil simulated is only moving and its shape is unchanged, the whole C-grid moves together. On the other hand, if the shape of the airfoil changes due to flexing, the grid is deformed to match the new shape of the airfoil using arc-length-based TFI (Jones and Samareh-abolhassani 1995). As mentioned earlier in the literature review, the arc-length-based transfinite interpolation is much better than Batina's (1990) spring based algorithm. The arc-length-based TFI is applied in the following ways:

1. Parameterize all grid points on a surface. Firstly, all of the arclengths on a surface are calculated by adding up all the displacements along a grid line. This is achieved by keeping the other index fixed while varying the other. Hence, the arclength parameter in the *i* direction, fixing *j* is given by:

$$s_{1,j} = 0$$
$$s_{i,j} = s_{i-1} + \sqrt{(x_{i,j} - x_{i-1,j})^2 + (y_{i,j} - y_{i-1,j})^2} \tag{3.35}$$

For $i = 2,\ldots, i_{max}$, where i_{max} is the maximum grid index in the i direction.

The normalized arclength parameter for this grid line is then defined as:

$F_{i,j} = s_{i,j} / s_{i\,max,\,j}$

The same procedure is used for the j direction as well and defined as $G_{i,j}$.

2. Compute all edge and corner point deformations.

3. Perform the 1D TFI of the deformations in the i and j directions given by:

$$\Delta E_{i,1} = (1 - F_{i,1})\Delta P_{1,1} + F_{i,1}\Delta P_{i\max,1} \text{ (in } i \text{ direction when } j = 1)$$

Where ΔE refers to the deformation of an edge, $\Delta P_{1,1}$ and $\Delta P_{i\,max,1}$ are the deformations of two corner points of the edge.

4. Perform the 2D TFI of the deformations. The 2D TFI is:

$$\begin{aligned}\Delta S_{i,j} &= A_{i,j}\Delta E_{1,j} + B_{i,j}\Delta E_{i\max,j} + C_{i,j}\Delta E_{i,1} + D_{i,j}\Delta E_{i,j\max} \\ &- A_{i,j}C_{i,j}\Delta P_{1,1} - B_{i,j}C_{i,j}\Delta P_{i\max,1} - A_{i,j}D_{i,j}\Delta P_{1,j\max} - B_{i,j}D_{i,j}\Delta P_{i\max,j\max}\end{aligned} \tag{3.36}$$

Where ΔS, ΔE and ΔP refer to the surface, edge and corner point deformations respectively. The subscripts refer to the indices of the grid and they vary from (1,1) to (i max, j max). A, B, C, D are blending functions proposed by Soni (1985) and given by:

$$\begin{aligned}A_{i,j} &= 1 - \eta_{i,j}, B_{i,j} = \eta_{i,j} \\ C_{i,j} &= 1 - \zeta_{i,j}, D_{i,j} = \zeta i_{i,j}\end{aligned} \tag{3.37}$$

Where

$$\begin{aligned}P_{i,j} &= 1 - (F_{i,j\max} - F_{i,1})(G_{i\max,j} - G_{1,j}) \\ \zeta_{i,j} &= \frac{F_{i,1} + G_{1,j}(F_{i,j\max} - F_{i,1})}{P_{i,j}} \\ \eta_{i,j} &= \frac{G_{1,j} + F_{i,1}(G_{i\max,j} - G_{1,j})}{P_{i,j}}\end{aligned} \tag{3.38}$$

5. Add the deformations to the original grid to get the final grid.

6. The grid velocity is given by $\dfrac{\left(x_{i,j}^{new} - x_{i,j}^{old}\right)}{\Delta t}$ or $\dfrac{\left(y_{i,j}^{new} - y_{i,j}^{old}\right)}{\Delta t}$ (3.39)

where the $\bullet^{new}$ and $\bullet^{old}$ superscripts refer to the x,y at their new and old positions

respectively. Δt is the time interval.

The space conservation law, proposed by Demirdizic and Peric (1988) has been incorporated to consistently compute the cell area for the moving boundary.

3.2.1.3 Boundary conditions

For the C-grid, the boundary conditions used are

1. Inflow boundary - $u_x = u_\infty = 1$, $u_y = 0$, $dp/dx = 0$ (3.40)
2. Top/bottom boundary - $u_y = 0$, $du_x/dy = 0$, $dp/dy = 0$ (3.41)
3. Outflow boundary - $\frac{\partial u_i}{\partial t} + c\frac{\partial u_i}{\partial x} = 0$, where c is space-averaged streamwise velocity at the exit (Pauley et al. 1990), $p = 0$ (3.42)

3.2.1.4 Force coefficients and efficiency computation

Since the Navier stokes equations have been non-dimensionalized, the thrust (C_t), lift (C_l), and pressure coefficients (C_p) are:

$$C_t = \frac{T}{0.5\rho U_\infty^2 c} \tag{3.43}$$

Due to non-dimensionalization, density ρ = 1 unit, freestream velocity U_∞ = 1 unit, aerofoil chord c = 1 unit, therefore

$$C_t = 2T \tag{3.44}$$

Similarly,

$$C_l = 2L \tag{3.45}$$

$$C_p = 2p \tag{3.46}$$

The non-dimensional thrust (T), lift force (L), and pressure are the outputs from the simulation program. Due to the conformal C-grid, the thrust and lift due to the pressure and viscous forces are obtained on the surface of the airfoil and then summed up. Power input ***P(t)*** can be defined as the amount of energy imparted to the airfoil to overcome the fluid forces. It is given as:

$$P(t) = -L(t)\frac{dh}{dt} - M(t)\frac{d\theta}{dt} \tag{3.47}$$

M(t) is the moment created by the lift and drag forces at the pitching axis. Propulsive efficiency, η, which is a measure of the energy lost in the wake versus energy used in creating the necessary thrust, is given by:

$$\eta = \frac{\bar{C}_t}{\bar{P}} \tag{3.48}$$

3.2.2 Verification of the SCNSS

In order to ensure the accuracy of the solver, the solver is validated using 5 tests. The experimental data from Vinc (2005) is not used for the verification of the simulation results because the original intention of the experiment is to validate against the 3D UVLM code. Hence, the aspect ratio of the wing of the test model for the wind tunnel is only 4. Moreover, the model flaps at its root and so it is inherently 3D. This makes the comparison difficult with a 2D solver very difficult.

The first test is a comparison with the experimental results of Koochesfahani (1989), as shown in Figure 3.18. The $\bar{C}_t$ obtained using the SCNSS are slightly higher than that of Ramamurti's (1999), although it still under-predicts the $\bar{C}_t$. The reason for this discrepancy has been discussed in Ramamurti (1999) and Young (2005). Several effects such as contribution of unsteady terms and pressure differences between the upstream/downstream had been ignored during the measurement of thrust forces and this could have contributed to its over-prediction.

The second test is a comparison with the results by Tuncer and Kaya (2003). The airfoil is simulated to be flapping at 2 different configurations. The first one is a pure heaving case using a NACA0014 airfoil, while the other is a combined pitching and heaving case, using a

NACA0012 airfoil. They are computed at Re = 1.0x10^4. Table 3.1 shows the parameters used and the results obtained. It shows that the current solver's results compare reasonably well with Tuncer and Kaya's (2003), although the mean thrust coefficient is higher than theirs in the second case.

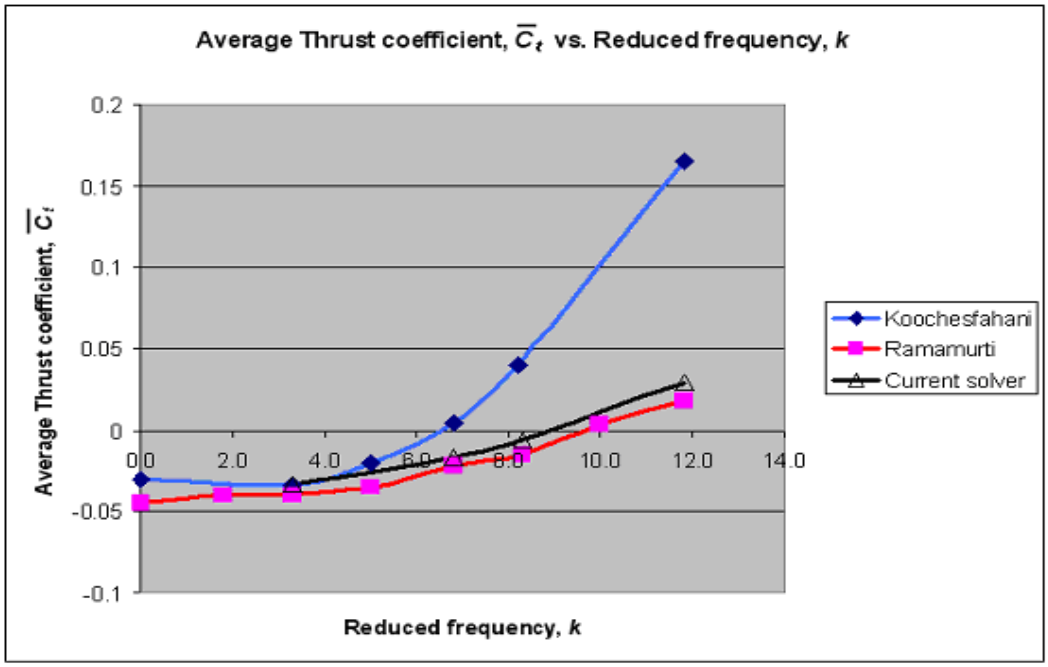

Figure 3.18: Mean thrust coefficient vs. reduced frequency[§] for a NACA0012 airfoil pitching at a maximum pitching amplitude of $\theta_0 = 2^o$

Table 3.1: Comparison between Tuncer and Kaya's and current results

	First case (NACA0014)	**Second case (NACA0012)**
h_0	0.4	0.45
θ_0 / degrees	0.0	15.4
k	2.0	1.0

[§] The reduced frequency defined in Koochesfahani's experiment is $\pi fc / U_\infty$

ϕ / degrees	Not applicable	82.4
Tuncer and Kaya's $\bar{C}_t$	0.25	0.08
Current $\bar{C}_t$	0.23	0.107
Tuncer and Kaya's η / %	Not applicable	58.5
Current η / %	Not applicable	55.0

The third test is a comparison with the experimental results from 2 test cases by Anderson et al. (1998), as shown in Figure 3.19 and Figure 3.20. The *Re* used in this case is 40,000. The laminar Navier Stokes numerical results by Young (2005) are also included in the graph. The flapping parameters, taken from Figure 6 and Figure 7 of Anderson et al. (1998), are given in Table 3.2. There is good agreement with the experimental results of Anderson et al. (1998) and Young (2005) in terms of shape and location of the peak η. The $\bar{C}_t$ results are very similar. However, the η of the current solver's and Young's (2005) numerical results are lower than that of Anderson et al. (1998). It is interesting to note that Young (2005) mentioned in his thesis that the experimental results give higher η than his Garrick or UPM models, both of which can be considered "ideal" cases in that there is no separation.

Table 3.2: Flapping parameters for comparison against experimental results, taken from Figure 6 to 9 of Anderson et al. (1998)

	h	α_0 [**]	ψ	k
Case 1	0.25	15°	90°	0.00 – 2.15
Case 2	0.75	15°	90°	0.00 – 1.06

[**] $\alpha_0 = -\theta_0 + \tan^{-1}(2kh)$, according to Anderson et al. (1998)

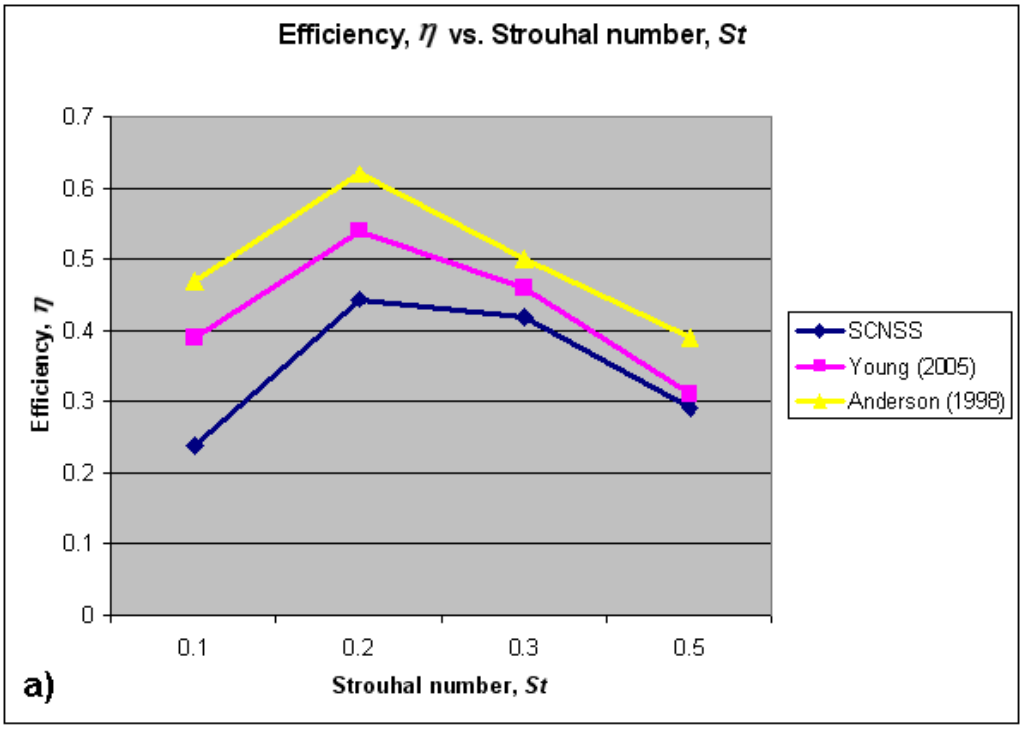

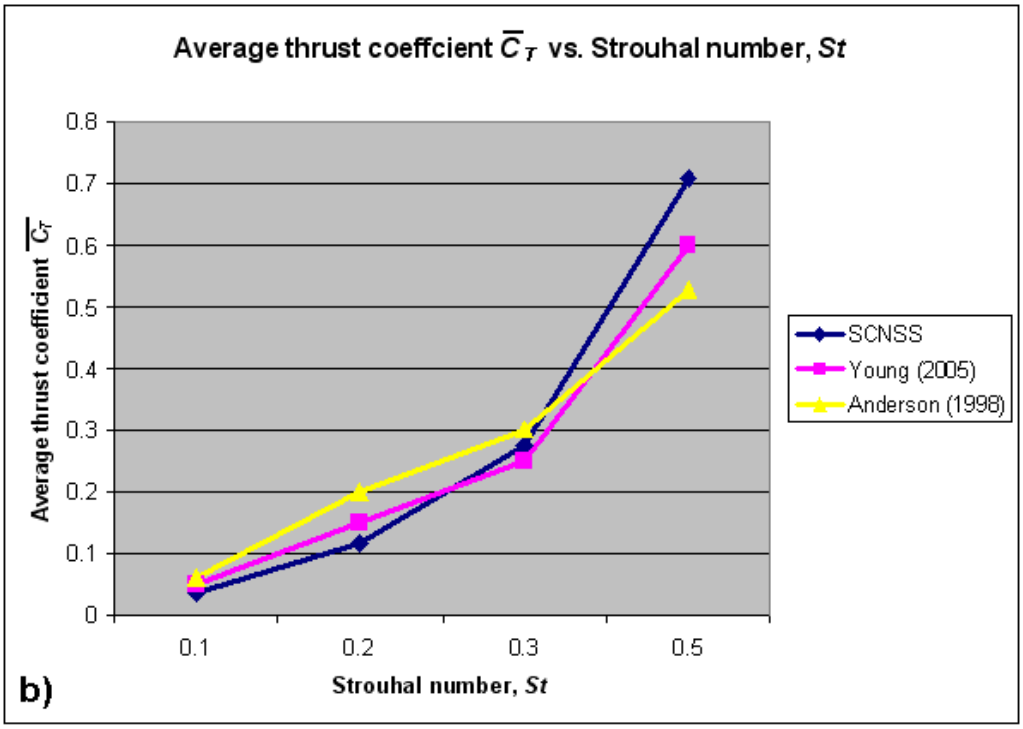

Figure 3.19: Result comparison of (a) η vs. *St* and (b) $\overline{C}_t$ vs. *St* with Anderson's Case 1

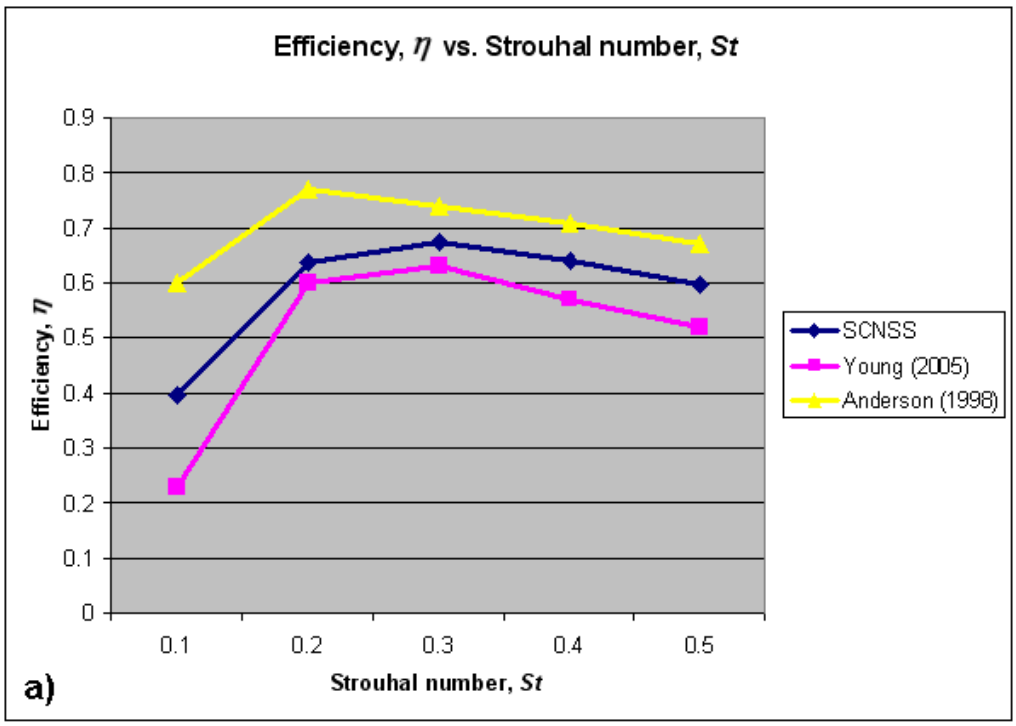

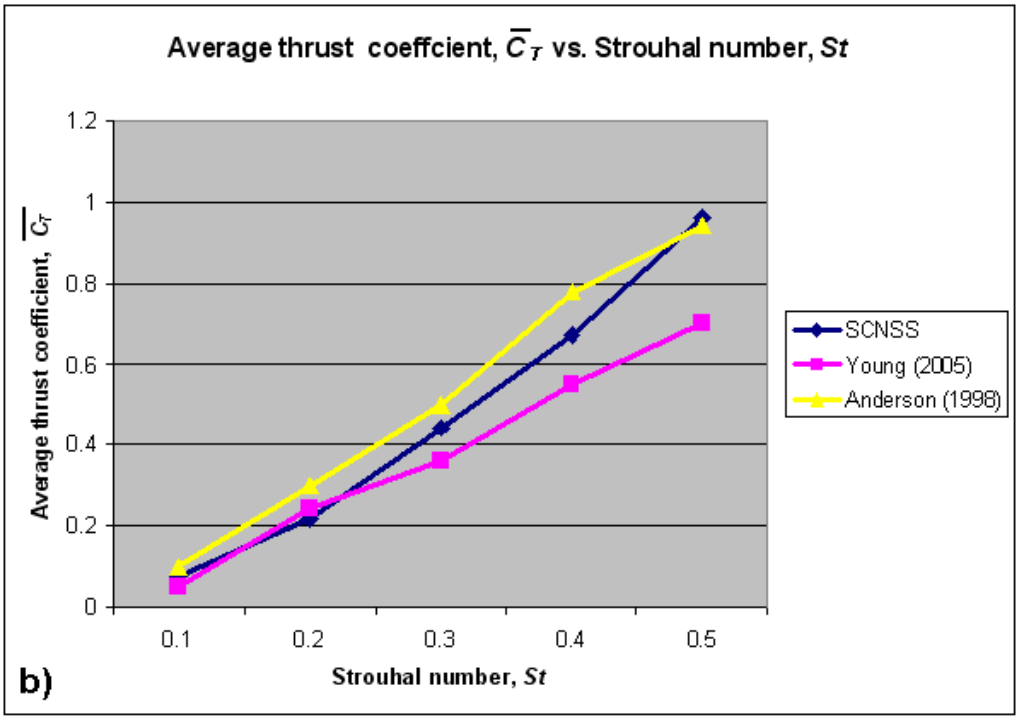

Figure 3.20: Result comparison of (a) η vs. *St* and (b) $\overline{C}_t$ vs. *St* with Anderson's Case 2

The next test is a comparison between the wake structures produced by the current solver, the solver by Young (2005) and experimental result by Lai and Platzer (1999). Figure 3.21 shows the wake structures produced by the different numerical solvers as well as the experimental

result at $k \sim 0.4$ and $h_0 = 0.0125$. Young (2005) uses filled contour plots of entropy (p / ρ^{γ}) and hence it is able to capture the filamentary nature of the wake in between vortices more readily than the current solver's vorticity diagram. Nevertheless, the current solver reproduces approximately the same qualitative aspects of the experimental wake vortex structure, with 2 roughly equal strength same-sign vortices shed per half cycle of airfoil motion, and upstream-tilted vortex pairs indicative of net drag.

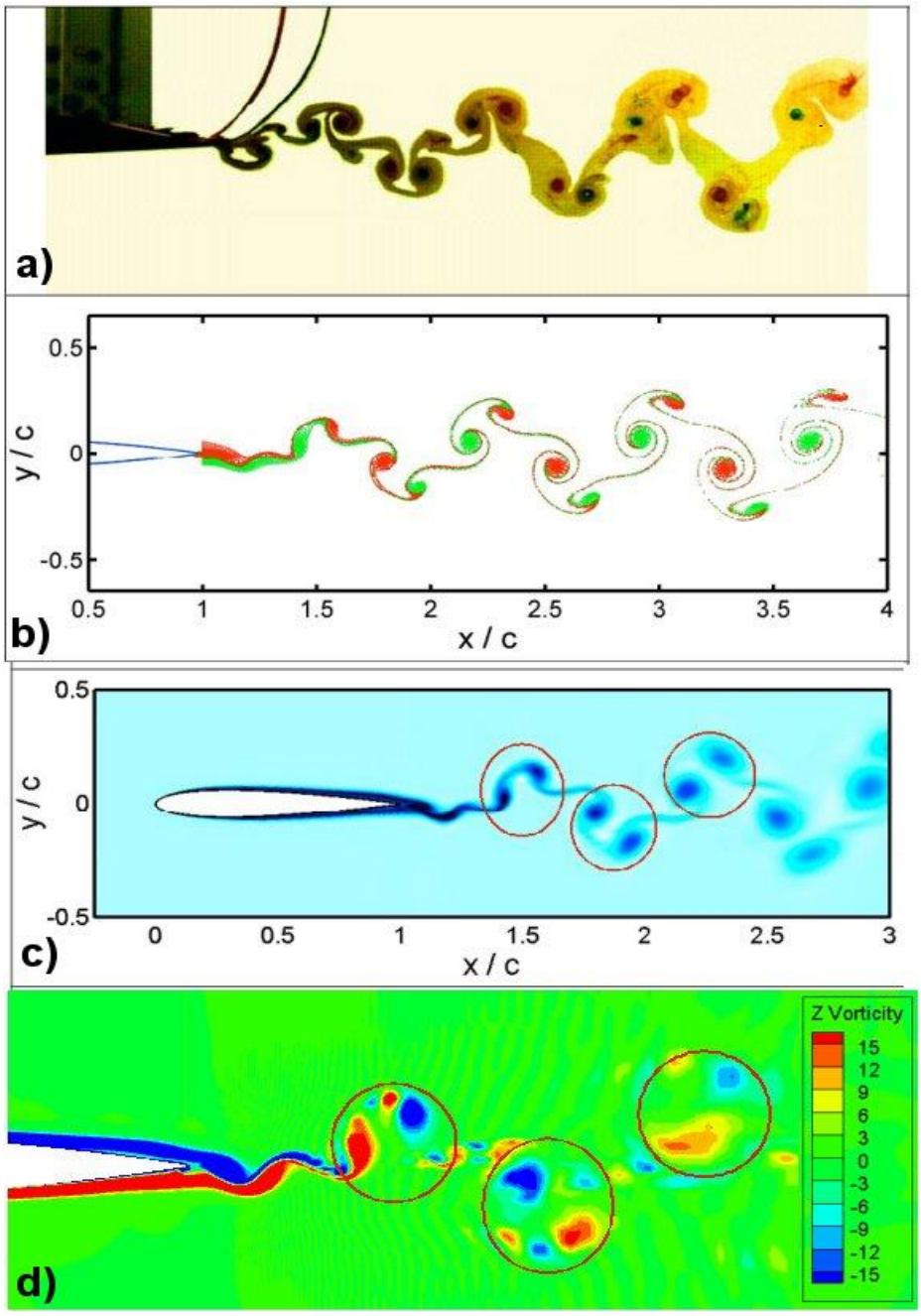

Figure 3.21: Wake structures comparison bet (a) experimental result of Lai and Platzer (1999), (b) numerical result of Young (2005), by releasing particles (c) numerical result of Young (2005), via filled contour plots of Entropy and (d) current solver's vorticity diagram

The last test is a verification of the flexing algorithm. In order to ensure the morphing of the airfoil is done correctly, some of the results found in the work of Miao and Ho (2006) are repeated. Table 3.3 shows a comparison of the results. Both groups of results for η and maximum C_t are very similar. However, the current solver gives higher C_l amplitude.

Table 3.3: Comparison between Miao and Ho's and current solver's results

	Miao and Ho's solver (estimated)			**Current solver**		
a_0	0.00	0.10	0.30	0.00	0.10	0.30
η	0.22	0.28	0.30	0.20	0.26	0.33
Maximum C_t	0.58	0.60	0.60	0.64	0.64	0.57
Maximum C_l	3.20	2.60	1.80	4.08	3.19	1.88

3.2.3 Grid Convergence Test

3.2.3.1 Quantitative validation – C_l and C_t measurements

Grid refinement is carried out using 2 test configurations. The first test (Figure 3.22a-b) uses the same parameters as that of Koochesfahani's (1989) experiment. The results show that both 140x40 and 240x80 grids produce the same C_t and C_l graphs. The first normal grid points for both grids are at 2.0×10^{-3} and 3.0×10^{-4} chord lengths from the surface respectively. The other test (Figure 3.22c-d) uses flapping parameters k = 1.0, St = 0.5, θ_0 = 17.5, ϕ = 90°. It corresponds to one of the Box-Behnken (BB) test (test number 4[††]) which will be used for the

[††] One can refer to Table A.1 for the flapping configuration corresponding to the test number

DOE test in the later part of the thesis. This case uses higher heave amplitude and pitch angle. Result now shows that the 650x100 grid, with the first normal grid point 4.0×10^{-5} chord lengths from the surface, and the 240x80 grids produce the same result. However, the 140x40 grid gives a different C_t graph. Hence, the 240x80 grid is chosen for the rest of the simulations using SCNSS in this study when only quantitative force results are required.

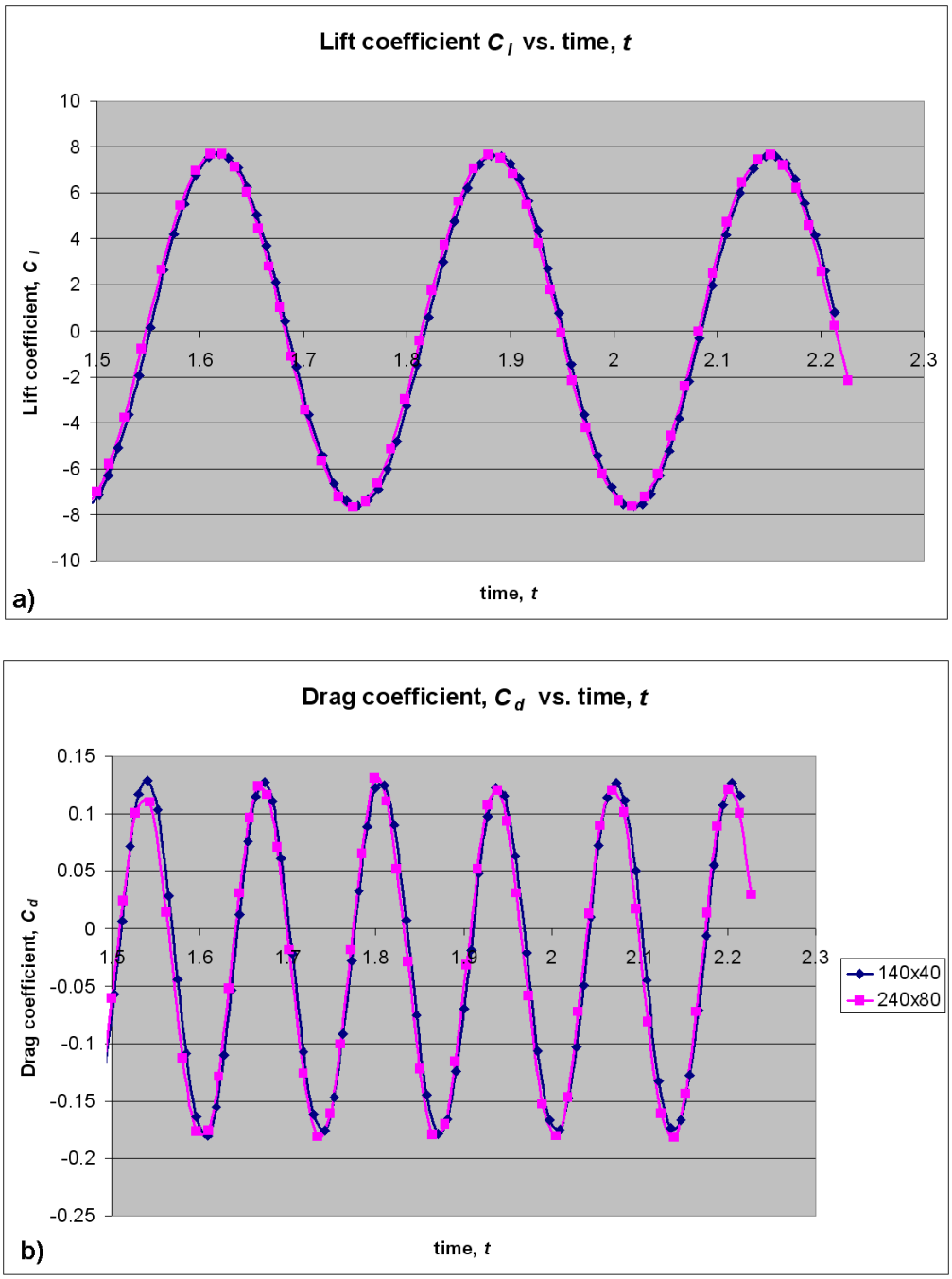

Figure 3.22: C_l and C_d vs. t plot using the (a,b) Koochesfahani's experiment at $k \sim 12$ and (c,d) Box-Behnken test 4 at different grid resolutions and sizes (continue on next page)

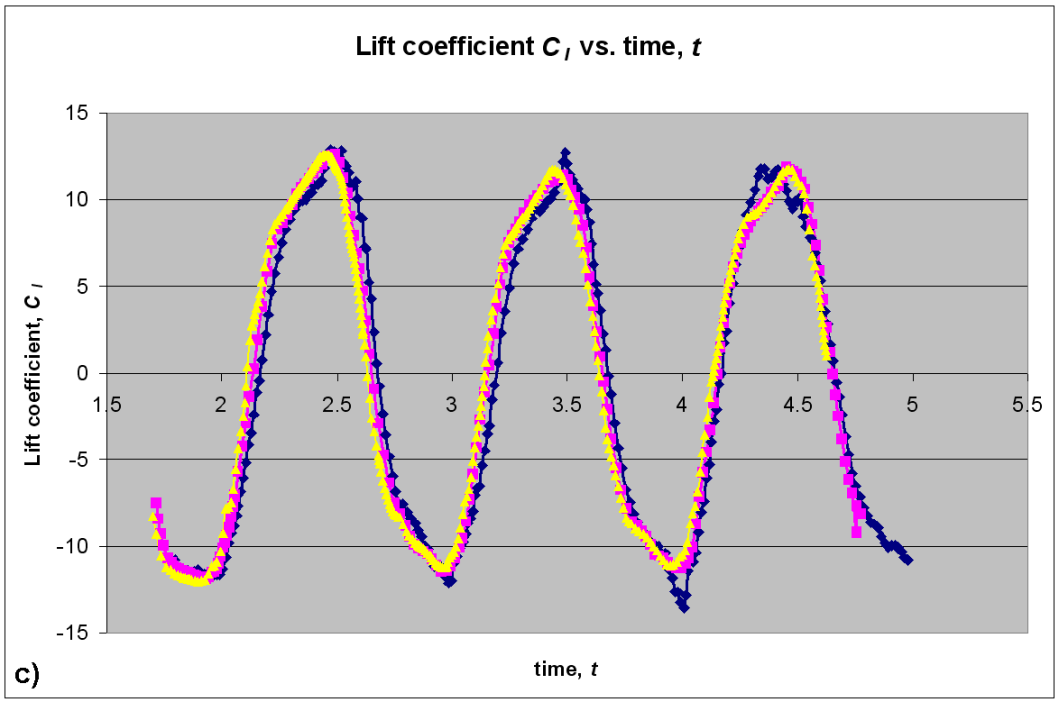

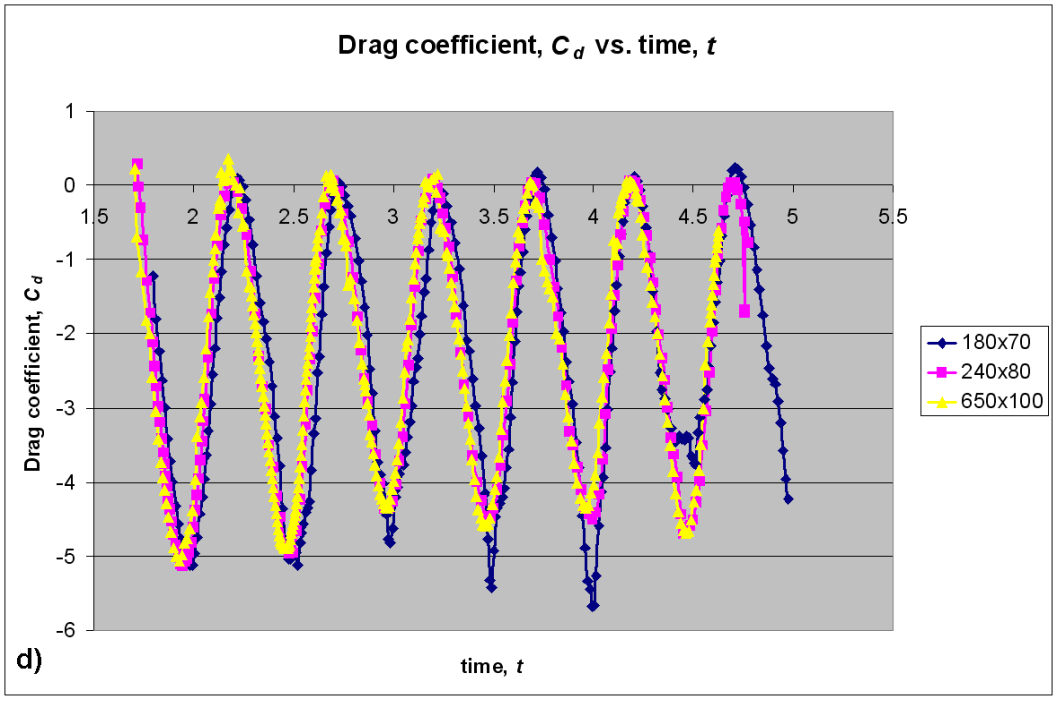

3.2.3.2 Qualitative validation – Vorticity Diagram

The vorticity diagrams of different grid resolutions and sizes (based on Table 3.4) are simulated to assess the appropriate number of grids for the vorticity diagram. Figure 3.23a to g show the different vorticity diagrams of the NACA0012 airfoil at approximately the same time. The flapping parameters used is the same as the earlier second test (BB test 4). The 1200x160

grid with the first normal grid point $6.0x10^{-4}$ chord lengths from the surface is chosen since it shows most of the important features in the vorticity diagram and it is computationally less expensive. A higher level of refinement is required to obtain the vorticity diagram of the simulation, compared to the aerodynamic forces. As mentioned by Young (2005), this is a result of the "small scale separation effects at the trailing edge determining the details of the wake vortices for these flapping parameters". Therefore, all the simulations are first computed using the 240x80 grid. Whenever it is necessary to visualize the vorticity diagram for a particular configuration, the configuration will be simulated again using the 1200x160 grid.

Table 3.4: The number of grid points and the distance of first grid point from surface

Order	**Number of grid points**	**Distance of first grid point from surface**
a	650x80	$8.0x10^{-5}$
b	1200x80	$4.0\ x10^{-5}$
c	650x160	$2.0\ x10^{-5}$
d	1200x160	$6.0\ x10^{-4}$
e	1200x160	$2.0\ x10^{-5}$
f	1200x240	$4.0\ x10^{-5}$
g	1800x160	$8.0\ x10^{-5}$

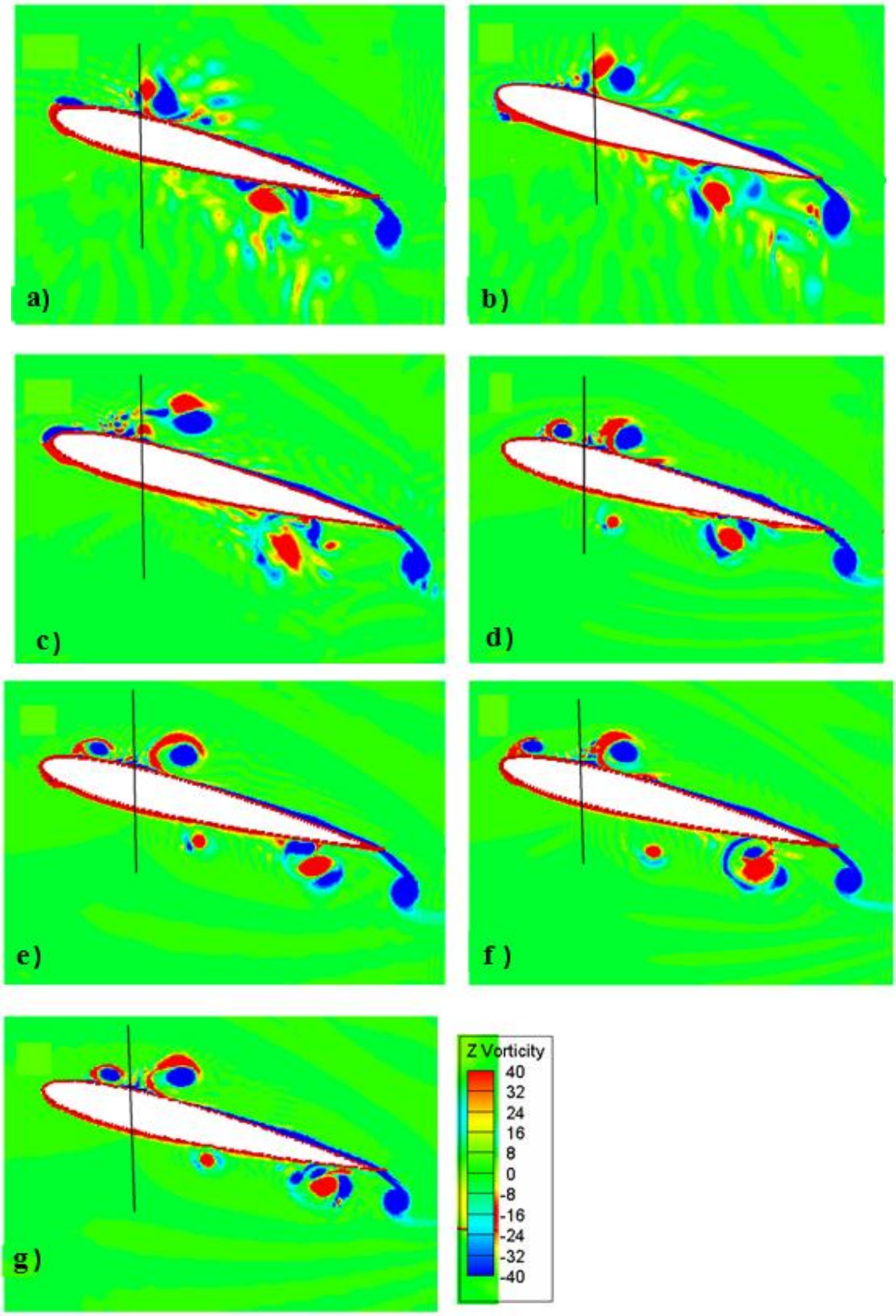

Figure 3.23: Vorticity diagram using the Box-Behnken test 4 at different grid resolutions[‡‡]. The black vertical line in the vorticity diagram indicates the approximate peak to peak heaving.

[‡‡] All subsequent vorticity plots use the color contour legend as the one in Figure 3.23.

3.3 Staggered Cartesian Grid Navier Stokes Solver with Immersed Boundary (IBCNSS)

Unlike the SCNSS, the IBCNSS uses the concept of immersed boundary (IB) (Mittal and Iaccarino 2005) to simulate the airfoils in tandem. As mentioned earlier in the literature review, this solver is preferred because although it is possible to modify the SCNSS to use overset grids, stability and conservation problems may arise (Mittal and Iaccarino 2005). The IB method is a good alternative and moreover, it is not restricted by the grid deformation. The IB method used in this research is based on the scheme by Ravoux et al. (2003). This method combines features from both the IB and the volume of fluid (VOF) in order to compute flows past moving and deformable bodies. The Ravoux scheme is chosen over the other IB schemes because it is simple to implement. There is also no ad-hoc computation such as "freshly cleared cells" problem (Udaykumar, 2001) when the body starts to move. The only problem is that the Ravoux scheme uses a staggered grid solver instead of the nonstaggered one. Hence, a new Navier Stokes Cartesian grid staggered solver has to be written. However, this is not as daunting as it seems because many parts of the SCNSS (for example the second order fully implicit scheme) still can be reused and it is only a Cartesian grid solver. Hence, the mathematics and interpolations are much easier.

There are two modifications done to the Ravoux scheme. Firstly, a fully implicit scheme is used of the original fully explicit scheme to improve the stability of the solver. Secondly, the solver is parallelized using MPI (Snir et al. 1998) to reduce the computation time. More details will be given in section 3.3.1.1 and 3.3.3.3.

3.3.1 Algorithm of the IBCNSS

3.3.1.1 Fractional step method

$$\nabla \cdot v = 0 \tag{3.49}$$

$$\frac{\partial v}{\partial t} = -v \cdot \nabla v + \frac{1}{\mathrm{Re}} \nabla^2 v - \nabla p + fc \tag{3.50}$$

In this algorithm, a fractional step method is used to solve the modified Navier Stokes equations in equation (3.49) and (3.50). It is similar to the improved projection method used by Gao et al. (2007), except that beside a semi-implicit scheme, a fully implicit scheme is also used. The velocity field is corrected by the pressure to satisfy the continuity equation. Similar to the SCNSS, the viscous term is approximated by the Crank Nicholson scheme. On the other hand, the convective term can either be approximated by the same scheme (fully implicit) or the Adams–Bashforth (semi implicit) scheme. All spatial derivatives are discretized using the second-order central difference scheme in a staggered grid.

The IB method by Ravoux et al. (2003) also includes the features of the volume of fluid (VOF) to compute flows past moving and deformable bodies. Similar to other IB method, an external body force density, *fc* is inserted into the fluid equations. This force signifies the presence of the solid body. The main idea is to consider the computational domain as a continuous fluid medium, which encompasses both the fluid and the body phase. The rigid body phase has a volume fraction of unity whereas the ordinary fluid phase has a volume fraction of zero. In between, the medium is partially made up of the fluid and rigid body phases and volume fraction has a value between zero and unity. The body force's magnitude is determined by satisfying the criteria that the velocity in the cells occupied by the solid must equal the velocity of the rigid body.

In the paper by Ravoux et al. (2003), a first order time accurate explicit scheme is used for the

momentum equation. It is replaced in this thesis by the more stable second order fully implicit scheme which is used in the SCNSS. The discretized equation is exactly the same as in Eqn (3.30). As mentioned earlier, a semi-implicit scheme has also been attempted but for certain sets of simulation, the answer may deviate unless a very small time step is used. Therefore, we decide to use only the fully implicit scheme for all simulations. Intermediate velocities $\hat{u}, \hat{v}$ are obtained by solving Eqn (3.30).

The next step forms the gist of the IB method whereby the system is considered a "binary" fluid. One phase corresponds to the rigid body while the other corresponds to the fluid, which is outside the body. A cell can belong to either phase or both phases if it happens to be at the interface between the body and the fluid. A volume fraction field, Φ is defined as the fraction of area of the cell occupied by the body. Thus, if the cell belongs to the fluid or body, Φ = 0 or 1 respectively. If the cell belongs to both phases, Φ has a value between 0 and 1. This was the original scheme proposed by Ravoux et al (2003). However, due to the high number of grids used in the simulations in this thesis (> 1000x1000), it is found that by simply assigning Φ = 1 or 0 for cells whose center are inside or outside the body respectively, the result obtained is almost the same compared to the original scheme. This simplifies greatly the computation of area of cell occupied by the body, which must be done in every time step. The Fortran algorithm PNPOLY by W. Randolph Franklin[§§] is used to test whether the center of each cell is inside or outside the body. Due to the staggered grid, it is possible that the cell's center can be inside or outside the body for the *u* and *v* velocity grids. Hence, Φ_x and Φ_y are used for the *u* and *v* grids.

By imposing a body force term *fc* in cells which are occupied by the body, the velocity field is

[§§] The fortran code and its description can be found at http://www.ecse.rpi.edu/Homepages/wrf/Research/Short_Notes/pnpoly.html.

modified to make it equal to the velocity of the cylinder. The body force *fc* is evaluated as:

$$\begin{aligned} f_x(i,j) &= \Phi_x(i,j)[u_{body}^{n+1} - u^*(i,j)]/dt \\ f_y(i,j) &= \Phi_y(i,j)[v_{body}^{n+1} - v^*(i,j)]/dt \end{aligned} \tag{3.51}$$

In order to make the velocity of the each cell in the ball having the same velocity as that of the body, but remain unchanged in the fluid phase, we let:

$$\begin{aligned} u^{**}(i,j) &= [1-\Phi_x(i,j)]\hat{u}(i,j) + \Phi_x(i,j)u_{body}^{n+1} \\ v^{**}(i,j) &= [1-\Phi_y(i,j)]\hat{v}(i,j) + \Phi_y(i,j)v_{body}^{n+1} \end{aligned} \tag{3.52}$$

Where u^{**}, v^{**} are the new intermediate velocities due to the body force constraint.

The next step is to obtain p^{n+1} by solving the Poisson equation in Eqn (3.53).

$$\nabla^2 \delta p^{n+1} = \frac{\nabla \cdot \mathbf{v}^{**}}{dt} \tag{3.53}$$

Once δp^{n+1} is obtained, we can get:

$$p^{n+1} = p^n + \delta p^{n+1} - \frac{\Delta t}{2\,\mathrm{Re}} \nabla^2 \delta p^{n+1} \tag{3.54}$$

$$u^{n+1} = u^{**} - dt \frac{\partial \delta p^{n+1}}{\partial x} \tag{3.55}$$

$$v^{n+1} = v^{**} - dt \frac{\partial \delta p^{n+1}}{\partial y} \tag{3.56}$$

Hence it can be seen that the body force term *fc* is not explicitly added in the Navier Stokes equations but applied implicitly through Eqn (3.52). More details of the immersed boundary algorithm can be found in the papers by Ravoux et al (2003) and Pederzani and Haj-Hariri (2006).

Similar to the SCNSS, the system of linear equations obtained from the momentum and Poisson equations are solved using PETSc (Balay et al. 2004), a linear equation solver and hypre (Falgout et al. 2006), a multigrid solver respectively. The code is also written entirely using Fortran90. The IBCNSS's code has been parallelized using Message Passing Interface

(MPI) (Snir et al. 1998) to shorten the runtime.

3.3.1.2 Cartesian grid and boundary conditions

For the IBCNSS, the grid is a Cartesian one. An example is shown in Figure 3.24. The domain size for the IBCNSS is 26.0x16.0 units. The distances of the top/bottom and farfield boundary to the airfoil are 8.0 and 17.5 units respectively. The grid near the airfoil is uniform. The boundary conditions used are exactly the same as that of the SCNSS and they are given from Eqns (3.40) to (3.42).

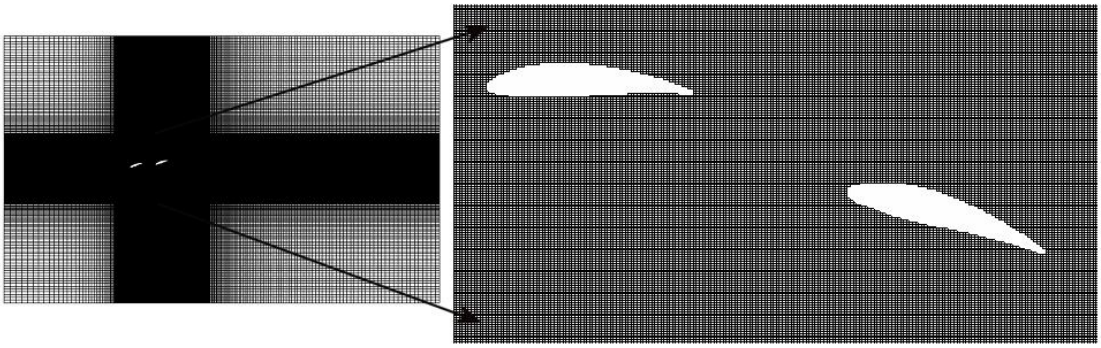

Figure 3.24: An example of the 1320x1120 Cartesian grid for the IBCNSS and its magnification

3.3.1.3 Force coefficients and efficiency

For the IBCNSS, due to the non-conformal grids, the force components are obtained by using the difference between the original and the updated velocity due to the presence of the body. They are given by:

$$F_x = \left[\sum_{i=1}^{M} \sum_{j=1}^{N} \left(f_x^n(i,j) - \frac{u_{body}^{n+1}(i,j) - u_{body}^{n}(i,j)}{dt} \right) dx_i dy_j \right] \tag{3.57}$$

$$F_y = \left[\sum_{i=1}^{M} \sum_{j=1}^{N} \left(f_y^n(i,j) - \frac{v_{body}^{n+1}(i,j) - v_{body}^{n}(i,j)}{dt} \right) dx_i dy_j \right] \tag{3.58}$$

The computation of force coefficients, efficiency are exactly the same as that of the SCNSS, as given from Eqns (3.44) to (3.48).

3.3.2 Verification of the IBCNSS

The accuracy of the solver is validated using two tests. The first test is the transverse oscillation of the cylinder. It is simulated to oscillate under Re = 185 at a frequency of f = 0.8*f_n and 1.2*f_n where f_n is the natural vortex shedding frequency. The grid size is 420x266. Table 3.5 shows that the current results are in excellent agreement with that of Guilmineau and Queutey (2002).

Table 3.5: Comparison of results between for the transverse oscillation of the cylinder

	Guilmineau and Queutey		**Current solver**	
f / f_n	$\bar{C}_D$	C_l (r.m.s.)	$\bar{C}_D$	C_l (r.m.s.)
0.8	1.24	0.08	1.23	0.076
1.2	1.39	0.92	1.40	0.92

The second verification is a comparison between the results of the S1020 airfoil flapping at h_0 = 0.15, k = 1.0, θ_0 = 30^o and ϕ = 90^o (BB test 4 configuration) using the IBCNSS and SCNSS. The Re is 1,000, instead of 10,000. This is because the grid requirement will be very high if the simulation is run at 10,000. This problem is mentioned earlier in section 2.1. The SCNSS and the IBCNSS use grid sizes of 240x80 and 1200x1080 respectively. The domain size for the IBCNSS is the same as that given in section 3.3.1.2. Figure 3.25 shows that there is only a slight difference in the coefficient plots. This shows that the IBCNSS is accurate.

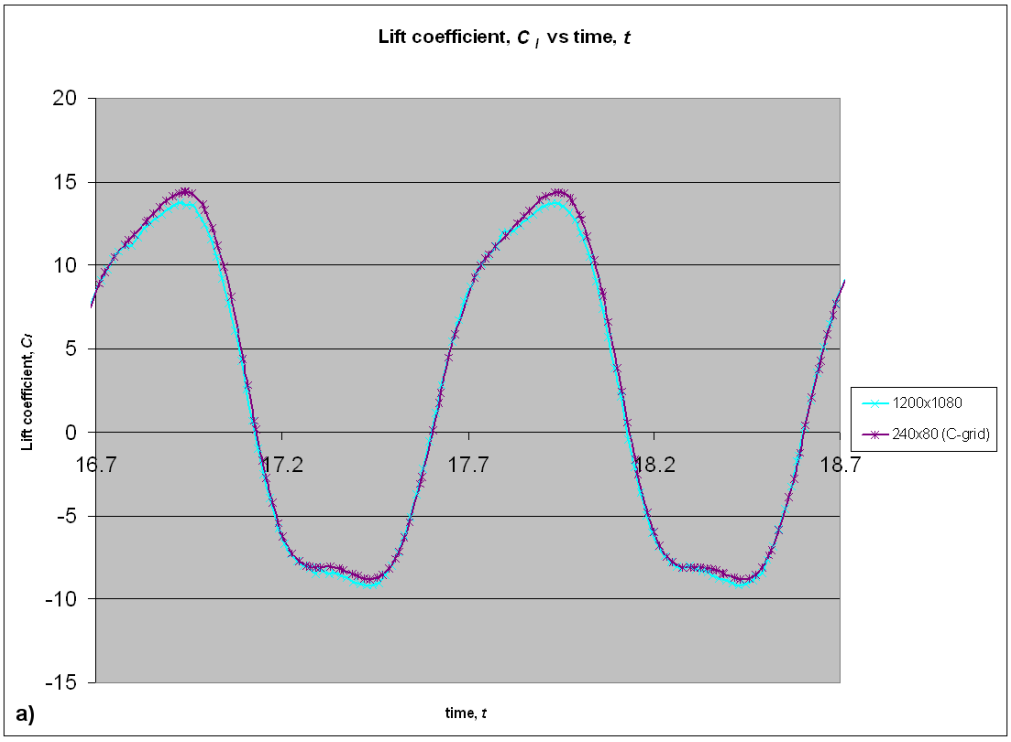

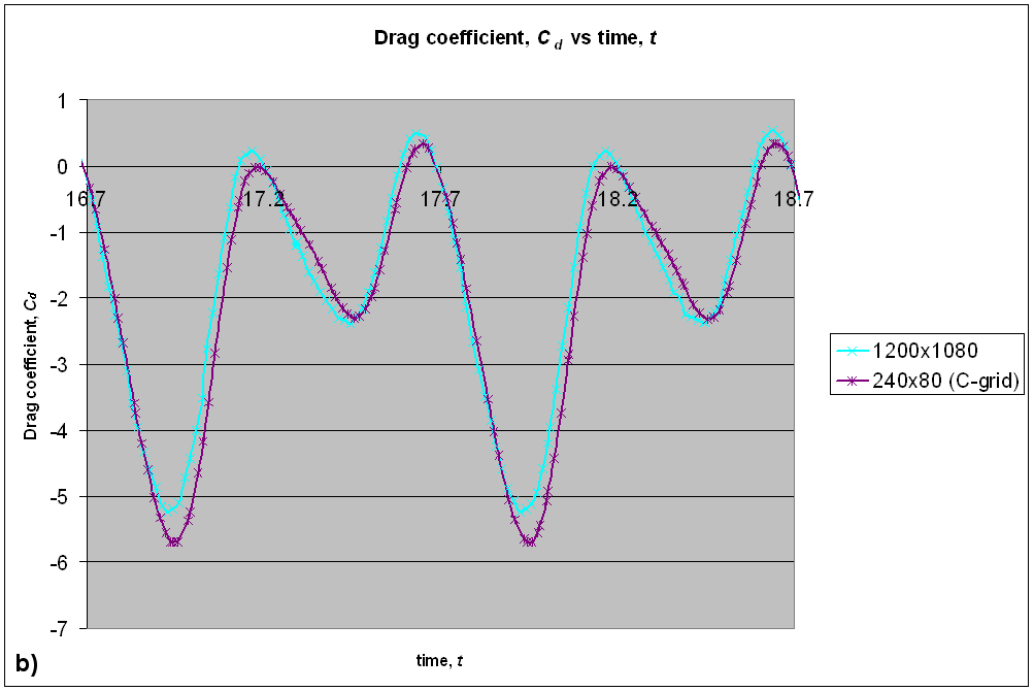

Figure 3.25: (a) Lift and (b) drag coefficient plots of the S1020 airfoil flapping at BB test 4 using the IBCNSS and SCNSS

3.3.3 Grid Convergence Test

3.3.3.1 Quantitative validation – C_l and C_t measurements

Grid refinement is carried out using the flapping parameters h_0 = 0.15, k = 1.0, θ_0 = 30^o and ϕ = 90^o (BB test 20 configuration). The S1020 airfoil is simulated with Re = 1,000. Due to the non-conformal nature of the IBCNSS, the grid requirement is much higher. Results on Figure 3.26 show that there is no difference in the lift coefficient plots even for the lowest grid of 600x1080. However, the drag coefficient plots show noticeable difference between the different grid resolutions. The 1200x1080 grid size is chosen as the grid resolution for the rest of the simulation because it is very close to the 1800x2160 grid size in terms of results and it is computationally cheaper. For the tandem arrangements, due to additional airfoil, the grid resolution is proportionally lengthened to a size of 1320x1120.

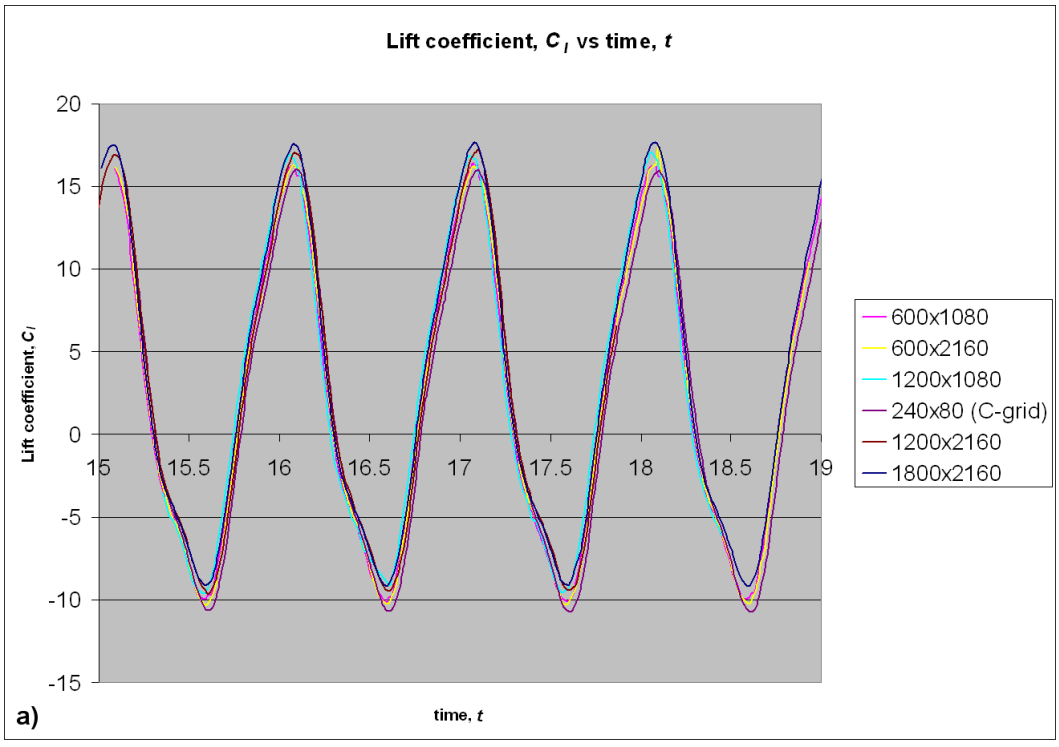

Figure 3.26: (a) Lift and (b) drag coefficient plots of the S1020 airfoil flapping at BB test 20 for the grid comparison (continue on next page)

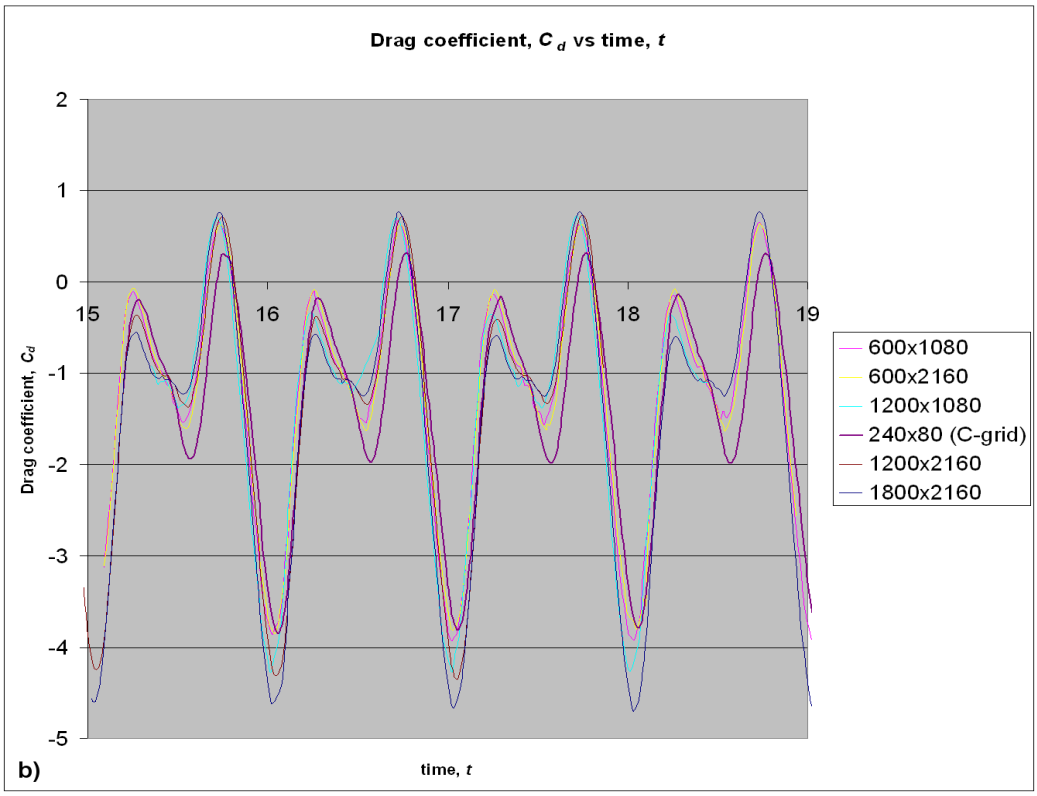

3.3.3.2 Qualitative validation – Vorticity Diagram

The vorticity diagrams of the S1020 airfoil flapping at the BB test 4 configuration at *Re* = 1,000 for the different grid resolutions are shown in Figure 3.27. Even at the lowest grid resolution of 360x540, there is no noticeable difference. However, since 1200x1080 (or 1320x1120) is used to obtain the C_l and C_t, the vorticity diagrams for the rest of the simulations will also use the same grid resolution.

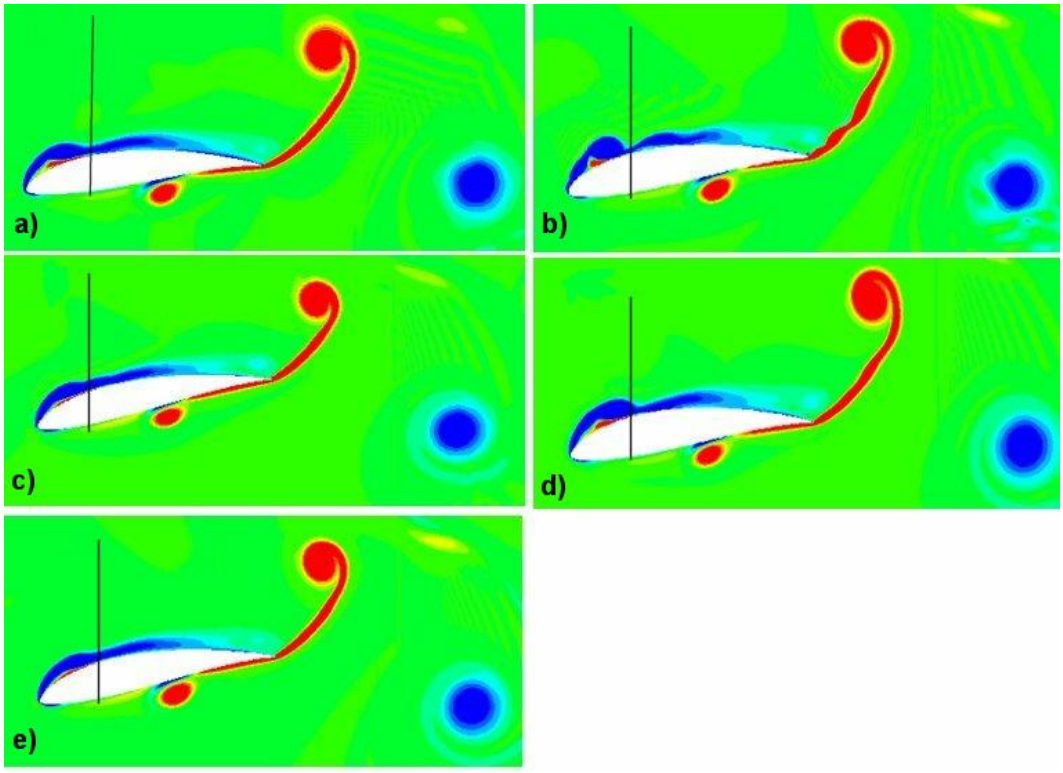

Figure 3.27: Vorticity diagrams of the S1020 airfoil flapping at BB test 4 at *Re* = 1,000 for grid resolutions of (a) 1200x160 (SCNSS) (b) 360x540 (c) 600x2160 (d) 600x1080 (e) 1200x1080

3.3.3.3 Parallelizing of the IBCNSS Code

In the original algorithm by Ravoux et al. (2003), the solver is meant to run on only one processor. However, due to the high grid number requirement of the IBCNSS, it is necessary to parallelize the code to shorten the runtime. The linear equation solver PETSc (Balay, 2003) supports the solving of equations in parallel. The other parts of the code which involves loops are also parallelized using MPI (Snir et al. 1998). The performance graph of the parallelization is shown in Figure 3.28. The scaling factor refers to the increase in performance as the number of processors increase. It is defined as $\frac{\text{Time taken to complete task for 1 processor}}{\text{Time taken to complete task for n processors}}$. In the ideal case, when processor number = n, scaling factor should be equal to n too. The graph shows the performance of the IBCNSS code and an example code included in the PETSc package, running on the atlas4 servers of the Supercomputing and Visualization Unit (SVU). The example code (ex2.f) involves the solving of the Laplace equation in parallel using PETSc.

It is a very simple code and should scale very well, only limited by the server's capability. This code serves as a good comparison with the more complicated IBCNSS code. The codes are run twice for each case and the average time of each is taken. The graph shows that the speedups for both codes are approximately linear for up to 4 processors. Beyond that number, the codes do not perform as well as they should. According to the system engineers at SVU, there are many factors that affect the speedup. These include high load on the cluster, communication between different processors or the way the code has been parallelized. Hence, for the IBCNSS simulations, either four or eight processors will be used, depending on the server load.

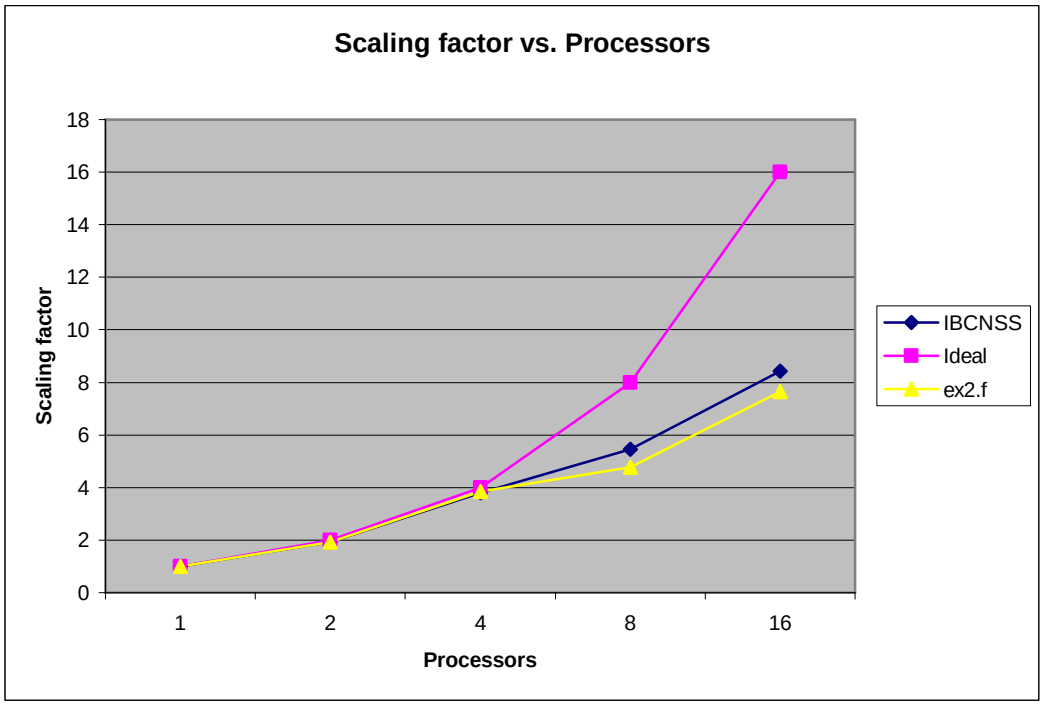

Figure 3.28: Performance graph of parallelization for the IBCNSS code

4 Methodology in Experimental study

The research is conducted in three separate phases. The first part involves using the Design of Experiment (DOE) methodology to determine the significance of the different variables and their interactions on the non-symmetrical airfoils. The flapping configurations which exhibit high η, $\overline{C}_t$ and $\overline{C}_l$ will be singled out for the second and third phase of study.

The second phase attempts to further improve the flapping configurations mentioned above by introducing chordwise flexing to the airfoils. Lastly, the third part attempts to improve the η, $\overline{C}_t$ and $\overline{C}_l$ by flapping the airfoils in tandem.

4.1 Design of Experiment (DOE): Box-Behnken (BB) Design

There are many parameters which may influence the performance of an oscillating airfoil. These parameters include rowing (movement of airfoil forward/backward) amplitude, heaving (movement of airfoil upward/downward) amplitude, maximum pitching angle, phase angles between heave/pitch/row, center of pitch rotation, reduced frequency, and Strouhal number. However, due to limited resources, only a subset of these factors can be tested in this research. The parameters investigated in this study include the reduced frequency (k), Strouhal number (St), maximum pitch angle (θ_0) and phase angle between pitching/heaving (ϕ).In this study, reduced frequency is defined as the frequency non-dimensionalized with respect to the freestream velocity and chord length. The Strouhal number, a dimensionless parameter describing the oscillating frequency of a flow, is defined as $\frac{fh_0}{U_\infty}$. According to many researchers, these parameters seem to be the more important factors. However, as discussed earlier, the simulations are done using a symmetrical airfoil. Their influences on lift and two-

factor interactions are not investigated as well.

There are three objectives to be accomplished in this phase of simulation. Firstly, we will like to determine if the factors selected has a significant effect on the η, $\overline{C}_t$ and $\overline{C}_l$ of the flapping airfoil. The next objective is to find out the presence of two-factor interactions among the factors. Lastly, it is to select three flapping configurations which give the highest η, $\overline{C}_t$ and $\overline{C}_l$, out of the many flapping configurations tested. In this study, a total of four other non-symmetrical airfoil shapes are used. The NACA0012 airfoil is also included in the study as a form of comparison. The airfoils and their descriptions are given in Table 4.1. The shapes of the airfoils are shown in Figure 4.1.

Table 4.1: Airfoils used in the DOE simulations and their descriptions

Airfoil	**Description**
NACA4404	Often used in small remote-control fixed wing model planes which fly at the *Re* of around 10,000
NACA6302	Resembles the slim hand-wing of the swift bird.
S1020	Also known as the ornithopter airfoil, used for the wings of the Harris/DeLaurier (2003) radio-controlled ornithopter. Shown to give attached flow for a wide range of angles of attack
Birdy	Modeled based on the cross section diagram of the arm-wing of the swift bird (Videler et al. 2004)
NACA0012	Included as a form of comparison

Vorticity diagrams are used to explain the results obtained. The *Re* used in this numerical study is 1.0×10^4, which is the typical regime of a MAV. Table 4.2 shows the calculation of the *Re* using typical values of a MAV. This is obtained by assuming fluid velocity = 3.2 m/s,

characteristic length = wing chord.

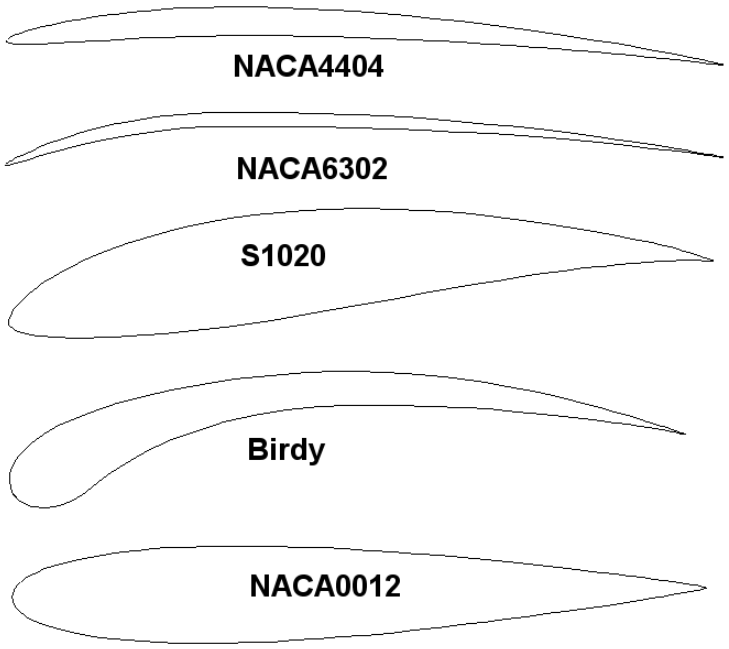

Figure 4.1: Shape of the different airfoils

Table 4.2: Calculation of *Re* of the flight regime of a MAV

Variables	**Value**
Fluid velocity (m/s)	3.2
Characteristic length (wing chord, m)	0.05
Fluid density (air, kg/m^3)	1.2
Fluid dynamic viscosity (air, kg/m.s)	1.88×10^{-5}
Re	1.02×10^{4}

The Box-Behnken (BB) design (Box and Behnken 1960) is the statistical method selected to achieve the objective mentioned earlier. It falls under the response surface methodology, which explores the relationships between factors and their responses. The main idea is to conduct a sequence of experiments, obtain the responses and analyze the results for the relationships present. This design allows the study of the influence of the main effects and two-factor interactions between the different variables. Three-factor and above interactions are usually

very rare and hence they are not included in the study.

In the Box-Behnken design, a second-degree polynomial model is used. The procedures to carry out and interpret the analysis can be simplified by using commercially available statistical software. In this case, the software Minitab is used because it is available for installation on the school's computer network. The steps to carry out the analysis are as follows:

1. Select Box-Behnken design. Input the number of factors in the study (four in this case) and specify their numerical ranges.
2. A total of 25 flapping configurations will be generated based on the four factors and their ranges. If a full factorial design is used, each airfoil will require 3^4 = 81 simulation tests. Hence, the BB design is more efficient. The 25 different test configurations can be found in Table A.1 in the appendix. The SCNSS will be used to simulate these configurations for the five airfoils. Hence there is a total of 25x5 = 125 configurations simulated.
3. The output (η, C_t, and C_l) from the SCNSS are then entered into the software analyzed. Minitab produces two types of graphs, main effects graphs and interactions graphs. The main effects graphs for each airfoil give the mean response for each level of each variable. This mean response is obtained by averaging over all levels of the other variables. The graph can be used to compare the relative effects of the various variables. The interaction graph between two variables, on the other hand, shows how the response changes when one variable remains fixed while the other changes. The "p_s" value calculated by Minitab for each variable is used to test whether the variable and its interactions are statistically significant or not. A value of p_s less than 0.05 indicates that it is significant. Error analysis is also carried out to check the fidelity of the response surface model and to ensure that the residuals are normally distributed and homoscedastic with respect to the design variables and the fitted values as required by the analysis method. Residual refers to the difference between the observed and predicted values. More details about the error analysis can be found in Tay and Lim

(2009).

The ranges of the factors selected are based on a number of reasons. It had been reported that the range of Strouhal number whereby most swimming and flying animals swim or fly at is between 0.2 and 0.4 (Triantafyllou et al. 1993; Taylor et al. 2003). The Strouhal number range is chosen to be slightly larger, in the range between 0.1 and 0.5. Phase angle has been reported to be optimum around 90^o and hence the levels are chosen at $\pm 30^o$ from 90^o. The reduced frequency k is given by $k = St/2/h_0$. Based on the design consideration of a MAV wing, the flapping heave amplitude is restricted to be less than 1.25 chord length. Since St has already been chosen, based on a maximum h_0 of 1.25, k is calculated to be between 0.2 and 1.0. In this study, since the chord c and U_∞ are both constant at 1.0, k is effectively f, the frequency of oscillation. Lastly, θ_0 is chosen to be between 5^o and 30^o.

The motion of the airfoil is specified by:

$$h = h_0 \sin(2\pi f(t - t_0) - \phi) \tag{3.59}$$

$$\theta = \theta_0 \sin(2\pi f(t - t_0)) \tag{3.60}$$

The center of pitch rotation is fixed at 0.25 units from the leading edge of the airfoil. Figure 4.2 shows the airfoil with its geometric parameters. The whole grid translates or rotates as a whole because there is no deformation involved.

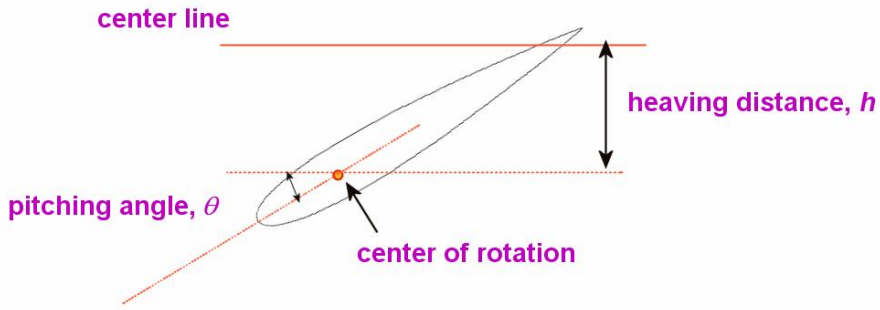

Figure 4.2: Diagram of airfoil with its geometric parameters

4.2 Airfoil Active Chordwise Flexing

The active flexing of the airfoil is similar to the method used by Miao and Ho (2006). In their paper, they use the symmetrical airfoil NACA0014. The airfoil is only configured to heave but it pitches due to the flexing of the airfoil's tail. The instantaneous profile of the airfoil is described by:

$$y = a_f x_{tf}^2 \cos(2\pi f(t - t_0) + \psi_f) \tag{3.61}$$

where a_f, x_{tf} and ψ_f denote the flexure amplitude, distance from the point on the chord line to the leading edge and phase angle respectively. Eqn (3.61) refers to the local x-y body coordinate system. In this study, ψ_f is fixed at $\pi/2$. Both a_f and x_{tf} have been non-dimensionalized with the airfoil chord *c*. Figure 2.1 gives a representation of the airfoil flexing used by Miao and Ho (2006).

However, as mentioned in the introduction, the current study involves more parameters as well as the use of non-symmetrical airfoils. Hence, Eqn (3.61) is insufficient to represent it. The new equations are given by:

$$h_{lf} = a_f (x_{lf})^2 \cos(2\pi f(t - t_0) + \psi_f) \tag{3.62}$$

$$h_{tf} = a_f (x_{tf})^2 \cos(2\pi f(t - t_0) + \psi_f) \tag{3.63}$$

$$\beta_{lf} = -2\sin^{-1}\left(h_{lf} \Big/ 2x_{lf}\right) \tag{3.64}$$

$$\beta_{tf} = 2\sin^{-1}\left(h_{tf} \Big/ 2x_{tf}\right) \tag{3.65}$$

The maximum possible value of h_{lf} or h_{tf} is a_f. β_{lf} and β_{tf} will be used to calculate the amount of curvature of the airfoil. Figure 4.3 shows the airfoil's trailing edge flexing. Moreover, a form of "one-sided" flexing is also investigated. In this form of flexing, the airfoil only flexes in one direction, instead of two. The equations are given by:

$$h_{lf} = -a_f (x_{lf})^2 \left|\cos(2\pi f(t - t_0) + \psi_f)\right| \tag{3.66}$$

$$h_{tf} = -a_f (x_{tf})^2 \left|\cos(2\pi f (t - t_0) + \psi_f)\right| \tag{3.67}$$

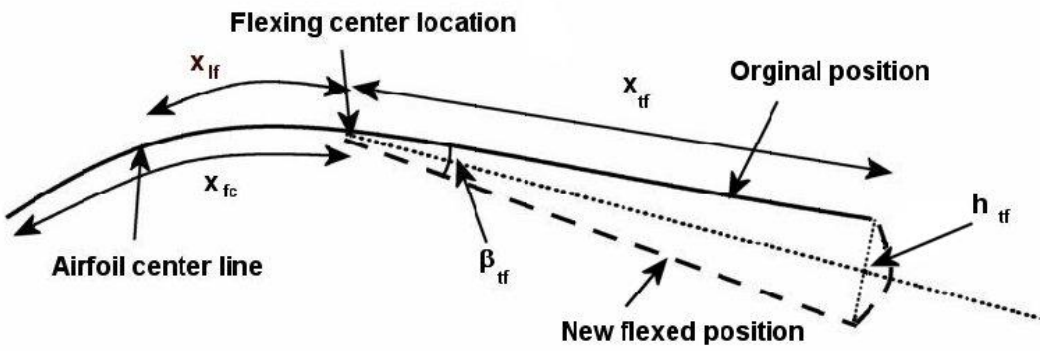

Figure 4.3: Diagram of the airfoil's trailing edge flexing

One problem which arises involves the amplitude of leading and trailing edge when the center of flexure changes. This is illustrated in Table 4.3 under the old method. From Table 4.3, with the same a_f, the amplitude of flexing at the trailing edge of the airfoil becomes much smaller (0.019) as the flexing center point, x_{fc} moves from the leading edge to the ¾ position of the airfoil center line. The proposed correction is to define a new nominal flexing amplitude, given by $\overline{a}_f$. The relationships between the nominal and original amplitudes are given by:

$$\overline{a}_f = a_{lf} (x_{fc})^2 \qquad \text{for leading edge flexing} \tag{3.68}$$

$$\overline{a}_f = a_{tf} (1.0 - x_{fc})^2 \qquad \text{for trailing edge flexing} \tag{3.69}$$

This will ensure that the amount of flexing will be similar for the same $\overline{a}_f$, as shown in Table 4.3. The flexing amplitude at the leading and trailing edge locations is exactly the same (0.3). Due to the quadratic nature of the formulas, the flexing amplitude at other locations on the airfoil will be slightly different. Moreover, the a_{lf} (leading edge) and a_{tf} (trailing edge) will now be different for the same $\overline{a}_f$. The new slightly modified equations are given by:

$$h_{lf} = \frac{\overline{a}_f}{(x_{fc})^2} (x_{lf})^2 \cos(2\pi f (t - t_0) + \psi_f) \tag{3.70}$$

$$h_{tf} = \frac{\bar{a}_f}{(1.0 - x_{fc})^2}(x_{tf})^2 \cos(2\pi f(t - t_0) + \psi_f) \tag{3.71}$$

$$h_{lf} = -\frac{\bar{a}_f}{(x_{fc})^2}(x_{lf})^2 \left|\cos(2\pi f(t - t_0) + \psi_f)\right| \tag{3.72}$$

$$h_{tf} = -\frac{\bar{a}_f}{(1.0 - x_{fc})^2}(x_{tf})^2 \left|\cos(2\pi f(t - t_0) + \psi_f)\right| \tag{3.73}$$

Table 4.3: Flexing amplitude problem at the trailing edge when x_{fc} moves

	x_{fc}	a_f (old method) or a_{tf} (new method)	x_{tf} (at trailing edge)	$a_f(x_{tf})^2$
Old method	0.00	0.3	1.00	0.300
	0.75	0.3	0.25	0.019
0.3	0.75	4.8	0.25	0.300

In order to simulate the flexed flapping airfoil, the grid is first deformed using arc-length-based TFI (Jones and Samareh-abolhassani 1995) to accommodate the flexing. The space conservation law, proposed by Demirdizic and Peric (1988) has been incorporated to consistently compute the cell area for the moving boundary. The entire new grid then rotates or translates in the x or y directions depending on the pitching and heaving requirement.

Due to the flexing of the airfoil, the angle of attack of the airfoil still changes throughout the cycle even though it only executes heaving motion. The angle of attack is defined as the angle the chord line makes with the horizontal.

The airfoils tested are the NACA0012, NACA6302 and the S1020 airfoils. They are used earlier in the simulation of non-symmetrical airfoil under different flapping configurations and hence the results obtained earlier can be used for comparisons. The NACA6302 and S1020

airfoils are selected because they represent the "thin" and "thick" classes of airfoils respectively. The flexing and morphing will be tested based on five flapping configurations. The first configuration is the heaving motion used by Miao and Ho (2006). This will enable a direct comparison with their results. The other three configurations are based on the non-symmetrical airfoil BB test results earlier which give the maximum η (Maximum Efficiency, ME) (BB test 11), $\overline{C}_t$ (Maximum Thrust, MT) (BB test 16) and $\overline{C}_l$ (Maximum Lift, ML) (BB test 20). The parameters used in these configurations are given in Table 4.4. The objective is to determine if the flexing of the airfoils can further improve the already optimal results. The last configuration uses the same parameters as that of the maximum efficiency (ME) for all the parameters except the θ_0. In the last configuration, $\theta_0 = 20^o$. The reason for doing this particular configuration is to test whether flexing can improve the η when the airfoil is not flapping at its optimum configuration.

Table 4.4: Parameters of the different test cases

Type	***k***	***St***	θ_0	ϕ	h_0 **(=*St*/(2*k))**
Pure heaving (PH)	0.32	0.25	0.0	NA	0.40
Maximum η (ME)	0.20	0.30	-30.0	90	0.75
Maximum $\overline{C}_t$ (MT)	0.60	0.50	-17.5	120	0.42
Maximum $\overline{C}_l$ (ML)	1.00	0.30	-17.5	120	0.15

The selected parameters are center of flexure, leading edge flexing and trailing edge flexing. The leading edge, center of airfoil and trailing edge will be chosen as the 3 center of flexure locations. In order to reduce the number of simulations required, they are conducted in the following fashion:

1. Begin the simulation with the smallest flexing amplitude and increase the flexing in equal divisions of 0.1 each, in either direction (positive or negative)
2. When $\eta < 0$, the simulation will stop immediately.

3. For $|\bar{a}_f| \leq 0.4$, the particular set of simulation will stop if the η, $\bar{C}_t$ and $\bar{C}_l$ all continue to decrease consecutively after 2 increments.
4. For $|\bar{a}_f| > 0.4$, as long as at least 1 variable increases, the simulation will still continue. The simulation will stop if the η, $\bar{C}_t$ and $\bar{C}_l$ all decrease after 1 increment.
5. The range of the parameters' amplitudes for a new set of simulation will change depending on the results of the previous sets of simulation.
6. In some cases, the grid will be distorted when the flexing amplitude is too high. As a result, the solution will diverge. Due to this limitation, the range of amplitude tested has to be decreased.

4.3 Tandem Airfoils

This section covers the simulation of 2 flapping airfoils in tandem using the IBCNSS. The aim is to determine how the interaction between the 2 airfoils can affect and improve the overall performance. Similar to the chordwise flexing simulation, the maximum η (ME), $\bar{C}_t$ (MT) and $\bar{C}_l$ (ML) configuration from the BB test will be used for the simulation in this section. For now however, 2 airfoils will be in tandem while undergoing the same flapping configuration. The differences between the current research and the other tandem arrangement research mentioned earlier are that:

1. The flapping configurations used in this section of the research are obtained from the earlier DOE simulations which already give high η, $\bar{C}_t$ and $\bar{C}_l$ for single flapping airfoil.
2. Unlike the flapping configuration of the dragonfly which is much more complicated, these sinusoidal ones are much easier to implement in practice for ornithopters.
3. Many researches focused on the phase difference between the airfoils only, whereas in this current research, the distance between the airfoil is also investigated.

One hopes to find out the how the phase difference and distance between the airfoils affect the

η, $\overline{C}_t$ and $\overline{C}_l$ of the airfoils for each of the flapping configurations. Another objective is to verify whether the effect of the in-phase and out-of-phase wing interaction shown in Wang and Russell (2007) applies to the three flapping configurations used here as well.

The flapping motion for the fore (upstream) airfoil will be:

$$h_0 = h_0 \sin(2\pi f(t - t_0) - \phi) \tag{3.74}$$

$$\theta = \theta_0 \sin(2\pi f(t - t_0)) \tag{3.75}$$

The flapping motion for the aft (downstream) airfoil will be:

$$h_0 = h_0 \sin(2\pi f(t - t_0) - \phi + \phi_{12}) \tag{3.76}$$

$$\theta = \theta_0 \sin(2\pi f(t - t_0) + \phi_{12}) \tag{3.77}$$

Where ϕ_{12} is the phase angle between the heaving position of the first and second airfoils.

The fully implicit scheme whereby the convective term is approximated by the Crank Nicholson scheme is used. As mentioned earlier in section 2.1, when the semi-implicit scheme (convective term approximated by the Adams–Bashforth scheme) is used, divergence of solution occurs. Due to the non-conformal grid of the IB, if the simulation runs at a ***Re*** of 10,000, it will require a very high resolution grid. Hence the simulation throughout this section uses a ***Re*** of 1,000, which will help to limit the grid requirements. Moreover, only the S1020 airfoil is used in this simulation because of the high computational cost. The S1020 airfoil is selected because it performs the best among all the airfoils tested in the earlier DOE test. Past studies (Anderson and Kerrebrock 1997) have shown that the C_t of flapping airfoil is relatively insensitive to ***Re*** changes. Nevertheless, the simulation is repeated at ***Re*** = 1,000 for the ME, MT and ML configurations. Figure 4.4 and Table 4.5 show that both MT and ML configurations give similar results (for averaged values) at ***Re*** = 1,000 and 10,000, although there is some difference in the force plots. On the other hand, the force plots of ME configuration at ***Re*** = 1,000 and 10,000 show obvious difference. The efficiencies at the two

different *Re* are also different. This shows that for some flapping configurations, the results obtained can be different. The vorticity diagrams for the ME configuration at *Re* = 1,000 and 10,000 are shown in Figure 4.5. The lower *Re* and low *k* (= 0.2) causes more flow separation than the higher *Re* case, resulting in a drop in the $\overline{C}_l$. With reference to the power input equation (Eqn (3.47)), since both cases are having the same flapping configurations, the only difference is the *L(t)*. A smaller C_l amplitude will decrease the power input (average *P* = 0.72 at *Re* = 1,000 vs. 0.96 at *Re* = 10,000). However, since C_t is decreases much more as *Re* decreases (0.55 to 0.24), the resulting η becomes much lower. Hence, the performance of the tandem airfoil configurations are now compared against the single flapping airfoils at *Re* = 1,000 to ensure a fair comparison.

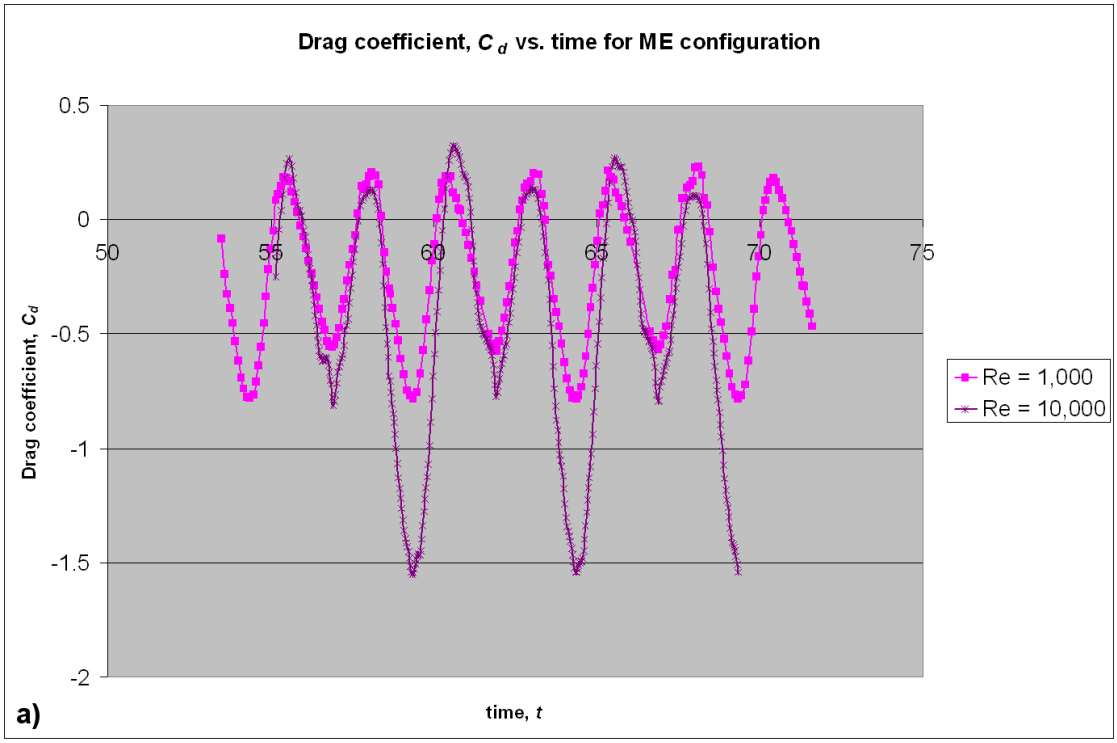

Figure 4.4: Drag and lift coefficient plots of the (a) ME, (b) MT and (c) ML configurations at *Re* = 1,000 and 10,000 (continue on next page)

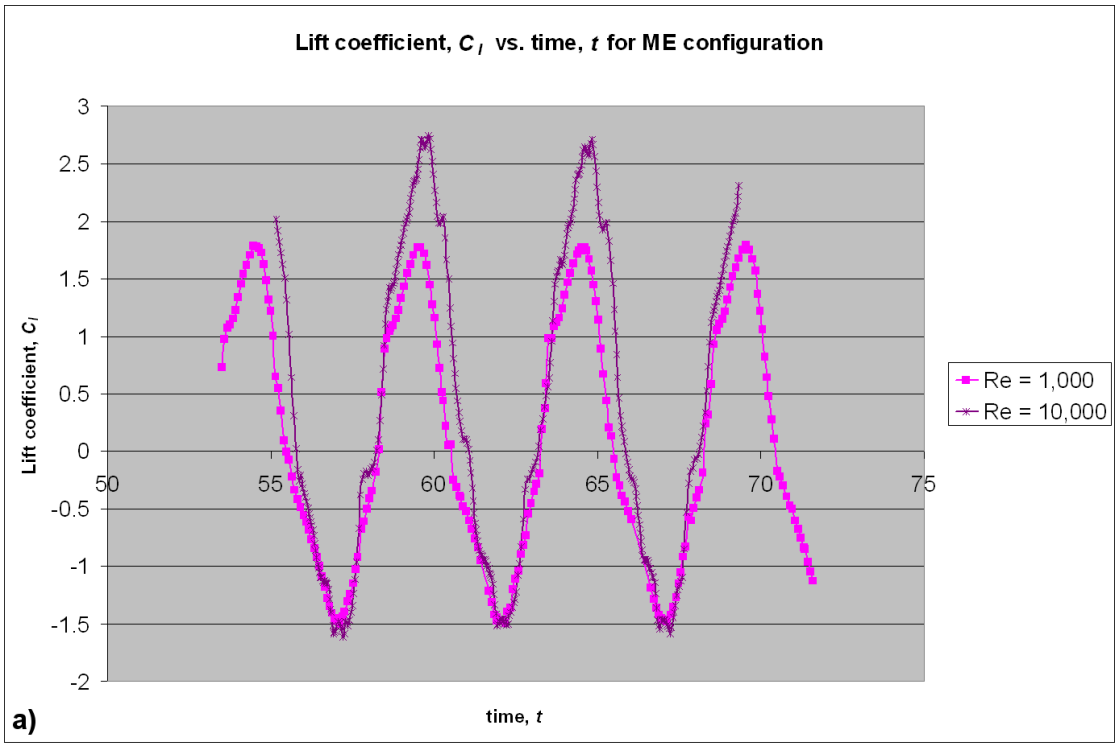
Lift coefficient, C_l vs. time, t for ME configuration
Lift coefficient, C_l
time, t
Re = 1,000
Re = 10,000
a)

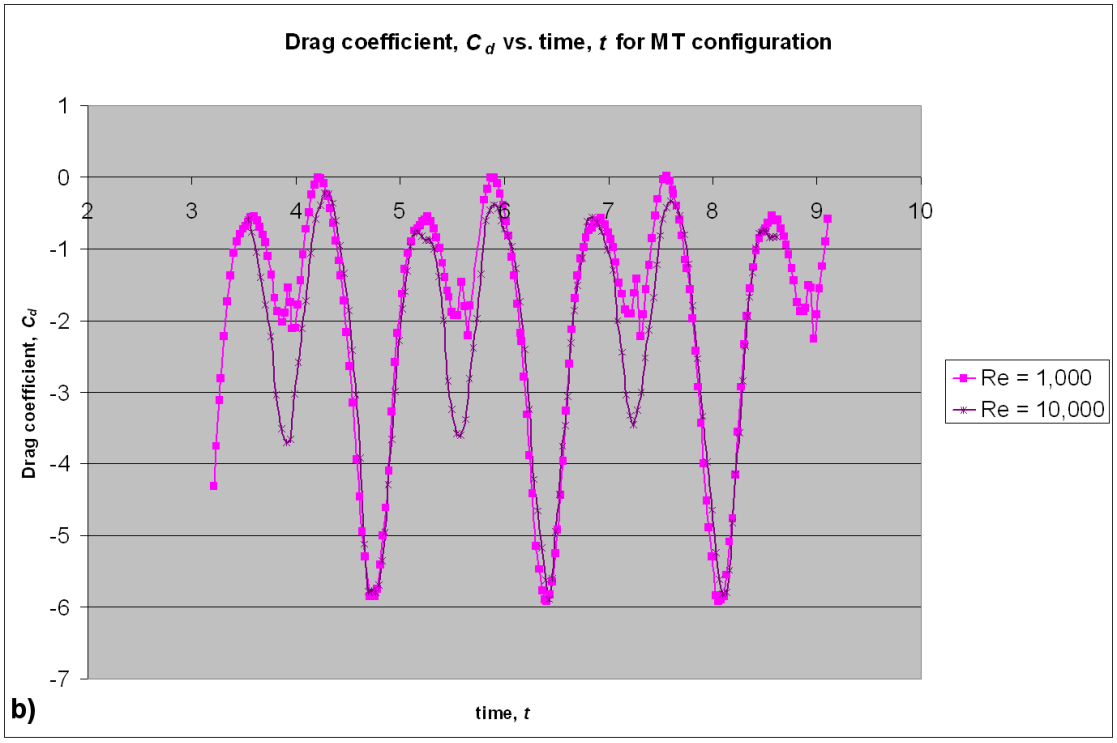
Drag coefficient, C_d vs. time, t for MT configuration
Drag coefficient, C_d
time, t
Re = 1,000
Re = 10,000
b)

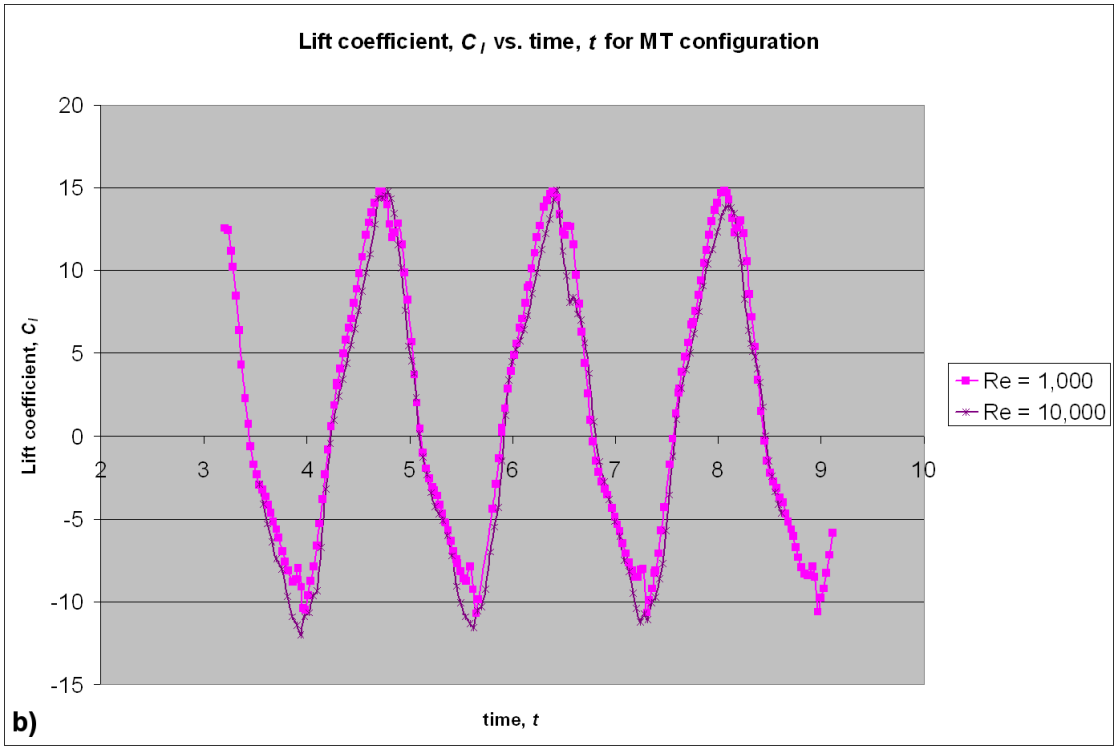
Lift coefficient, C_l vs. time, t for MT configuration
Lift coefficient, C_l
time, t
Re = 1,000
Re = 10,000
b)

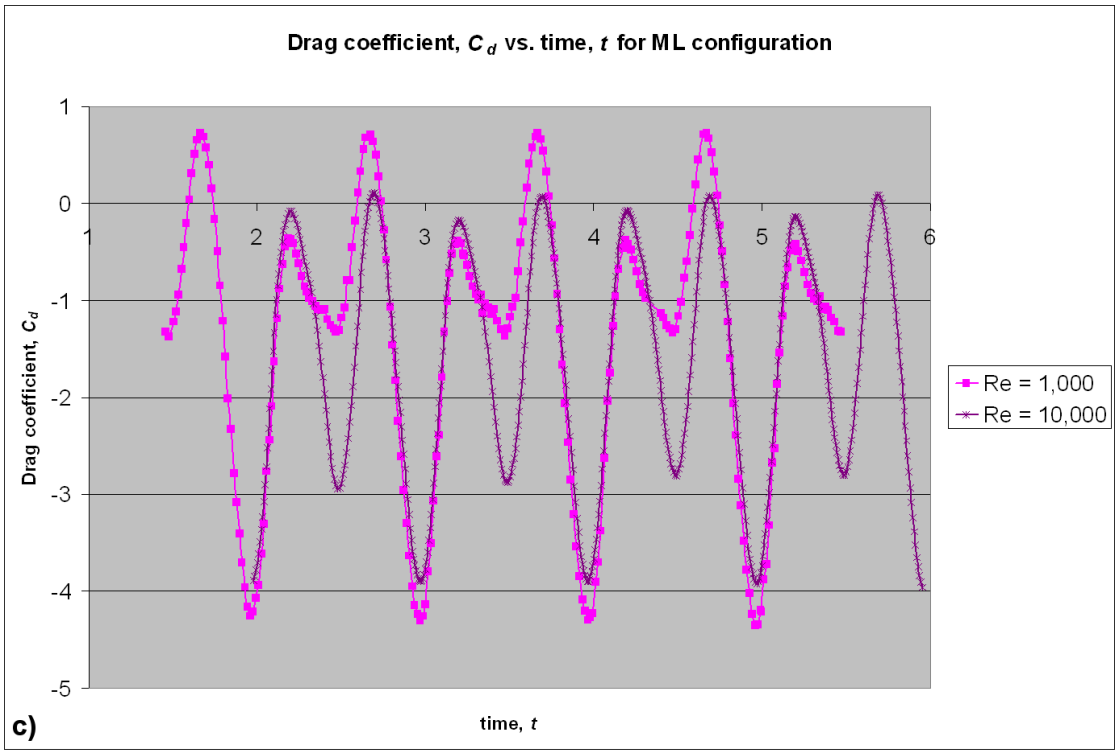
Drag coefficient, C_d vs. time, t for ML configuration
Drag coefficient, C_d
time, t
Re = 1,000
Re = 10,000
c)

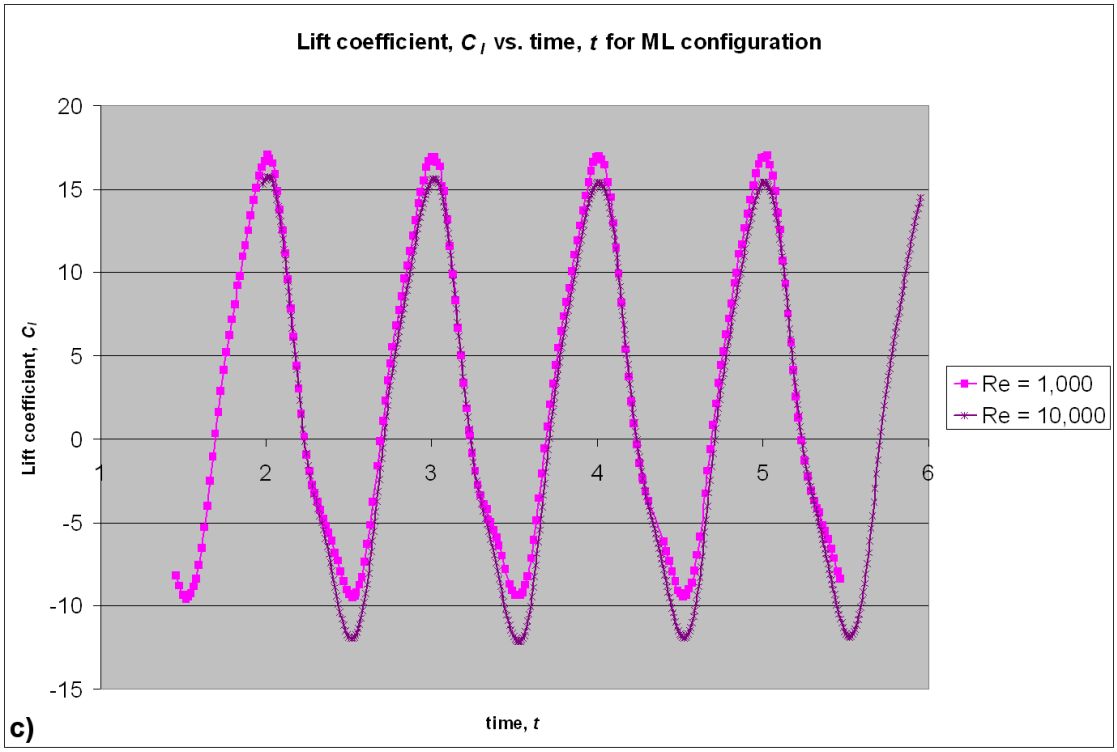

Table 4.5: Comparison of BB test results at *Re* 1,000 and 10,000

Type	**ME**		**MT**		**ML**	
Re	1,000	10,000	1,000	10,000	1,000	10,000
η	0.33	0.57	0.23	0.26	0.18	0.20
$\bar{C}_t$	0.22	0.55	2.05	2.33	1.40	1.63
$\bar{C}_l$	0.03	0.51	2.22	1.35	3.04	1.93

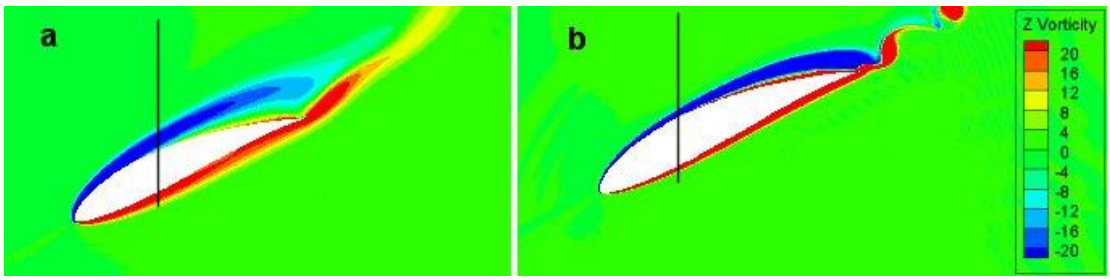

Figure 4.5: Vorticity diagram of ME configuration at *Re* = (a) 1,000 (b) 10,000

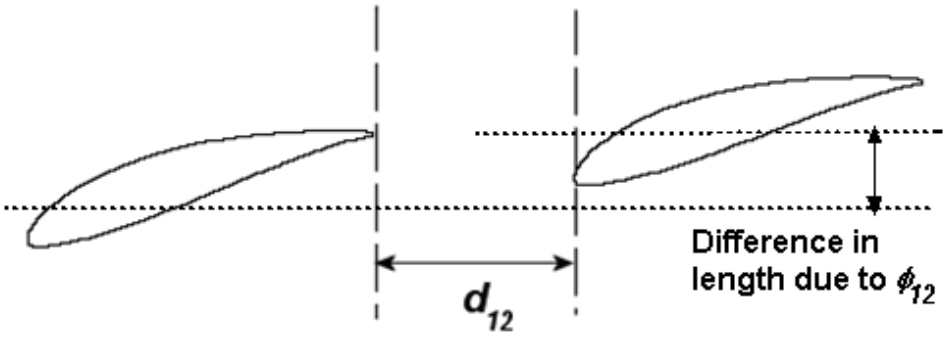

Figure 4.6: Definition of d_{12} and ϕ_{12} illustrated

The parameters are the distance between the 2 airfoils (d_{12}) (as shown in Figure 4.6) and the phase difference between their heaving positions (ϕ_{12}). Similar to the chordwise flexing simulations, the parameter space is relatively large. Moreover, the tandem simulations using the IBCNSS are much more expensive. The efficiency, average thrust and lift coefficients of the tandem configurations are now defined as:

$$\bar{C}_{t,o} = \bar{C}_{t,\,fore\ airfoil} + \bar{C}_{t,aft\ airfoil} \tag{3.78}$$

$$C_{l,o} = \bar{C}_{l,\,fore\ airfoil} + \bar{C}_{l,aft\ airfoil} \tag{3.79}$$

$$\eta_o = \frac{\bar{C}_{T,\,fore\ airfoil} + \bar{C}_{T,aft\ airfoil}}{\bar{P}_{fore\ airfoil} + \bar{P}_{aft\ airfoil}} \tag{3.80}$$

The definition of η_o is similar to that of Akhtar et al. (2007). An index known as the performance index I_p is defined to determine the overall performance of the tandem airfoils. Its formula is given as

$$I_p = \frac{\eta_o(d_{12}\ or\ \phi_{12})}{\max(all\ \eta_o(d_{12}\ \text{or}\ \phi_{12}))} + \frac{\bar{C}_{t,o}(d_{12}\ or\ \phi_{12})}{\max(all\ \bar{C}_{t,o}(d_{12}\ \text{or}\ \phi_{12}))} + \frac{\bar{C}_{l,o}(d_{12}\ or\ \phi_{12})}{\max(all\ \bar{C}_{l,o}(d_{12}\ \text{or}\ \phi_{12}))} \tag{3.81}$$

The simulations will be conducted in a similar fashion to the chordwise flexing case as follows

1. Begin the simulation with d_{12} = 2.5, ϕ_{12} = -90^o for each of the flapping configuration and decrease the value of d_{12} by 0.25 as the simulation proceeds until d_{12} = 1.25. ϕ_{12} is

fixed. Although simulating at d_{12} > 2.5 is possible, it is not practical to design an ornithopter which is very long. The results by Akhtar et al. (2007) show that when ϕ_{12} = -108°, the η and $\bar{C}_t$ of the tandem configuration are much higher than that of the single airfoil's. Hence, the starting value of ϕ_{12} is chosen as -90°.

2. Once the value of d_{12} at which I_p is a maximum has been determined, ϕ_{12} will start to vary, starting from ϕ_{12} = 150°. , now keeping d_{12} fixed at the maximum I_p found earlier. The value of ϕ_{12} will decrease by 30° as the simulation proceeds until ϕ_{12} = -180°.

Although running the above simulations is not a foolproof way to obtain the maximum I_p, it is computationally cheaper than running all the possible permutations. Moreover, the objective of the study is to see if the performance of the airfoil can be improved with the help of using a tandem arrangement. Obtaining the optimal d_{12} and ϕ_{12} at the absolute maximum I_p is of secondary importance.

5 Results and Discussions from the DOE

The results and discussions from the DOE Box-Behnken (BB) test are discussed in this chapter. The SCNSS is used to simulate these test configurations. For each configuration, the simulation will stop once the lift and drag coefficient have reached a periodic state. This will allow the average lift, thrust coefficient and propulsive efficiency to be computed. The results for the different airfoils can be found in Table A.2 to Table A.6 in the appendices.

Unfortunately, for some test configurations, the lift and drag coefficients do not reach a steady periodic state. The maximum and minimum C_l and C_t do not reach a fixed value as the simulation proceeds. Increasing the grid resolution or number of points and reducing the CFL number do not make any difference to the solution. The only possible explanation is that these configurations are truly unsteady. A C_t vs. t graph of one of these cases (NACA4404 airfoil, BB test 10) is shown in Figure 5.1 while its vorticity diagrams are shown in Figure 5.2. The diagram shows that the vortex shed (circled) stays in the vicinity of the airfoil and it is not convected away. It then interacts with the newly shed vortex. As more vortices are shed, more of these interactions happen and the result can be very unpredictable. This may have explained why the lift and drag coefficients do not reach a steady periodic state. In these cases, the simulations are computed over at least 10 periods. They are also marked with a (*) next to the BB test number in the simulation results of the different airfoils in Table A.2 to Table A.6 in the appendicies. Jones et al. (2002) also reported similar non-periodic findings. They observed that it is often true in cases where shedding and separation are predominant. Different airfoils have different BB test cases which are non-periodic, although some test cases are non-periodic in all airfoils.

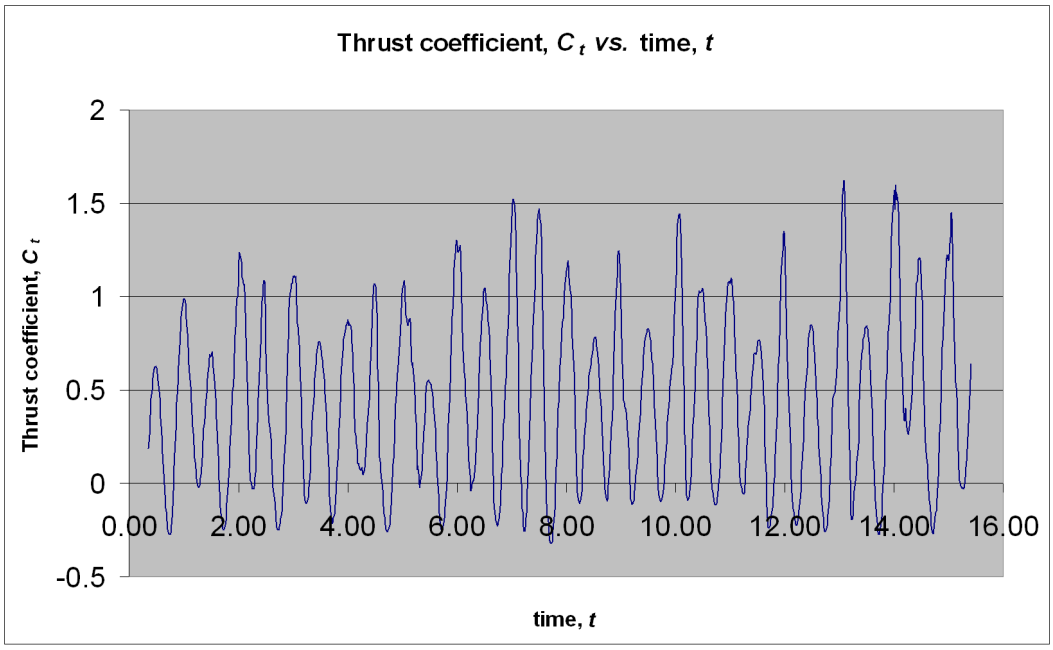

Figure 5.1: C_t vs. t plot of the NACA4404 airfoil simulated using BB test 10

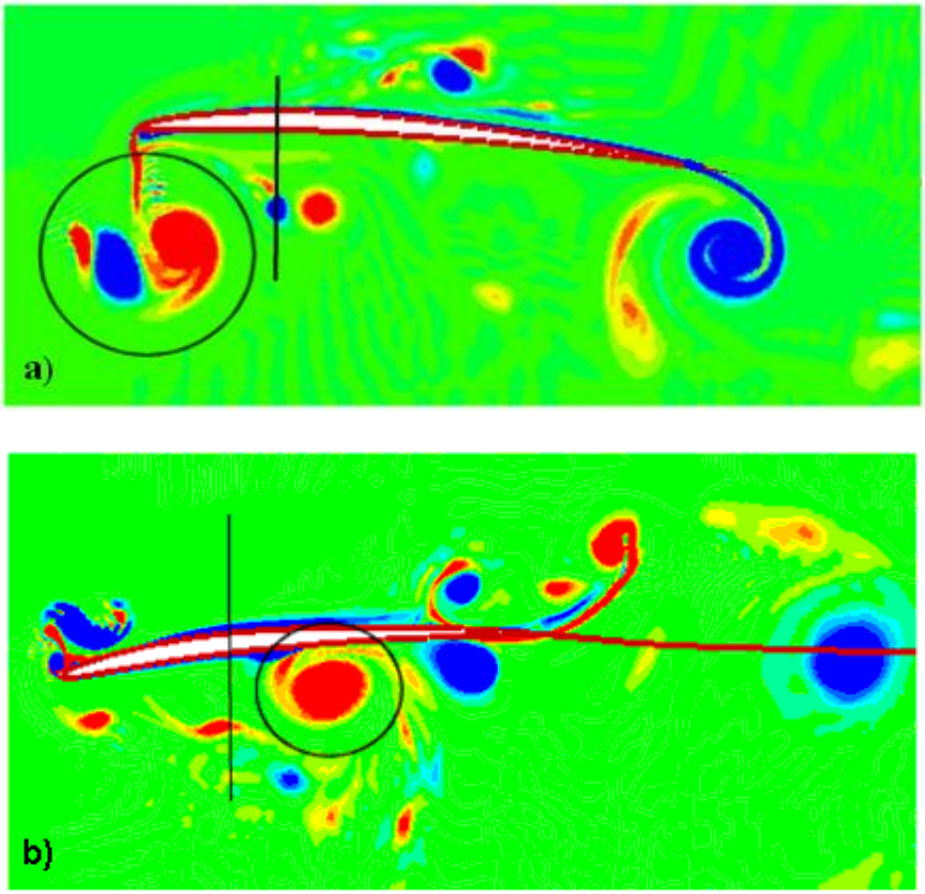

Figure 5.2: (a) Newly shed vortex at leading edge (b) Vortex not convected away but stay around the NACA4404 airfoil (c) Old vortex interacts with newly shed vortex (continue on next page)

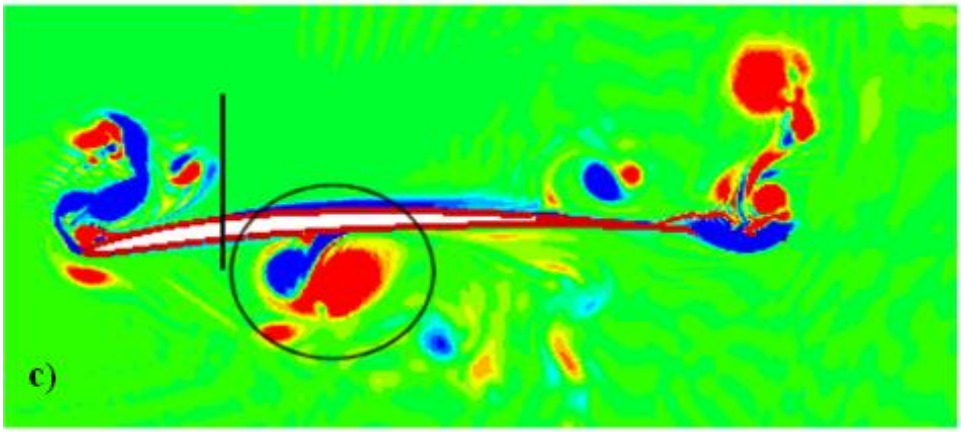

The DOE software Minitab is used to analyze the results to determine the significance and interactions of the variables. The residuals diagnostic plots generated by Minitab are also checked and it has been found that the residuals are normally distributed and homoscedastic with respect to the design variables and the fitted values as required by the analysis method.

5.1 The Box-Behnken (BB) Test

The BB test is used to determine the significance of reduced frequency (k), Strouhal number (St), maximum pitch angle (θ_0) and phase angle between pitching/heaving (ϕ). The BB design allows the study of the significance of the main effects and two-factor interactions between the different variables. Three-factor and above interactions are usually very rare and hence they are not included in the study.

It must be emphasized that one must be careful in analyzing main effects in the presence of interactions. This is because main effect is the effect of a particular factor **on average**. When interactions exist, its response will be different. For example, the main effects graph of η vs. k on Figure 5.3a shows maximum η when k = 0.2 for the NACA0012 airfoil. However, interaction graph between k and θ_0 on Figure 5.5 shows that when $\theta_0 = 5^o$, η is maximum when k = 1.0. One can refer to Dallal (2007) for a more detailed explanation.

This section is divided into three parts - efficiency, average thrust and lift coefficients. Each part will discuss how the variables (example *St*) and their interactions affect the different airfoils' η, $\overline{C}_t$ or $\overline{C}_l$. Main effects and two-factor interactions, if they are shown to be significant by most airfoils, will be discussed. The p_s value calculated by Minitab is used to test whether the above mentioned factors and their interactions are statistically significant or not. A value of p_s less than *0.05* indicates that it is significant. Table 5.1 to 5.3 show the relative significance of each factor, their quadratic effects and the effects of the two-factor interactions on the efficiency, average thrust and lift coefficients of each airfoil respectively.

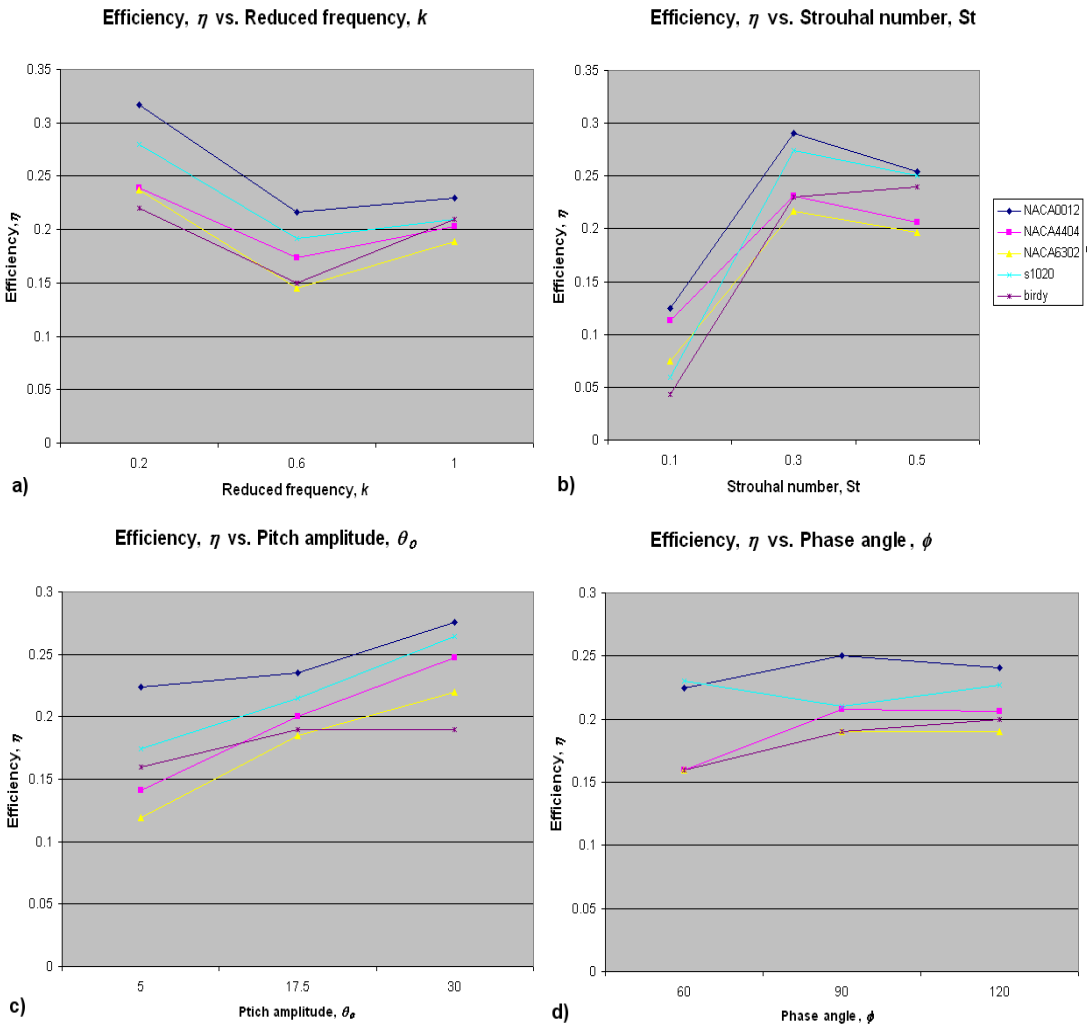

Figure 5.3: Main effects plot of efficiency vs. each of the factors

Table 5.1: Test of significance results for efficiency

p_s	NACA0012	NACA4404	NACA6302	S1020	birdy
St	**0.008**[***]	0.126	**0.026**	**0.002**	**0.003**
θ_0	0.268	0.055	**0.031**	0.129	0.579
*St*St*	**0.005**	**0.031**	**0.012**	**0.004**	**0.015**
$k*\theta_0$	**0.003**	**0.038**	**0.043**	**0.008**	**0.037**
$St*\theta_0$	0.063	**0.027**	**0.046**	0.262	0.283

5.2 Significance and Effect of Variables on Efficiency

In general, *St* is found to have a significant effect on η for all airfoils except the NACA4404 airfoil (p_s = 0.126, > 0.05). The level of significance of each factor is also different on each airfoil, indicating that the shape of the airfoil also affects propulsive efficiency. The quadratic relationship of the variables with η can be obtained from the p_s values of the quadratic rows in Table 5.1 and also from the graph in Figure 5.3. In all cases, the interaction between *k* and θ_0 is very strong.

Overall, the NACA0012 airfoil gives the best η, using the BB test 11. Figure 5.4 shows its vorticity diagram. It can be observed that the vortices generated are small, compact, and coherent, hence resulting in very high efficiency (η = 0.61). The generation of the vortices only happens during the extreme top and bottom position, where the airfoil undergoes fast rotation. There is also no leading edge separation. The S1020 and NACA4404 airfoils also give relatively high efficiency (η = 0.57 - 0.58) using the same test. The birdy airfoil yields the

[***] Numbers in bold indicate that the variable or their interaction is significant (≤0.05). If the entire row is insignificant, it is removed from the table and not shown.

lowest efficiency at η = 0.46.

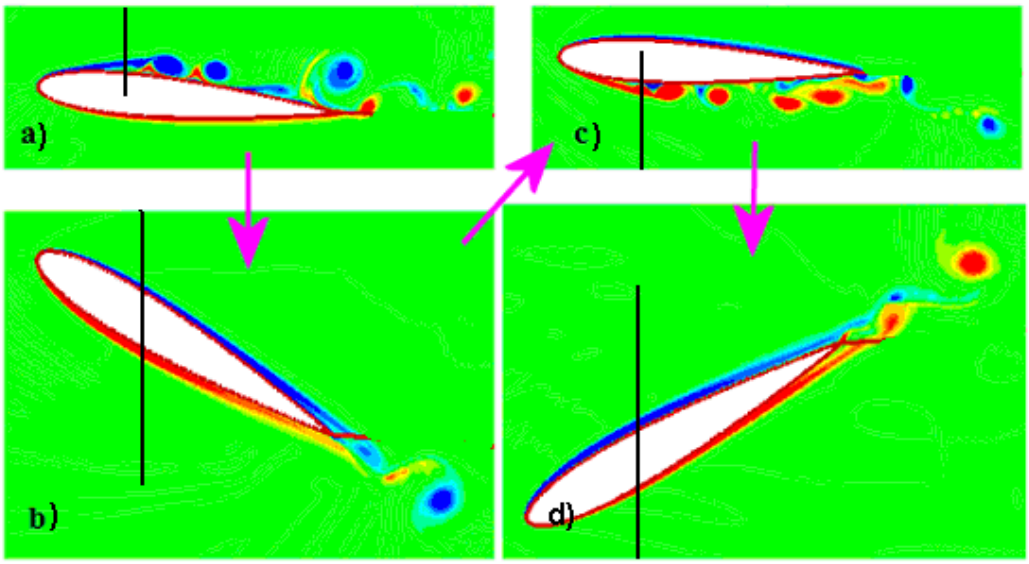

Figure 5.4: Vorticity diagram of NACA0012 airfoil undergoing the BB test 11, (a) extreme bottom (b) mid, moving up (c) extreme top (d) mid, moving down position

5.2.1 Significance of k and θ_0 and their Interaction

The effect of k is only marginally significant for NACA0012 and much less significant for the other airfoils. The main effects graph of η vs. k shows that on average, low k is preferred for high efficiency for all airfoils since the vortices generated are more coherent. The influence of θ_0 is only significant for the NACA6302 airfoil. On average, increasing θ_0 is beneficial for η in all cases.

Although both the effects of k and θ_0 on their own are not strong in almost all airfoils, the interaction between the two of them proved to be significant, as shown in Figure 5.5. For all airfoils, it is evident that low k, high θ_0 combination provides high efficiency. Figure 5.6 shows the vorticity diagrams of the NACA0012 airfoil undergoing (a) low k, low θ_0 (BB test 9), (b) low k, high θ_0 (BB test 11), (c) high k, low θ_0 (BB test 10) and (d) high k, high θ_0 (BB test 12) simulations. Since St is the same for all these cases, the heaving amplitude will be different for different k. Hence, if the airfoil travels through a large heaving distance with a small θ_0 and k

(case (a)), separation will occur easily along the leading edge. As a result, non-compact vortices will be generated and coherent flow will be disrupted. Separation occurs most likely because of the ample time and large heaving travelling distance of the airfoil. Interestingly, when θ_0 is high, separation only happens during the extreme heaving positions. The vortices generated are much smaller and coherent and results in very high efficiency. The reason is that the airfoil "snakes" through the flow, resulting in a low angle of attack. This is also mentioned by Pedro et al. (2003) in his paper. On the other hand, at high k (case (c) and (d)), η is low. This is true also for all other combinations of variables when k is high. As discussed earlier, high reduced frequency (k) is equivalent to high frequency of oscillation (f). Hence, more energy is then injected into the flow resulting in the production of less compact, coherent vortices, lowering its efficiency, as shown by the Figure 5.6c and d cases.

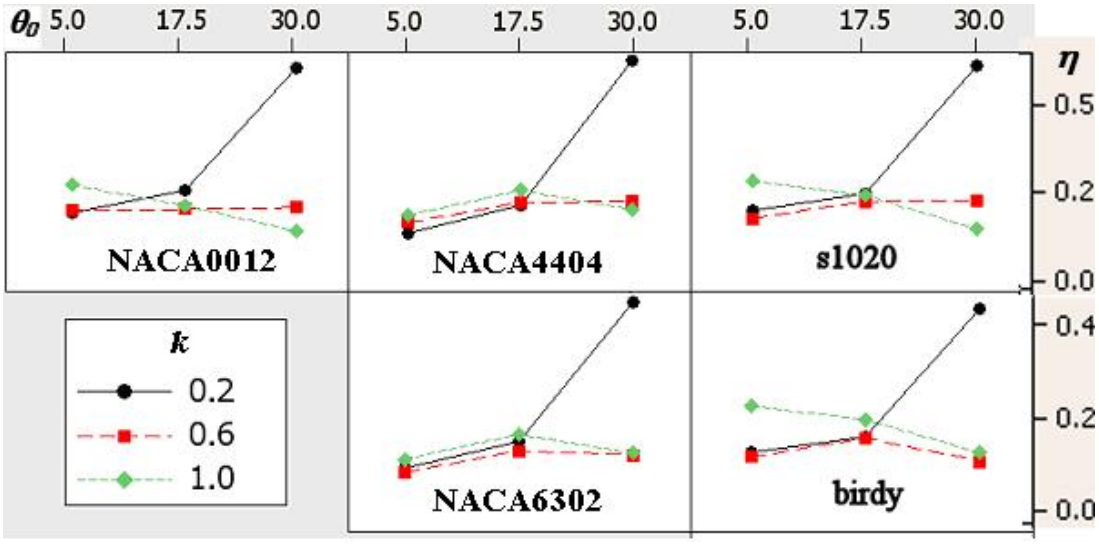

Figure 5.5: Two-factor interaction plot of k and θ_0 vs. efficiency

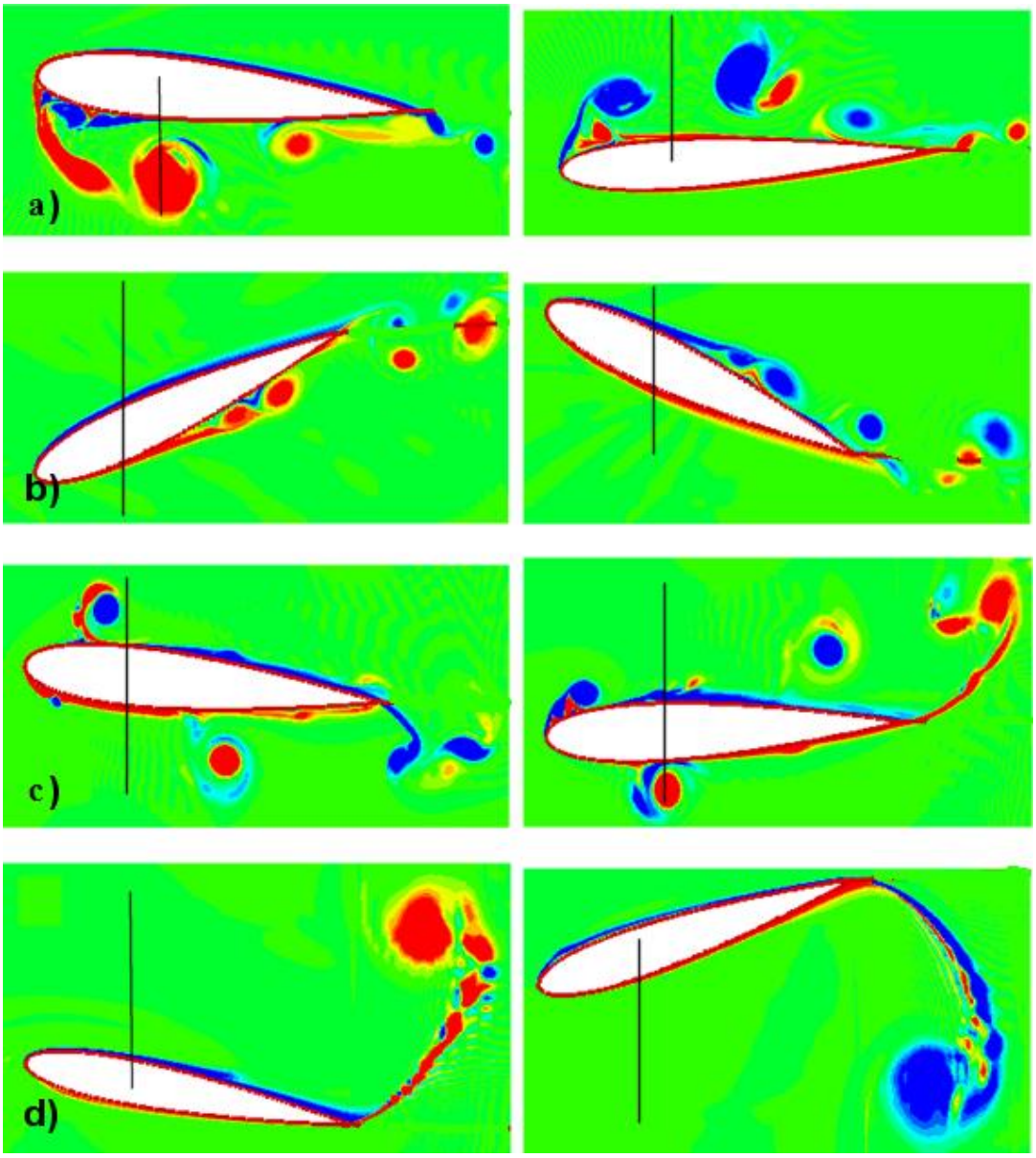

Figure 5.6: Vorticity diagram of the NACA0012 airfoil undergoing simulation at (a) low *k*, low θ_0 (b) low *k*, high θ_0 (c) high *k*, lowθ_0 (d) high *k*, high θ_0

5.2.2 Significance of *St*

Results show that in all airfoils except NACA4404, *St* is an important factor (p_s for NACA4404's η is 0.126, which is bigger than 0.05). Out of these airfoils, only the NACA4404 and NACA6302 airfoils have significant *St* and θ_0 interactions. Hence it is safe to focus on the analysis of the main effects plot of η vs. *St*. The low value of p_s for *St***St* of all airfoils indicates that there is a high degree of curvature present. In other words, the relationship

between *St* and η is a quadratic one. The graph of η vs. *St* also illustrates the quadratic relationship. It shows that the η increases from *St* = 0.1 to 0.3 and the decreases. Although there are only 3 levels of *St* , the low value of p_s for *St***St* and the variation of η in this small *St* range indicate that there is a high probability that maximum η lies around *St* = 0.3. This confirms the earlier finding (Triantafyllou et al. 1993; Taylor et al. 2003) which states that most birds fly in the range of $0.2 < St < 0.4$ since it is the most efficient mode of flying.

Figure 5.7a and b show the vorticity diagrams of the NACA0012 airfoil undergoing simulation at *St* = 0.1 and 0.5[†††] respectively. All other factors are at the same level as the BB test 11 in Figure 5.4, where *St* = 0.3. Figure 5.7a shows that the vortices shed are small and compact but on Figure 5.7b, they are much larger and not as orderly. Moreover, leading edge separation is visible. Since $St = \frac{fh_0}{U_\infty}$, $k = f$ and $St = kh_0$, at a fixed reduced frequency *k*, *St* is directly proportional to h_0. Based on the definition of efficiency, it depends on the $\overline{C}_t$ produced as well. As will be discussed in the later section, the $\overline{C}_t$ produced depends heavily on the *St* value. Hence, at low *St*, the $\overline{C}_t$ produced is very small or even negative. In fact, at *St* = 0.1, the NACA0012 airfoil is producing drag. Therefore, at low *St*, η is very low or zero. On the other hand, higher *St* results in higher heaving amplitude, velocity, and higher energy input. As seen in Figure 5.7b, the high *St* creates large and non-orderly vortices, increasing the power input. The larger heaving amplitude will cause the airfoil to be more prone to leading-edge separation, since it is translating at a large relative angle of attack for a relatively longer distance. These lower the $\overline{C}_t$. As a result, efficiency is optimal at the mid level.

[†††] These two cases do not belong to the 25 test configurations generated based on the Box-Behnken design

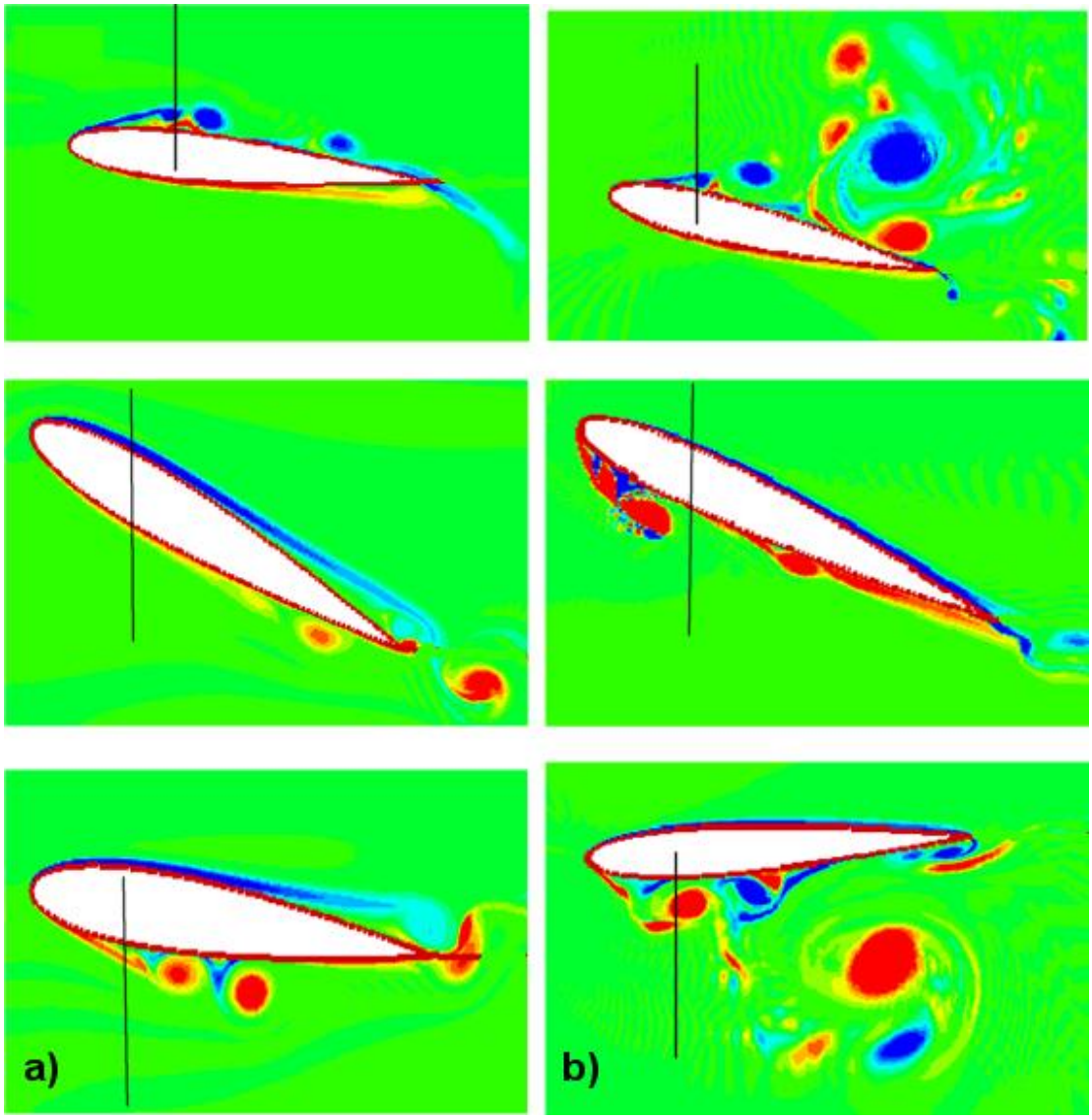

Figure 5.7: Vorticity diagram of the NACA0012 airfoil undergoing simulation at *St* = (a) 0.1 and (b) 0.5, moving up from extreme bottom to extreme top position

5.2.3 Significance of ϕ and θ_0

Results show that the effects of ϕ and θ_0 are not significant in most airfoils. Increasing θ_0 generally increases η for all airfoils. For ϕ, it is interesting to note that as reported by some studies (Isogai et al. 1999; Ramamurti and Sandberg 1999), $\phi = 90^o$ results in maximum efficiency for the NACA0012 airfoil, as shown in the main effects plot of Figure 5.3d. However, the other non-symmetrical airfoils have different preferred ϕ value for maximum efficiency.

5.2.4 Comparison of Efficiency of Different Airfoils

Different airfoils give different efficiencies even though the flapping parameters are exactly the same. This is evident from Figure 5.3. In general, the shape of the graph for each variable is similar for most of the airfoils but some are positioned higher than others. The NACA0012 is usually the best efficient airfoil followed by the s1020 airfoil and the NACA4404 airfoil. Both the NACA6302 and birdy airfoils tend to give poorer efficiency compared to the other airfoils. Comparing between the two extremes, the NACA0012 airfoil is the best with η = 0.61 while the birdy is the worst with η = 0.46. In general, the birdy airfoil gives lower η as compared to other airfoils for all BB tests. The vorticity diagrams of the NACA0012 and birdy airfoils at BB test 11 are shown in Figure 5.8. The plots show that the vortex shedding on the convex top surface of both airfoils are similar. The flow remains attached for most part of the cycle and only shed during rotation at the extreme top and bottom positions. However, the concave bottom surface of the birdy airfoil resulted in the vortices being shed throughout the cycle. Leading edge separation is clearly evident in Figure 5.8b for the birdy airfoil. The vortices generated are also bigger and less coherent. This must have resulted in its lower efficiency. One may think that the shape of a bird's wing should perform better after many years of revolution. However, factors such as the absence of flexibility and feathers may influence the results.

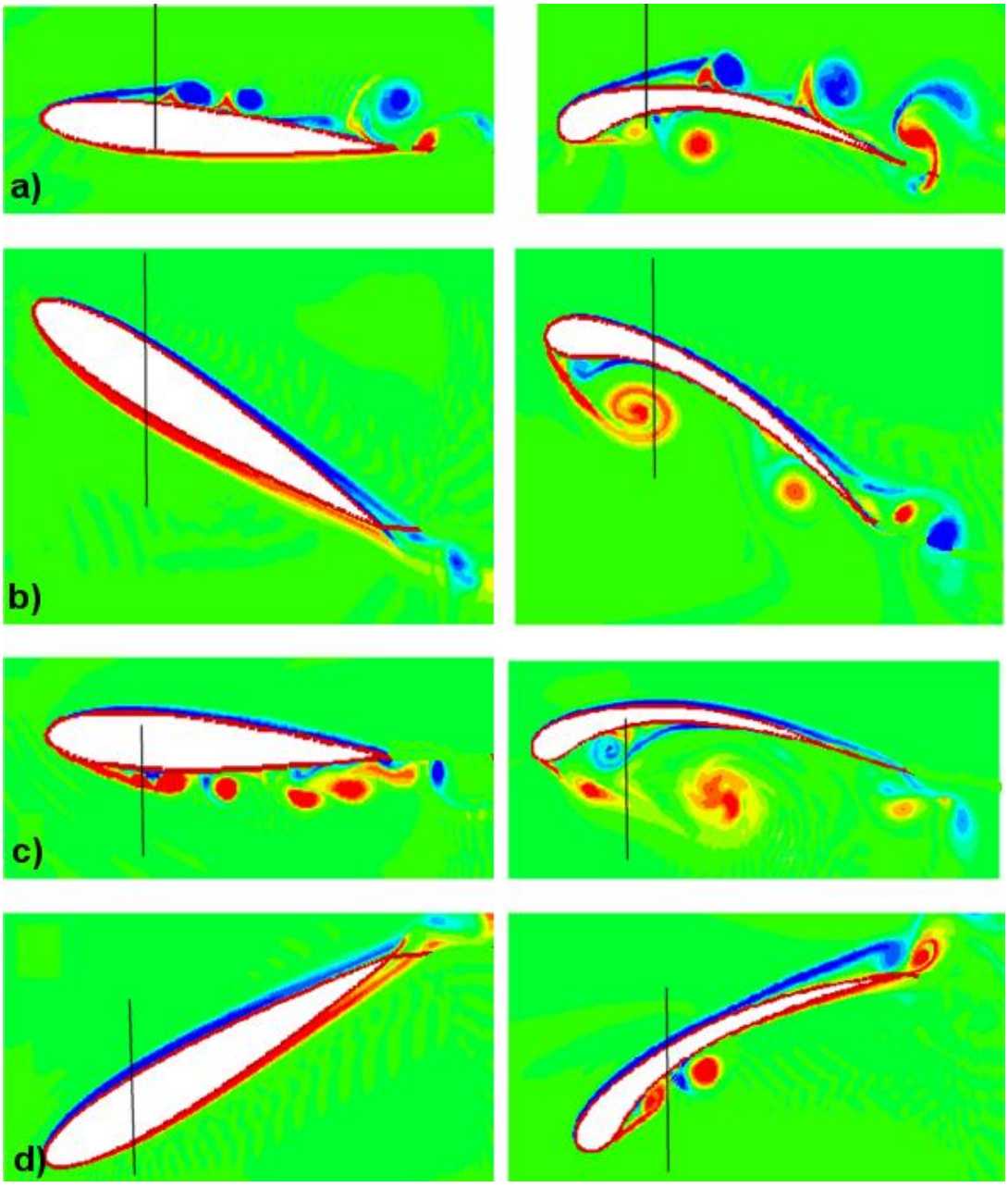

Figure 5.8: Vorticity diagram of the NACA0012 (left) and birdy (right) airfoils flapping with the same configuration (a) lowest position, after rotation, moving up (b) middle position, moving up (c) top position, after rotation, moving down (d) middle position, moving down

5.3 Significance and Effect of Variables on Thrust

For thrust, it seems all the factors have significant effects on the airfoils, as shown in Table 5.2. Quadratic relationship for *St* is significant for all airfoils except the NACA4404 and NACA6302 airfoils. It also shows that two-factor interactions are very strong in all airfoils. In this case, two-factor interactions must be analyzed together with the main effects plots to give

a more complete picture. Out of all the BB tests, the NACA0012 airfoil undergoing BB test 16 produces slightly higher average thrust coefficient ($\overline{C}_t$ = 2.53) compared to the rest of the airfoils.

Table 5.2: Test of significance results for average thrust coefficient

p_s	NACA0012	NACA4404	NACA6302	S1020	birdy
k	**0.000**	**0.000**	**0.000**	**0.000**	**0.000**
St	**0.000**	**0.000**	**0.000**	**0.000**	**0.000**
θ_0	**0.000**	**0.000**	**0.000**	**0.000**	**0.000**
ϕ	**0.000**	**0.000**	**0.000**	**0.000**	**0.000**
*St*St*	**0.010**	0.117	0.378	**0.003**	**0.050**
*k*St*	0.084	**0.039**	0.102	0.091	0.152
$k*\theta_0$	**0.002**	**0.001**	**0.003**	**0.003**	**0.006**
$k*\phi$	**0.001**	**0.001**	**0.006**	**0.001**	**0.002**
$St*\theta_0$	**0.036**	**0.001**	**0.006**	**0.021**	**0.047**
$St*\phi$	**0.000**	**0.001**	**0.008**	**0.000**	**0.001**
$\theta_0*\phi$	**0.002**	**0.008**	**0.023**	**0.001**	**0.002**

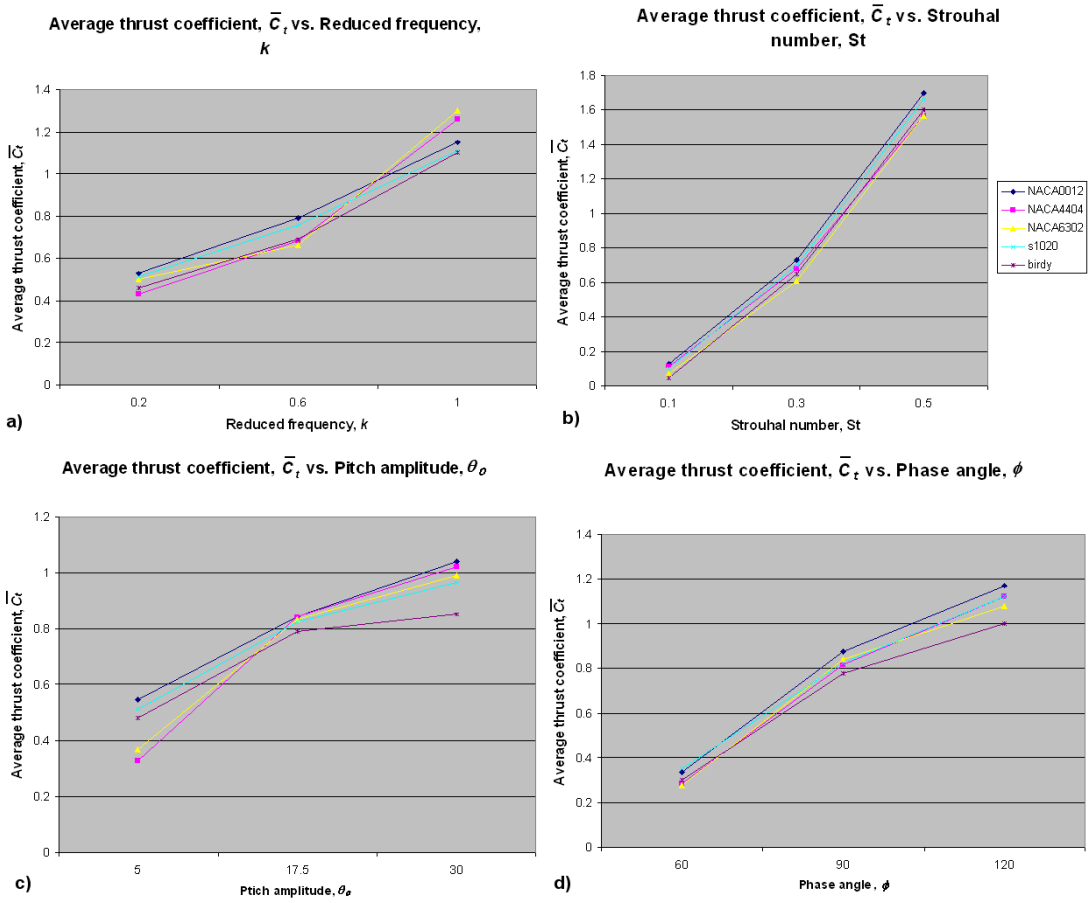

Figure 5.9: Main effects plot of $\bar{C}_t$ vs. each of the factors

5.3.1 Significance of *k* and θ_0 and their Interaction

The main effects plots on Figure 5.9 show that $\bar{C}_t$ increases when *k* or θ_0 increases. On the other hand, the interaction plots of Figure 5.10 show that it is significant only when *k* is high. At *k* = 0.2, the effect is not obvious. The vorticity diagrams of the NACA0012 airfoils are shown in Figure 5.6. The reason is that at low *k*, energy input is low; hence it does not matter if the pitch angle is high or low. However, at high *k*, it seems that the high θ_0 causes the vortices to be shed only at the trailing edge. The flow remains mostly attached and the energy is directed to generate strong trailing edge vortices which give high $\bar{C}_t$. On the other hand, at low θ_0, vortices are shed at the lower leading edge and trailing edge as well, unlike the earlier case. Therefore, to get high $\bar{C}_t$, both *k* and θ_0 must be high. Unfortunately, as discussed earlier,

this combination also results in low efficiency.

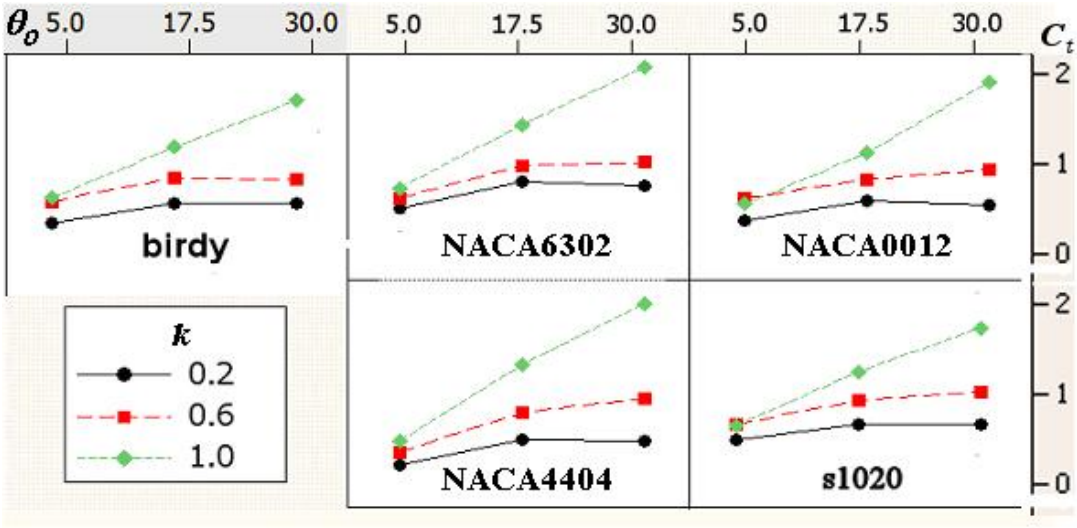

Figure 5.10: Two-factor interaction plot of k and θ_0 vs. $\overline{C}_t$

5.3.2 Significance of k and ϕ and their Interaction

Similarly in this case, increasing k or ϕ in general increases the $\overline{C}_t$. Read et al. (2003) also reported that $\overline{C}_t$ increases as ϕ increases for certain sets of experiments conducted. The interaction plot on Figure 5.11 further shows that this is only true when k is high. At low k, the influence of ϕ is weak. When ϕ = 60° (BB test 18), at the highest position of the heaving motion, the airfoil will pitch upwards. On the other hand, at ϕ = 120° (BB test 20), it will pitch downwards at the same position. In other words, if ϕ = 60°, the airfoil is paddling in the opposite direction to the flow. Therefore, the $\overline{C}_t$ produced is lower, as compared to the airfoil with ϕ = 120°. In that case, it is paddling in the same direction and so $\overline{C}_t$ is higher. Similar to the above case, at low k, the energy input is low and so it does not matter whether ϕ = 60° or 120°.

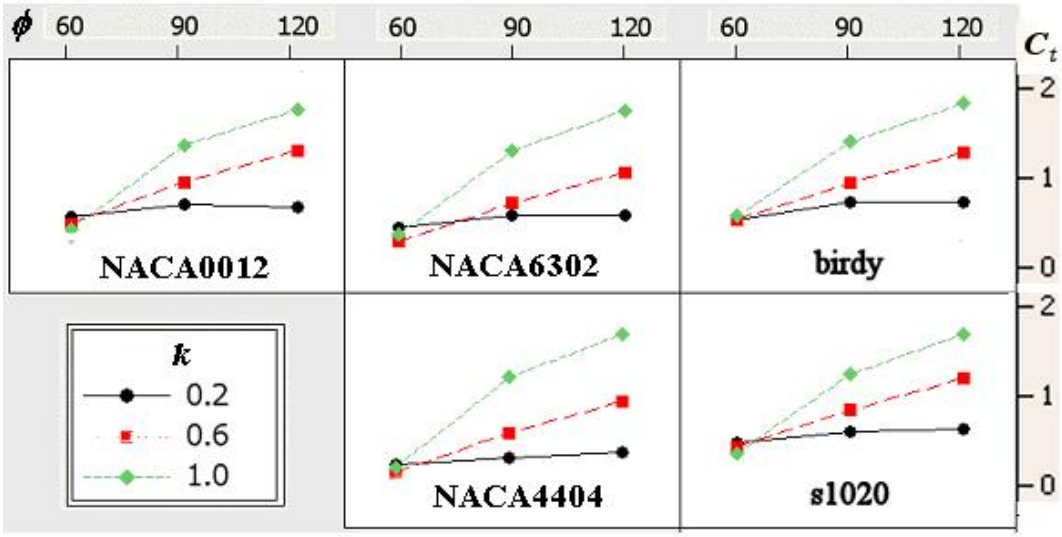

Figure 5.11: Two-factor interaction plot of k and ϕ vs. $\overline{C}_t$

The vorticity diagrams of the NACA4404 airfoil on Figure 5.12 and 5.13 show its orientation at the highest and lowest position of the heaving motion respectively. The figure on the left has ϕ = 120° while the one on the right has ϕ = 60°. It can be observed that the trailing edge vortices generated on the right is much smaller.

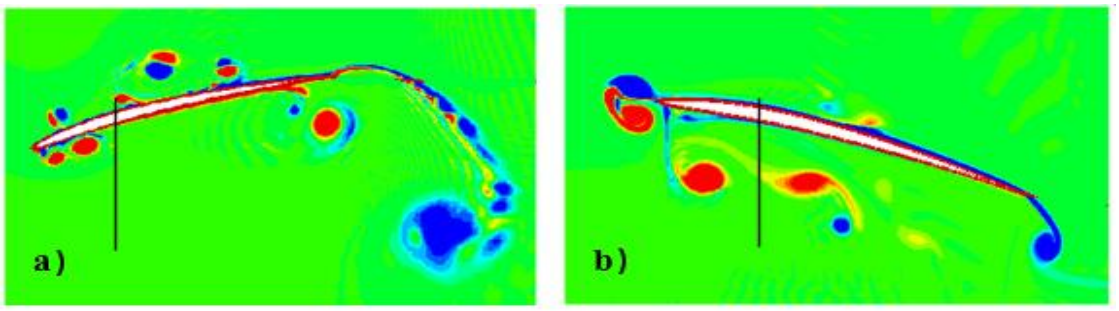

Figure 5.12: Vorticity diagram of the NACA4404 airfoil at its highest heaving position when (a) ϕ = 120° (BB case 20) and (b) ϕ = 60° (BB case 18)

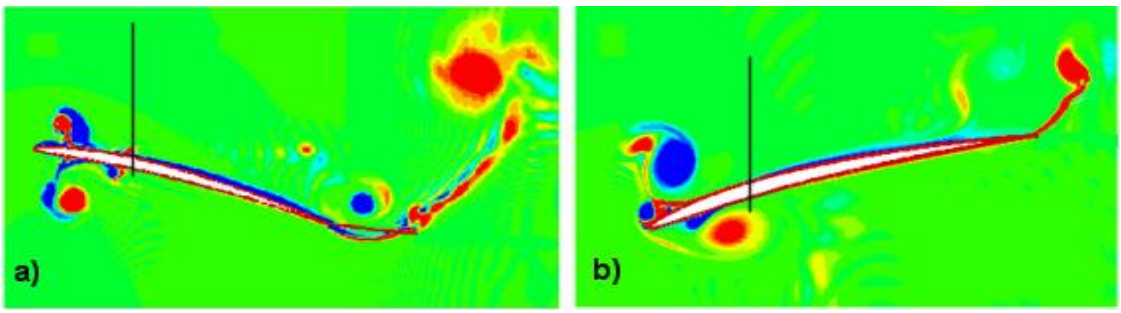

Figure 5.13: Vorticity diagram of the NACA4404 airfoil at its lowest heaving position when (a) ϕ = 120° (BB case 20) and (b) ϕ = 60° (BB case 18)

5.3.3 Significance of *St* and its Interactions with ϕ and θ_0

On average, as *St* increases, $\overline{C}_t$ of all airfoils increases. Moreover, as shown in Figure 5.9, the gradient is very steep, especially from *St* = 0.3 to 0.5, thus indicating the degree of its significance. With other factors constant, high *St* results in high heaving amplitude. Figure 5.14 (and also Figure 5.7) shows the NACA0012 airfoil at (a) *St* = 0.1 and (b) *St* = 0.5. This gives a heaving amplitude of h_0 = 0.833 for *St*=0.1 and h_0 = 0.417 for *St* = 0.5. More energy is imparted into the flow on the right, resulting in bigger vortices being generated and hence higher $\overline{C}_t$. However, from the interaction graphs of Figure 5.15 and 5.16, the above statement is true only when *St* is high. When *St* is low, the energy input is low and the resulting $\overline{C}_t$ is low. In this case, changing the values of ϕ and θ_0 do not have a significant effect.

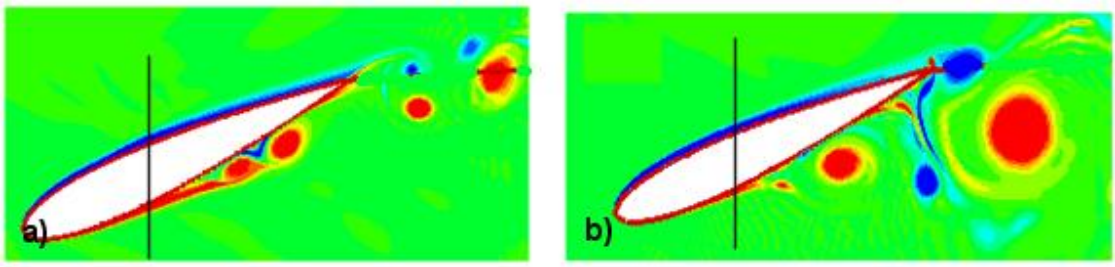

Figure 5.14: Vorticity diagram of the NACA0012 airfoil undergoing simulation at *St* = (a) 0.1 and (b) 0.5

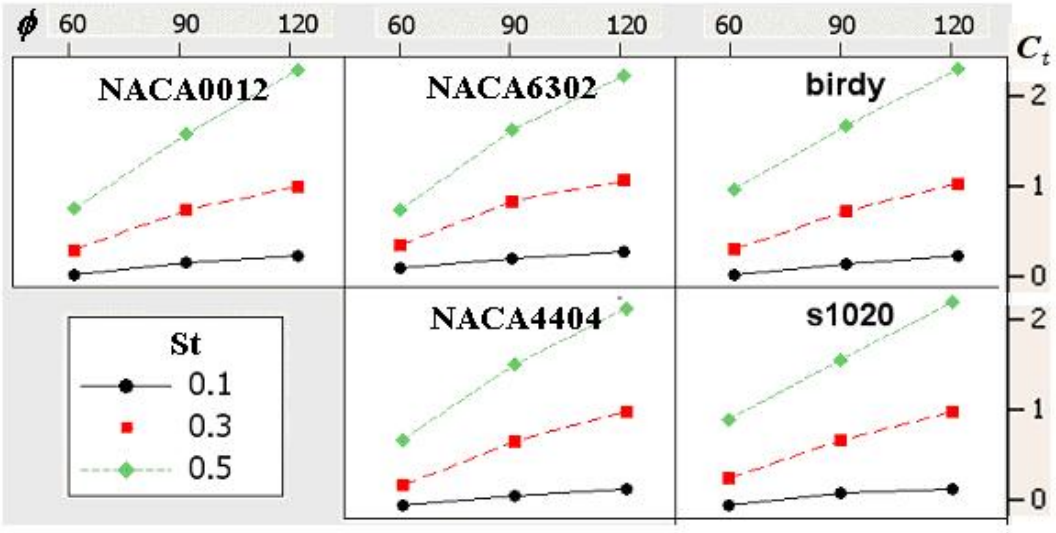

Figure 5.15: Two-factor interaction plot of *St* and ϕ vs. $\overline{C}_t$

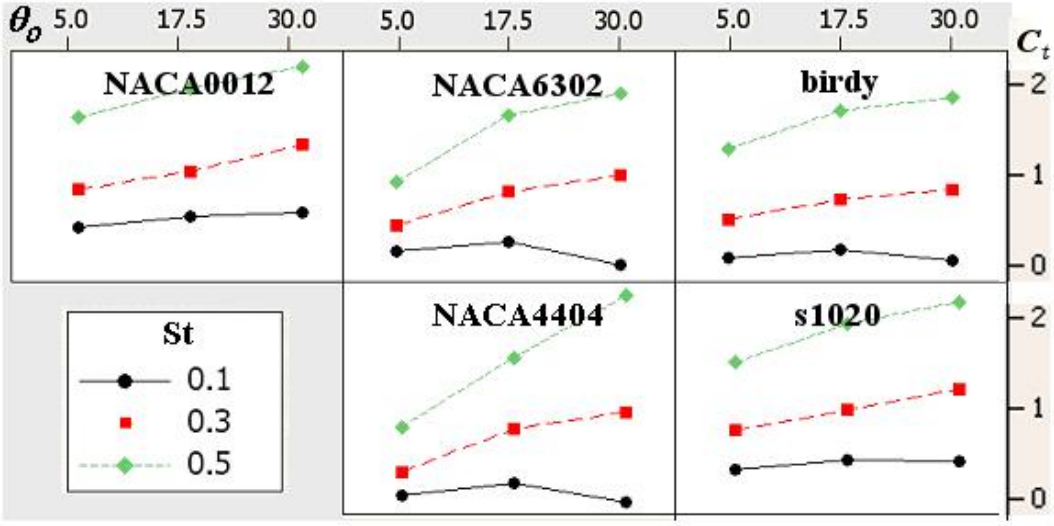

Figure 5.16: Two-factor interaction plot of *St* and θ_0 vs. $\overline{C}_t$

Critics may question the lack of an increase in $\overline{C}_t$ when θ_0 increases. In fact, as shown in Figure 5.16, there is even a slight decrease in $\overline{C}_t$ for some airfoils. An increase in pitch should also mean a higher energy input since the rotational velocity is higher. Firstly, the graphs of C_t vs. t plots at low and high θ_0 on Figure 5.17 show that the amplitude of C_t does increase with increasing θ_0. However, the high C_t generated at high θ_0 is accompanied by high C_d as well. A look at the vorticity diagrams of the NACA6302 airfoil on Figure 5.18 show that the vortices shed form both reverse Von Karman street (evident from the anti-clockwise positive red vortex on top and the clockwise blue vortex below) and the Von Karman street. This indicates that thrust and drag are both produced. Hence, the timing of motion of the vortices and their interactions are very important.

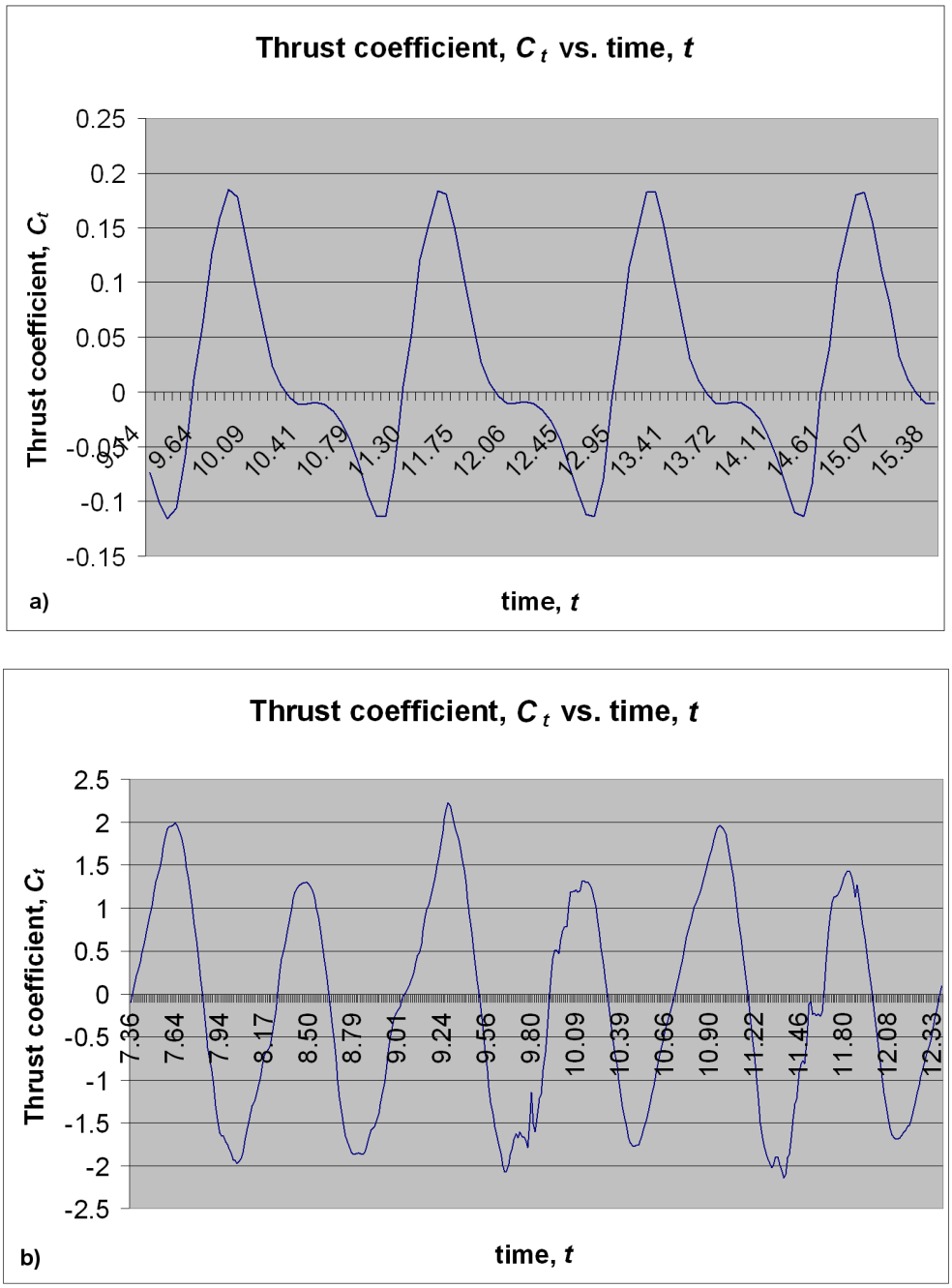

Figure 5.17: C_t vs. t plot of the NACA6302 airfoil undergoing simulation at St = 0.1 and θ_0 = (a) 5° (BB test 21) (b) 30° (BB test 23)

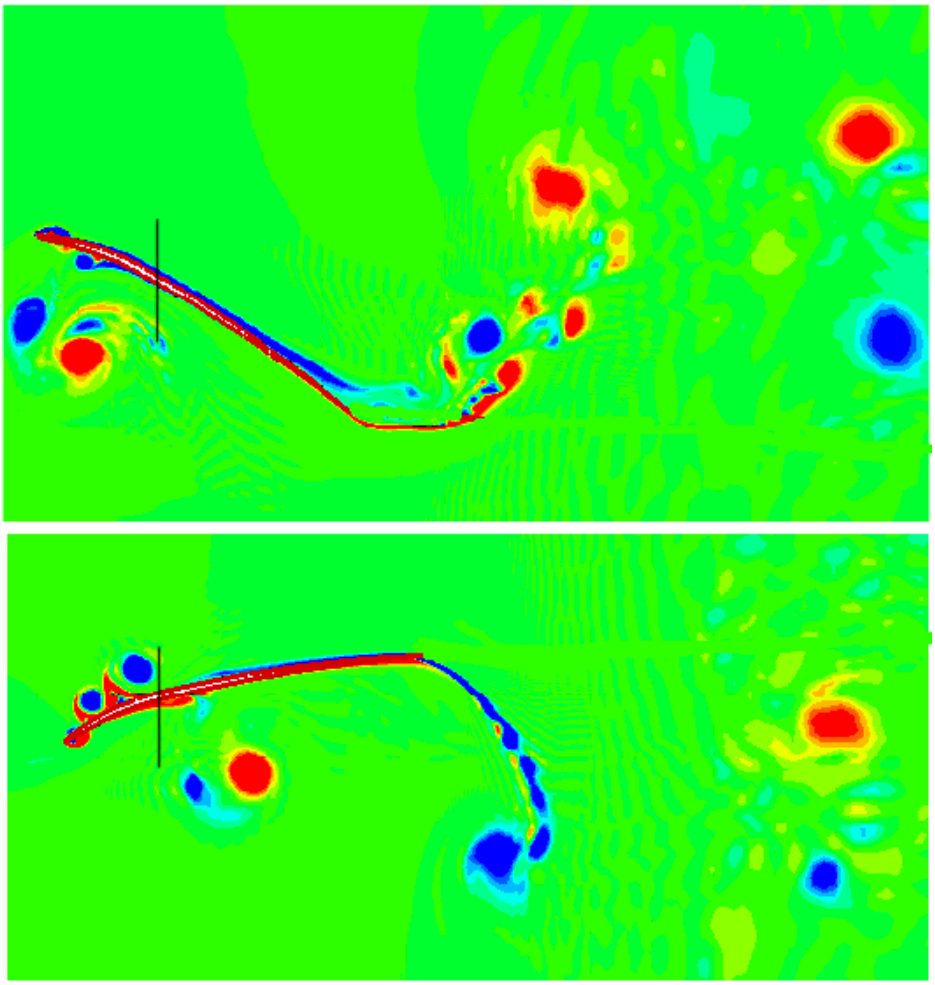

Figure 5.18: Vorticity diagrams of the NACA6302 airfoil undergoing simulation at St = 0.1 and $\theta_0 = 30^o$ (BB test 23)

5.3.4 Interaction between θ_0 and ϕ

The interaction plots on Figure 5.19 show that when θ_0 is small, the phase angle does not have a strong influence on the $\overline{C}_t$. But when θ_0 is high, $\overline{C}_t$ increases as ϕ increases. At low θ_0, the influence of the phase angle is not significant because energy input is low and hence the above mentioned paddling effect is very small.

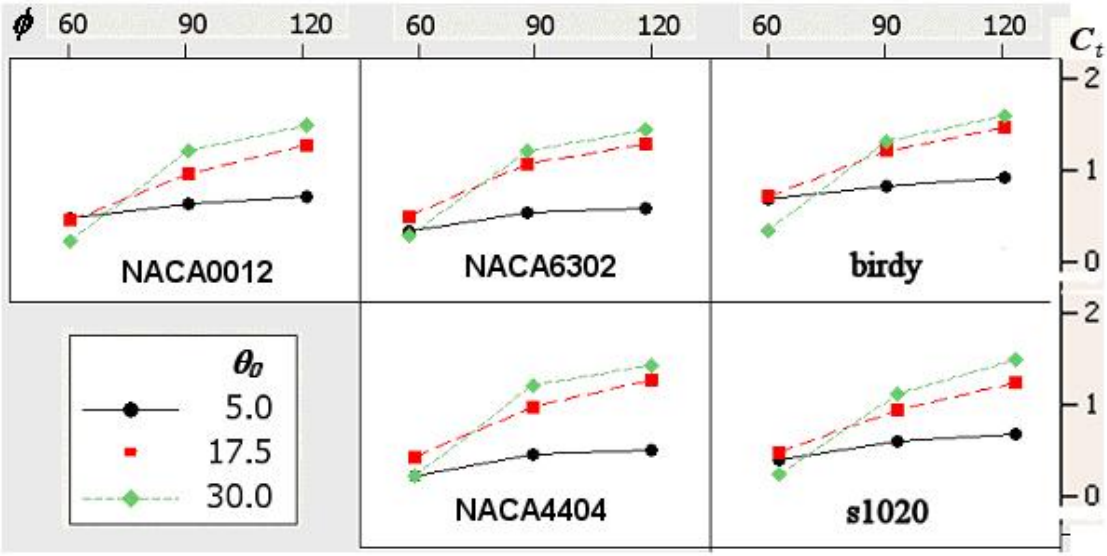

Figure 5.19: Two-factor interaction plot of ϕ and θ_0 vs. $\overline{C}_t$

5.3.5 Comparison of Thrust of Different Airfoils

From Figure 5.9, one can see that in almost all cases, both the shapes and positions of the graphs for different airfoils are very similar. This shows that the effect of airfoil shape on the $\overline{C}_t$ is very small.

5.4 Significance and Effect of Variables on Lift

Figure 5.20 shows that of all the airfoils, the NACA0012 airfoil generates the least amount of $\overline{C}_l$. This is not surprising since the symmetrical airfoil shape prevent any effective lift to be generated. For most airfoils, as shown in Table 5.3, both factors *k* and ϕ have a significant or marginally significant effect on the $\overline{C}_l$. Two-factor interactions for $\overline{C}_l$ are much weaker for most airfoils compared to $\overline{C}_t$. Only the NACA4404 and the S1020 airfoils have significant interactions between k,ϕ and θ_0,ϕ. For the birdy and NACA6302 airfoils, there is no interaction at all. The different levels of interactions for different airfoils show that the shape of the airfoil indirectly influences the variables.

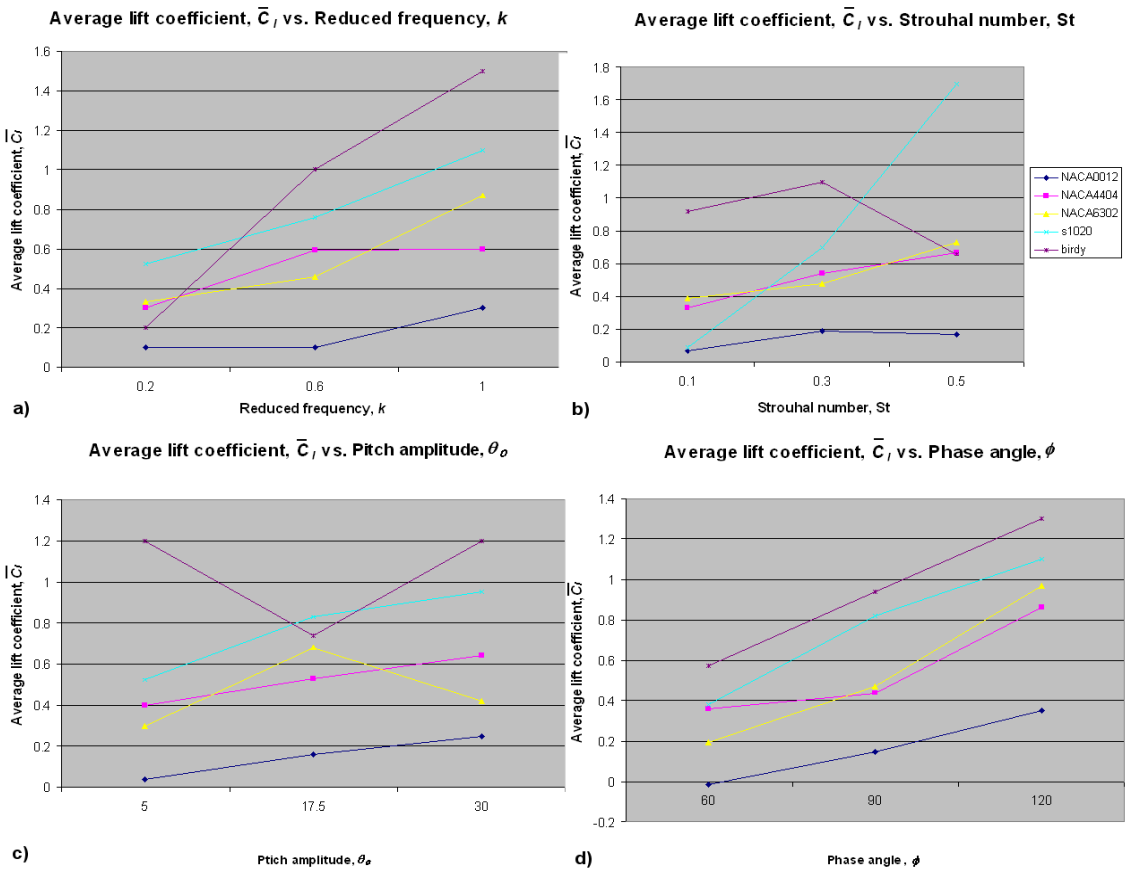

Figure 5.20: Main effects plot of $\bar{C}_l$ vs. each of the factors

Table 5.3: Test of significance results for average lift coefficient (BB test)

p_s	NACA0012	NACA4404	NACA6302	S1020	birdy
k	0.184	0.053	**0.048**	**0.000**	**0.000**
St	0.465	**0.033**	0.819	**0.027**	0.306
ϕ	0.016	**0.005**	0.072	**0.002**	**0.012**
$k*\phi$	0.157	**0.032**	0.172	0.216	0.155
$\theta_0*\phi$	**0.011**	0.707	0.885	**0.013**	0.089

The birdy airfoil gives the highest $\bar{C}_l$ at BB test 12 ($\bar{C}_l$ = 2.23), with the S1020 slightly less at BB test 20 ($\bar{C}_l$ = 1.93). A vorticity diagram of the S1020 flapping with BB test 12 shows that at k = 1.0 and θ_0 = 30°, most of the flow remains attached at the top and bottom of the airfoil,

as shown in Figure 5.21. Interestingly, no leading edge vortex is observed for any of the flapping configuration. The most likely reason is that the current *Re* number of 10,000, together with the current set of flapping configurations, does not enable a leading edge vortex to remain stable for a sufficient amount of time.

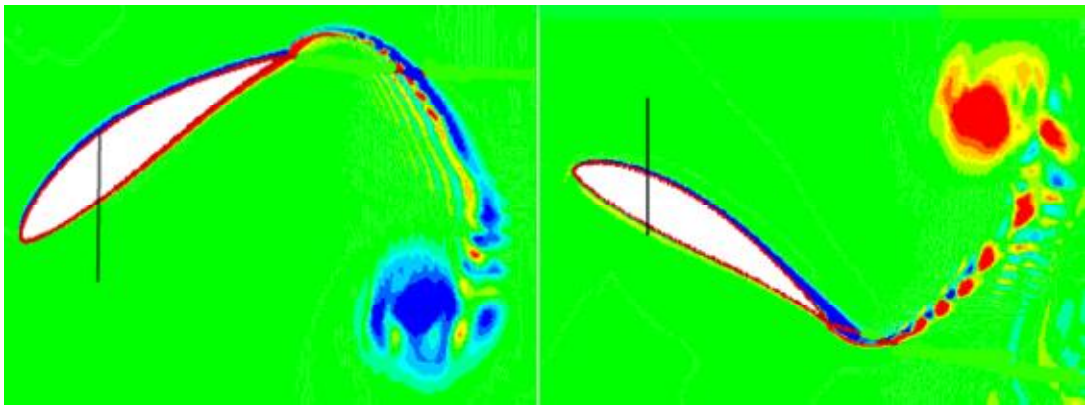

Figure 5.21: Vorticity diagram of the S1020 airfoil undergoing BB test 12 simulation at different instances

5.4.1 Reduced Frequency *k*

This factor is very significant for the S1020 and Birdy airfoils. It is also moderately significant for the other two non-symmetrical airfoils. High *k* generally results in high $\overline{C}_l$ for all the airfoils. The vorticity diagram of the S1020 airfoil flapping at a low *k* (0.2) is shown in Figure 5.22. In Figure 5.21, the high flapping rate ensures that the flow is attached at the top and bottom of the airfoil. On the other hand, in Figure 5.22a, there is leading edge separation as well as a small amount of trailing edge separation at the bottom of the airfoil. In Figure 5.22b, the flow is seriously detached at the top of the airfoil. This is because the slower rate of flapping gives ample time for the flow to become detached. This is despite the fact that the heaving amplitude is only 0.15 unit. Hence, the $\overline{C}_l$ generated is much lower.

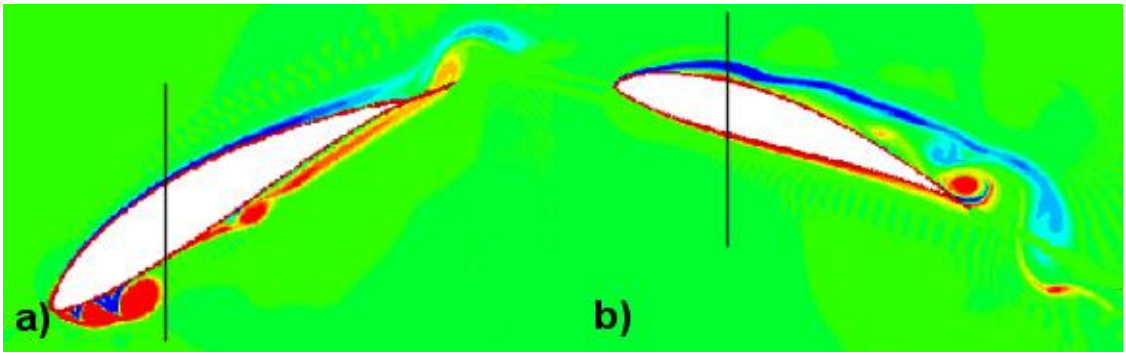

Figure 5.22: Vorticity diagram of the S1020 airfoil undergoing the same parameter as BB test 12 except k = 0. 2 at different instances

5.4.2 Significance of ϕ

Phase angle ϕ has a significant effect on $\bar{C}_l$ for almost all airfoils. The plot of $\bar{C}_l$ vs. ϕ on Figure 5.20d shows that higher ϕ generates better $\bar{C}_l$. Comparing between BB test 6 and 8, the latter which has $\phi = 120^o$ generated much higher $\bar{C}_l$ than the former ($\bar{C}_l$ = 1.91, maximum C_l = 13.56 vs. $\bar{C}_l$ = 0.21, maximum C_l = 1.39). The vorticity diagrams (not shown) of the two BB tests do not show much difference. The pressure coefficient contour plots on Figure 5.23 show the instant when the C_l of each test is at its maximum. The maximum and minimum pressure coefficients of the BB test 8 are much larger than BB test 6. At $\phi > 90^o$, the airfoil is paddling in the same direction as the flow and hence the $\bar{C}_l$ is greater.

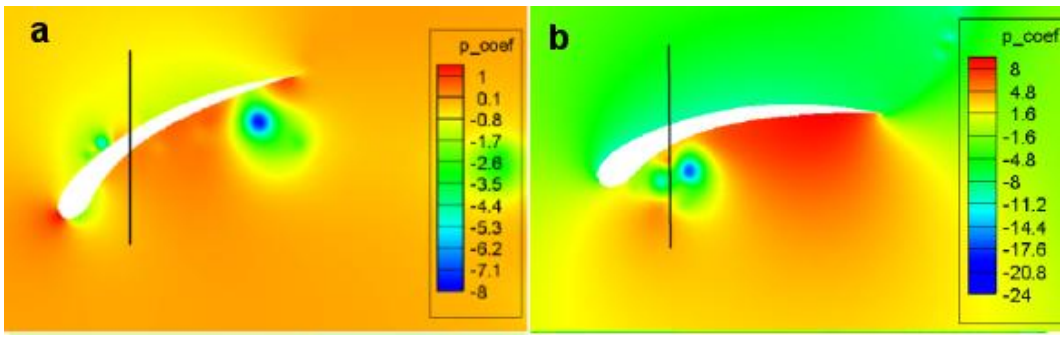

Figure 5.23: Pressure coefficient contour plots of the birdy airfoil undergoing (a) BB test 6 and (b) BB test 8

5.4.3 Two-factor Interactions

Two-factor interactions for $\bar{C}_l$ are much weaker for most airfoils compared to that of $\bar{C}_t$. Only the NACA4404 and the S1020 airfoils have significant interactions between k,ϕ and θ_0,ϕ. For the birdy and NACA6302 airfoils, there is no two-factor interaction for $\bar{C}_l$ at all.

5.4.4 Comparison of Lift of Different Airfoils

From Figure 5.20, one can see that the $\bar{C}_l$ generated by each airfoil can be very different under the same flapping configuration. In this case, both the shape and the numerical values are different for each airfoil. This show that the airfoil shape has a very significant effort on the $\bar{C}_l$. In general, excluding the NACA0012 airfoil, thick airfoils such as the S1020 and the birdy generate much higher $\bar{C}_l$ than the thin ones for most cases. On the other hand, the thinner airfoils do not generate as much $\bar{C}_l$ compared to their thicker counterparts. Figure 5.24 shows the vorticity diagrams of the NACA6302 airfoil undergoing the BB test 12. Comparing between this diagram and Figure 5.21 of the S1020 airfoil, one can see that there is some separation occurring in the NACA6302 airfoil. These could have resulted in lower $\bar{C}_l$ generated ($\bar{C}_l$ =1.74 for the S1020 vs. $\bar{C}_l$ =1.30 for the NACA6302). Hence, the high $\bar{C}_l$ generated in this case is due to the shape of the airfoil and flapping configuration.

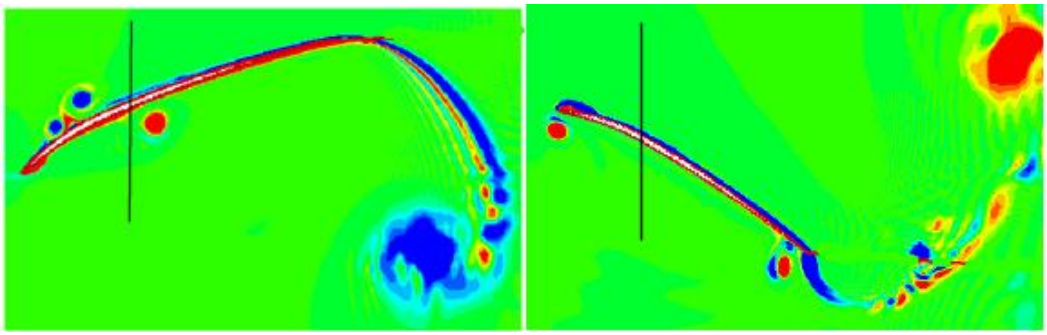

Figure 5.24: Vorticity diagram of the NACA6302 airfoil undergoing BB test 12 at different instances

5.5 Chapter Summary

The simulation results show that besides the flapping configuration, airfoil shape also has a profound effect on the η, $\overline{C}_t$ and $\overline{C}_l$. The four factors (*k*, *St*, θ_0, and ϕ) have different levels of significance on the responses, indicating the shape of the airfoil plays a part as well. $\overline{C}_t$ depends more heavily on these parameters, rather than the shape of the airfoil. On the other hand, $\overline{C}_l$ is primarily dominated by its airfoil shape. Efficiency falls somewhere in between. Two-factor interactions exist in all two responses. Hence in some cases, different factors must be analyzed at the same time.

Based on the simulations tested, the best airfoil for high η and $\overline{C}_t$ is the NACA0012 airfoil. The efficiency and average thrust coefficient are 0.61 (BB test 11) and 2.53 (BB test 16) respectively. As for $\overline{C}_l$, the birdy airfoil is the best. It manages to achieve a maximum $\overline{C}_l$ of 2.23 (BB test 12). This shows that the use of non-symmetrical airfoils can greatly improve the lift performance of an ornithopter without the need to change the stroke angle as mentioned earlier. Unfortunately, these optimal configurations do not coincide at the same flapping configuration. Hence there must be a compromise during the design of the ornithopter's wing. Overall, the S1020 airfoil is the best airfoil for most applications. It is able to provide relatively good efficiency and at the same time generate high $\overline{C}_t$ and $\overline{C}_l$. The birdy airfoil, although provide good $\overline{C}_t$ and $\overline{C}_l$, does not give good efficiency. All these information can be used to help in the design of a better ornithopter's wing.

6 Results and Discussion for Airfoil Chordwise Flexing

The SCNSS is also used to simulate the chordwise flexing of flapping wings. The grid now needs to both deform and move in order to handle the flexible flapping airfoil. The details on how the grid deforms can be found in section 3.2.1.2. The effects of flexing on the five different types of flapping configuration are tested. More details about these flapping configurations can be found in section 4.2. The results and discussions are arranged according to the type of flapping configurations used. There are also comparisons on the effects of flexure between different airfoils and different flapping configurations. The detailed results of the flexing simulations can be found in Table B.1 to Table B.16 in the appendices.

6.1 Flexing – Pure Heaving

6.1.1 Double sided flexing (Figure 6.1)

Figure 6.1a shows the plot of the efficiency against the flexing amplitude. For example, the "NACA0012 (x_{fc} = 0.5)" line shows how the efficiency of the NACA0012 airfoil varies as the flexing amplitude a_f changes, when the airfoil's center of flexure = 0.5. For the x_{fc} = 0.0 case, as the $\overline{a}_f$ increases, the efficiencies of all the three airfoils increases until they reach a maximum value, after which they decrease. On the other hand, for the x_{fc} = 1.0 case, efficiencies of airfoils increase as $\overline{a}_f$ decreases. In other words, the airfoils in the x_{fc} = 0.0 case and x_{fc} = 1.0 case flex in opposite directions to achieve an increase in efficiency. When x_{fc} = 0.0, maximum efficiency is 0.33 at $\overline{a}_f$ = 0.3 for the NACA0012 airfoil. This result is very similar to the result given by Miao and Ho (2006) for the NACA0014 airfoil, which is expected

because the shape of the NACA0012 airfoil is very similar to that of the NACA0014 airfoil. The vorticity diagram for the original non-flexing and the pure heaving cases are shown in Figure 6.2a and b respectively. The un-flexed case generates bigger and less orderly vortices compared to the flexed case. Hence, the efficiency of the flexed case is better.

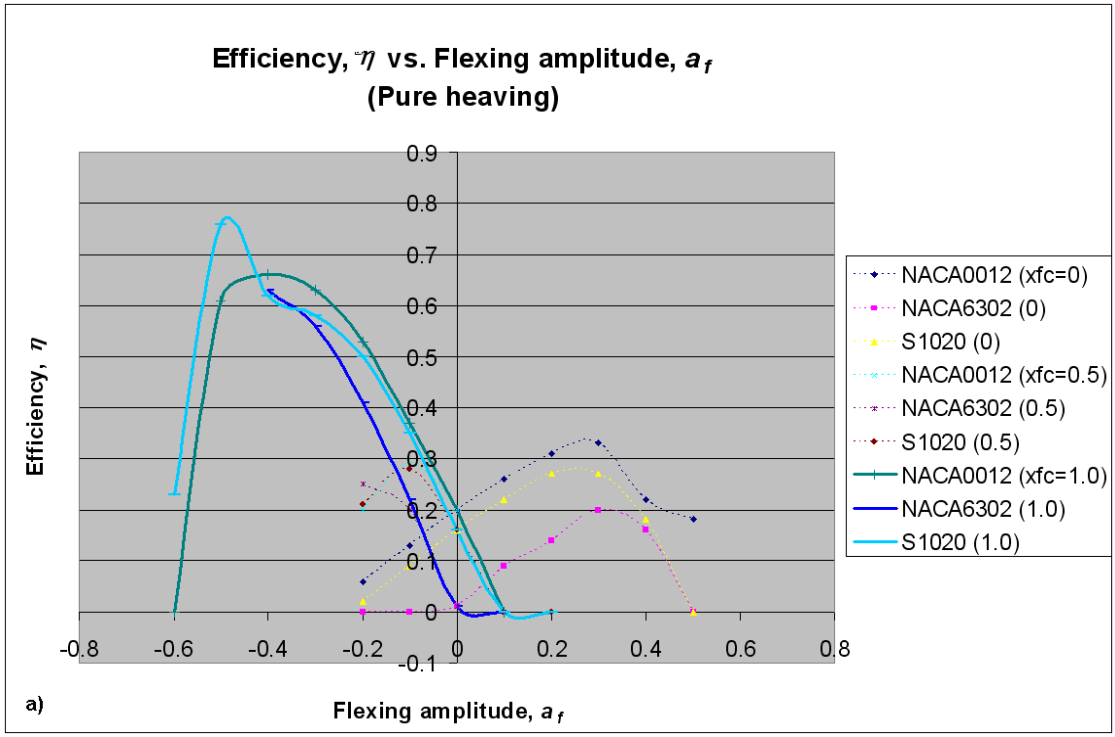

Figure 6.1: Graph of (a) efficiency, (b) average thrust and (c) lift coefficients against flexing amplitude for pure heaving (continue on next page)[‡‡‡]

[‡‡‡] The dotted lines represent the less significant results.

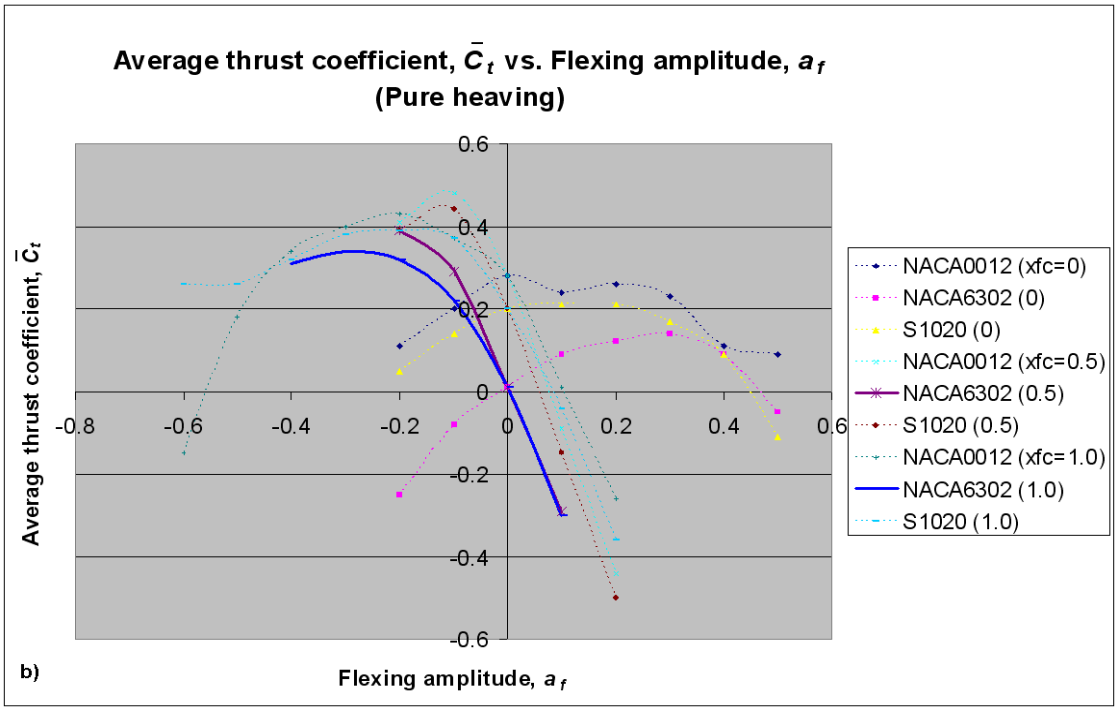
Average thrust coefficient, $\bar{C}_t$ vs. Flexing amplitude, a_f
(Pure heaving)
Average thrust coefficient, $\bar{C}_t$
Flexing amplitude, a_f
0.6
0.4
0.2
0
-0.2
-0.4
-0.6
-0.8
-0.6
-0.4
-0.2
0
0.2
0.4
0.6
NACA0012 (xfc=0)
NACA6302 (0)
S1020 (0)
NACA0012 (xfc=0.5)
NACA6302 (0.5)
S1020 (0.5)
NACA0012 (xfc=1.0)
NACA6302 (1.0)
S1020 (1.0)

b)

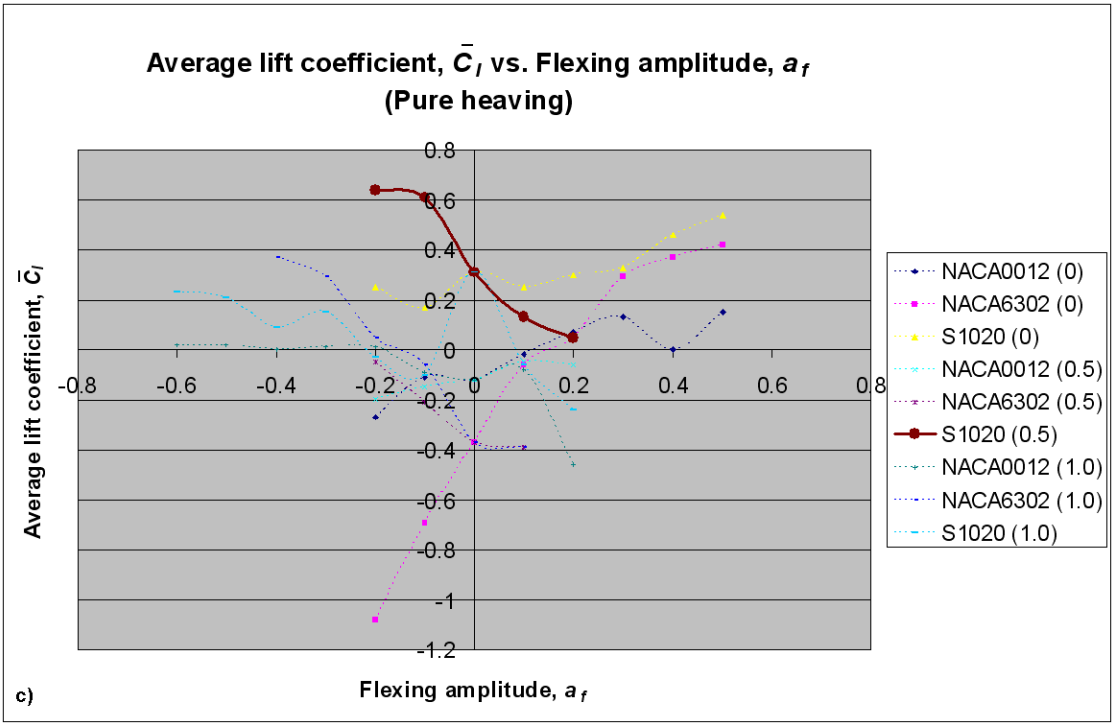
Average lift coefficient, $\bar{C}_l$ vs. Flexing amplitude, a_f
(Pure heaving)
Average lift coefficient, $\bar{C}_l$
Flexing amplitude, a_f
0.8
0.6
0.4
0.2
0
-0.2
-0.4
-0.6
-0.8
-1
-1.2
-0.8
-0.6
-0.4
-0.2
0
0.2
0.4
0.6
0.8
NACA0012 (0)
NACA6302 (0)
S1020 (0)
NACA0012 (0.5)
NACA6302 (0.5)
S1020 (0.5)
NACA0012 (1.0)
NACA6302 (1.0)
S1020 (1.0)

c)

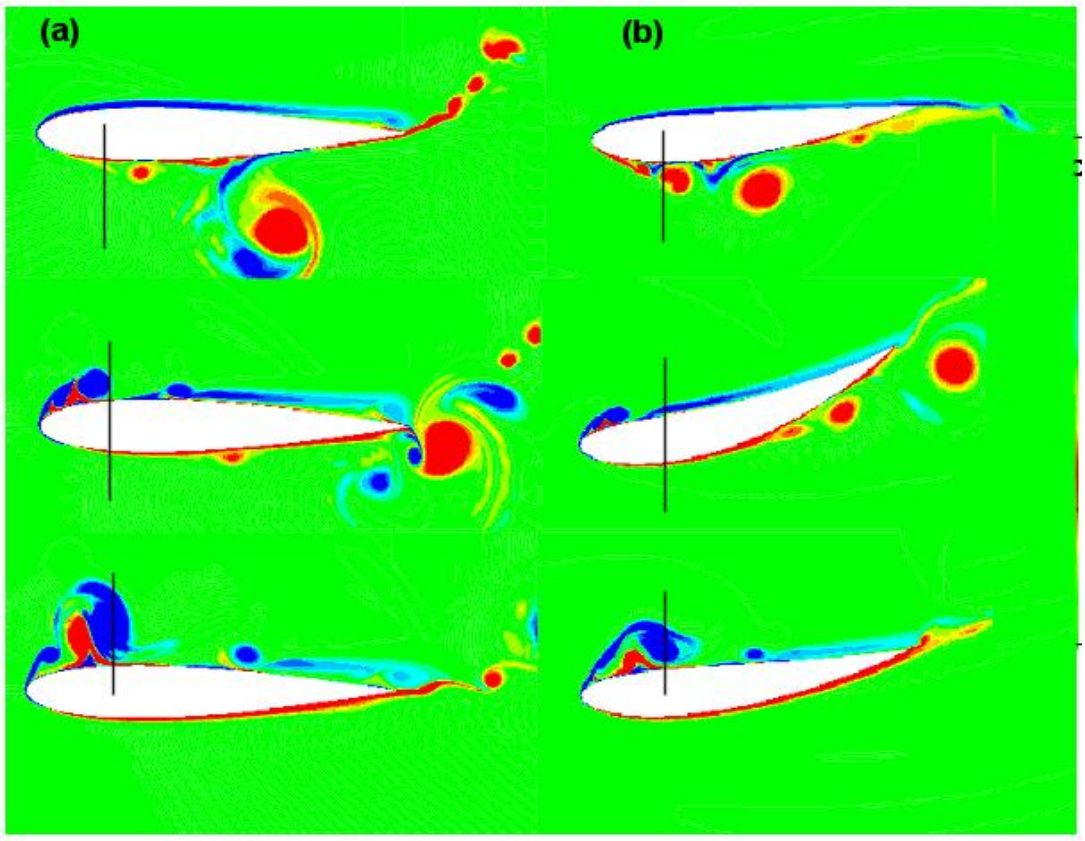

Figure 6.2: Vorticity diagram of NACA0012 airfoil undergoing pure heaving (a) without flexing (b) with flexing at x_{fc} = 0.0 and $\bar{a}_f$ = 0.3 during the heaving down cycle

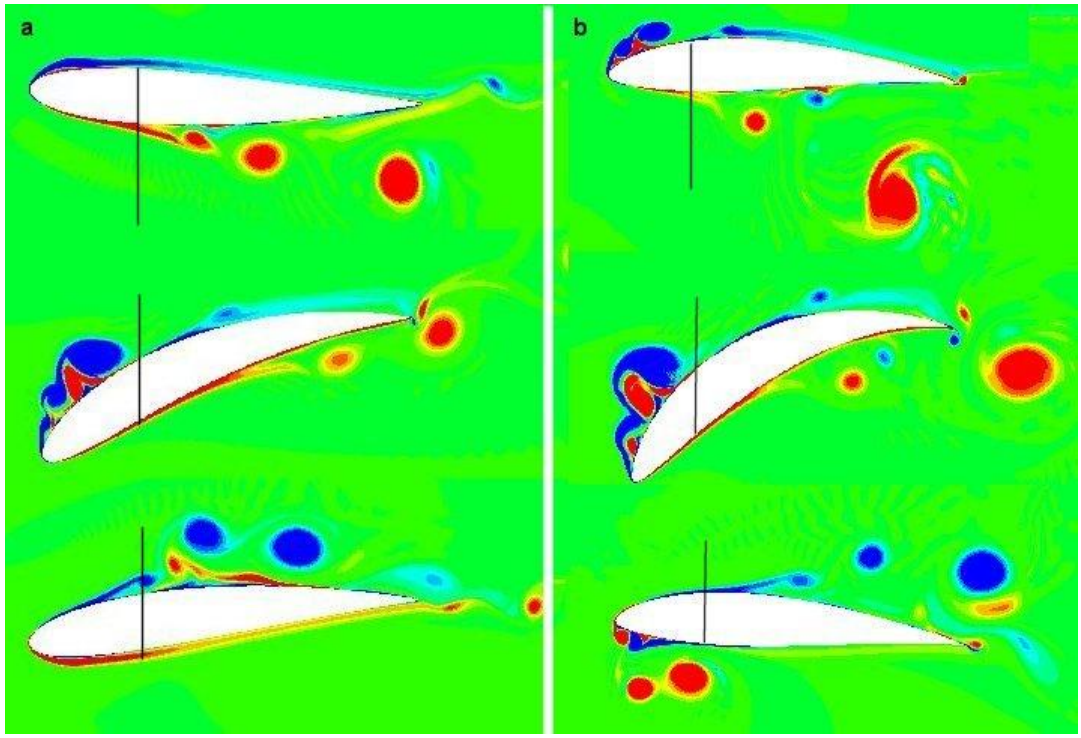

Figure 6.3: Vorticity diagram of the (a) NACA0012 airfoil undergoing pure heaving with flexing at x_{fc} = 1.0, $\bar{a}_f$ = -0.4 and (b) the S1020 airfoil undergoing pure heaving with flexing at x_{fc} = 1.0, $\bar{a}_f$ = -0.5 during the heaving down cycle

At x_{fc} = 1.0, maximum efficiency of 0.66 by the NACA0012 airfoil when x_{fc} = 1.0 and $\bar{a}_f$ = -0.4. This efficiency of 0.66 is twice as high as the previous maximum efficiency result (0.33). The other two airfoils also give very high efficiency, especially the S1020 airfoil. The S1020 airfoil is able to reach an efficiency of 0.76 at x_{fc} = 1.0 and $\bar{a}_f$ = -0.5. The vorticity diagram of the NACA0012 airfoil when x_{fc} = 1.0 and $\bar{a}_f$ = -0.4 is shown in Figure 6.3a. There is little difference in the vorticity diagram in Figure 6.3a compared to Figure 6.2b. However, the C_l amplitude of the former case (Figure 6.3a) is approximately 1.5 compared to the latter case (Figure 6.2b) of nearly 2.0. The definition of the power input is given in Eqn (3.47). Since the flapping configuration is the same for both cases, the main component which determines the ***P(t)*** is the C_l.. Hence, when C_l amplitude is minimized, the power input also decreases (average P = 0.68 at x_{fc} = 0.0, $\bar{a}_f$ = 0.3 vs. 0.51 at x_{fc} = 1.0, $\bar{a}_f$ = -0.4). Another factor is the higher $\bar{C}_t$ for the x_{fc} = 1.0 case ($\bar{C}_t$ = 0.34 compared to 0.23). Higher $\bar{C}_t$ indicates higher power output (Eqn (3.48)). Both factors result in higher efficiency for the x_{fc} = 1.0 case. The vorticity diagram of the S1020 airfoil at x_{fc} = 1.0 and $\bar{a}_f$ = -0.5 is shown in Figure 6.3b. It is similar to Figure 6.3a, except that the airfoil flexes even more now. The average power input/output of the S1020 and NACA0012 airfoils are 0.35/0.26 and 0.51/0.34 respectively. In other words, the unique shape of the S1020 airfoil after flexing requires much lower power input and this helps to increase the efficiency further. At x_{fc} = 0.5, there is also an increase of efficiency as $\bar{a}_f$ decreases but it is much smaller compared to the above 2 cases (x_{fc} = 0.0 and 1.0).

Figure 6.1b shows the plot of the $\bar{C}_t$ against the flexing amplitude. At x_{fc} = 0.0, $\bar{C}_t$ either remains almost constant or drops as the flexing increases in either directions for the NACA0012 and the S1020 airfoils. As mentioned earlier in the efficiency section, the flexed case of the NACA0012 airfoil in Figure 6.2b generates smaller vortices compared to the un-

flexed case of Figure 6.2a. Hence, the $\overline{C}_t$ is lower for the flexed case. For the NACA6302 airfoil, there is an increase of $\overline{C}_t$, reaching a maximum value of 0.14 at $\overline{a}_f$ =0.3. Its original value was approximately 0. At x_{fc} = 0.5 and 1.0, $\overline{C}_t$ increases as $\overline{a}_f$ decreases for all airfoils. The NACA0012 at x_{fc} = 0.5, $\overline{a}_f$ = 0.1 reaching the highest $\overline{C}_t$ of 0.48. The NACA6302 and S1020 also increase to values of 0.39 and 0.44 respectively.

Figure 6.1c shows the plot of the $\overline{C}_l$ against the flexing amplitude. Unlike the efficiency and $\overline{C}_t$ plot, the graph of $\overline{a}_f$ against flexing amplitude does not follow a parabolic trend. Flexing in the "correct" direction generally improves the $\overline{C}_l$ generated for the non-symmetrical NACA6302 and S1020 airfoils. The "correct" direction is different for different airfoils at different x_{fc}. For example, the $\overline{C}_l$ generated by the NACA6302 airfoil at x_{fc} = 0.0 increases as the flexing amplitude increases from 0.0 to 0.5. However, its $\overline{C}_l$ at x_{fc} = 1.0 increases as the flexing amplitude decreases from 0.0 to -0.4. A maximum $\overline{C}_l$ value of 0.64 is attained by the S1020 airfoil at x_{fc} = 0.5, $\overline{a}_f$ = 0.2. On the other hand, the NACA6302 airfoil generates a $\overline{a}_f$ of 0.42 at x_{fc} = 0.0, $\overline{a}_f$ = 0.5. Due to the symmetrical nature of the NACA0012 airfoil, the $\overline{C}_l$ it generates is only slightly affected by the flexing.

6.1.2 Single-sided flexing (Figure 6.4)

Figure 6.4a, b and c show the plot of the η, $\overline{C}_t$ and $\overline{C}_l$ against the flexing amplitude. Efficiency decreases rapidly as flexing increases for all value of x_{fc}, except for the NACA6302 at x_{fc} = 0.0 case. In the x_{fc} = 0.0 case, the original efficiency at $\overline{a}_f$ = 0.0 is already very low. It increases from 0.01 to 0.02 when $\overline{a}_f$ increases from 0.0 to 0.1.

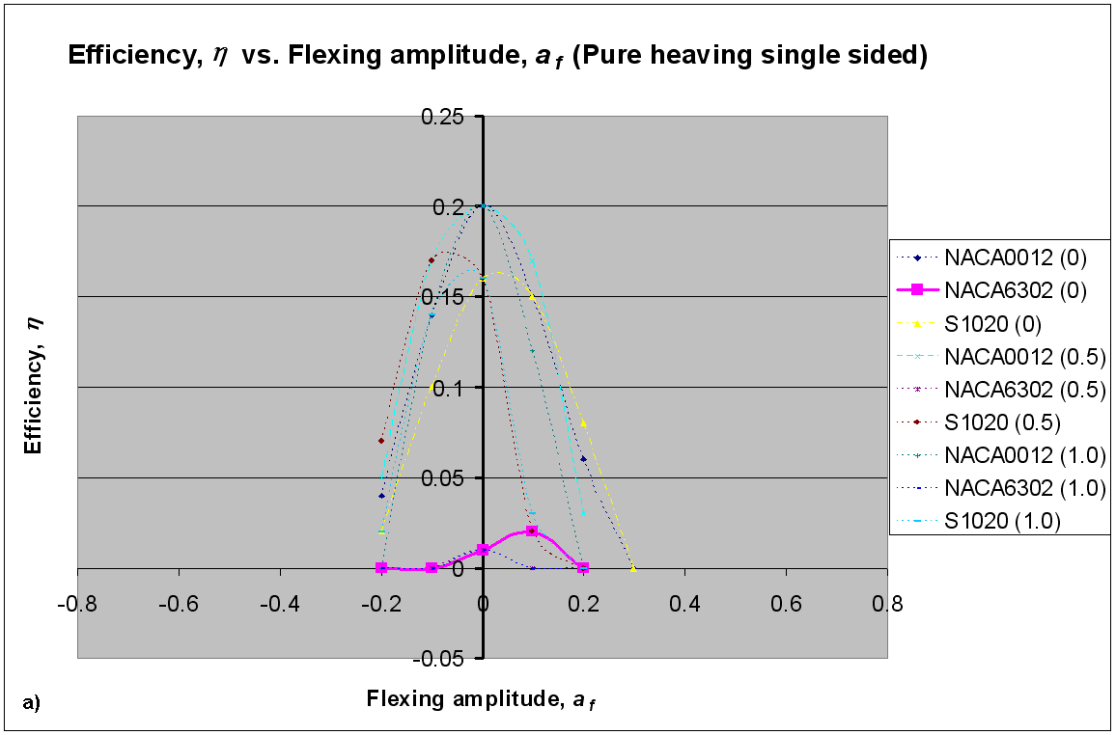

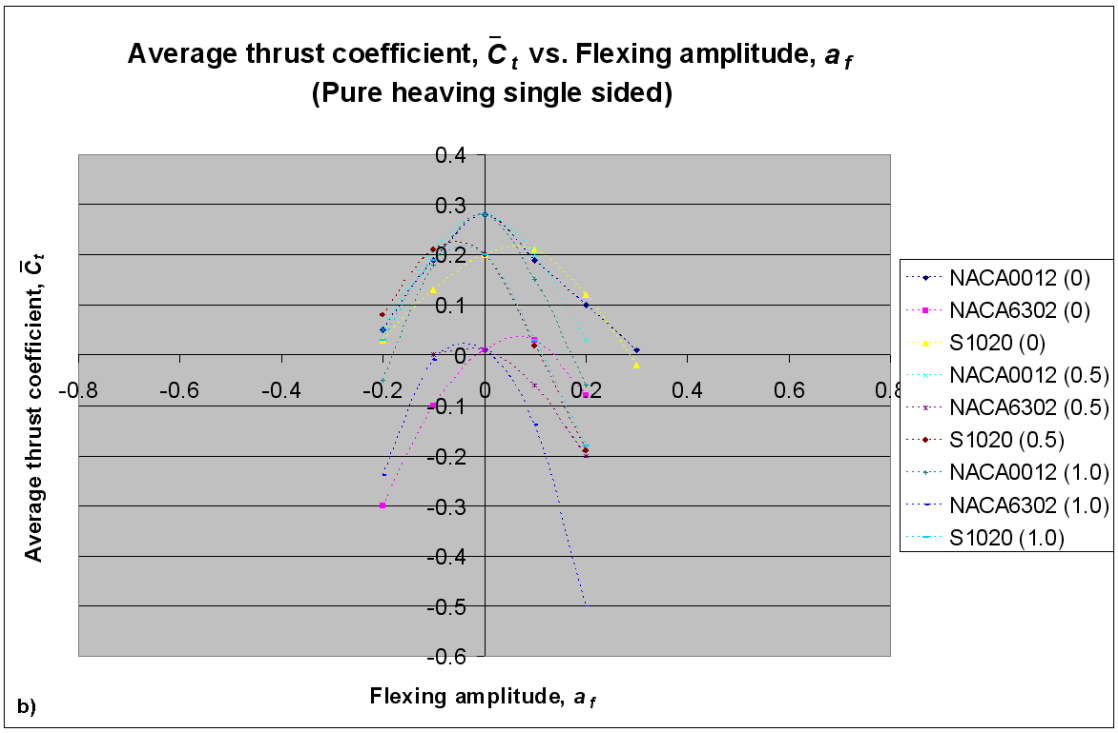

Figure 6.4: Graph of (a) efficiency, (b) average thrust and (c) lift coefficients against flexing amplitude for pure heaving single sided (continue on next page)

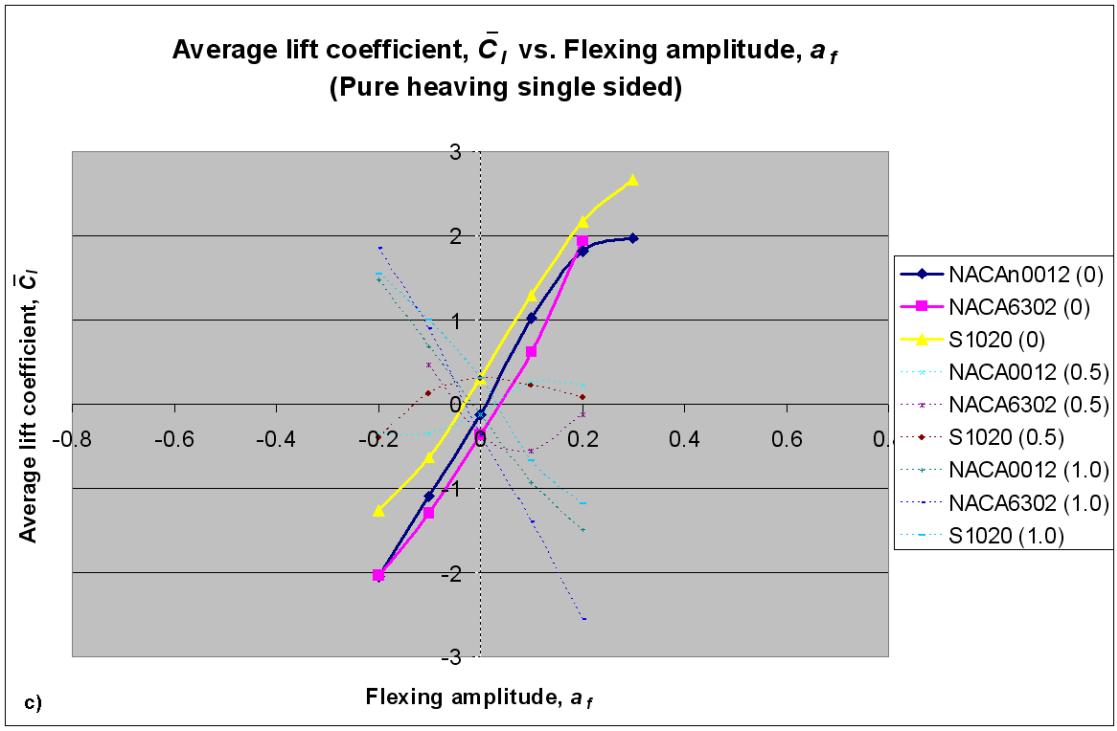

$\bar{C}_t$ decreases rapidly to give drag as flexing increases for all value of x_{fc}. The cause for the low efficiency is two-fold. Firstly, the $\bar{C}_t$ is now much lower and so the power output is lower. Secondly, as mentioned in the previous section, when C_l amplitude is increased, the power input will increase as well. A small numerator together with a large denominator thus results in the rapid decrease of the efficiency.

$\bar{C}_l$ increases rapidly as $\bar{a}_f$ increases for x_{fc} = 0.0 and as $\bar{a}_f$ decreases for x_{fc} = 1.0. However, the x_{fc} = 0.0 case usually gives higher η, $\bar{C}_t$ and $\bar{C}_l$ values. The S1020 airfoil doing single-sided flexing at x_{fc} = 0.0, $\bar{a}_f$ = 0.3 gives the highest $\bar{C}_l$ of 2.67. However, the single-sided flexing S1020 airfoil is already generating a very small amount of drag ($\bar{C}_t$ = -0.02) at this configuration. Similarly, the symmetrical NACA0012 airfoil also manages to give a high $\bar{C}_l$ of 1.97 at the same flexing configuration. The pressure coefficient diagrams of the NACA0012 airfoil for the x_{fc} = 0.0, $\bar{a}_f$ = 0.2 (with $\bar{C}_t$ = 0.10, $\bar{C}_l$ = 1.81) are shown in Figure 6.5 while

the un-flexed version is shown in Figure 6.6. The pressure diagram shows that as the airfoil plunges down, there is a growing leading edge vortex on top of the airfoil. This creates a low pressure suction region which improves the lift coefficient generated by the airfoil greatly. This is also the time when the lift coefficient is at its maximum (C_l = 7.0). Although both figures have the leading edge vortex, the magnitude of the vorticity on Figure 6.5 is much larger. Moreover, the leading edge vortex stays attached to the airfoil for a longer period of time before shedding away. On heaving up, a leading edge vortex is also formed at the bottom of the airfoil for both figures. However, the vortex on Figure 6.5 is very much smaller and detaches after a very short while. Hence, this imbalance results in very high lift coefficient. On the other hand, the un-flexed airfoil has similar leading edge vortices on the top and bottom of the airfoil, resulting in a very small $\overline{C}_l$.

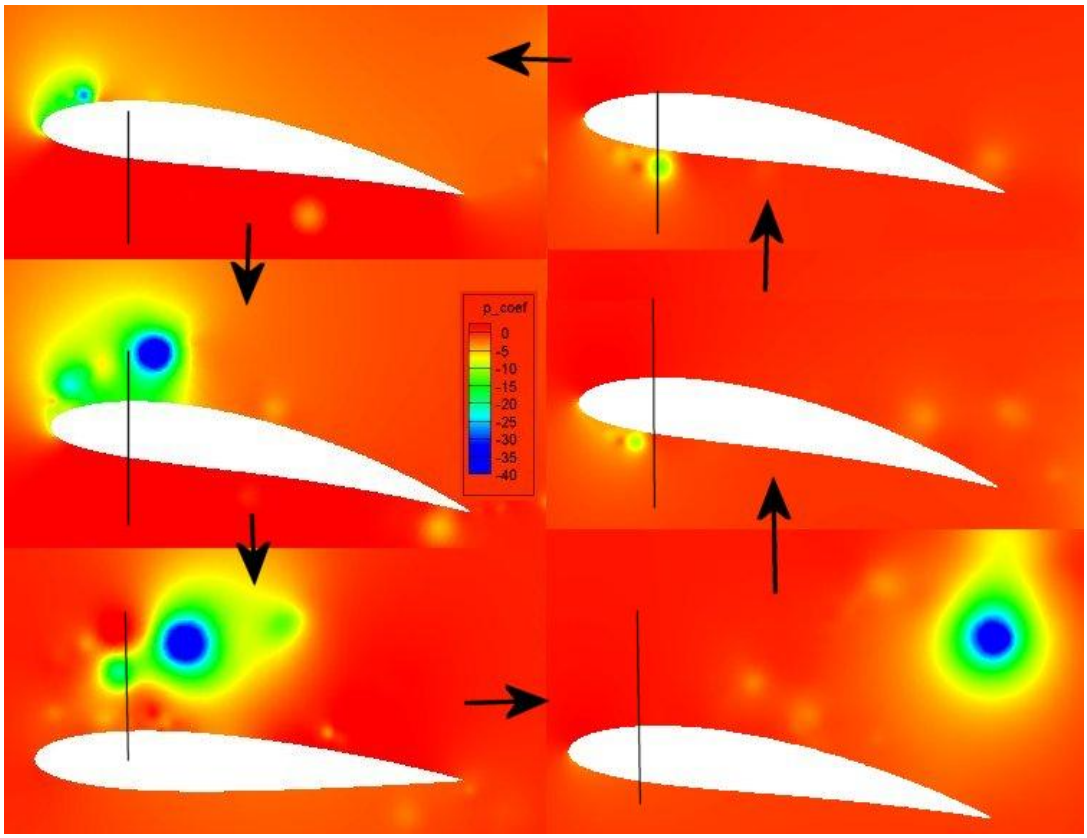

Figure 6.5: Pressure coefficient diagram of the NACA0012 airfoil undergoing pure heaving with singled sided flexing at x_{fc} = 0.0 and $\overline{a}_f$ = 0.2

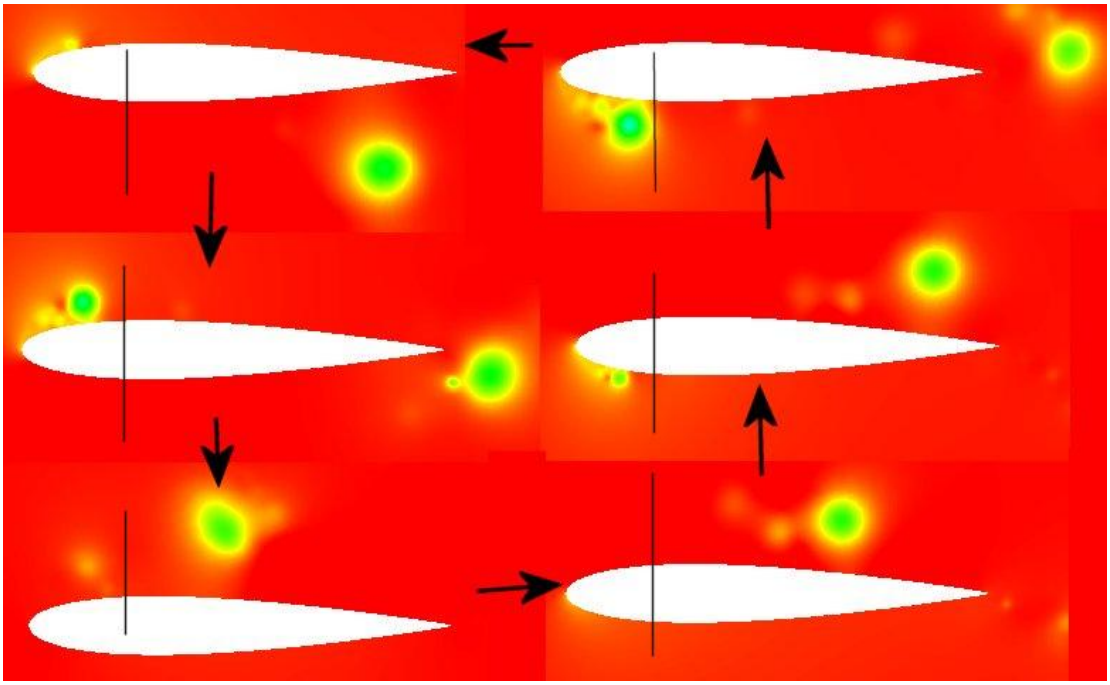

Figure 6.6: Pressure coefficient diagram of the NACA0012 airfoil undergoing pure heaving without flexing (same legend as Figure 6.5)

6.2 Flexing – ME Configuration (h_0 = 0.75, k = 0.2, θ_0 = 30°, ϕ = 90°)

6.2.1 Double sided flexing (Figure 6.7)

Figure 6.7a, b and c show the plot of the η, $\overline{C}_t$ and $\overline{C}_l$ against the flexing amplitude. This flapping configuration gives a high efficiency of 0.54 to 0.61 for the different airfoils when the airfoils are rigid. Unfortunately, flexing does not confer any benefit to the η for all cases.

$\overline{C}_t$ also decreases as flexing increases for all cases except for the x_{fc} = 0.0, 0.5 cases with decreasing $\overline{a}_f$. The increase in $\overline{C}_t$ is most substantial for the NACA0012 airfoil. A maximum $\overline{C}_t$ of 0.9 occurs at x_{fc} = 0.0, $\overline{a}_f$ = -0.4, which is nearly twice the original value of 0.5. However, the η at this configuration is only 0.38. The vorticity diagram for the x_{fc} = 0.0, $\overline{a}_f$ = -

0.3 case (which also gives a high $\bar{C}_t$ of approximately 0.8) is compared against the un-flexed version in Figure 6.8a and b. More vortices can be seen shedding into the wake, which helps to increase the $\bar{C}_t$. However, since the vortices are now less orderly and cohesive, the η has decreased.

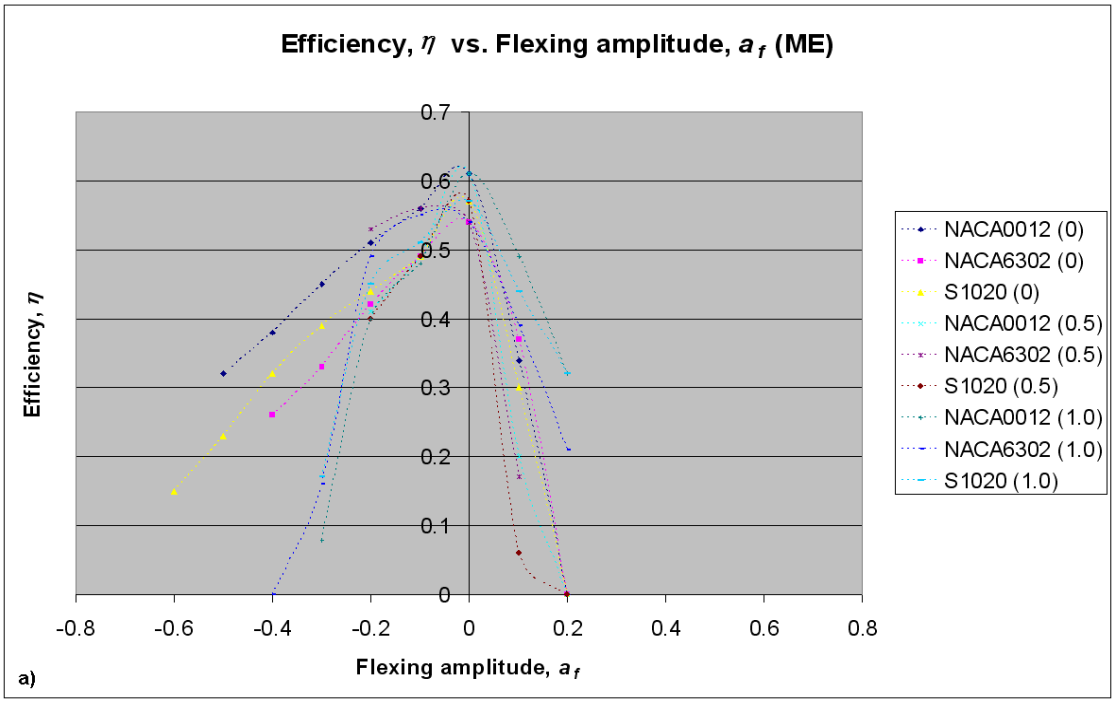

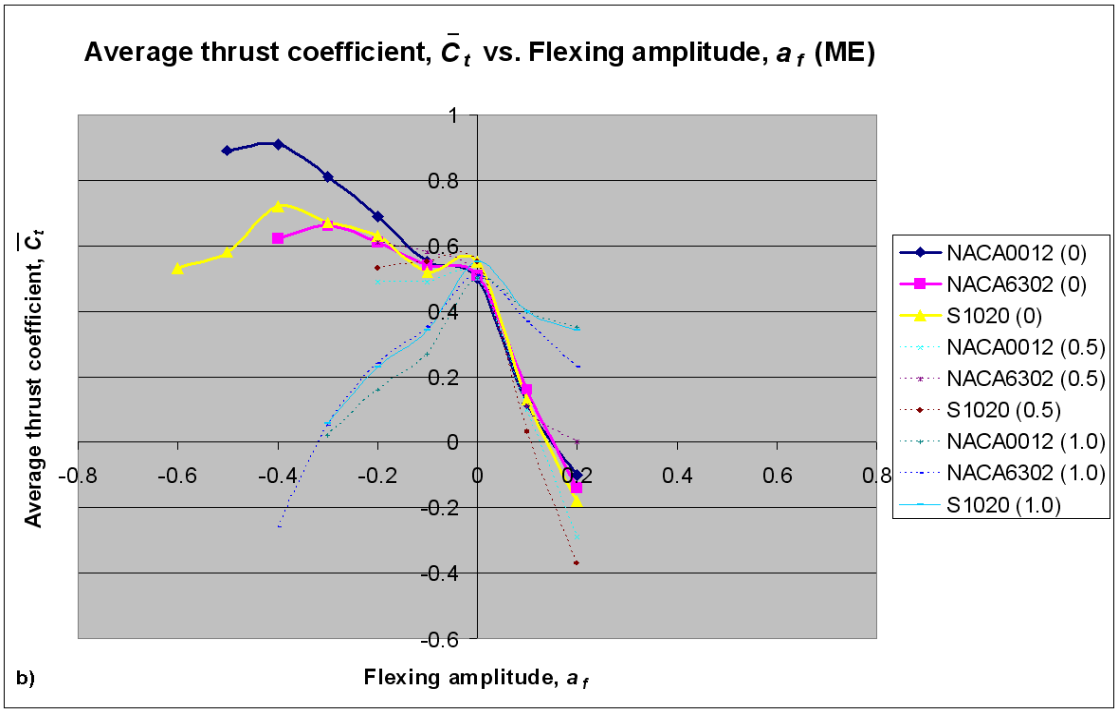

Figure 6.7: Graph of (a) efficiency, (b) average thrust and (c) lift coefficients against flexing amplitude for ME (continue on next page)

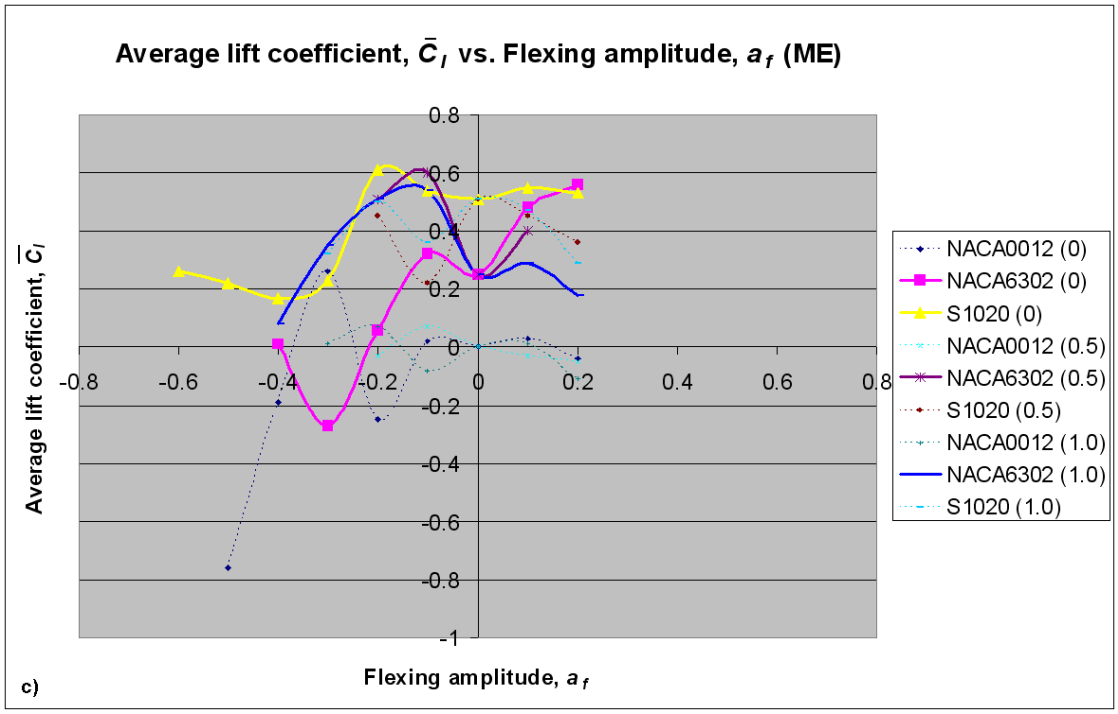

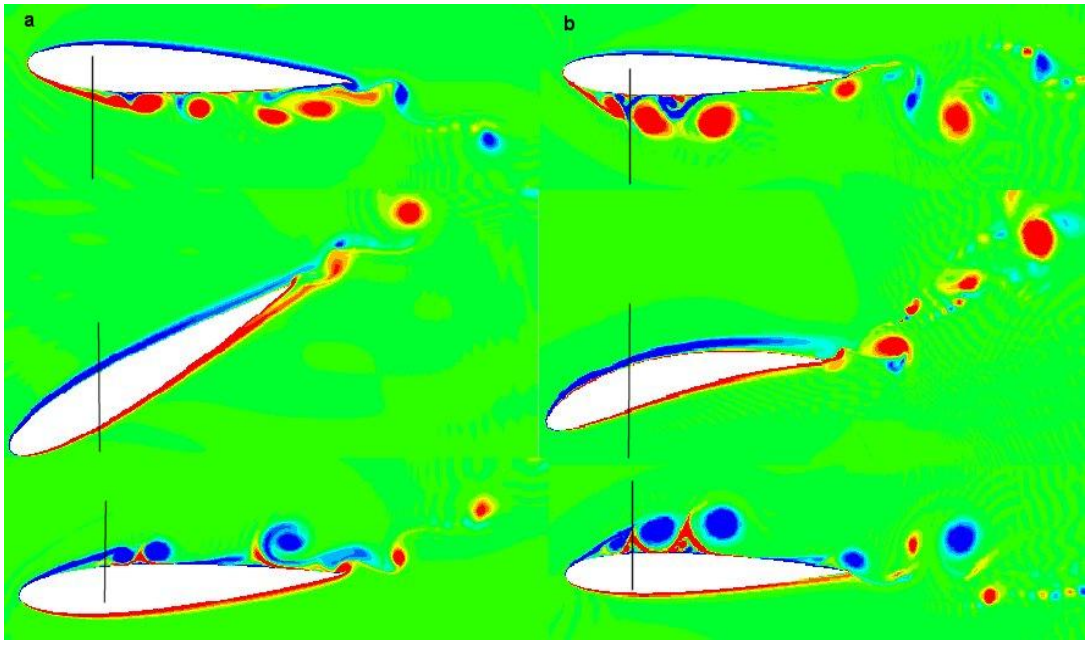

Figure 6.8: Vorticity diagram of NACA0012 airfoil undergoing BB test 11 (a) without flexing (b) with flexing at x_{fc} = 0.0 and $\bar{a}_f$ = -0.3 during the heaving down cycle

There is no noticeable trend for the change of $\bar{C}_l$ as flexing increases. From Figure 6.7c, for certain flexing configurations $\bar{C}_l$ increases. However, at other flexing configurations, the $\bar{C}_l$ decreases, even resulting in negative $\bar{C}_l$.

6.2.2 ME Single-sided flexing (Figure 6.9)

Figure 6.9a, b and c show the plot of the η, $\overline{C}_t$ and $\overline{C}_l$ against the flexing amplitude. The trends observed with the ME single-sided airfoils are similar to that of the single-sided pure heaving case. The η and $\overline{C}_t$ decrease with increasing flexing.

On the other hand, $\overline{C}_l$ increases as the amplitude increases for x_{fc} = 0.0, 0.5 and as the amplitude decreases for x_{fc} = 1.0. This trend generally applies to all cases except for the NACA6302 airfoil at x_{fc} = 0.5. For the NACA6302 airfoil at x_{fc} = 0.5, the $\overline{C}_l$ drops after $\overline{a}_f$ = 0.1 instead of increasing. Moreover, the increase in $\overline{C}_l$ is most significant for all airfoils at the x_{fc} = 0.0 case. The NACA0012 and S1020 airfoils provide high $\overline{C}_l$ of more than 3 at $\overline{a}_f$ = 0.4, giving better results compared to the heaving case. The simulations at x_{fc} = 0.0, 0.5, $\overline{a}_f \leq$ -0.1 and x_{fc} = 1.0, $\overline{a}_f \geq$ 0.1 are not attempted for the NACA6302 and S1020 airfoils because the results obtained using these parameters for the NACA0012 airfoil are worse than the original un-flexed case.

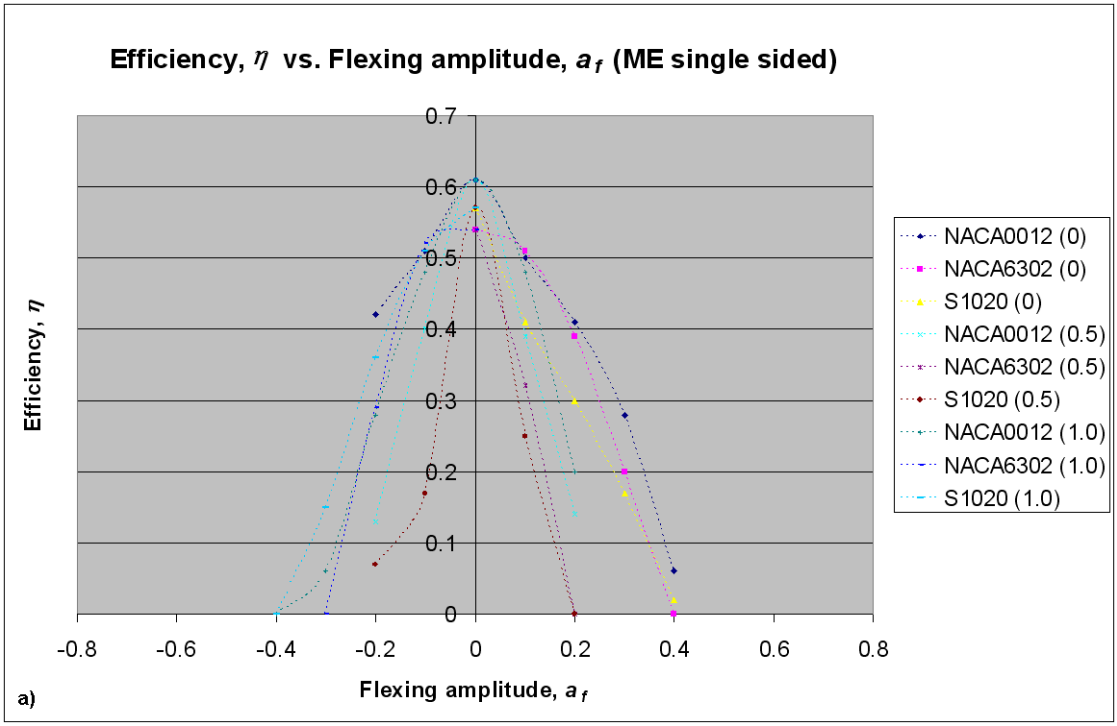

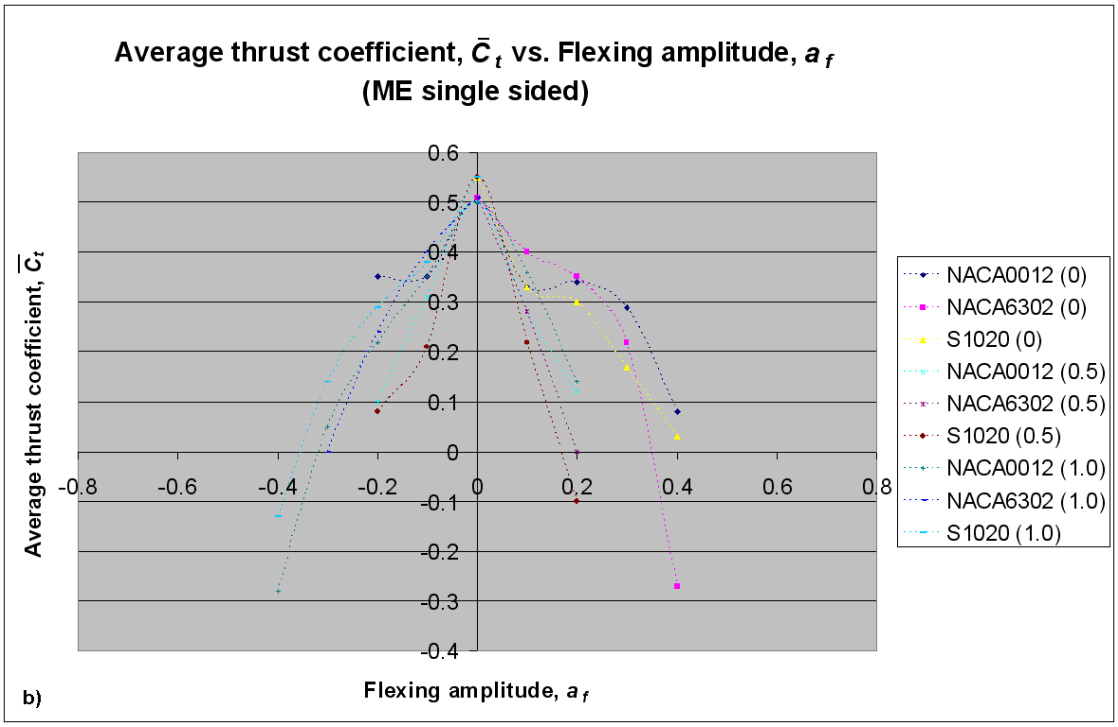

Figure 6.9: Graph of (a) efficiency, (b) average thrust and (c) lift coefficients against flexing amplitude for ME single sided flexing (continue on next page)

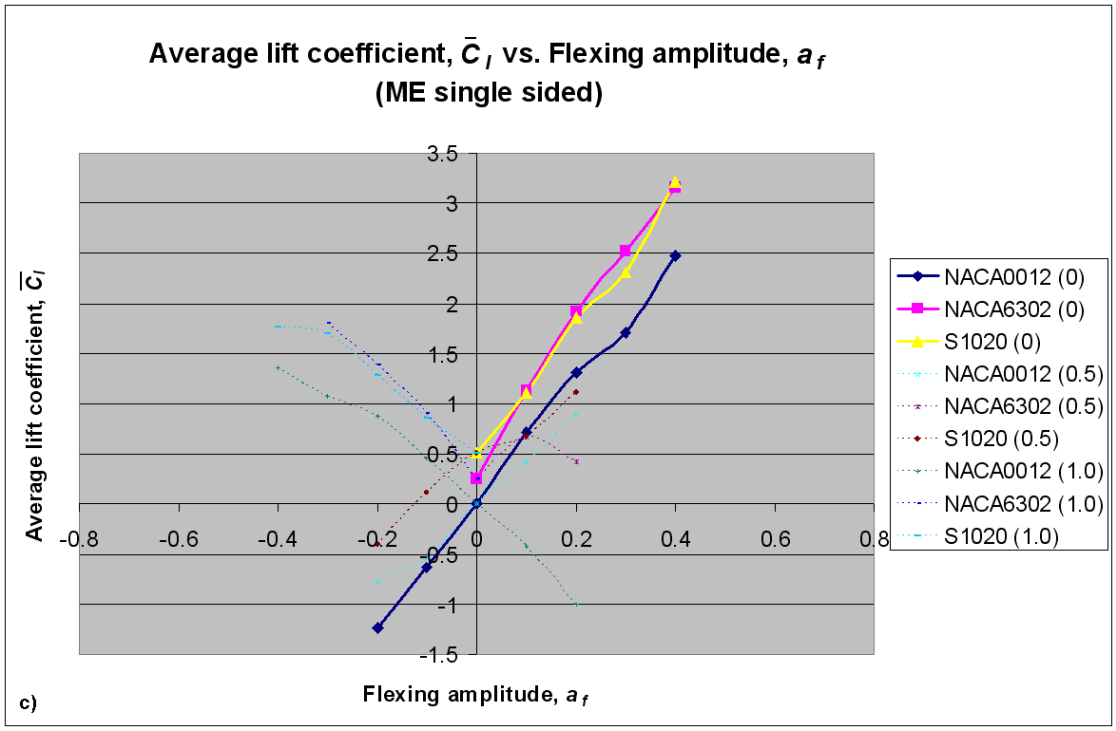

6.3 ME (20°) Configuration (h_0 = 0.75, k = 0.2, θ_0 = 20°, ϕ = 90°)

6.3.1 Double sided flexing (Figure 6.10)

Figure 6.10a, b and c show the plot of the η, $\bar{C}_t$ and $\bar{C}_l$ against the flexing amplitude. The simulations are repeated again using the same ME configuration's parameters except the θ_0 which is now 20^0. As mentioned earlier, the reason for this change is to test whether flexing can improve the η when the airfoil is not flapping at its optimum configuration. Results show that there is an improvement in η in some of the cases tested, especially at x_{fc} = 1.0. The NACA6302 airfoil reaches an η of 0.66 at x_{fc} = 1.0, $\bar{a}_f$ = -0.3, which is close to a 60% increase.

The S1020 airfoil at the x_{fc} = 1.0 case does not follow the standard parabolic trend. As $\bar{a}_f$ decreases, η decreases until $\bar{a}_f$ = -0.2 and then increases as $\bar{a}_f$ increases further. It manages to reach a maximum η of 0.58 at $\bar{a}_f$ = -0.3.

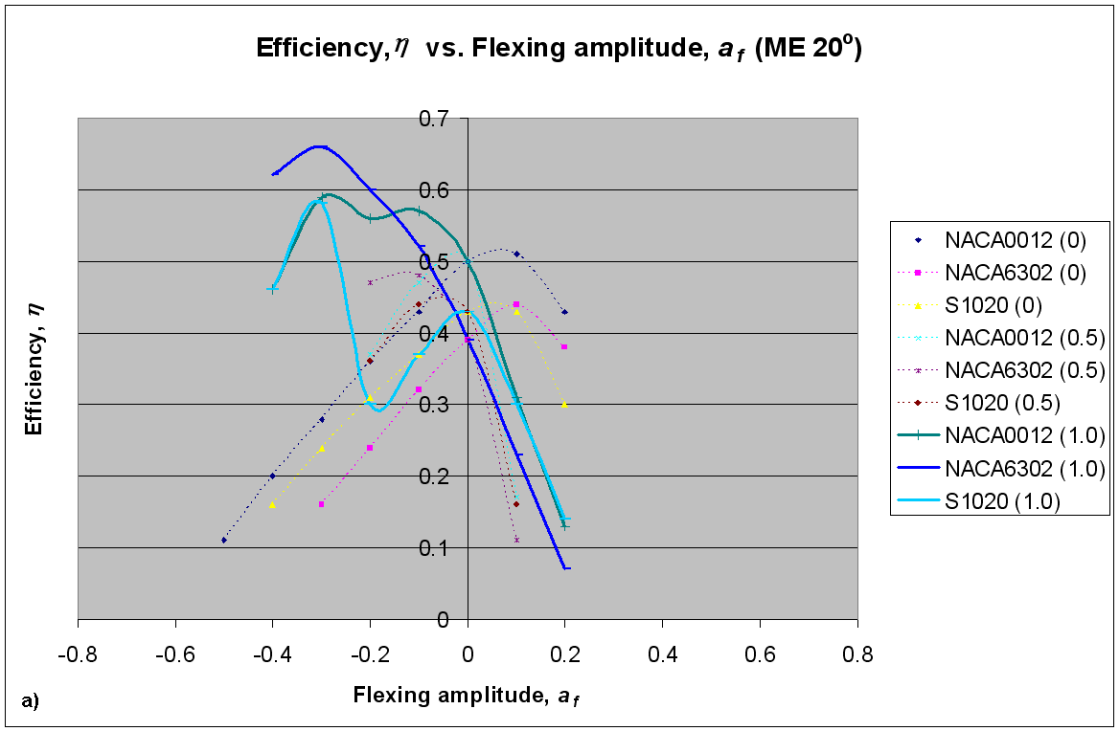

Figure 6.10: Graph of (a) efficiency, (b) average thrust and (c) lift coefficients against flexing amplitude for ME (20°) (continue on next page)

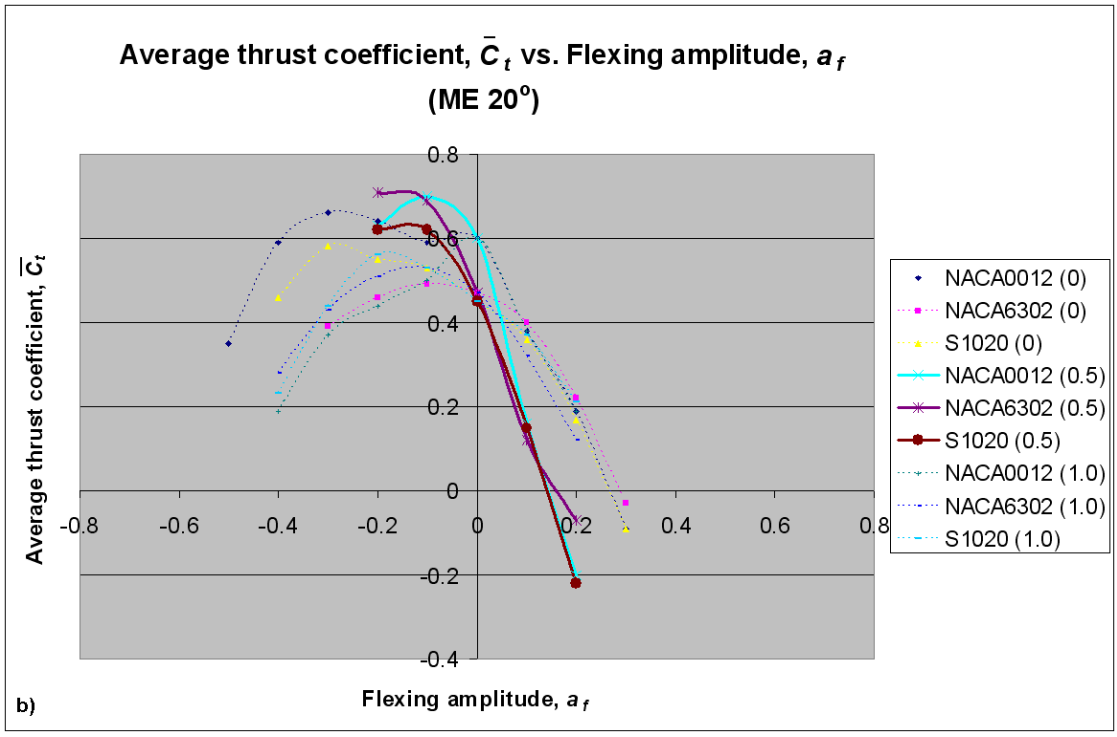
Average thrust coefficient, $\bar{C}_t$ vs. Flexing amplitude, a_f
(ME 20°)
Average thrust coefficient, $\bar{C}_t$
Flexing amplitude, a_f
0.8
0.6
0.4
0.2
0
-0.2
-0.4
-0.8
-0.6
-0.4
-0.2
0
0.2
0.4
0.6
0.8
NACA0012 (0)
NACA6302 (0)
S1020 (0)
NACA0012 (0.5)
NACA6302 (0.5)
S1020 (0.5)
NACA0012 (1.0)
NACA6302 (1.0)
S1020 (1.0)

b)

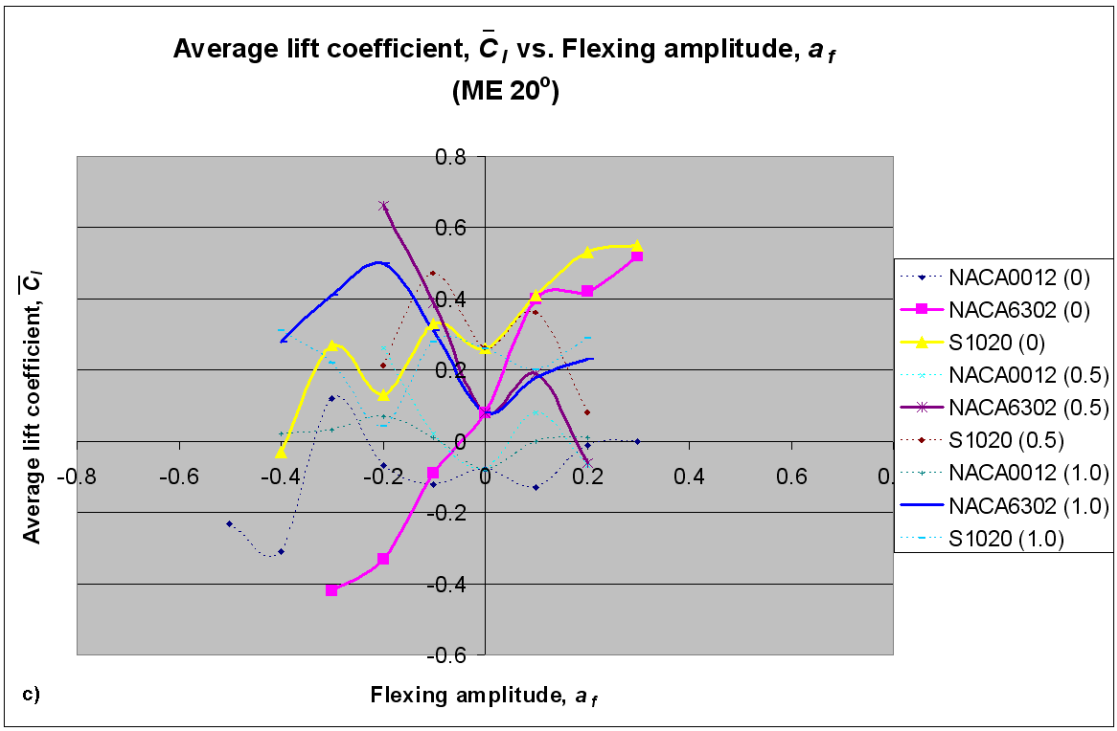
Average lift coefficient, $\bar{C}_l$ vs. Flexing amplitude, a_f
(ME 20°)
Average lift coefficient, $\bar{C}_l$
Flexing amplitude, a_f
0.8
0.6
0.4
0.2
0
-0.2
-0.4
-0.6
-0.8
-0.6
-0.4
-0.2
0
0.2
0.4
0.6
NACA0012 (0)
NACA6302 (0)
S1020 (0)
NACA0012 (0.5)
NACA6302 (0.5)
S1020 (0.5)
NACA0012 (1.0)
NACA6302 (1.0)
S1020 (1.0)

c)

The vorticity diagrams of the un-flexed case and the flexed case for the NACA6302 airfoil at x_{fc} = 1.0 and $\bar{a}_f$ = -0.3 are shown in Figure 6.11 and Figure 6.12 respectively. It is evident that the vortices are much more orderly and coherent in the flexed case. This shows that in certain cases, when the airfoil is not flapping at optimum η, a small amount of flexing can help to improve it. Interestingly, when it is already flapping at an optimum flapping configuration (when $\theta_0 = 30^0$), flexing is actually detrimental to the η.

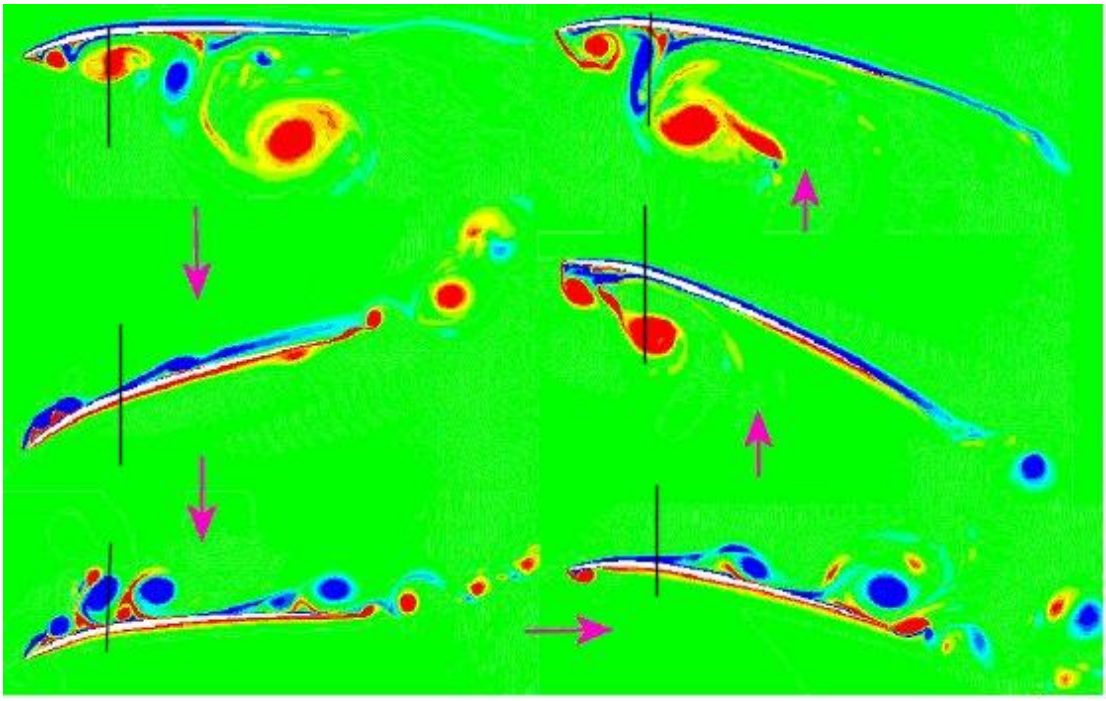

Figure 6.11: Vorticity diagram of the NACA6302 airfoil undergoing simulation with ME (θ_0 = 20^o), without flexing

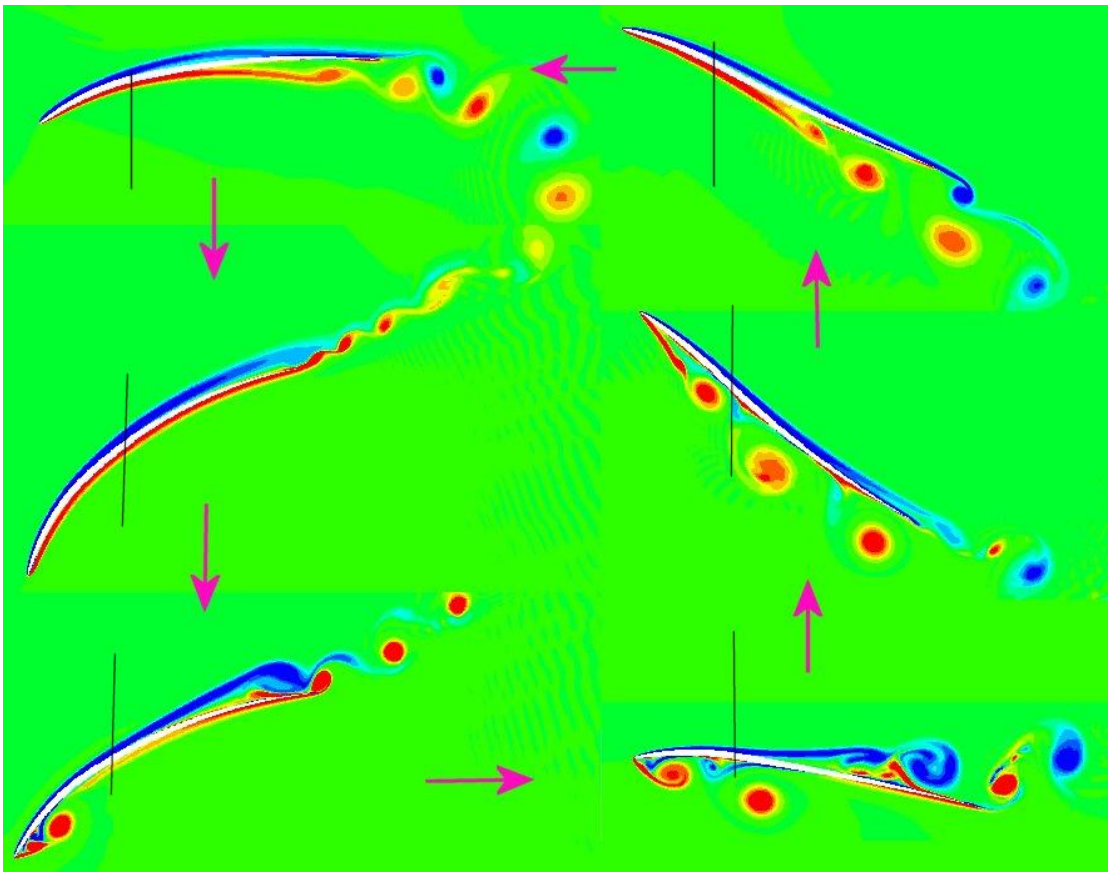

Figure 6.12: Vorticity diagram of the NACA6302 airfoil undergoing simulation with ME (θ_0 = 20^o), with flexing at x_{fc} = 1.0 and $\bar{a}_f$ = -0.3

$\bar{C}_t$ increases slightly as $\bar{a}_f$ decreases for all values of x_{fc}. Compared to the cases with ME configuration, the increase in $\bar{C}_t$ is much smaller. For certain combinations of x_{fc} and $\bar{a}_f$, the $\bar{C}_l$ generated by the non-symmetrical airfoils shows improvement. As mentioned earlier in section 2.3 by Tang et al. (2007), the effect of flexing is similar to that of pitching. Therefore, a pitching amplitude $\theta_0 = 20^0$ plus a small of amount of flexing is similar to $\theta_0 = 30^0$ and hence it should give a better η. However, $\theta_0 = 30^0$ plus a small of amount of flexing will mean a $\theta_0 > 30^0$. This configuration has passed the optimum point[§§§] and therefore the η is lower.

[§§§] Simulations have been carried out with the ME flapping configuration with θ_0 = 20^o to 45^o for the different airfoils. It is found that θ_0 = 30^o gives the best efficiency.

On the other hand, comparing between the average thrust and lift coefficients of the airfoils for the ME and ME(20^o) cases (Figure 6.7b,c and Figure 6.10b,c), the response of these coefficients to flexing is very different for the two cases. Hence, although flexing is in some ways similar to pitching, it does not always give the same result.

6.3.1.1 Single-sided flexing (Figure 6.13)

Figure 6.13a, b and c show the plot of the η, $\bar{C}_t$ and $\bar{C}_l$ against the flexing amplitude. The trends observed with ME (20^0) single-sided are very similar to the single-sided ME configuration's cases. However, the ME (20^0) single-sided flexing is able to provide slightly better η, $\bar{C}_t$ and $\bar{C}_l$ at the same flexing amplitude. The simulations at x_{fc} = 1.0, $\bar{a}_f \geq 0.1$ are not attempted for the NACA6302 and S1020 airfoils because the results for the NACA0012 airfoil are worse than the original un-flexed case.

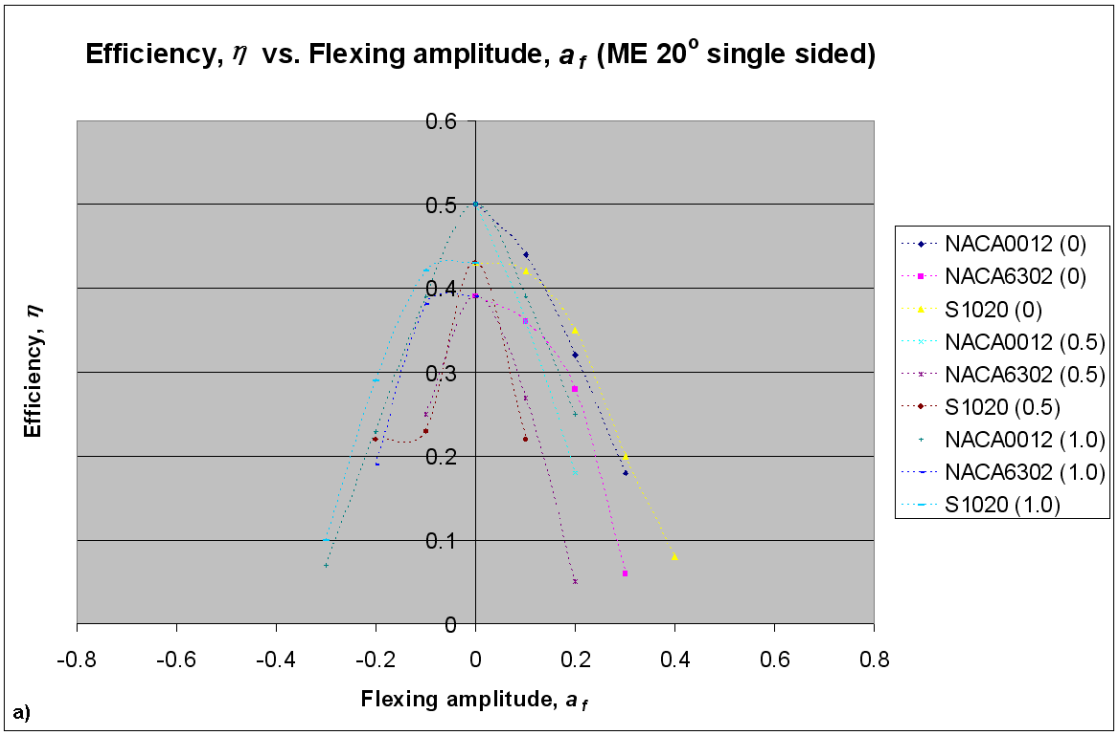

Figure 6.13: Graph of (a) efficiency, (b) average thrust and (c) lift coefficients against flexing amplitude for ME (20^o) single sided (continue on next page)

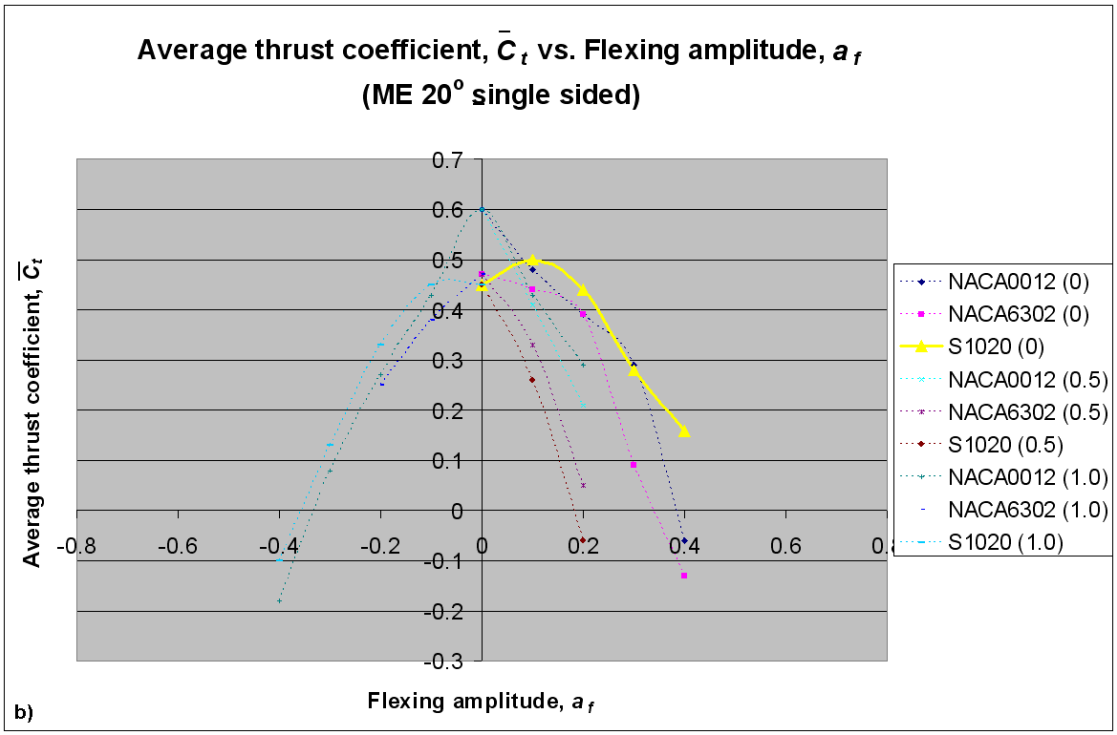
Average thrust coefficient, $\bar{C}_t$ vs. Flexing amplitude, a_f
(ME 20° single sided)
Average thrust coefficient, $\bar{C}_t$
Flexing amplitude, a_f
0.7
0.6
0.5
0.4
0.3
0.2
0.1
0
-0.1
-0.2
-0.3
-0.8
-0.6
-0.4
-0.2
0
0.2
0.4
0.6
NACA0012 (0)
NACA6302 (0)
S1020 (0)
NACA0012 (0.5)
NACA6302 (0.5)
S1020 (0.5)
NACA0012 (1.0)
NACA6302 (1.0)
S1020 (1.0)

b)

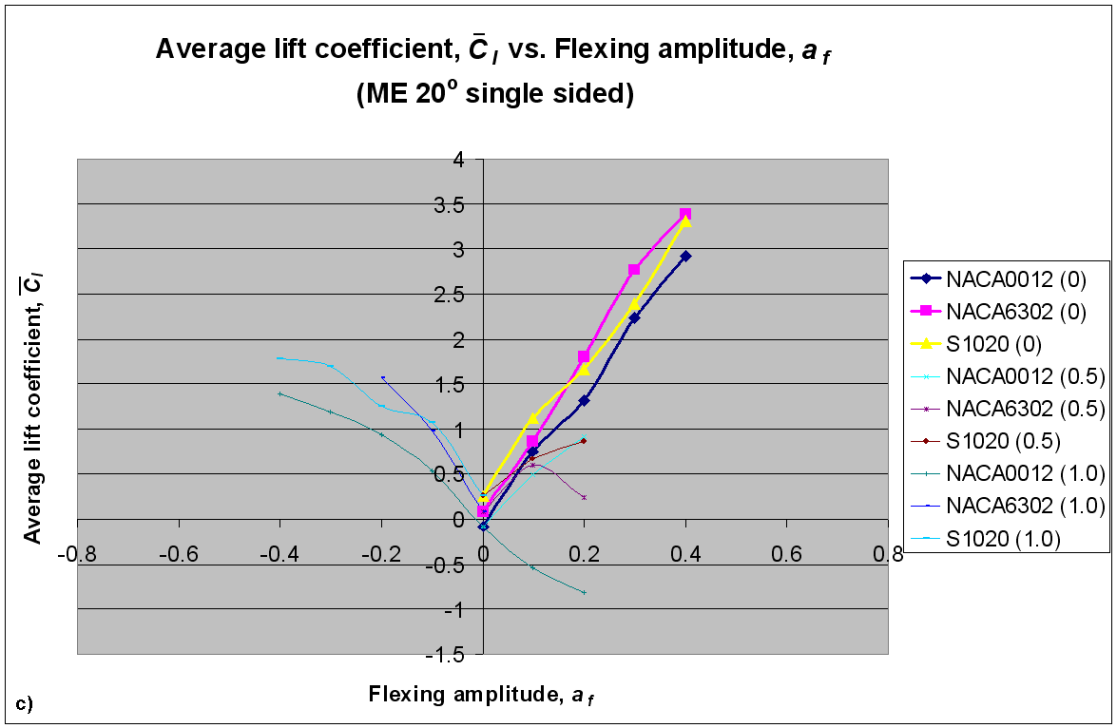
Average lift coefficient, $\bar{C}_l$ vs. Flexing amplitude, a_f
(ME 20° single sided)
Average lift coefficient, $\bar{C}_l$
Flexing amplitude, a_f
4
3.5
3
2.5
2
1.5
1
0.5
0
-0.5
-1
-1.5
-0.8
-0.6
-0.4
-0.2
0
0.2
0.4
0.6
0.8
NACA0012 (0)
NACA6302 (0)
S1020 (0)
NACA0012 (0.5)
NACA6302 (0.5)
S1020 (0.5)
NACA0012 (1.0)
NACA6302 (1.0)
S1020 (1.0)

c)

6.4 Flexing – MT Configuration (h_0 = 0.42, k = 0.6, θ_0 = 17.5°, ϕ = 120°)

6.4.1 Double sided flexing (Figure 6.14)

Figure 6.14a, b and c show the plot of the η, $\bar{C}_t$ and $\bar{C}_l$ against the flexing amplitude. There is a small increase in η for some of the x_{fc} = 0.5, 1.0 cases as $\bar{a}_f$ decreases. The NACA6302 airfoil's η achieves the highest increment from 0.21 to 0.28 at x_{fc} = 1.0, $\bar{a}_f$ = -0.3. This configuration is able to generate a high $\bar{C}_t$ of 2.10 to 2.50 for the un-flexed airfoils. In this case, flexing still increases the $\bar{C}_t$ slightly. Similar to the η case (Figure 6.14a), for some of the x_{fc} = 0.5, 1.0 cases, as $\bar{a}_f$ decreases, the $\bar{C}_t$ increases. Moreover, at x_{fc} = 0.0 case, as $\bar{a}_f$ increases, the $\bar{C}_t$ also increases. In other words, both η and $\bar{C}_t$ increase, albeit by a small amount.

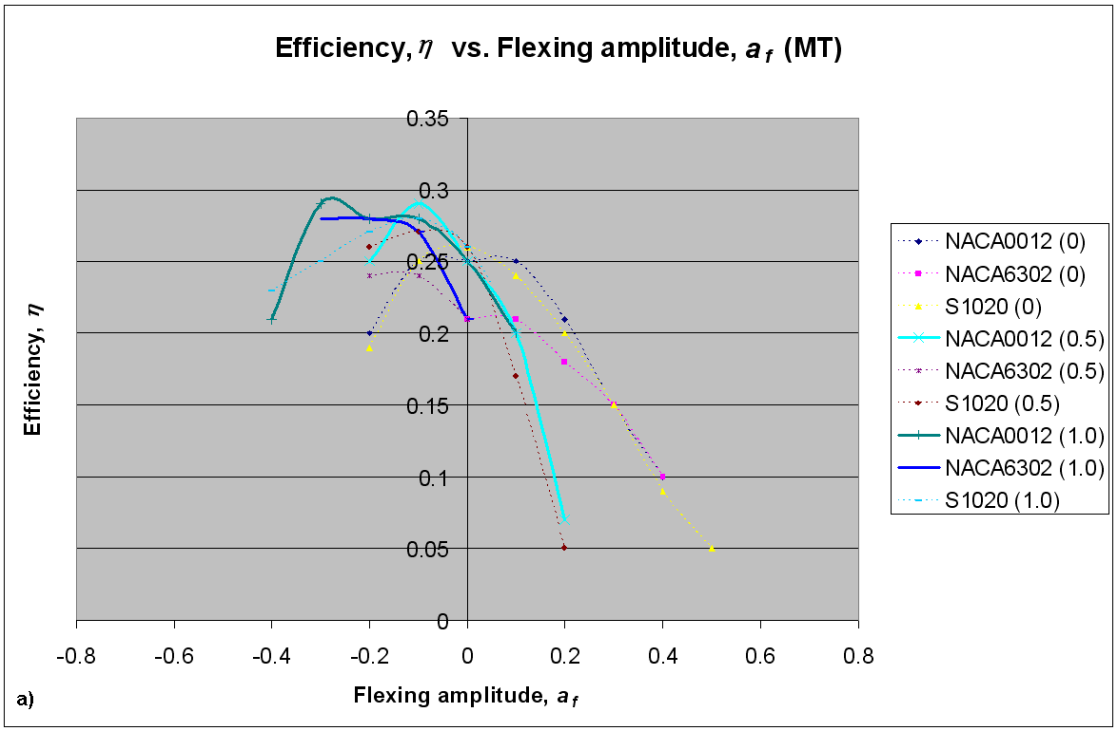

Figure 6.14: Graph of (a) efficiency, (b) average thrust and (c) lift coefficients against flexing amplitude for MT (continue on next page)

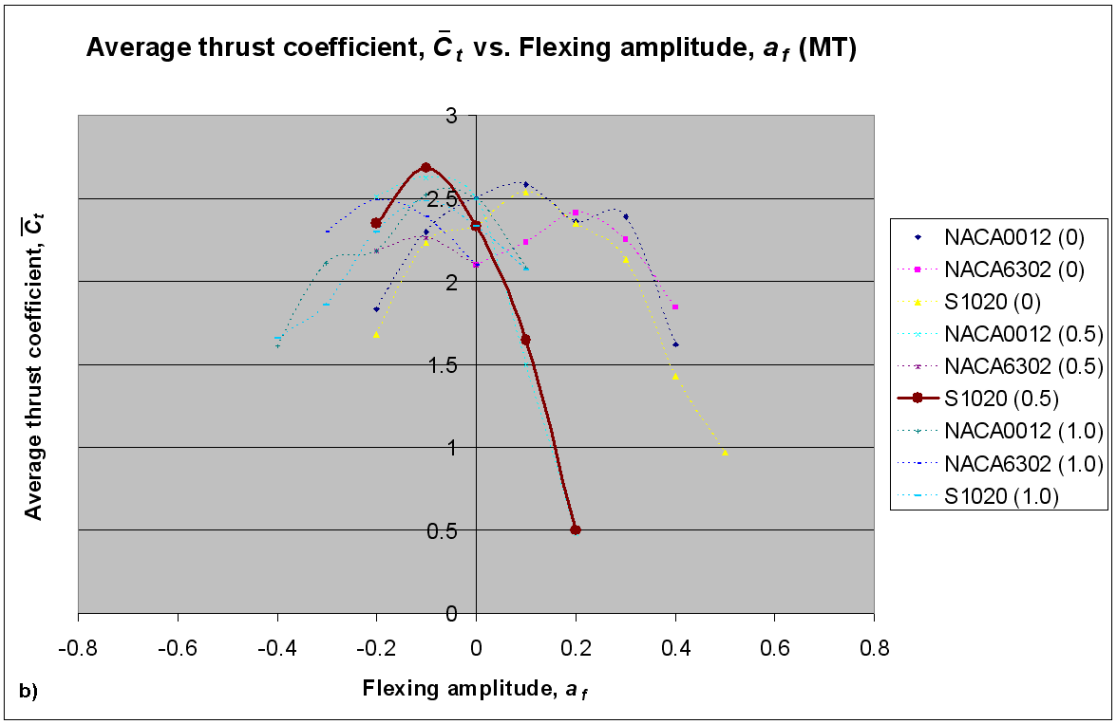

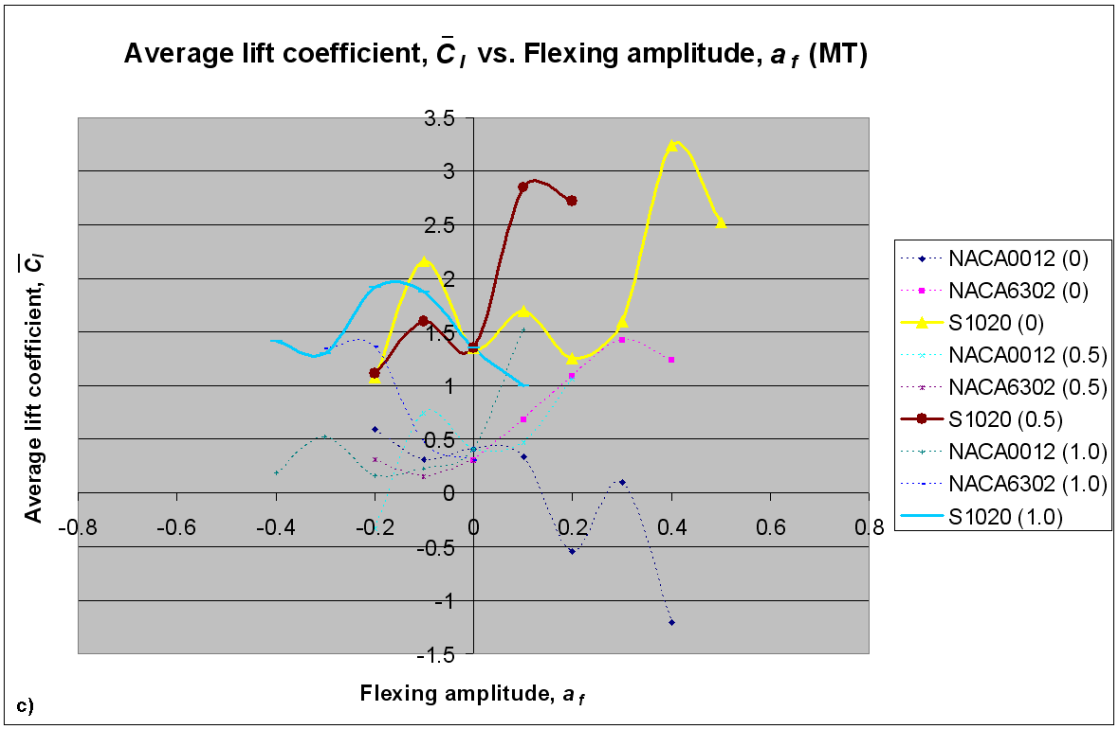

Figure 6.14c shows that the variation of the $\bar{C}_l$ is very irregular as the amount of flexing increases. However, for some cases, such as at x_{fc} = 0.0, $\bar{a}_f$ = 0.4 and x_{fc} = 0.5, $\bar{a}_f$ = 0.1, the

$\overline{C}_l$ can reach as high as 3.24 and 2.85 for the S1020 airfoil respectively.

6.4.2 Single-sided flexing (Figure 6.15)

Figure 6.15a, b and c show the plot of the η, $\overline{C}_t$ and $\overline{C}_l$ against the flexing amplitude. As in the other single-sided test cases, $\overline{C}_l$ increases as flexing increases. However, compared to the ME configuration and pure heaving case, η and $\overline{C}_t$ now decrease more slowly when the flexure increases. $\overline{C}_l$ is as high as 4.61 for the S1020 airfoil at x_{fc} = 1.0, $\overline{a}_f$ = -0.3. The simulations at x_{fc} = 0.5, $\overline{a}_f \leq$ -0.1 and x_{fc} = 1.0, $\overline{a}_f \geq$ 0.1 are not attempted for the NACA6302 and S1020 airfoils because the results for the NACA0012 airfoil is worse than the original un-flexed case.

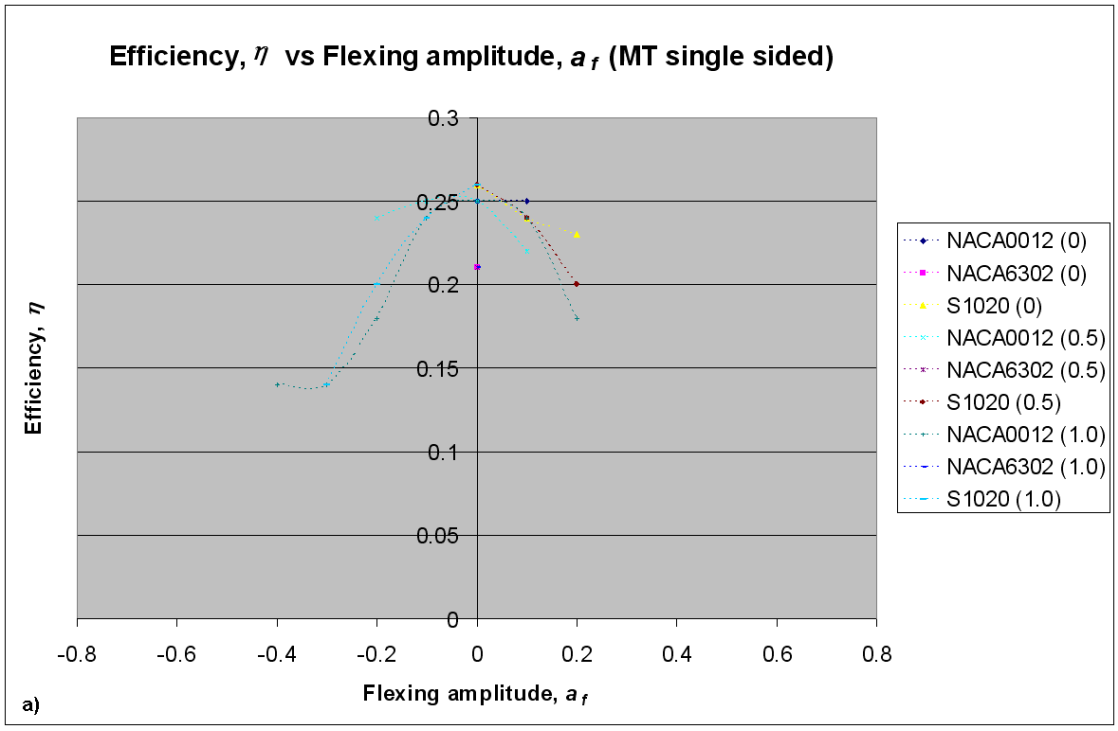

Figure 6.15: Graph of (a) efficiency, (b) average thrust and (c) lift coefficients against flexing amplitude for MT single sided (continue on next page)

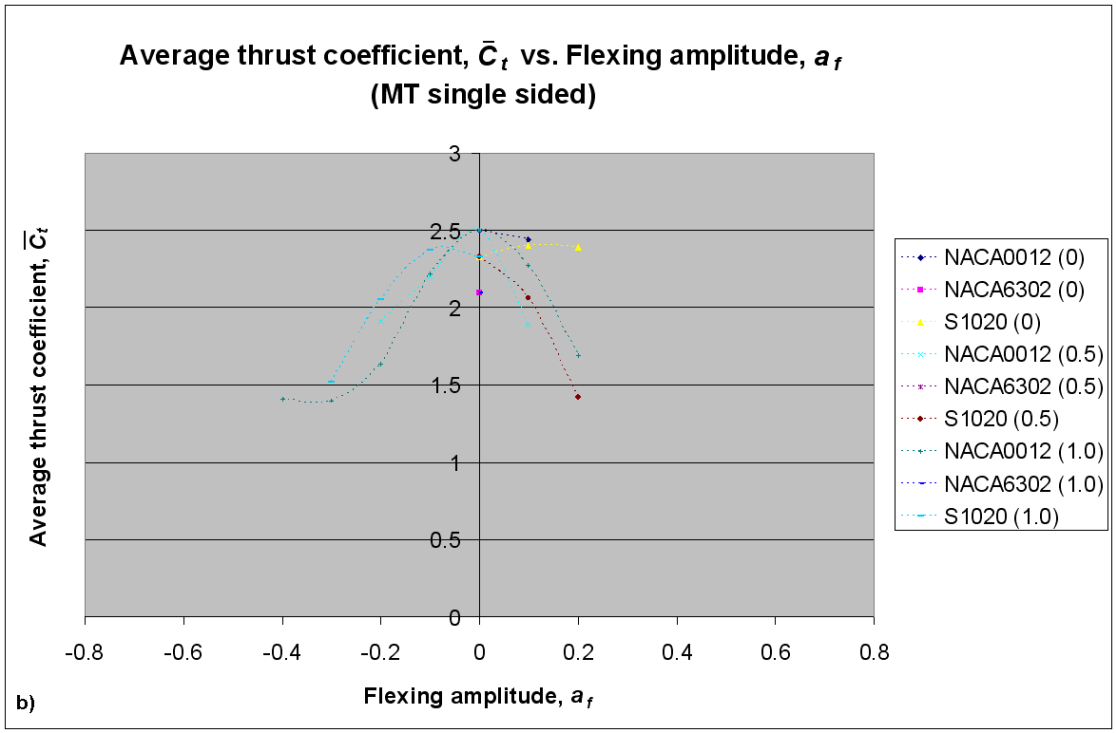
Average thrust coefficient, $\bar{C}_t$ vs. Flexing amplitude, a_f
(MT single sided)
Average thrust coefficient, $\bar{C}_t$
3
2.5
2
1.5
1
0.5
0
-0.8
-0.6
-0.4
-0.2
0
0.2
0.4
0.6
0.8
Flexing amplitude, a_f
NACA0012 (0)
NACA6302 (0)
S1020 (0)
NACA0012 (0.5)
NACA6302 (0.5)
S1020 (0.5)
NACA0012 (1.0)
NACA6302 (1.0)
S1020 (1.0)
b)

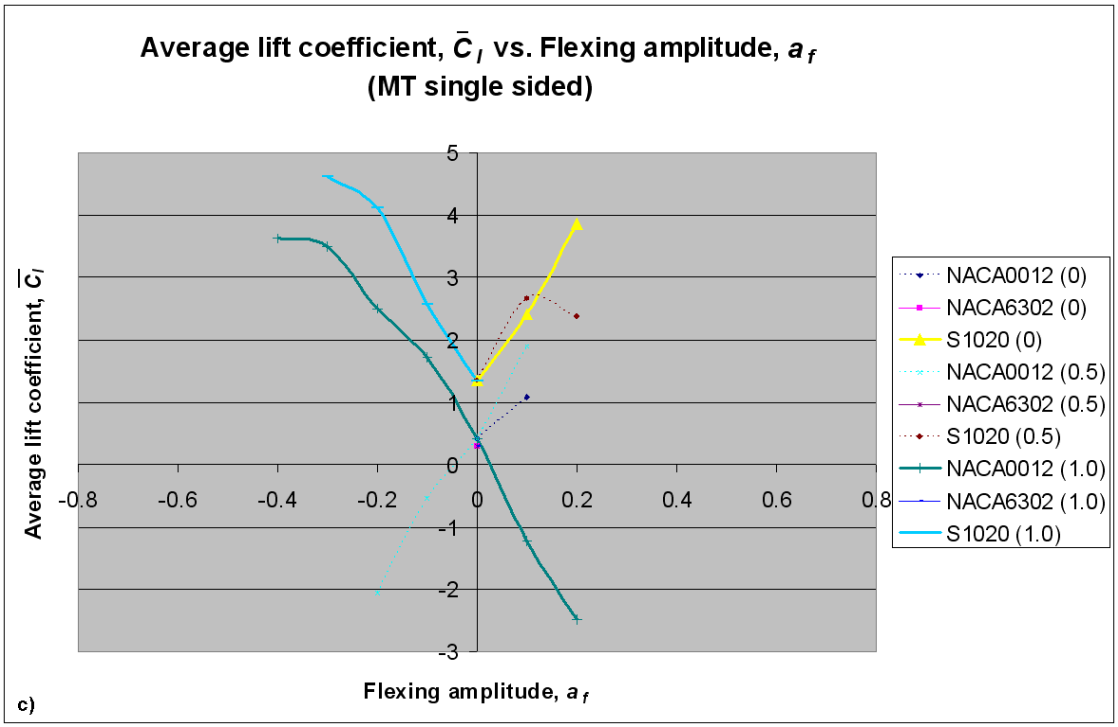
Average lift coefficient, $\bar{C}_l$ vs. Flexing amplitude, a_f
(MT single sided)
Average lift coefficient, $\bar{C}_l$
5
4
3
2
1
0
-1
-2
-3
-0.8
-0.6
-0.4
-0.2
0
0.2
0.4
0.6
0.8
Flexing amplitude, a_f
NACA0012 (0)
NACA6302 (0)
S1020 (0)
NACA0012 (0.5)
NACA6302 (0.5)
S1020 (0.5)
NACA0012 (1.0)
NACA6302 (1.0)
S1020 (1.0)
c)

6.5 Flexing – ML Configuration (h_0 = 0.15, k = 1.0, θ_0 = 17.5°, ϕ = 120°)

6.5.1 Double sided flexing (Figure 6.16)

Figure 6.16a, b and c show the plot of the η, $\overline{C}_t$ and $\overline{C}_l$ against the flexing amplitude for the NACA6302 and S1020 airfoils. Since the initial focus is on $\overline{C}_l$, this group of simulations does not include the NACA0012 airfoil. There is a small increase in η for some of the x_{fc} = 0.0, 0.5 cases as $\overline{a}_f$ decreases. Similarly, flexing at x_{fc} = 0.0 and 0.5 also lead to an increase in $\overline{C}_t$. Moreover, the increase in $\overline{C}_t$ for the S1020 airfoil at x_{fc} = 0.0, $\overline{a}_f$ = 0.3 shoots to more than twice the original value (3.57 vs. 1.63), although the η also drops to about half the original value. $\overline{C}_l$ decreases for almost all cases except at x_{fc} = 0.0, $\overline{a}_f$ = 0.4 for the S1020 airfoil, where the $\overline{C}_l$ increases slightly.

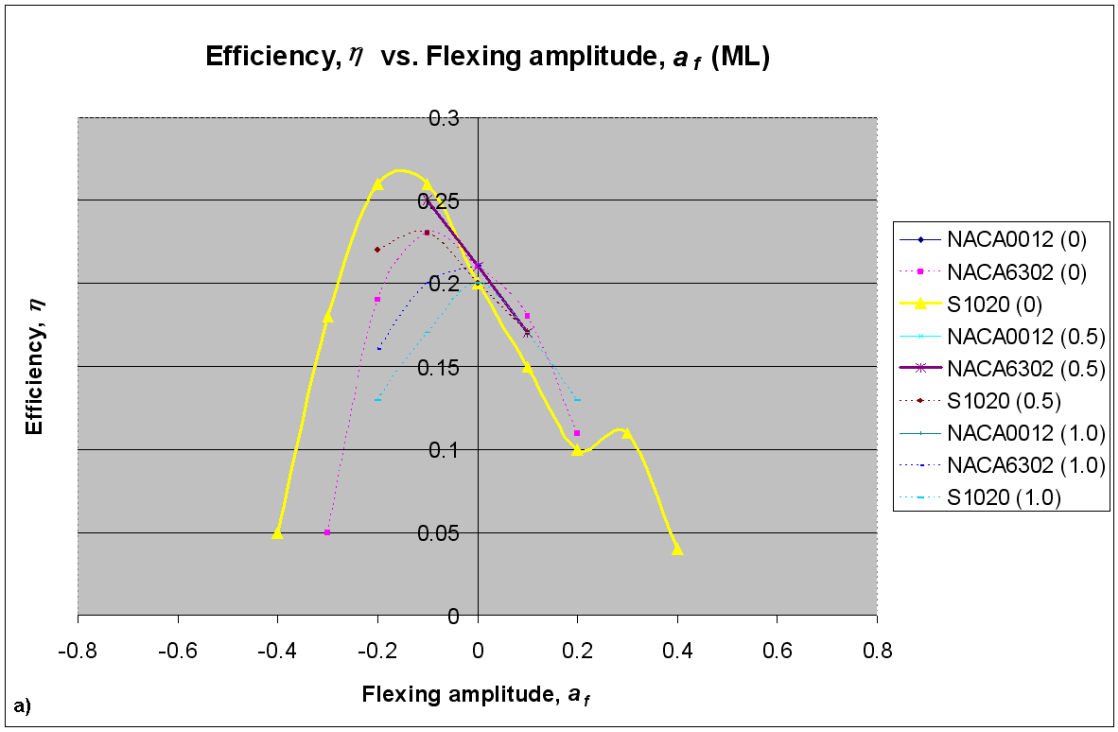

Figure 6.16: Graph of (a) efficiency, (b) average thrust and (c) lift coefficients against flexing amplitude for ML (continue on next page)

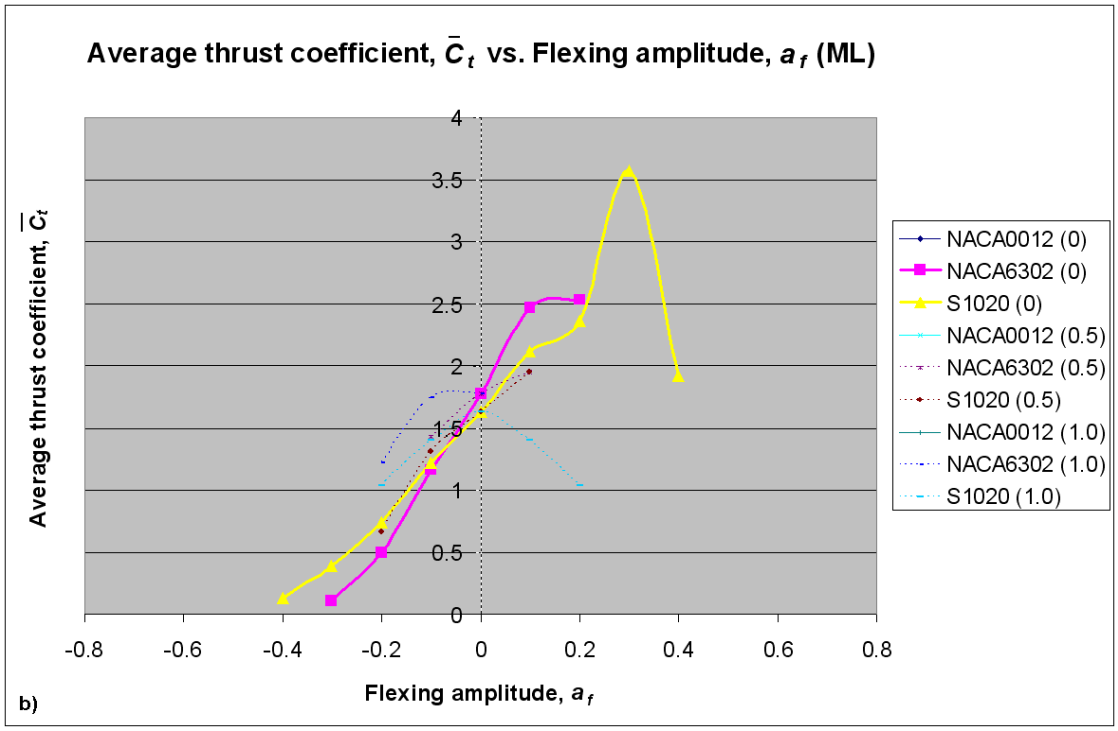
Average thrust coefficient, $\bar{C}_t$ vs. Flexing amplitude, a_f (ML)
Average thrust coefficient, $\bar{C}_t$
Flexing amplitude, a_f
4
3.5
3
2.5
2
1.5
1
0.5
0
-0.8
-0.6
-0.4
-0.2
0
0.2
0.4
0.6
0.8
NACA0012 (0)
NACA6302 (0)
S1020 (0)
NACA0012 (0.5)
NACA6302 (0.5)
S1020 (0.5)
NACA0012 (1.0)
NACA6302 (1.0)
S1020 (1.0)
b)

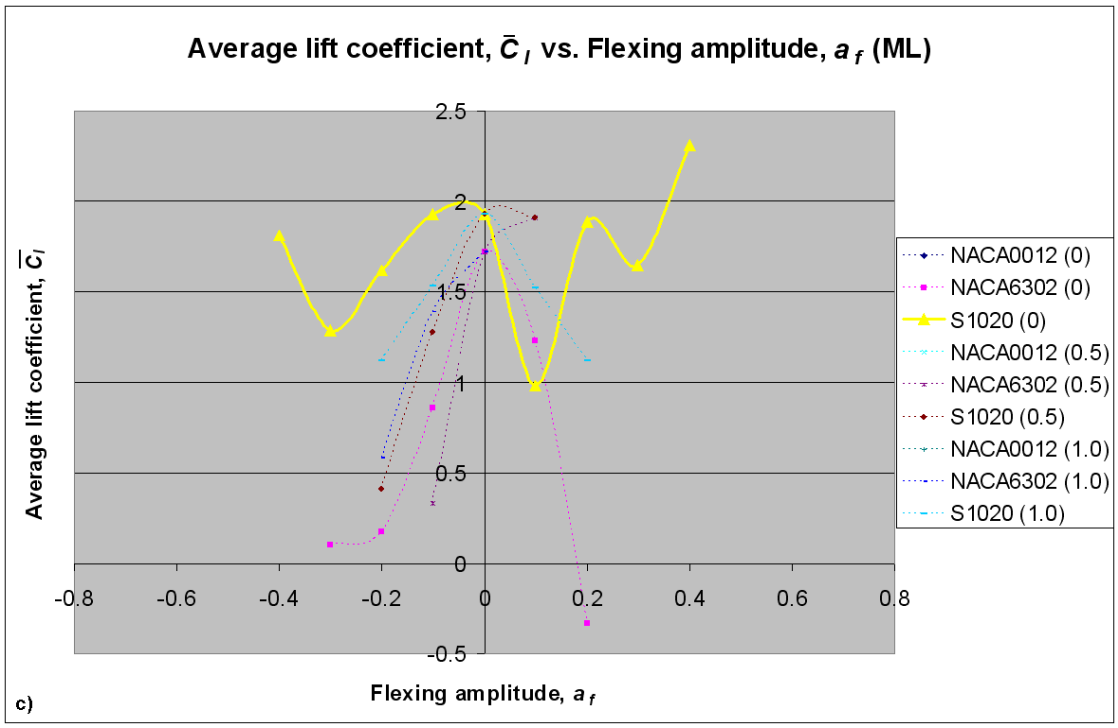
Average lift coefficient, $\bar{C}_l$ vs. Flexing amplitude, a_f (ML)
Average lift coefficient, $\bar{C}_l$
Flexing amplitude, a_f
2.5
2
1.5
1
0.5
0
-0.5
-0.8
-0.6
-0.4
-0.2
0
0.2
0.4
0.6
0.8
NACA0012 (0)
NACA6302 (0)
S1020 (0)
NACA0012 (0.5)
NACA6302 (0.5)
S1020 (0.5)
NACA0012 (1.0)
NACA6302 (1.0)
S1020 (1.0)
c)

6.5.2 Single-sided flexing (Figure 6.17)

Figure 6.17a, b and c show the plot of the η, $\overline{C}_t$ and $\overline{C}_l$ against the flexing amplitude. Due to the divergence of the solutions at $\overline{a}_f$ as small as ±0.1 or ±0.2, it is not possible to determine the trend of the effect of flexing in this group. However, in general, under small amounts of flexing, the η remains almost the same. $\overline{C}_t$ and $\overline{C}_l$ increase for some cases. Figure 6.17a and b show that at this configuration, the η and $\overline{C}_t$ are very similar to the un-flexed case. The vorticity diagrams of the un-flexed and flexed S1020 airfoil at x_{fc} = 1.0, $\overline{a}_f$ = -0.2 are shown in Figure 6.18a and b respectively. The vorticity diagrams show that the only difference lies in the presence of a leading edge vortex near the front top end of the flexed airfoil. The vortex creates a low pressure region and aids to increase the $\overline{C}_l$.

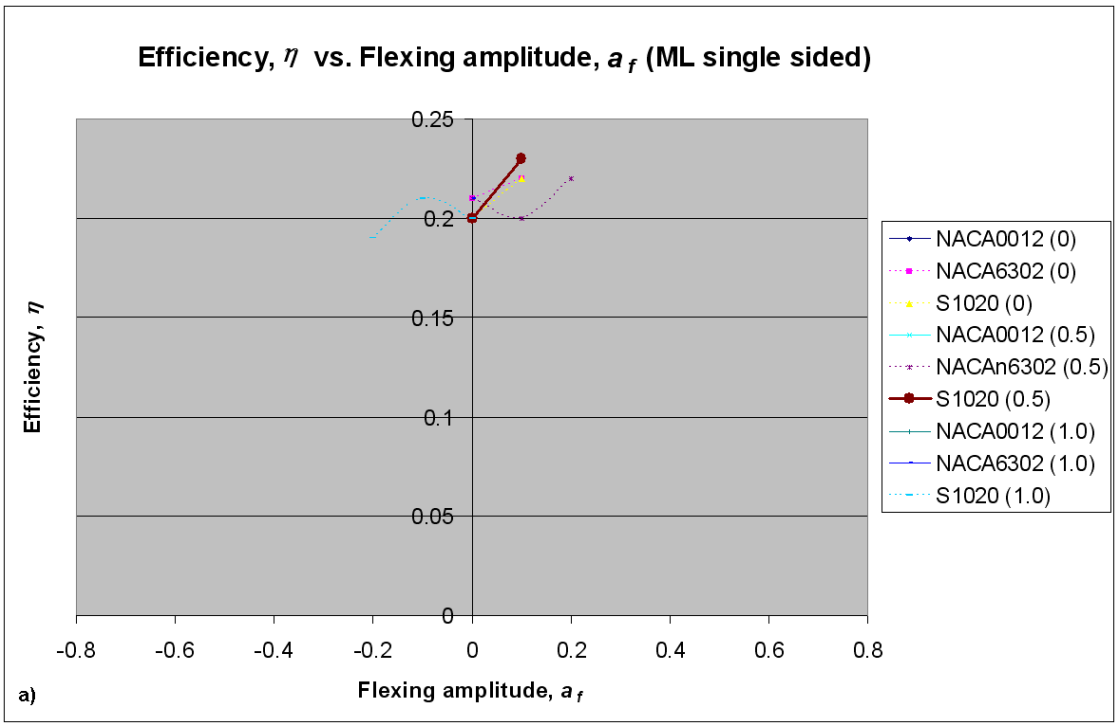

Figure 6.17: Graph of (a) efficiency, (b) average thrust and (c) lift coefficients against flexing amplitude for ML single sided (continue on next page)

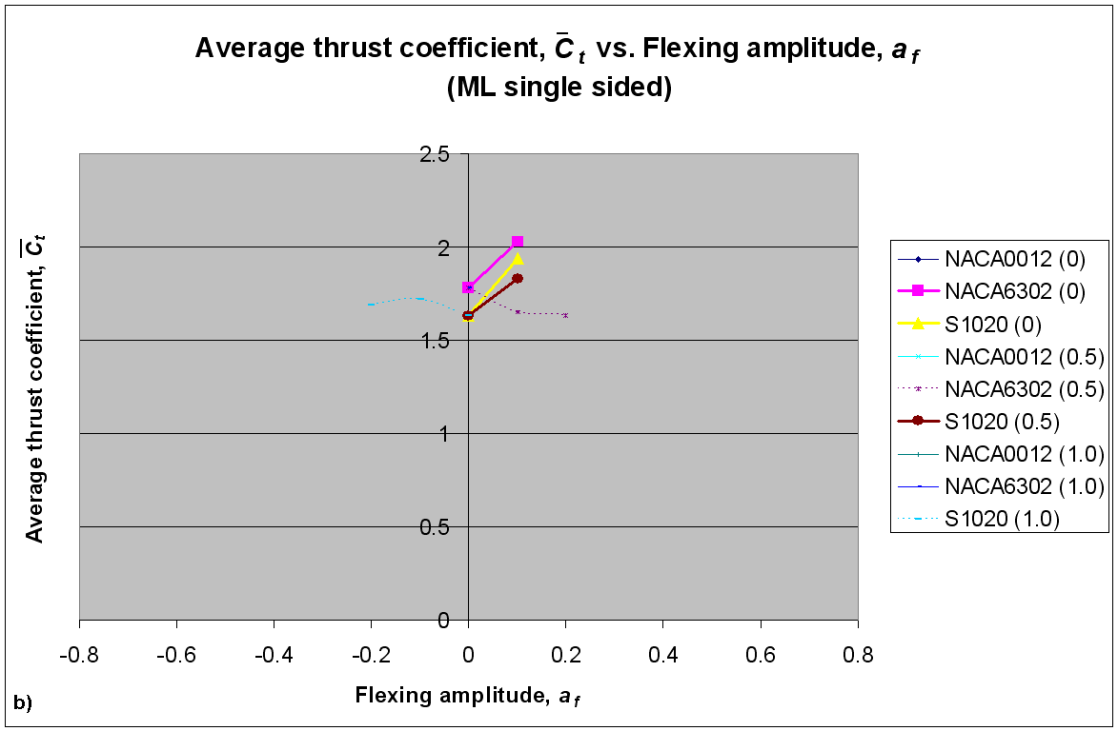
Average thrust coefficient, $\bar{C}_t$ vs. Flexing amplitude, a_f
(ML single sided)
Average thrust coefficient, $\bar{C}_t$
2.5
2
1.5
1
0.5
0
-0.8
-0.6
-0.4
-0.2
0
0.2
0.4
0.6
0.8
Flexing amplitude, a_f
NACA0012 (0)
NACA6302 (0)
S1020 (0)
NACA0012 (0.5)
NACA6302 (0.5)
S1020 (0.5)
NACA0012 (1.0)
NACA6302 (1.0)
S1020 (1.0)
b)

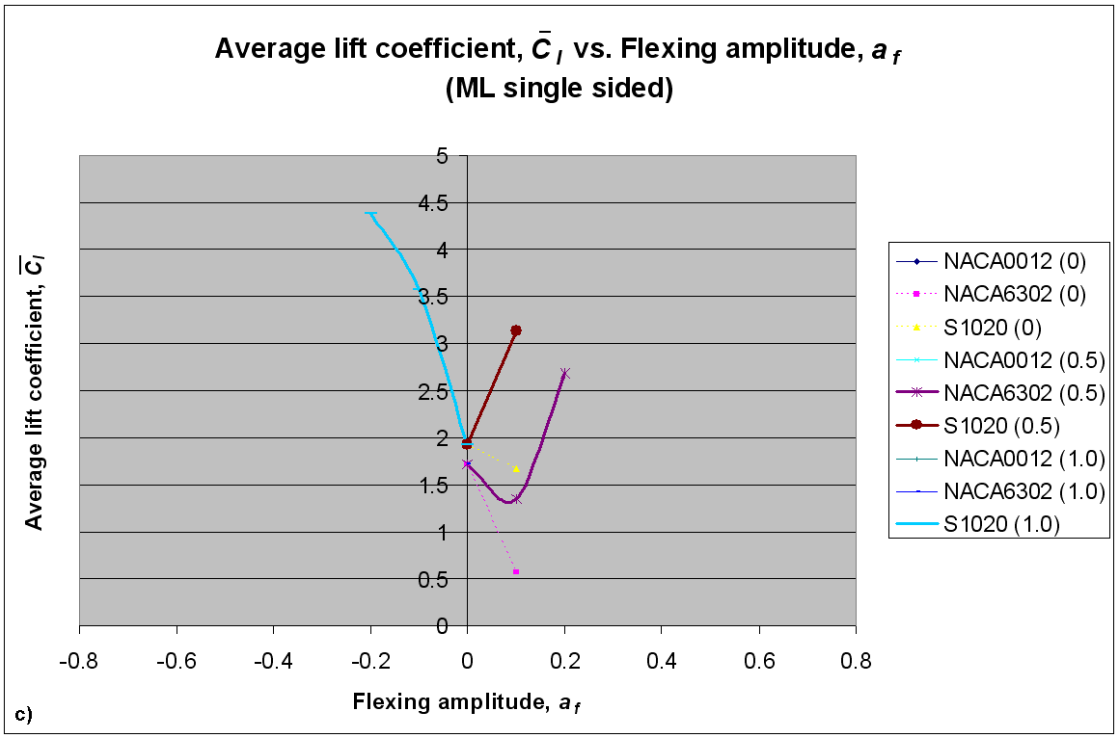
Average lift coefficient, $\bar{C}_l$ vs. Flexing amplitude, a_f
(ML single sided)
Average lift coefficient, $\bar{C}_l$
5
4.5
4
3.5
3
2.5
2
1.5
1
0.5
0
-0.8
-0.6
-0.4
-0.2
0
0.2
0.4
0.6
0.8
Flexing amplitude, a_f
NACA0012 (0)
NACA6302 (0)
S1020 (0)
NACA0012 (0.5)
NACA6302 (0.5)
S1020 (0.5)
NACA0012 (1.0)
NACA6302 (1.0)
S1020 (1.0)
c)

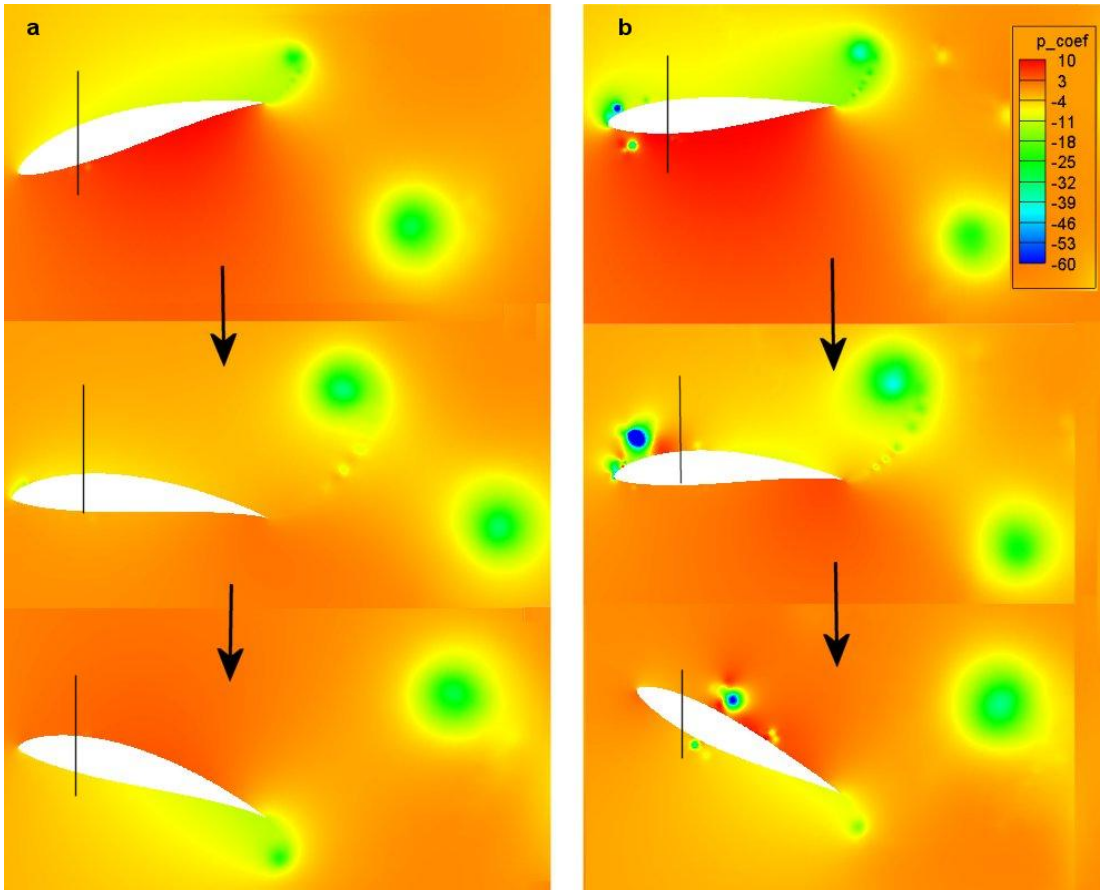

Figure 6.18: Vorticity diagrams of the un-flexed and flexed S1020 airfoil at x_{fc} = 1.0, $\bar{a}_f$ = -0.3 for the ML single sided case

6.6 Comparison of Effect of Flexure between Different Flapping Configurations

The effect of flexing is simulated on the airfoils under different flapping parameters. These include the pure heaving, ME, ME (20^0), MT and ML configurations. Under the same flexing condition, the effect of flexing on η, $\bar{C}_t$ and $\bar{C}_l$ can be very different when different flapping parameters are used. For example at x_{fc} = 0.0, η increases to a maximum of 0.33 as $\bar{a}_f$ increases for the NACA0012 airfoil heaving case (Figure 6.1). However, for the ME configuration, η drops rapidly and produces drag at $\bar{a}_f$ = 0.2 (Figure 6.7b).

Similarly for $\overline{C}_t$, the effect of flexing can be beneficial or detrimental. For the NACA0012 airfoil, when flapping with the ME configuration's parameters, x_{fc} = 0.0, $\overline{a}_f$ = -0.2 produces 60% more $\overline{C}_t$ compared to the un-flexed case (0.50 to 0.81) (Figure 6.7b). The flexing causes more vortices to be shed into the wake and increase the $\overline{C}_t$. On the other hand, with the MT configuration, the same flexing parameters cause the $\overline{C}_t$ to drop by 27% (2.50 to 1.83) (Figure 6.10b). The same observation is also true for the $\overline{C}_l$.

However, for the single-sided simulations, the trend is the same for all the flapping configurations except the ML configuration. The η and $\overline{C}_t$ decrease as the flexing increases. Depending on the direction of flexing, the $\overline{C}_l$ will increase or decrease. In the ML configuration, η and $\overline{C}_t$ do increase in some cases as the flexing increases (see Figure 6.17a and b). Of all the flapping configurations, the effect of flexure seems to benefit the MT configuration much better.

6.7 Comparison of Effect of Flexure between Different Airfoils under Similar Flapping Configurations

In the earlier DOE research, it was found that different airfoils produced similar $\overline{C}_t$ under the same flapping configurations. On the other hand, the $\overline{C}_l$ produced relied more on the shape of the airfoil. *H* is influenced both by the flapping configuration and the shape of the airfoil. As the flexing amplitude increases, certain flapping configurations show a marked difference in $\overline{C}_t$ and η while some others do not. For example, the $\overline{C}_t$ produced by the un-flexed ME configuration is very similar for the different airfoils (Figure 6.7b). However, at x_{fc} = 0.0, $\overline{a}_f$ =

-0.5, the $\overline{C}_t$ produced by the NACA0012 and S1020 airfoils are 0.89 and 0.58 respectively. The difference in η between the airfoils is also larger now.

On the other hand, under the ML configuration, the η and $\overline{C}_t$ are similar for the un-flexed NACA6302 and S1020 airfoils. At x_{fc} = 0.0, $\overline{a}_f$ = 0.2, both the η of the NACA6302 and S1020 airfoils have dropped to half their original values (0.11 and 0.10) and $\overline{C}_t$ has increased to similar values (2.53 and 2.36) (Figure 6.16a and b).

For $\overline{C}_l$, different airfoils give different results. The NACA0012 airfoil generates the least $\overline{C}_l$ due to its symmetrical nature. On comparison, the S1020 airfoil performs better than the NACA6302 airfoil, especially with regards to the single-sided simulations.

6.8 Chapter Summary

The simulation results show that flexing is not necessarily beneficial for the airfoils. The performance of the airfoil depends on the type of flapping configurations. For η and $\overline{C}_t$, as the flexing increases ($\overline{a}_f$ increases or decreases), these 2 factors either follow a parabolic or strictly decreasing trend (if flexing is detrimental to η / $\overline{C}_t$). Only 3 cases (S1020 airfoil, ME(x_{fc} = 0.0), ME(20^0, x_{fc} = 1.0) and NACA0012 airfoil, pure heaving(x_{fc} = 0.0)) are exceptions. On the other hand, $\overline{C}_l$ does not follow similar trend among the different flapping configurations.

In certain cases, such as the pure heaving case, η is as high as 0.66 and 0.76 for the NACA0012 and S1020 airfoils respectively. These improvements are much higher than Miao and Ho's (2006) flexible NACA0014 airfoil which is also undergoing pure heaving motion.

The main differences lie in the choice of the flexing center location and the flexing direction. The high η produced by the pure heaving case is very attractive because it is much easier to design an ornithopter which flaps in one dimension (pure heaving), compared to one which heaves, pitches and rows (movement of airfoil in forward/backward direction). In the past, it is not possible to obtain high η in a pure heaving case when the airfoil is rigid. Moreover, the simplification in the flapping mechanism design will also produce a much lighter ornithopter.

$\overline{C}_t$ increases for some of the flapping configurations when flexing occurs. The most significant increase occurs at x_{fc} = 0.0, $\overline{a}_f$ = 0.3 for the ML (maximum lift) configuration of the S1020 airfoil where the $\overline{C}_t$ increases from 1.63 to 3.57 (Figure 6.16b).

The performance of lift generation is discussed only briefly in Miao and Ho's paper because a symmetrical NACA0014 airfoil undergoing pure heaving motion is simulated. This resulted in an averaged lift coefficient of zero. The performance of lift generation differs for different flapping configurations under standard flexing in the current study. It can be either beneficial or detrimental. However, under single-sided flexing, $\overline{C}_l$ generally increases as the amplitude increases for x_{fc} = 0.0, 0.5 and decreases for x_{fc} = 1.0. Average lift coefficient is as high as 4.61 for the S1020 airfoil (x_{fc} = 1.0, $\overline{a}_f$ = -0.3).

Flexing does not guarantee improved η, $\overline{C}_t$ and $\overline{C}_l$, such as in the ME (maximum efficiency) case. Interestingly, results show that when the airfoil is already performing at the maximum η, $\overline{C}_t$ and $\overline{C}_l$ (as in the ME, MT and ML cases), flexing will at most introduce a small amount of benefit to the respective variable. For example, for the MT case, $\overline{C}_t$ only improves by a very small amount after flexing. On the other hand, in some cases where the flapping configuration is not optimal, such as the ME (20^0) case, flexing is able to improve the performance of the

airfoil more substantially.

In some cases, the shape of the airfoil also influences the effect of flexing, resulting in a difference in the results between two different airfoils flexing with the same amplitude under the same flapping configuration. In general, the S1020 airfoil gives better $\overline{C}_l$ than the NACA6302 airfoil.

By carefully controlling the flexing amplitude and selecting a suitable type of flexing (single or double sided) for an airfoil, the η, $\overline{C}_t$ or $\overline{C}_l$ can be improved compared to their rigid counterparts. For example, if η is the most important criteria, the S1020 airfoil flapping at pure heaving motion with x_{fc} = 1.0 and $\overline{a}_f$ = -0.5 is selected. On the other hand, if $\overline{C}_l$ is the most important criteria, the S1020 airfoil flapping at MT single-sided motion with x_{fc} = 1.0 and $\overline{a}_f$ = -0.3 is selected instead. This information can aid in the design of a better ornithopter's wing and hence improve the endurance and payload capability of an ornithopter.

7 Results and Discussion for Tandem Airfoils

The IBCNSS is used for the simulation of the tandem airfoils. The 2 airfoils move independently and hence the SCNSS is not able to carry out the simulations. The results and discussions are divided into 3 parts, according to the type of flapping configurations used. The objective is to see if the performance of the airfoil can be improved with the help of using a tandem arrangement.

7.1 Tandem ME Configuration

7.1.1 $\phi_{12} = -90^o$, $1.25 \leq d_{12} \leq 2.50$

Table 7.1 shows the performance of the ME configuration in single and tandem airfoil arrangements. For the tandem arrangement, d_{12} varies from 1.25 to 2.50 while ϕ_{12} is fixed at -90^o. The I_p of the single airfoil is only 1.38 while that of the tandem arrangement with d_{12} = 2.0 is 2.55, nearly twice the original value. The vorticity diagrams[****] of the single and tandem airfoils at d_{12} = 2.0 are shown in Figure 7.1 and Figure 7.2 respectively. The η, $\overline{C}_t$ and $\overline{C}_l$ of the fore airfoil (or η_{fore}, $\overline{C}_{t,\,fore}$ and $\overline{C}_{l,\,fore}$) in tandem arrangement is almost the same as that of the single airfoil.

[****] The contour vorticity for all the ME configuration at *Re* = 1,000 is ±10 instead of ±40 in other vorticity diagrams

Table 7.1: Performance of the ME configuration in single and tandem airfoil arrangements, ϕ_{12} = -90°, 1.25 ≤ d_{12} ≤ 2.50

$d_{12}/^o$	η_{fore}	$\bar{C}_{t,\,fore}$	$\bar{C}_{l,\,fore}$	η_{aft}	$\bar{C}_{t,aft}$	$\bar{C}_{l,aft}$	η_o	$\bar{C}_{t,o}$	$\bar{C}_{l,o}$	I_p
Single	0.33	0.23	0.03	0.33	0.23	0.03	0.33	0.23	0.03	1.38
2.5	0.32	0.22	-0.01	**0.38**	**0.39**	0.10	**0.36**	**0.61**	0.09	2.27
2.25	0.34	**0.25**	**0.07**	0.36	0.30	0.10	0.35	0.55	0.17	2.37
2.00	**0.35**††††	**0.25**	0.06	0.31	0.17	0.27	0.33	0.42	0.32	**2.55**
1.75	**0.35**	0.24	0.03	0.16	0.05	**0.32**	0.29	0.29	**0.34**	2.29
1.50	0.33	0.21	-0.04	0.00	-0.07	0.13	0.19	0.15	0.09	1.02
1.25	0.31	0.20	0.01	0.00	-0.11	0.06	0.12	0.08	0.07	0.67

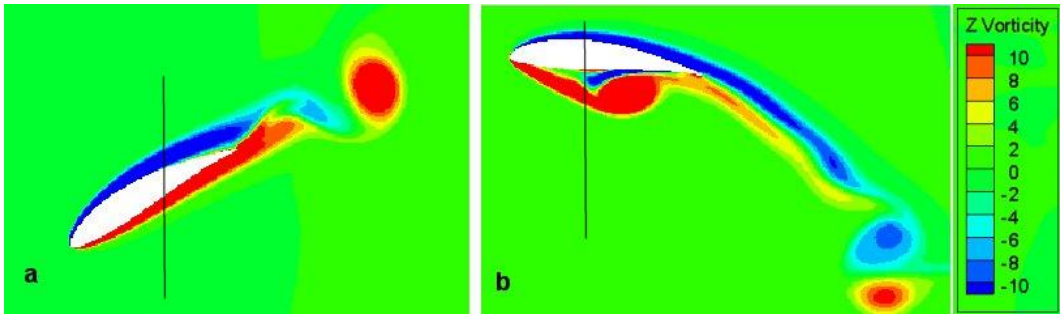

Figure 7.1: Vorticity diagrams‡‡‡‡ of the ME single airfoil arrangement during heaving (a) down and (b) up positions

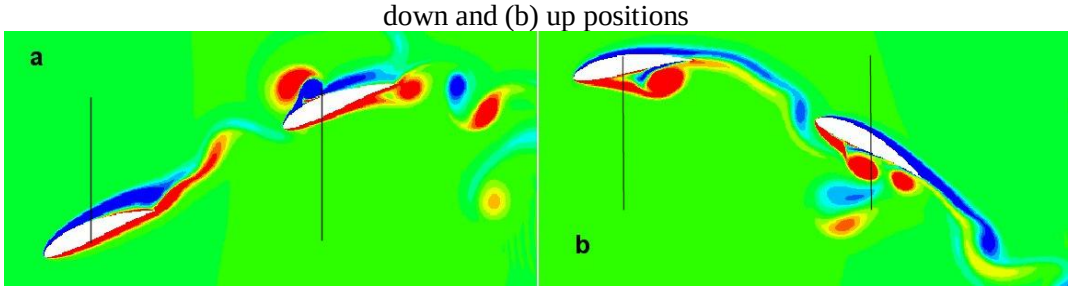

Figure 7.2: Vorticity diagrams of the ME tandem airfoils arrangement at different instant at d_{12} = 2.0, ϕ_{12} = -90°

†††† The values in bold indicate that it is the maximum value of that particular column.

‡‡‡‡ For all the ME configurations in subsequent vorticity diagrams, the vorticity contours will range between ±10

However, comparing between the single and aft airfoil, the η_{aft} and $\overline{C}_{t,aft}$ of the aft airfoil are slightly smaller, but its $\overline{C}_{l,aft}$ is much larger. In a single airfoil configuration, as seen in Figure 7.1, vortices are shed only at the trailing edge. During the heaving down motion, one large vortex of positive (counter-clockwise) vorticity is shed. On the other hand, a pair of smaller vortices is shed at the heaving up motion. For the tandem arrangement with d_{12} = 2.0, ϕ_{12} = -90^o, the fore airfoil displays similar characteristic as the single airfoil. However, the counter-clockwise vortex shed from the fore airfoil interacts with the top of the aft airfoil. This causes a clockwise vortex on the aft airfoil to shed. This occurs much earlier compared to a single airfoil arrangement. On the other hand, the smaller pair of vortices from the fore airfoil, shed during the heaving up cycle, does not interact with the aft airfoil.

As mentioned earlier, the main difference between the single and the tandem airfoils arrangements is the large increase in $\overline{C}_{l,aft}$ for the aft airfoil. Figure 7.3 shows the corresponding pressure coefficient plot in the single and tandem configuration. Comparing between the two plots, the tandem one shows that the pressure coefficient on the top leading edge of the aft airfoil is very low, indicating a low pressure region. The presence of the low pressure region is due to the interaction between the fore airfoil's vortex and aft airfoil. Moreover, the pressure at the bottom leading edge of the aft airfoil is also higher. This is the reason for the high $\overline{C}_{l,aft}$. And it enables d_{12} = 2.0 to achieve the highest I_p among different values of d_{12} tested. The low pressure region shown at the bottom trailing edge of the single airfoil corresponds to the shedding of the counter-clockwise vortex. The low pressure region at the bottom trailing edge is also present in the aft airfoil of the tandem arrangement but it is shed slightly earlier. Hence, the low pressure region is not seen in the pressure coefficient plot.

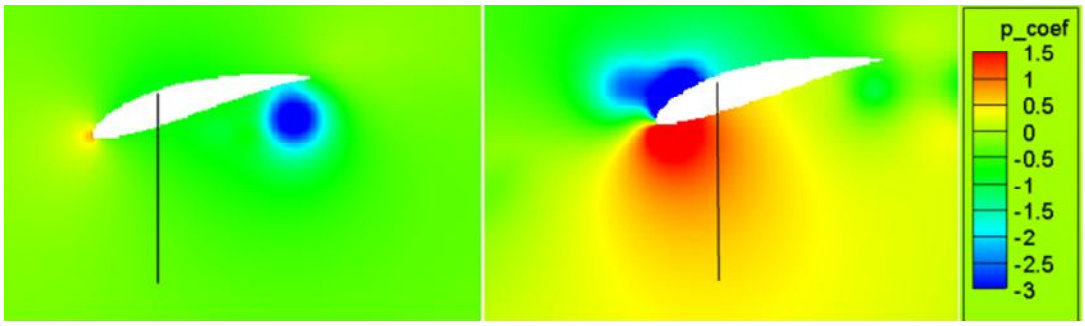

Figure 7.3: Pressure coefficient plot for the ME configuration of the (a) single and (b) tandem aft airfoils at d_{12} = 2.0, ϕ_{12} = -90^o

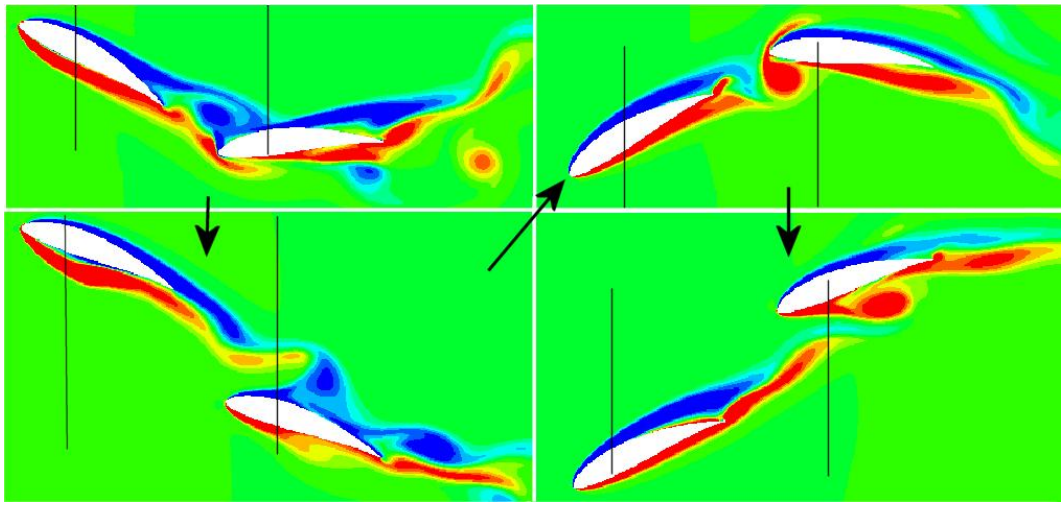

Figure 7.4: Vorticity diagrams of the ME tandem airfoils arrangement at different instant at d_{12} = 1.25, ϕ_{12} = -90^o

When d_{12} = 1.25, both airfoils are very close together, as shown in Figure 7.4. The vortex shed from the fore airfoil directly impinges on the leading edge of the aft airfoil. In the heaving down cycle, the large counter-clockwise vortex from the fore airfoil interacts with the bottom leading edge of the aft airfoil and is then shed away. Similarly, during the heaving up cycle, the pair of vortices form the fore airfoil interacts with the aft airfoil, resulting in the formation of a large clockwise vortex on top of the aft airfoil. This clockwise vortex sheds into the wake. Figure 7.5 shows the C_d and C_l versus time plots. The amplitudes of the C_t and C_l of the aft airfoil have decreased by a large margin and drag is also produced instead. This is due to interaction with the fore airfoil's vortices, which prevents the aft airfoil having a strong clockwise vortex and counter-clockwise vortex at the top and mid heaving positions respectively. Hence in this case, the interaction of the vortices is actually detrimental to the

performance of the tandem airfoils.

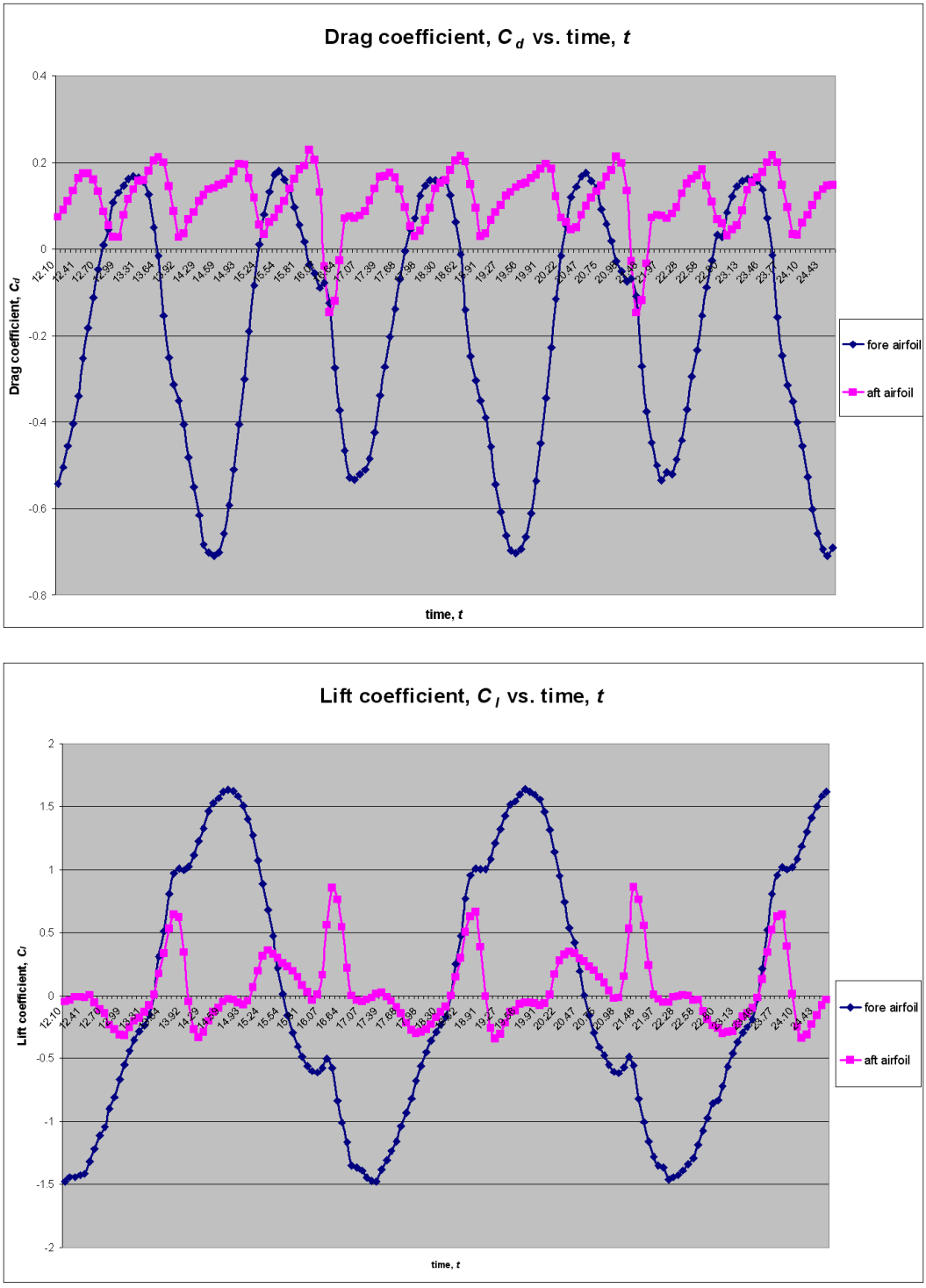

Figure 7.5: (a) Drag coefficient and (b) lift coefficient versus time plots of the ME tandem airfoils arrangement at different instant at d_{12} = 1.25, ϕ_{12} = -90°

7.1.2 d_{12} = 2.0, -180° ≤ ϕ_{12} ≤ 150°

Table 7.2: Performance of the ME configuration in single and tandem airfoil arrangements, d_{12} = 2.0, -180° ≤ ϕ_{12} ≤ 150°

ϕ_{12}/°	η_{fore}	$\overline{C}_{t,\,fore}$	$\overline{C}_{l,\,fore}$	η_{aft}	$\overline{C}_{t,aft}$	$\overline{C}_{l,aft}$	η_o	$\overline{C}_{t,o}$	$\overline{C}_{l,o}$	I_p
150	0.35	0.25	0.05	0.11	0.04	0.05	0.26	0.30	0.11	1.20
120	0.35	0.27	0.00	0.30	0.17	0.13	0.33	0.43	0.13	1.56
90	0.34	0.26	0.03	0.35	0.28	0.05	0.35	0.54	0.07	1.60
60	0.34	0.26	0.02	0.41	0.44	0.01	0.38	0.70	0.03	1.77
30	0.36	0.29	0.01	**0.45**	**0.61**	-0.14	**0.41**	**0.90**	-0.13	1.70
0	**0.37**	**0.30**	0.11	0.43	0.59	0.22	**0.41**	0.89	0.33	2.70
-30	0.36	0.27	**0.15**	0.39	0.46	**0.31**	0.38	0.73	**0.45**	**2.72**
-60	0.35	0.25	0.07	0.39	0.39	0.20	0.37	0.65	0.27	2.22
-90	0.35	0.25	0.06	0.31	0.17	0.27	0.33	0.42	0.32	1.98
-120	0.33	0.22	0.00	0.00	-0.02	0.12	0.23	0.20	0.21	1.25
-150	0.33	0.22	-0.01	0.00	-0.13	0.21	0.13	0.10	0.11	0.65
-180	0.34	0.25	0.04	0.00	-0.09	0.08	0.18	0.16	0.12	0.87

Table 7.2 shows the performance of the ME configuration in tandem airfoil arrangements with d_{12} = 2.0, -180° ≤ ϕ_{12} ≤ 150°. ϕ_{12} = -30° when the highest I_p is achieved. Compared to the single airfoil arrangement, the η_o, $\overline{C}_{t,o}$ and $\overline{C}_{l,o}$ have all increased. Unlike the previous case, there is little interaction between the fore airfoil's vortices and the aft airfoil. However, the favourable timing of the vortex shedding of the fore and aft airfoils results in the formation of the reverse von Kármán vortex street (as shown in Figure 7.6), which increases the $\overline{C}_{t,o}$ and η_o as well. The low pressure region, similar to the one seen in Figure 7.3b for the d_{12} = 2.0, ϕ_{12} = 90° case, is also observed in the pressure coefficient plot for this case in Figure 7.7.

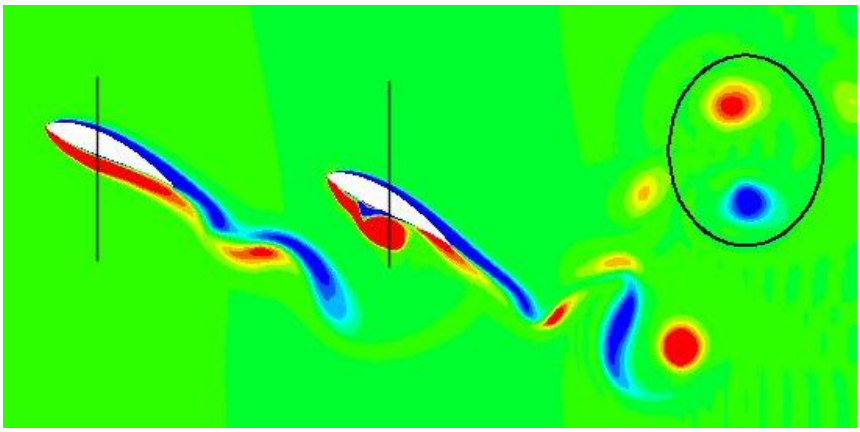

Figure 7.6: Vorticity diagrams of the ME tandem airfoils arrangement at d_{12} = 2.0, ϕ_{12} = -30^o

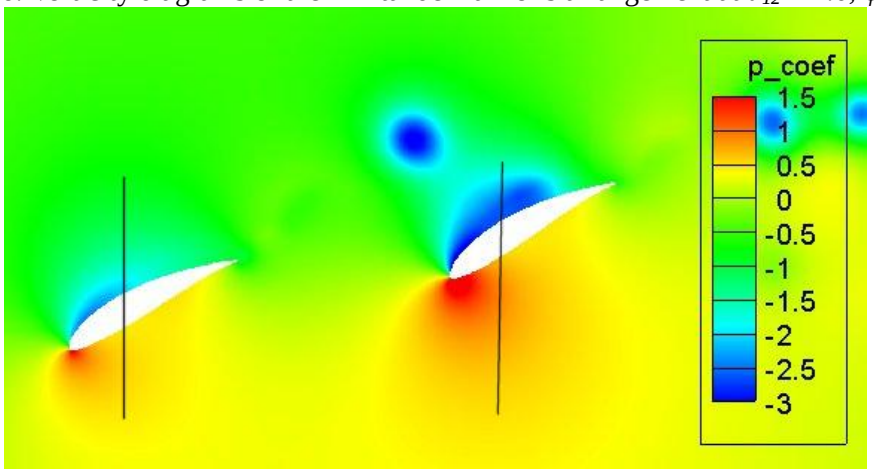

Figure 7.7: Pressure coefficient plot of the ME tandem airfoils arrangement at d_{12} = 2.0, ϕ_{12} = -30^o

7.2 Tandem MT Configuration

7.2.1 ϕ_{12} = -90°, 1.25 ≤ d_{12} ≤ 2.50

Table 7.3: Performance of the MT configuration in single and tandem airfoil arrangements, ϕ_{12} = -90°, 1.25 ≤ d_{12} ≤ 2.25

$d_{12}/^o$	η_{fore}	$\bar{C}_{t,\,fore}$	$\bar{C}_{l,\,fore}$	η_{aft}	$\bar{C}_{t,aft}$	$\bar{C}_{l,aft}$	η_o	$\bar{C}_{t,o}$	$\bar{C}_{l,o}$	I_p
Single	**0.23**	**2.05**	**2.22**	**0.23**	2.05	**2.22**	**0.23**	2.05	2.22	2.29
2.50	0.21	1.73	1.44	0.15	1.45	-0.56	0.18	3.18	0.88	1.78
2.25	0.21	1.71	1.21	0.16	2.22	0.45	0.18	3.93	1.66	2.25
2.00	0.21	1.65	1.30	0.19	**3.07**	1.00	0.20	4.72	2.30	2.73
1.75	0.21	1.79	1.37	0.19	2.94	1.21	0.20	4.73	**2.57**	**2.84**
1.50	0.22	1.90	1.40	0.21	2.94	0.71	0.21	**4.84**	2.11	2.76
1.25	**0.23**	1.93	0.83	0.20	1.81	0.73	0.21	3.74	1.56	2.33

Table 7.3 shows the performance of the MT configuration in single and tandem airfoil arrangements. For the tandem arrangement, d_{12} varies from 1.25 to 2.25 while ϕ_{12} is fixed at -90°. In the single airfoil arrangement, the MT configuration is able to achieve a high $\bar{C}_t$ and $\bar{C}_l$ of 2.05 and 2.22 and η of 0.23.

In the tandem airfoil arrangement, the $\bar{C}_{t,aft}$ for the aft airfoil increases to approximately 3 for 1.5 ≤ d_{12} ≤ 2.0. However, for the fore airfoil, there is a slight drop in the $\bar{C}_{t,\,fore}$. Nevertheless, the value of $\bar{C}_{t,o}$ for the tandem airfoils reaches 4.84, which is more than twice the $\bar{C}_t$ for the single airfoil. The I_p for the d_{12} = 1.75 case is the highest of all the d_{12}. The $\bar{C}_{l,o}$ of the tandem airfoils is also slightly higher than the $\bar{C}_l$ of the single airfoil case. Its vorticity diagram is shown in Figure 7.8. The reverse von Kármán vortex street producing thrust can be seen

clearly. However, the $\overline{C}_{l,o}$ only reaches 2.57, slightly higher than the single airfoil $\overline{C}_l$ of 2.22. This is because the fore and aft airfoils' individual $\overline{C}_l$ has dropped to 1.37 and 1.21 respectively.

The pressure coefficient plots of the single and tandem airfoil arrangement are shown in Figure 7.9. At the bottom of the heaving cycle, there is a region of very low pressure on the top leading edge of the single airfoil. When the airfoil reaches the top of the heaving cycle, the reverse happens but the pressure at the bottom of the airfoil is not as low at the previous case. This results in a high $\overline{C}_l$. However, for the fore airfoil, the low pressure region occurring at the top part of the airfoils during the bottom heaving cycle is similar in magnitude to the low pressure region occurring at the bottom part of the airfoil during the top heaving cycle. Hence, the $\overline{C}_{l,\,fore}$ is smaller. The same thing occurs for the aft airfoil, except that now, the low pressure region occurs approximately during the mid heaving cycle. This simulation also shows that in some cases, the presence of the aft airfoil can affect the fore airfoil as well.

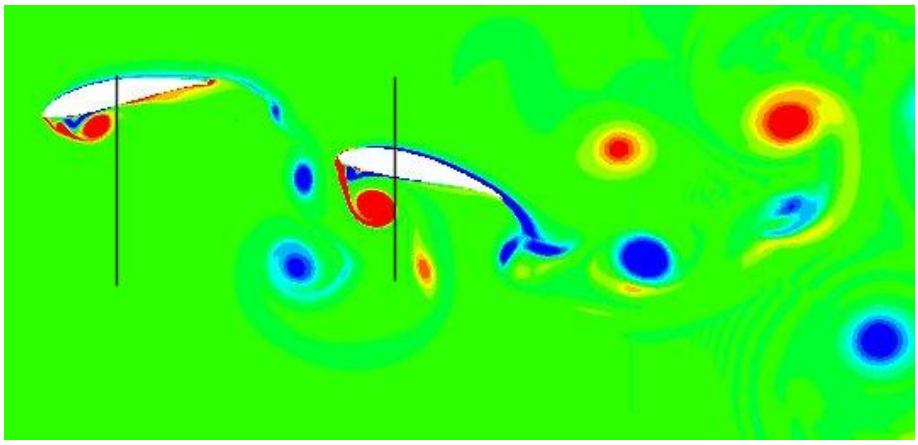

Figure 7.8: Vorticity diagram of the MT tandem airfoils arrangement at d_{12} = 1.75, ϕ_{12} = -90^o

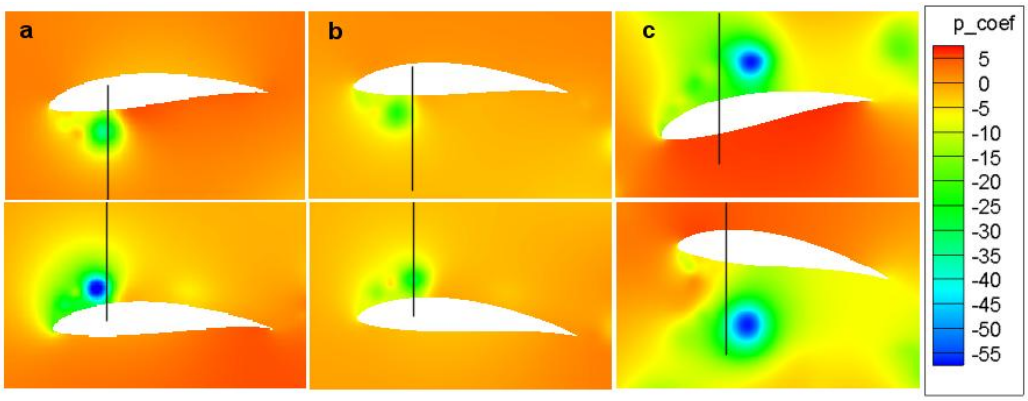

Figure 7.9: Pressure coefficient plots of the MT configuration with (a) single (b) fore (c) aft airfoil at d_{12} = 1.75, ϕ_{12} = -90°

7.2.2 d_{12} = 1.75, -180° ≤ ϕ_{12} ≤ 150°

Table 7.4: Performance of the MT configuration in single and tandem airfoil arrangements, d_{12} = 1.75, -180° ≤ ϕ_{12} ≤ 150°

ϕ_{12}/°	η_{fore}	$\bar{C}_{t,\,fore}$	$\bar{C}_{l,\,fore}$	η_{aft}	$\bar{C}_{t,aft}$	$\bar{C}_{l,aft}$	η_o	$\bar{C}_{t,o}$	$\bar{C}_{l,o}$	I_p
150	**0.23**	1.93	**2.34**	0.14	0.48	0.76	**0.21**	2.42	**3.10**	2.47
120	0.22	1.87	1.53	0.00	0.00	0.65	0.19	1.87	2.18	1.97
90	0.22	**2.05**	1.31	0.00	-0.18	0.36	0.18	1.87	1.67	1.78
60	0.21	1.96	0.37	0.02	0.05	-0.87	0.16	2.01	-0.49	1.03
30	0.20	1.97	0.44	0.14	0.99	-0.24	0.18	2.96	0.20	1.51
0	0.20	1.98	0.44	0.15	1.83	-0.14	0.17	3.81	0.30	1.72
-30	0.20	1.91	0.93	0.17	2.66	0.65	0.18	4.57	1.59	2.44
-60	0.20	1.80	0.83	0.18	**2.96**	0.45	0.19	**4.75**	1.28	2.38
-90	0.21	1.79	1.37	0.19	2.94	1.21	0.20	4.73	2.57	**2.91**
-120	0.22	1.72	1.35	**0.21**	2.90	0.87	**0.21**	4.62	2.22	2.82
-150	0.22	1.70	0.98	**0.21**	2.20	0.96	**0.21**	3.90	1.94	2.58
-180	0.22	1.77	1.25	0.20	1.30	**1.28**	**0.21**	3.06	2.53	2.62

Table 7.4 shows the performance of the MT configuration in tandem airfoil arrangements with d_{12} = 1.75 and -180° ≤ ϕ_{12} ≤ 150°. The ϕ_{12} = -90° case still gives the highest I_p. Nevertheless,

the $\overline{C}_t$ for different ϕ_{12} are still high. The $\overline{C}_{l,o}$ drops more drastically as ϕ_{12} deviates from -90°. When ϕ_{12} = 0°, $\overline{C}_{l,o}$ drops to only 0.30. $\overline{C}_l$ for the fore airfoil is only 0.44 while that of the aft airfoil is -0.14.

Figure 7.10 shows that the vortex from the fore airfoil interacts with the newly shed vortex of the aft airfoil. As shown in Figure 7.11b, the interaction causes the pressure on the bottom of the aft airfoil to be much lower than the top, resulting in negative $\overline{C}_l$. By comparing with the single airfoil arrangement on Figure 7.11a, the fore airfoil is also affected in the same way, although by a lesser degree. Hence, the $\overline{C}_l$ of the fore airfoil also drops, although positive $\overline{C}_l$ is still produced.

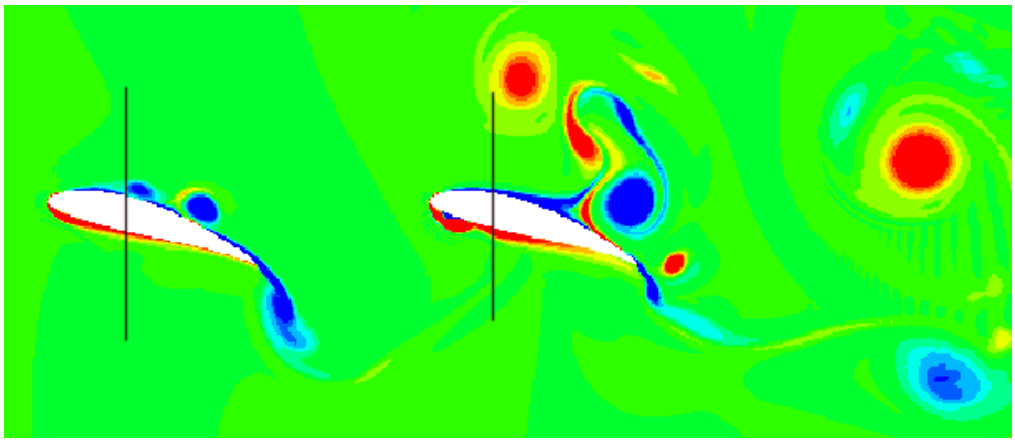

Figure 7.10: Vorticity diagram of the MT tandem airfoils arrangement at d_{12} = 1.75, ϕ_{12} = 0°

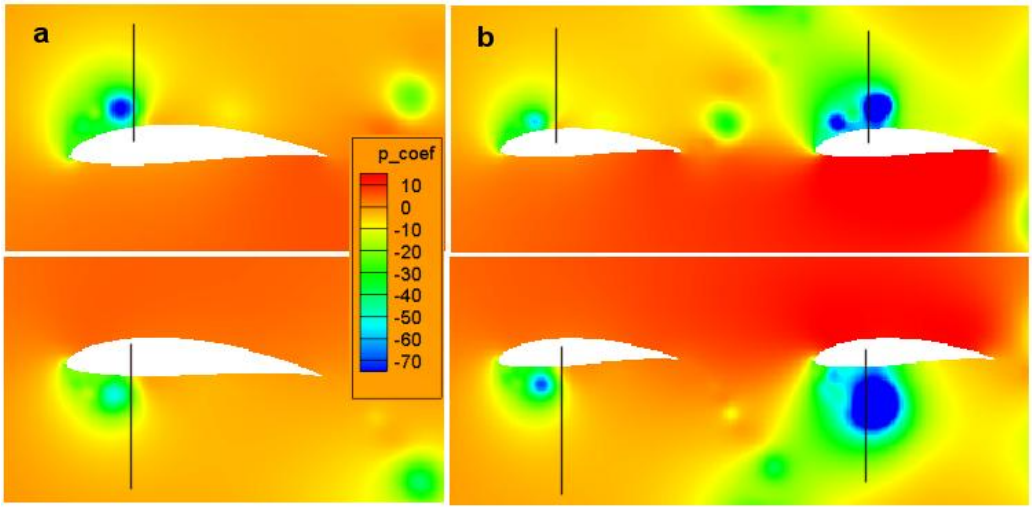

Figure 7.11: Pressure coefficient plots of the MT configuration with (a) single (b) tandem airfoil arrangement at d_{12} = 1.75, ϕ_{12} = 0°

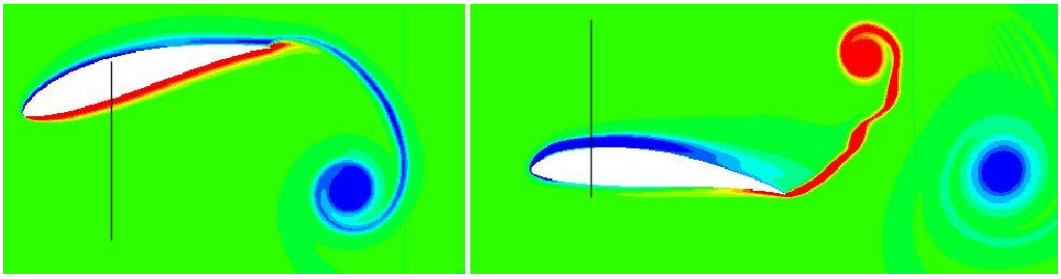

Figure 7.12: Vorticity diagram of the ML configuration in single airfoil arrangement

7.3 Tandem ML Configuration

7.3.1 ϕ_{12} = -90°, 1.25 ≤ d_{12} ≤ 2.50

Table 7.5: Performance of the ML configuration in single and tandem airfoil arrangements, ϕ_{12} = -90°, 1.25 ≤ d_{12} ≤ 2.50

ϕ_{12}/°	η_{fore}	$\bar{C}_{t,\,fore}$	$\bar{C}_{l,\,fore}$	η_{aft}	$\bar{C}_{t,aft}$	$\bar{C}_{l,aft}$	η_o	$\bar{C}_{t,o}$	$\bar{C}_{l,o}$	I_p
Single	**0.18**	1.40	**3.04**	0.18	1.40	**3.04**	**0.18**	1.40	3.04	2.25
2.5	0.14	1.14	1.26	0.20	0.84	0.41	0.16	1.97	1.68	1.95
2.25	0.16	1.15	1.77	0.07	0.17	0.78	0.14	1.32	2.55	1.84
2.00	**0.18**	1.32	2.80	0.13	0.47	0.99	0.16	1.79	**3.78**	**2.46**
1.75	0.13	0.91	1.34	**0.21**	1.40	-0.34	0.17	2.31	1.00	1.91
1.50	0.13	0.90	1.39	0.18	1.78	0.38	0.16	2.68	1.77	2.17
1.25	0.14	**2.68**	0.94	0.20	**2.06**	0.12	**0.18**	**3.17**	1.06	2.23

Table 7.5 shows the performance of the ML configuration in single and tandem airfoil arrangements. For the tandem arrangement, d_{12} varies from 1.25 to 2.50 while ϕ_{12} is fixed at -90°. In the single airfoil arrangement, the $\bar{C}_t$ and $\bar{C}_l$ are 1.40 and 3.04 respectively. The vorticity diagram of the airfoil is shown in Figure 7.12. The vortices are shed only at the trailing edge and the reverse von Kármán vortex street is seen clearly. For the tandem arrangements, the d_{12} = 2.0 case achieves the highest I_p. The η, $\bar{C}_t$ and $\bar{C}_l$ of the fore airfoil are very similar to the single airfoil arrangement. However, the aft airfoil does not perform as

well. Its η, $\overline{C}_t$, $\overline{C}_l$ are 0.13, 0.47 and 0.99 respectively. Hence, its η, $\overline{C}_t$ and $\overline{C}_l$ are lower compared to the single airfoil case.

The vorticity diagram for the tandem arrangement at d_{12} = 2.0 is shown in Figure 7.13. There is no difference in the vortex shedding between the fore and single airfoil case. The aft airfoil shed a clockwise vortex near its top leading edge. Together with counter-clockwise vortex from fore airfoil, the two vortices get "pushed" upward and away at the trailing edge. The clockwise vortex from the fore airfoil combines with the counter-clockwise vortex just shed at the bottom leading edge of the aft airfoil and the combined vortex moves downwards and away. The direction of shedding is not along the *x* direction and therefore the $\overline{C}_{t,o}$ is low.

On the other hand, in Figure 7.14, when d_{12} = 1.5, the pair of vortices on top of the aft airfoil now follows the contour of the airfoil and "slides" down the trailing edge. Similarly, the clockwise vortex from the fore airfoil forms a pair with the newly shed counter-clockwise vortex at the aft airfoil's leading edge and the pair of vortices moves into the wake. In this case, the shed vortices pairs are directed more towards the *x* direction, giving a higher $\overline{C}_{t,aft}$ for the aft airfoil. Unfortunately, the performance of its fore airfoil is much poorer. Interestingly, the vorticity diagram and pressure coefficient plots of the single and fore airfoil do not show any obvious difference.

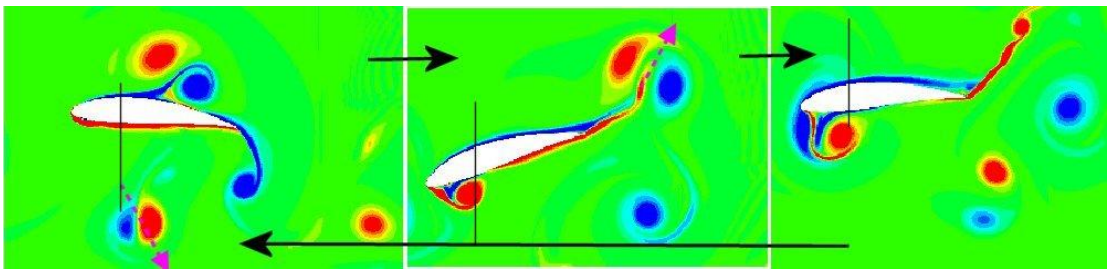

Figure 7.13: Vorticity diagram of the aft airfoil with the ML tandem configuration with d_{12} = 2.0, ϕ_{12} = -90^o, the dotted arrows refer to the direction of the vortices' movement

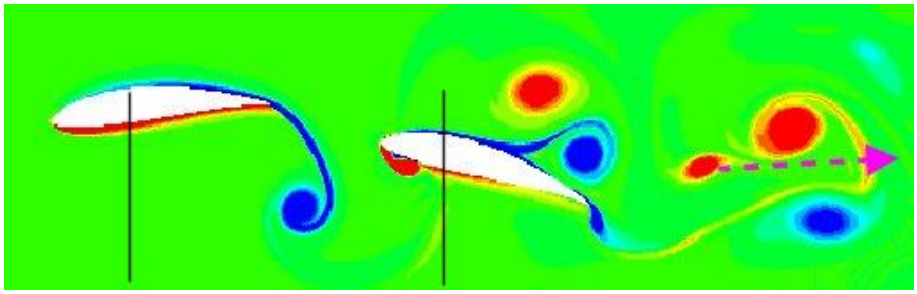

Figure 7.14: Vorticity diagram of the ML tandem configuration with d_{12} = 1.5, ϕ_{12} = -90^o

7.3.2 d_{12} = 2.0, -180^o ≤ ϕ_{12} ≤ 150^o

Table 7.6: Performance of the ML configuration in single and tandem airfoil arrangements, d_{12} = 2.0, -180^o ≤ ϕ_{12} ≤ 150^o

$\phi_{12}/^o$	η_{fore}	$\bar{C}_{t,\,fore}$	$\bar{C}_{l,\,fore}$	η_{aft}	$\bar{C}_{t,aft}$	$\bar{C}_{l,aft}$	η_o	$\bar{C}_{t,o}$	$\bar{C}_{l,o}$	I_p
150	0.17	1.13	1.28	0.17	1.79	0.82	0.17	2.91	2.11	2.39
120	**0.20**	1.32	2.56	0.16	1.79	2.03	0.18	**3.11**	**4.59**	3.04
90	0.19	1.29	2.41	0.19	**1.81**	**2.11**	**0.19**	3.10	4.52	**3.10**
60	0.18	1.32	**2.80**	0.13	0.47	0.99	0.16	1.79	3.78	2.37
30	0.16	1.25	1.63	0.14	0.68	0.80	0.15	1.93	2.44	2.06
0	0.17	**1.33**	1.91	0.11	0.39	1.10	0.15	1.73	3.00	2.15
-30	0.17	1.18	1.93	0.08	0.20	1.00	0.14	1.38	2.93	1.95
-60	0.17	1.19	1.82	0.10	0.30	1.01	0.15	1.49	2.83	2.00
-90	0.18	1.32	**2.80**	0.13	0.47	0.99	0.16	1.79	3.78	2.42
-120	0.19	1.27	2.41	0.17	1.08	1.79	0.18	2.35	4.21	2.81
-150	0.17	1.06	0.76	**0.21**	1.56	0.56	**0.19**	2.62	1.32	2.28
-180	0.17	1.18	1.57	0.17	1.55	0.50	0.17	2.73	2.07	2.39

Table 7.6 shows the performance of the ML configuration in tandem airfoil arrangements with d_{12} = 2.0 and -180^o ≤ ϕ_{12} ≤ 0^o. Results show that the ϕ_{12} = 90^o case gives the highest I_p. Its vorticity diagram on Figure 7.15 shows only slight difference compared to the ϕ_{12} = -90^o case. Due to the phase difference, its shed vortices which form the reverse von Kármán vortex street,

are directed more towards the *x* direction, resulting in a higher $\overline{C}_t$. Moreover, the $\overline{C}_l$ of the aft airfoil is also much higher than in the ϕ_{12} = -90° case.

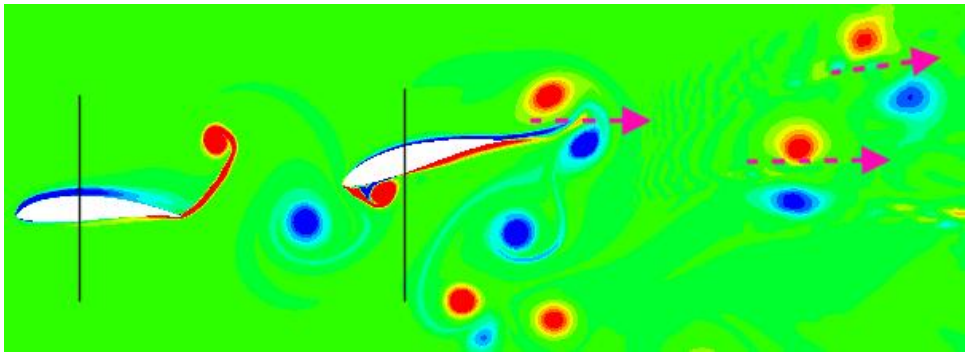

Figure 7.15: Vorticity diagram of the ML tandem configuration with d_{12} = 2.0, ϕ_{12} = -90°

7.4 Effect of d_{12} and ϕ_{12} on the Performance of the Airfoils

The results for the different flapping configurations all showed an increase in performance by varying degrees. Some researches (Alexandra 1984, 1986, Wakeling and Ellington, 1997) on dragonfly and tandem arrangements simulations (Mittal et al., 2002) had revealed that when ϕ_{12} = 0°, $\overline{C}_{t,o}$ would be at its maximum. However, there are others who have different results as well (Akhtar et al. 2007). This shows that the argument is not universal. In the present simulation, this phenomenon is not true. Different configurations (ME, MT or ML) have different ϕ_{12} for maximum $\overline{C}_{t,o}$. There are several reasons for the discrepancy. Firstly, the flapping configurations simulated here is different from the ones used by other researchers. The airfoil shape is different; it is much thicker. Lastly, the d_{12} used is also not the same.

The paper by Somps and Luttges (1985) suggested based on their experiment that forewing–hindwing interaction might enhance aerodynamic force production. On the other hand, Wang and Sun (2005) found that the interaction between the fore and aft airfoils was detrimental to lift production. The current results show that in both the MT and ML flapping configurations

tested, the interaction between the fore and aft airfoils is detrimental to lift production. All the $\overline{C}_l$ of the fore and aft airfoils of these configurations are smaller than the $\overline{C}_l$ of the single airfoil cases, regardless of the d_{12} and ϕ_{12}.

Wang and Sun (2005) mentioned that in order to produce an upward force, a downward flow must be generated. Thus, in general, a wing would move in the downwash-velocity field induced by the other wing, reducing its vertical force. However, this phenomenon is not true for the ME configuration. Under the single airfoil arrangement, the $\overline{C}_l$ generated is very small. When the tandem arrangement is used, the aft airfoil's $\overline{C}_l$ becomes much larger while the fore airfoil's $\overline{C}_l$ remains almost the same. As mentioned earlier, the reasons for the discrepancy may be due to the different flapping configurations or airfoils.

7.5 Chapter Summary

This chapter investigates the effect of tandem airfoil arrangements. Results show that under optimum conditions (optimum d_{12} and ϕ_{12}), the η, $\overline{C}_t$ and $\overline{C}_l$ of the tandem arrangements will improve, compared to the single airfoil configuration.

For the ME configuration, at the optimum value of d_{12} = 2.0 and ϕ_{12} = -30^0, the $\overline{C}_t$ and $\overline{C}_l$ has become much larger, from its small initial values (from $\overline{C}_{t,o}$ = 0.23 to 0.73, $\overline{C}_{l,o}$ = 0.03 to 0.45). However, the η_o has increased by only 15% (from η_o = 0.33 to 0.38). Higher η_o is possible at ϕ_{12} = 0^0 (η_o = 0.41) but lift is then slightly less. For the MT configuration, the optimal d_{12} and ϕ_{12} is 1.75 and -90^0 respectively. The $\overline{C}_{t,o}$ has increased by more than twice the value (from $\overline{C}_{t,o}$ = 2.05 to 4.73). Lift also increases slightly ($\overline{C}_{l,o}$ = 2.22 to 2.57). Interestingly, the η_o remains similar. Lastly, d_{12} = 2.0 and ϕ_{12} = -120^0 gives the highest I_p for the ML configuration.

Both the $\overline{C}_{t,o}$ and $\overline{C}_{l,o}$ increase (from $\overline{C}_{t,o}$ = 1.40 to 3.10, $\overline{C}_{l,o}$ = 3.04 to 4.52). Similarly, as in the MT configuration, the level of η_o does not fluctuate greatly.

The addition of an extra pair of wings will no doubt increase the complexity of the design of an ornithopter. This will led to an increase in the overall weight of the ornithopter. However, depending on the ingenuity of the design, the weight increase may not be substantial. With the proper selection of d_{12} and ϕ_{12} , the increase in the $\overline{C}_{t,o}$ and $\overline{C}_{l,o}$ can be 1.5 to more than twice as much. Hence, these improvements justify the design of a tandem ornithopter which can outperform one with a single pair of wing.

8 Applying Simulation Results to Actual Ornithopters

The results obtained in the simulations have been very encouraging. It shows that high η, $\overline{C}_t$ and $\overline{C}_l$ can be obtained under the right flapping configuration. Depending on the actual requirement of each mission objective, different configuration is selected.

If high η is desired, the best configuration of the ornithopter will be a flexible s1020 wing with x_{fc} = 1.0 and $\overline{a}_f$ = -0.5 and undergoing simple heaving. The ornithopter can attain an η as high as 0.76 and carry out mission which requires long endurance. Power usage will be at a minimal. When the ornithopter needs to move faster, its thrust output must be high. In this case, the flexible S1020 wing with x_{fc} = 0.0, $\overline{a}_f$ = 0.3 and undergoing the ML flapping configuration is the most suitable option since it can generate a $\overline{C}_t$ of 3.57. On the other hand, an ornithopter with a heavy payload will require a large $\overline{C}_l$ to stay aloft. This will need the use of single-sided flexing S1020 airfoil with x_{fc} = 1.0, $\overline{a}_f$ = -0.3. The wing will flap with the MT flapping configuration to achieve a high $\overline{C}_l$ of 4.61

If higher $\overline{C}_t$ is required, a tandem wing configuration can be used. Flapping with a MT configuration, with d_{12} = 1.5 and ϕ_{12} = -90^0, the S1020 wing is able to obtain an impressive $\overline{C}_t$ of 4.84. However, as mentioned earlier, the addition of an extra pair of wings will no doubt increase the complexity of the design and lead to an increase in the overall weight of the ornithopters.

9 Conclusion

Investigations have been conducted to determine the relationships between the different flapping variables, the effect of flexing and the tandem airfoil configuration on the performances of η, $\overline{C}_t$ and $\overline{C}_l$ of the different airfoils.

The BB test simulation results show that besides the flapping configuration, airfoil shape also has a profound effect on the η, $\overline{C}_t$ and $\overline{C}_l$. The four factors (*k*, *St*, θ_0 and ϕ) have different levels of significance on the performance of different airfoils, indicating the shape of the airfoil also affect the performance. These four factors affect the $\overline{C}_t$ to a greater extent compared to the effect of the shape of the airfoil. On the other hand, $\overline{C}_l$ is primarily determined by its airfoil shape. Efficiency is affected by the said variables and also the shape of the airfoil. Two-factor interactions exist in all three responses. Hence in some cases, different factors must be analyzed simultaneously. Based on the simulations tested, the NACA0012 airfoil has proven to be the best airfoil for η (η = 0.61) and $\overline{C}_t$ ($\overline{C}_t$ = 2.53). The birdy airfoil produces the greatest $\overline{C}_l$ ($\overline{C}_l$ = 2.23).

Unfortunately, these optimal configurations do not coincide. Hence there must be a compromise during the design of the ornithopter's wing. Overall, the S1020 airfoil is the best airfoil for most applications. It is able to provide relatively good η and at the same time generate high $\overline{C}_t$ and $\overline{C}_l$. Although the birdy airfoil provides good $\overline{C}_t$ and $\overline{C}_l$, it does not yield good efficiency.

The next phase of simulations involves the study of the effect of active chordwise flexing on the flapping airfoil's performance. The simulation results show that flexing may or may not be

beneficial for the airfoils. It depends on the type of flapping configurations. In certain cases, such as the pure heaving case, η can reach as high as 0.66 and 0.76 for the NACA0012 and S1020 airfoils respectively. These results are significant because previously, it is not possible to obtain such high efficiencies using only pure heaving motion for rigid airfoils; pitching must be added and it adds to the complexity to the design of an ornithopter.

$\overline{C}_t$ increases for some of the flapping configurations when flexing occurs. The most significant increase occurs at x_{fc} = 0.0 for the ML configuration of the S1020 airfoil where the $\overline{C}_t$ increases from 1.63 to 3.57. The performance of $\overline{C}_l$ varies differently for different flapping configurations under standard flexing. However, under single sided flexing, as the amplitude increases for x_{fc} = 0.0, 0.5, $\overline{C}_t$ increases and when x_{fc} = 1.0, $\overline{C}_l$ decreases. $\overline{C}_l$ can reach as high as 4.61 for the S1020 airfoil. Flexing does not guarantee improved η, $\overline{C}_t$ or $\overline{C}_l$, such as in the ME case. On the other hand, in some cases whereby the flapping configuration is not optimal, such as the ME (20^o) case, flexing is able to improve the performance of the airfoil.

In some cases, the shape of the airfoil influences the flexing, resulting in a different results between two different airfoils flexing with the same amplitude under the same flapping configuration. Similar to the previous DOE results, the S1020 airfoil gives better performance than the NACA6302 airfoil in general.

The last phase of the research investigates the effect of tandem airfoil arrangements. Results show that under optimum conditions (optimum d_{12} and ϕ_{12}), the η_o, $\overline{C}_{t,o}$ and $\overline{C}_{l,o}$ can improve. The improvement in $\overline{C}_{t,o}$ and $\overline{C}_{l,o}$ can be dramatic and the $\overline{C}_{t,o}$ and $\overline{C}_{l,o}$ of tandem arrangements may be double the value compared to the single airfoil configuration.

For the ME configuration, the $\overline{C}_{t,o}$ and $\overline{C}_{l,o}$ managed to increase from its small initial values to higher values (from $\overline{C}_{t,o}$ = 0.23 to 0.73, $\overline{C}_{l,o}$ = 0.03 to 0.45) at an optimum value of d_{12} = 2.0 and ϕ_{12} = -30°. However, the η_o has increased by only 15%. Higher η_o is possible at ϕ_{12} = 0° but $\overline{C}_{l,o}$ is then slightly less.

For the MT configuration, the optimal d_{12} and ϕ_{12} is 1.75 and -90° respectively. Despite having similar η_o, the $\overline{C}_{t,o}$ has increased by more than twice the value (from $\overline{C}_{t,o}$ = 2.05 to 4.73). $\overline{C}_{l,o}$ also increases slightly ($\overline{C}_{l,o}$ = 2.22 to 2.57). Lastly, d_{12} = 2.0 and ϕ_{12} = -120° gives the highest I_p for the ML configuration. Both the $\overline{C}_{t,o}$ and $\overline{C}_{l,o}$ increase (from $\overline{C}_{t,o}$ = 1.40 to 3.10, $\overline{C}_{l,o}$ = 3.04 to 4.52). Similarly, as in the MT configuration, the η_o does not change much.

Lastly, the usefulness of the simulation results in relation to the MAVs has been discussed. Depending on the mission objective, different types of flapping configurations can be used to achieve the best performance. The research data obtained from the studies of DOE, airfoil's flexing and tandem configuration will enable the design of a better performing ornithopter in terms of efficiency, thrust and lift production.

10 Recommendations

The DOE study only tests the effects of the four factors, which are k, St, θ_0 and ϕ. As mentioned earlier, some other factors are not included due to limited resources and the complication involved. Hence, another set of study can be conducted using other factors like center of rotation, rowing and the phase angle difference between rowing/heaving or rowing/pitching. It will be interesting to investigate if efficiency, thrust or lift can be further improved.

During the simulation of the flexing of airfoils, some simulations are not completed because the solutions diverged. This is due to the distortion of the grids. IBSNSS can be modified to allow flexing of the airfoils. However, the simulation will have to be run at a lower Re. On the other hand, more complexities can be added to the simulation to further improve the performance of the airfoils. In the current simulation, only three x_{fc} values are selected (0.0, 0.5 and 1.0). Other values such as x_{fc} = 0.25 can also be tested. The flexing amplitude a_f is the same for the leading and trailing edge. Hence, the leading and trailing edge flexing amplitude in the new set of simulations can be different. Lastly, it is also possible to allow the x_{fc} to move along the chord as the airfoil is flapping. For example, when airfoil is at its highest heaving position, x_{fc} = 0.0. As the airfoil moves down to the lowest heaving position, x_{fc} moves from 0.0 to 1.0.

The tandem arrangement simulations are run at Re = 1,000 using the IBSNSS. It will be interesting to run the simulations at higher Re. However, due to the non-conformal nature of the grids, it will only be practical when more computing resources are available. Moreover, due to the flexibility of the IBSNSS, other types of airfoil arrangements can also be simulated without any problem.

All the simulations in this thesis are run in 2D. 3D effects such as tip vortices are neglected. Hence, running the simulations in 3D will be more realistic. Spanwise flexing investigation can then be carried out. However, it will be more expensive in terms of computational costs (Lai and Peskin 2000), especially for the IBSNSS. Moreover, experimental studies must also be conducted. However, it must be noted that designing an actual wing which mimics the flexing or a tandem wing configuration is not trivial.

11 References

Akbari, M. H. and S. J. Price. Simulation of the flow over elliptic airfoils oscillating at large angles of attack, Journal of Fluids and Structures, 14(6), pp. 757-777. 2000.

Akhtar, I., et al. Hydrodynamics of a biologically inspired tandem flapping foil configuration, Theoretical and Computational Fluid Dynamics, 21(3), pp. 155-170. 2007.

Ames, R., et al. On the flowfield and forces generated by a flapping rectangular wing at low Reynolds number. In Fixed and flapping wing aerodynamics for micro air vehicle applications, 195, ed by M. T. J., pp. 287-305: AIAA. 2002.

Anderson, J. M. and P. A. Kerrebrock. Vorticity control unmanned undersea vehicle (VCUUV) - an autonomous vehicle employing fish swimming propulsion and maneuvering. Proceedings of the International Symposium on Unmanned Untethered Submersible Technology,1997.

Anderson, J. M., et al. Oscillating foils of high propulsive efficiency, Journal of Fluid Mechanics, 360, pp. 41-72. 1998.

Azuma, A. and T. Watanabe. Flight performance of a dragonfly, Journal of Experimental Biology, 137, pp. 221-252. 1988.

Balay, S., et al. (2004). PETSc 2.0 Users Manual: Revision 2.1.5. United States**:** 202p.

Batina, J. T. Unsteady Euler airfoil solutions using unstructured dynamic meshes, AIAA Journal, 28(8), pp. 1381-1388. 1990.

Box, G. and D. Behnken. Some new three level designs for the study of quantitative variables, Technometrics, 2, pp. 455-475. 1960.

Cai, J. S., et al. A parallel viscous flow solver on multi-block overset grids, Computers & Fluids, 35(10), pp. 1290-1301. 2006.

Chew, C. S., et al. A generalized finite-difference (GFD) ALE scheme for incompressible flows

around moving solid bodies on hybrid meshfree-Cartesian grids, Journal of Computational Physics, 218(2), pp. 510-548. 2006.

Dallal, G. E. (2007). "The Little Handbook of Statistical Practice." from http://www.tufts.edu/~gdallal/LHSP.HTM.

DeLaurier, J. D. Ornithopter wing design, Canadian Aeronautics and Space Journal, 40(1), pp. 10-18. 1994.

Demirdzic, I. and M. Peric. Space Conservation Law in finite Volume Calculations of fluid-flow, International Journal for Numerical Methods in Fluids, 8(9), pp. 1037-1050. 1988.

Ellington, C. P., et al. Leading-edge vortices in insect flight, Nature, 384(6610), pp. 626-630. 1996.

Falgout, R. D., et al. The design and implementation of hypre, a library of parallel high performance preconditioners. In Numerical solution of partial differential equations on parallel computers, 51, ed by, pp. 267--294. Berlin: Springer. 2006.

Fritz, T. E. and L. N. Long. Object-oriented unsteady vortex lattice method for flapping flight, Journal of Aircraft, 41(6), pp. 1275-1290. 2004.

Gandhi, F. and L. Tauszig. Critical evaluation of various approaches for the numerical detection of helicopter blade-vortex interactions, Journal of the American Helicopter Society, 45(3), pp. 179-190. 2000.

Gao, T., et al. An improved hybrid Cartesian/immersed boundary method for fluid-solid flows, International Journal for Numerical Methods in Fluids, 55(12), pp. 1189-1211. 2007.

Guilmineau, E. and P. Queutey. A numerical simulation of vortex shedding from an oscillating circular cylinder, Journal of Fluids and Structures, 16(6), pp. 773-794. 2002.

Heathcote, S. and I. Gursul. Flexible flapping airfoil propulsion at low Reynolds numbers, Aiaa Journal, 45(5), pp. 1066-1079. 2007.

Heathcote, S., et al. Effect of spanwise flexibility on flapping wing propulsion, Journal of Fluids and Structures, 24(2), pp. 183-199. 2008.

Hirt, C. W., et al. An Arbitrary Lagrangian-Eulerian Computing Method for All Flow Speeds, Journal of Computational Physics, 135(2), pp. 203-216. 1997.

Hover, F. S., et al. Effect of angle of attack profiles in flapping foil propulsion, Journal of Fluids and Structures, 19(1), pp. 37-47. 2004.

Hu, Y., et al. (2006). The analysis of cyclogyro using unsteady vortex lattice method. 25th international congress of aeronautical sciences.

Isogai, K., et al. Unsteady three-dimensional viscous flow simulation of a dragonfly hovering, Aiaa Journal, 42(10), pp. 2053-2059. 2004.

Isogai, K., et al. Effects of dynamic stall on propulsive efficiency and thrust of flapping airfoil, Aiaa Journal, 37(10), pp. 1145-1151. 1999.

Jardine, A. P., et al. Shape memory alloy TiNi actuators for twist control of smart wing designs,1996, San Diego, CA, USA, SPIE-Int. Soc. Opt. Eng.

Jardine, A. P., et al. Shape memory alloy TiNi actuators for twist control of smart wing designs,1996, San Diego, CA, USA.

Jones, K. D., et al. (2003). Development and Flight Testing of Flapping-Wing Propelled Micro Air Vehicles. 2nd AIAA Unmanned Unlimited Systems, Technologies, and Operations (Aerospace, Land, and Sea) Conference and Workshop 2002. San Diego. AIAA Paper No. 2003-6549.

Jones, K. D., et al. (2002). A Numerical and Experimental Investigation of Flapping-Wing Propulsion in ground effect. 40th Aerospace Sciences Meeting & Exhibit. Reno, NV. AIAA-2002-0866.

Jones, K. D., et al. A Collaborative Numerical and Experimental Investigation of Flapping-Wing Propulsion. AIAA 40th Aerospace Sciences Meeting, Reno, Nevada,2002.

Jones, W. T. and J. Samareh-abolhassani (1995). Grid Generation System for Multi-Disciplinary Design Optimization. United States**:** 11p.

Katz, J. and A. Plotkin. Low Speed Aerodynamics: Cambridge University Press.2001.

Kim, D. and H. Choi. A second-order time-accurate finite volume method for unsteady incompressible flow on hybrid unstructured grids, Journal of Computational Physics, 162(2), pp. 411-428. 2000.

Koochesfahani, M. M. Vortical patterns in the wake of an oscillating airfoil, AIAA Journal,

27(9), pp. 1200-1205. 1989.

Lai, J. C. S. and M. F. Platzer. Jet characteristics of a plunging airfoil, Aiaa Journal, 37(12), pp. 1529-1537. 1999.

Lai, M. C. and C. S. Peskin. An immersed boundary method with formal second-order accuracy and reduced numerical viscosity, Journal of Computational Physics, 160(2), pp. 705-719. 2000.

Lan, S. L. and M. Sun. Aerodynamic force and flow structures of two airfoils in flapping motions, Acta Mechanica Sinica, 17(4), pp. 310-331. 2001.

Lu, X. Y., et al. Propulsive performance and vortex shedding of a foil in flapping flight, Acta Mechanica, 165(3-4), pp. 189-206. 2003.

Mathews, P. Design of Experiments with MINITAB. pp. 448 - 458.2005.

Miao, J. M. and M. H. Ho. Effect of flexure on aerodynamic propulsive efficiency of flapping flexible airfoil, Journal of Fluids and Structures, 22(3), pp. 401-419. 2006.

Mittal, R. and G. Iaccarino. Immersed boundary methods, Annual Review of Fluid Mechanics, 37, pp. 239-261. 2005.

Mueller, T. J. and J. D. DeLaurier. Aerodynamics of small vehicles, Annual Review of Fluid Mechanics, 35, pp. 89-111. 2003.

Pauley, L. L., et al. The Structure of 2-Dimensional Separation, Journal of Fluid Mechanics, 220, pp. 397-411. 1990.

Pederzani, J. and H. Haj-Hariri. Numerical analysis of heaving flexible airfoils in a viscous flow, Aiaa Journal, 44(11), pp. 2773-2779. 2006.

Pederzani, J. and H. Haj-Hariri. A numerical method for the analysis of flexible bodies in unsteady viscous flows, International Journal for Numerical Methods in Engineering, 68(10), pp. 1096-1112. 2006.

Pedro, G., et al. A numerical study of the propulsive efficiency of a flapping hydrofoil, International Journal for Numerical Methods in Fluids, 42(5), pp. 493-526. 2003.

Pornsin-Sirirak, T. N., et al. MEMS wing technology for a battery-powered ornithopter,2000, Piscataway, NJ, USA, IEEE.

Ramamurti, R. and W. Sandberg. Simulation of flow about flapping airfoils using finite element incompressible flow solver. AIAA 37th Aerospace Sciences Meeting and Exhibit,1999, Reno, Nevada.

Ravoux, J. F., et al. An embedding method for bluff body flows: interactions of two side-by-side cylinder wakes, Theoretical and Computational Fluid Dynamics, 16(6), pp. 433-466. 2003.

Read, D. A., et al. Forces on oscillating foils for propulsion and maneuvering, Journal of Fluids and Structures, 17(1), pp. 163-183. 2003.

Sarkar, S. and K. Venkatraman (2005). Propulsion characteristics of a non-sinusoidally heaving airfoil. 35th AIAA Fluid Dynamics Conference and Exhibit. Westin Harbour Castle Toronto, Ontario, Canada. AIAA paper 2005-5157.

Schouveiler, L., et al. Performance of flapping foil propulsion. 12th International Conference on Composites in Engineering (ICCE-12),2005, Tenerife, SPAIN.

Scully, M. P. (1968). On the Computation of Helicopter Rotor Wake Geometry. United States**:** 9p.

Shyy, W., et al. Computational aerodynamics of low Reynolds number plunging, pitching and flexible wings for MAV applications, Acta Mechanica Sinica, 24(4), pp. 351-373. 2008.

Smith, M. J. C., et al. The advantages of an unsteady panel method in modelling the aerodynamic forces on rigid flapping wings, Journal of Experimental Biology, 199(5), pp. 1073-1083. 1996.

Snir, M., et al. MPI: The Complete Reference: The MIT Press.1998.

Soni, B. K. Two and three-dimensional grid generation for inernal flow applications of computational fluid dynamics,1985, New York, NY, USA, AIAA (CP854).

Streitlien, K. and G. S. Triantafyllou. On thrust estimates for flapping foils, Journal of Fluids and Structures, 12(1), pp. 47-55. 1998.

Szymendera, C. J. Computational free wake analysis of a helicopter rotor.M.Sc, Department of Aerospace Engineering. 2002.

Takahashi, S., et al. (2007). Aerodynamic Design Exploration of Flapping Wing, Viewpoint of Shape and Kinematics. 45th AIAA Aerospace Sciences Meeting and Exhibit. Reno, Nevada,

U.S.A. AIAA-2007-0481.

Tang, J., et al. A study of aerodynamics of low reynolds number flexible airfoils,2007, Miami, FL, United States, American Institute of Aeronautics and Astronautics Inc., Reston, VA 20191-4344, United States.

Tay, W. B. and K. B. Lim. Analysis of non-symmetrical flapping airfoils, Acta Mechanica Sinica, 25(4), pp. 433-450. 2009.

Taylor, G. K., et al. Flying and swimming animals cruise at a Strouhal number tuned for high power efficiency, Nature, 425(6959), pp. 707-711. 2003.

Triantafyllou, G. S., et al. Optimal thrust development in oscillating foils with application to fish propulsion, Journal of Fluids and Structures, 7(2), pp. 205-224. 1993.

Tseng, Y. H. and J. H. Ferziger. A ghost-cell immersed boundary method for flow in complex geometry, Journal of Computational Physics, 192(2), pp. 593-623. 2003.

Tuncer, I. H. Two-dimensional unsteady Navier-Stokes solution method with moving overset grids. AIAA 34th Aerospace Sciences Meeting and Exhibit,1996, Reno, Nv.

Tuncer, I. H. and M. Kaya. Thrust generation caused by flapping airfoils in a biplane configuration, Journal of Aircraft, 40(3), pp. 509-515. 2003.

Tuncer, I. H. and M. Kaya. Optimization of flapping airfoils for maximum thrust and propulsive efficiency, Aiaa Journal, 43(11), pp. 2329-36. 2005.

Udaykumar, H. S., et al. A sharp interface cartesian grid method for simulating flows with complex moving boundaries, Journal of Computational Physics, 174(1), pp. 345-380. 2001.

Videler, J. J., et al. Leading-edge vortex lifts swifts, Science, 306(5703), pp. 1960-1962. 2004.

Vinh, H. D. Dynamics and control of a flapping-wing aircraft.M.Eng, Department of mechanical engineering. 2005.

Wang, J. K. and M. Sun. A computational study of the aerodynamics and forewing-hindwing interaction of a model dragonfly in forward flight, Journal of Experimental Biology, 208(19), pp. 3785-3804. 2005.

Wang, Z. J. and D. Russell. Effect of forewing and hindwing interactions on aerodynamic forces and power in hovering dragonfly flight, Physical Review Letters, 99(14). 2007.

Wu, J. H. and M. Sun. The influence of the wake of a flapping wing on the production of aerodynamic forces, Acta Mechanica Sinica, 21(5), pp. 411-418. 2005.

Ye, T., et al. An accurate Cartesian grid method for viscous incompressible flows with complex immersed boundaries, Journal of Computational Physics, 156(2), pp. 209-240. 1999.

Young, J. Numerical simulation of the unsteady aerodynamics of flapping airfoils.Ph.D. Dissertation, School of Aerospace, Civil and Mechanical Engineering. 2005.

Zhu, Q. Numerical simulation of a flapping foil with chordwise or spanwise flexibility, Aiaa Journal, 45(10), pp. 2448-2457. 2007.

12 Publication from this Research

12.1 Journal Articles (In Review)

Tay W.B. and Lim K.B. Analysis of non-symmetrical flapping airfoils, Acta Mechanica Sinica, Vol 25, 4 (2009), Page 433-450.

Tay W.B. and Lim K.B. Numerical Analysis of Active Chordwise Flexibility on the Performance of Non-Symmetrical Flapping Airfoils, Journal of Fluids and Structures, undergoing first revision.

Lim K.B. and Tay W.B. Numerical Analysis of the S1020 Airfoils in Tandem under Different Flapping Configurations, Acta Mechanica Sinica, accepted

12.2 Conference Papers

Hu, Y., Tay, W. B. and Lim K. B. The analysis of cyclogyro using unsteady vortex lattice method, 25th international congress of the aeronautical sciences. 2006.

Hu, Y., Lim K. B. and Tay, W. B. The investigation of cyclogyro design and the performance, 25th international congress of the aeronautical sciences. 2006.

Tay W. B. and Lim K. B. Analysis of Non-symmetrical Flapping Airfoils, American Physical Society, Division of Fluid Dynamics 60th Annual DFD Meeting. 2007.

Appendices

A DOE

A.1 Test Configurations and Results for BB test

Table A.1: Test configurations based on the BB test (continue on next page)

Number	k	St	θ_0	ϕ	h_0 (=St/(2*k))
1	0.2	0.1	-17.5	90	0.25
2	1.0	0.1	-17.5	90	0.05
3	0.2	0.5	-17.5	90	1.25
4	1.0	0.5	-17.5	90	0.25
5	0.6	0.3	-5.0	60	0.25
6	0.6	0.3	-30.0	60	0.25
7	0.6	0.3	-5.0	120	0.25
8	0.6	0.3	-30.0	120	0.25
9	0.2	0.3	-5.0	90	0.75
10	1.0	0.3	-5.0	90	0.15
11	0.2	0.3	-30.0	90	0.75
12	1.0	0.3	-30.0	90	0.15
13	0.6	0.1	-17.5	60	0.08
14	0.6	0.5	-17.5	60	0.42
15	0.6	0.1	-17.5	120	0.08
16	0.6	0.5	-17.5	120	0.42
17	0.2	0.3	-17.5	60	0.75
18	1.0	0.3	-17.5	60	0.15
19	0.2	0.3	-17.5	120	0.75
20	1.0	0.3	-17.5	120	0.15
21	0.6	0.1	-5.0	90	0.08
22	0.6	0.5	-5.0	90	0.42

23	0.6	0.1	-30.0	90	0.08
24	0.6	0.5	-30.0	90	0.42
25	0.6	0.3	-17.5	90	0.25

Table A.2: η, $\bar{C}_t$ and $\bar{C}_l$ results of the test configurations for NACA0012 (BB test) (continue on next page)

Number	η	$\bar{C}_t$	$\bar{C}_l$
1	0.123	0.009	0.032
2	0.158	0.382	0.123
3	0.256	1.333	0.027
4	0.260	2.204	-0.034
5	0.247	0.400	-0.682
6	0.234	0.133	0.089
7	0.263	0.634	0.659
8	0.204	1.456	-0.046
9	0.191	0.326	0.255
10	0.285	0.539	0.118
11	0.611	0.509	0.159
12	0.152	1.838	0.735
13	0.009	0.002	0.045
14(*)[§§§§]	0.237	0.863	0.280
15	0.180	0.184	0.099
16(*)	0.253	2.525	0.412
17	0.359	0.418	0.017

[§§§§] (*) denotes unsteady non-periodic simulation

18	0.298	0.278	0.004
19	0.345	0.581	0.142
20	0.202	1.693	0.851
21	0.178	0.022	0.002
22(*)	0.170	1.354	-0.133
23	0.067	0.162	0.092
24	0.362	2.123	0.462
25	0.404	0.641	0.125

Table A.3: η, $\bar{C}_t$ and $\bar{C}_l$ results of the test configurations for NACA4404 (BB test) (continue on next page)

Number	η	$\bar{C}_t$	$\bar{C}_l$
1	0.000	-0.043	0.267
2	0.201	0.492	0.293
3	0.206	1.067	0.274
4	0.227	2.265	0.720
5(*)	0.078	0.154	0.526
6(*)	0.241	0.145	0.211
7	0.154	0.421	0.994
8	0.202	1.335	0.865
9	0.109	0.202	0.234
10(*)	0.158	0.459	0.031
11	0.576	0.455	0.434
12	0.174	2.044	1.018
13	0.048	0.011	0.340
14(*)	0.145	0.735	0.684
15	0.190	0.198	0.376

16(*)	0.213	2.235	1.126
17	0.275	0.351	0.251
18(*)	0.260	0.322	0.137
19	0.264	0.486	0.359
20	0.214	1.790	1.441
21	0.235	0.031	0.290
22(*)	0.088	0.802	0.351
23	0.000	-0.049	0.405
24	0.341	2.037	0.868
25	0.372	0.664	0.576

Table A.4: η, $\overline{C}_t$ and $\overline{C}_l$ results of the test configurations for NACA6302 (BB test) (continue on next page)

Number	η	$\overline{C}_t$	$\overline{C}_l$
1	0.000	-0.027	0.447
2	0.181	0.455	0.334
3	0.213	1.295	0.365
4	0.226	2.446	1.461
5	0.088	0.166	0.225
6(*)	0.189	0.106	-0.022
7	0.151	0.442	0.751
8	0.204	1.378	0.381
9	0.124	0.254	0.253
10(*)	0.144	0.482	0.451
11	0.540	0.511	0.250
12	0.179	2.206	1.302
13	0.000	-0.045	0.363

14(*)	0.141	0.700	0.628
15	0.135	0.143	0.346
16(*)	0.210	2.101	0.302
17	0.282	0.386	0.070
18	0.248	0.341	-0.039
19	0.267	0.533	0.608
20	0.210	1.778	1.722
21	0.133	0.018	0.353
22(*)	0.079	0.792	-0.217
23	0.000	-0.142	0.486
24	0.321	1.921	0.127
25	0.354	0.691	0.516

Table A.5: η, $\bar{C}_t$ and $\bar{C}_l$ results of the test configurations for S1020 (BB test) (continue on next page)

Number	η	$\bar{C}_t$	$\bar{C}_l$
1	0.000	-0.051	0.242
2	0.138	0.343	0.851
3	0.244	1.321	0.564
4	0.245	2.107	1.195
5	0.231	0.374	1.490
6	0.249	0.150	0.541
7	0.248	0.601	1.220
8	0.195	1.334	1.724
9	0.185	0.312	0.261
10	0.262	0.559	1.040
11	0.571	0.550	0.510

12	0.134	1.609	1.749
13	0.000	-0.020	0.565
14(*)	0.251	1.051	0.967
15	0.154	0.168	1.058
16	0.256	2.330	1.351
17	0.341	0.395	0.021
18	0.313	0.339	0.792
19	0.337	0.597	0.527
20	0.200	1.628	1.935
21	0.018	0.002	0.350
22(*)	0.155	1.280	1.213
23	0.039	0.097	1.324
24	0.361	1.946	1.269
25	0.378	0.579	0.818

Table A.6: η, $\bar{C}_t$ and $\bar{C}_l$ results of the test configurations for birdy (BB test) (continue on next page)

Number	η	$\bar{C}_t$	$\bar{C}_l$
1(*)	0.000	-0.080	0.275
2	0.155	0.374	1.406
3(*)	0.227	1.269	-0.037
4	0.243	2.110	1.470
5	0.196	0.345	1.787
6	0.000	-0.006	0.213
7	0.221	0.575	1.921
8(*)	0.185	1.248	1.913
9	0.151	0.269	0.155

10(*)	0.251	0.553	1.379
11	0.460	0.488	0.546
12	0.150	1.630	2.231
13	0.000	-0.097	0.670
14(*)	0.228	0.942	0.266
15	0.101	0.111	1.112
16	0.226	2.260	0.549
17	0.246	0.294	-0.027
18	0.294	0.334	0.516
19	0.263	0.497	0.271
20	0.195	1.608	2.093
21	0.000	-0.039	0.623
22(*)	0.148	1.165	1.332
23	0.000	0.000	1.428
24	0.340	1.769	0.380
25	0.356	0.646	1.050

B Chordwise Flexing

B.1 Results for Chordwise Flexing

Table B.1: Pure heaving results for $0 \leq \bar{a}_f \leq 0.4$ (continue on next page)

$\bar{a}_f$	$x_{fc} = 0.0$								
	η			$\bar{C}_t$			$\bar{C}_l$		
	NACA0012	NACA6302	S1020	NACA0012	NACA6302	S1020	NACA0012	NACA6302	S1020
0.0	0.20	0.01	0.16	0.28	0.01	0.20	-0.12	-0.37	0.31
0.1	0.26	0.09	0.22	0.24	0.09	0.21	-0.02	-0.06	0.25
0.2	0.31	0.14	0.27	0.26	0.12	0.21	0.07	0.05	0.30
0.3	0.33	0.20	0.27	0.23	0.14	0.17	0.13	0.29	0.33

0.4	0.22	0.16	0.18	0.11	0.09	0.09	0.0	0.37	0.46
0.5	0.18	NA[*****]	NA	0.09	-0.05	-0.11	0.15	0.42	0.54
$\bar{a}_f$					x_{fc} = 0.5				
		η			$\bar{C}_t$			$\bar{C}_l$	
	NACA0012	NACA6302	S1020	NACA0012	NACA6302	S1020	NACA0012	NACA6302	S1020
0.0	0.20	0.01	0.16	0.28	0.01	0.20	-0.12	-0.37	0.31
0.1	NA	NA	NA	-0.09	-0.29	-0.15	-0.05	-0.39	0.13
0.2	NA	ND[†††††]	NA	-0.44	ND	-0.50	-0.06	ND	0.05
$\bar{a}_f$					x_{fc} = 1.0				
		η			$\bar{C}_t$			$\bar{C}_l$	
	NACA0012	NACA6302	S1020	NACA0012	NACA6302	S1020	NACA0012	NACA6302	S1020
0.0	0.20	0.01	0.16	0.28	0.01	0.20	-0.12	-0.37	0.31

[*****] Not applicable due to generation of drag (NA)

[†††††] Not done due to previous unsatisfactory results (ND)

0.1	0.0	NA	NA	0.01	-0.30	-0.04	-0.08	-0.39	-0.06
0.2	NA	SD‡‡‡‡‡	NA	-0.26	SD	-0.36	-0.46	SD	-0.24

‡‡‡‡‡ Solution diverged (SD)

Table B.2: Pure heaving results for $-0.4 \leq \bar{a}_f \leq 0$ (continue on next page)

$\bar{a}_f$	x_{fc} = 0.0								
	η			$\bar{C}_t$			$\bar{C}_l$		
	NACA0012	NACA6302	S1020	NACA0012	NACA6302	S1020	NACA0012	NACA6302	S1020
0.0	0.20	0.01	0.16	0.28	0.01	0.20	-0.12	-0.37	0.31
-0.1	0.13	NA	0.09	0.20	-0.08	0.14	-0.11	-0.69	0.17
-0.2	0.06	NA	0.02	0.11	-0.25	0.05	-0.27	-1.08	0.25
$\bar{a}_f$	x_{fc} = 0.5								
	η			$\bar{C}_t$			$\bar{C}_l$		
	NACA0012	NACA6302	S1020	NACA0012	NACA6302	S1020	NACA0012	NACA6302	S1020
0.0	0.20	0.01	0.16	0.28	0.01	0.20	-0.12	-0.37	0.31
-0.1	0.29	0.20	0.28	0.48	0.29	0.44	-0.15	-0.21	0.61
-0.2	0.20	0.25	0.21	0.41	0.39	0.39	-0.20	-0.05	0.64
-0.3	SD	SD	SD	SD	SD	SD	SD	SD	SD
$\bar{a}_f$	x_{fc} = 1.0								

	η			$\bar{C}_t$			$\bar{C}_l$		
	NACA0012	NACA6302	S1020	NACA0012	NACA6302	S1020	NACA0012	NACA6302	S1020
0.0	0.20	0.01	0.16	0.28	0.01	0.20	-0.12	-0.37	0.31
-0.1	0.37	0.22	0.35	0.37	0.22	0.37	-0.09	-0.06	-0.10
-0.2	0.53	0.41	0.50	0.43	0.32	0.39	0.01	0.05	-0.03
-0.3	0.63	0.56	0.58	0.40	0.34	0.38	0.01	0.29	0.15
-0.4	0.66	0.63	0.62	0.34	0.31	0.32	0.0	0.37	0.09
-0.5	0.61	SD	0.76	0.18	SD	0.26	0.02	SD	0.21
-0.6	ND	ND	0.23	0.01	ND	0.26	0.02	ND	0.23

Table B.3: Pure heaving results for $0 \leq \bar{a}_f \leq 0.4$ Single-sided (continue on next page)

$\bar{a}_f$	x_{fc} = 0.0								
	η			$\bar{C}_t$			$\bar{C}_l$		
	NACA0012	NACA6302	S1020	NACA0012	NACA6302	S1020	NACA0012	NACA6302	S1020
0.0	0.20	0.01	0.16	0.28	0.01	0.20	-0.12	-0.37	0.31
0.1	0.15	0.02	0.15	0.19	0.03	0.21	1.02	0.62	1.30
0.2	0.06	NA	0.08	0.10	-0.08	0.12	1.81	1.94	2.17
0.3	0.0	ND	NA	0.01	ND	-0.02	1.97	ND	2.67
$\bar{a}_f$	x_{fc} = 0.5								
	η			$\bar{C}_t$			$\bar{C}_l$		
	NACA0012	NACA6302	S1020	NACA0012	NACA6302	S1020	NACA0012	NACA6302	S1020
0.0	0.20	0.01	0.16	0.28	0.01	0.20	-0.12	-0.37	0.31
0.1	0.17	NA	0.02	0.20	-0.06	0.02	0.26	-0.55	0.22
0.2	0.03	NA	NA	0.03	-0.20	-0.19	0.22	-0.12	0.08
$\bar{a}_f$	x_{fc} = 1.0								

	η			$\bar{C}_t$			$\bar{C}_l$		
	NACA0012	NACA6302	S1020	NACA0012	NACA6302	S1020	NACA0012	NACA6302	S1020
0.0	0.20	0.01	0.16	0.28	0.01	0.20	-0.12	-0.37	0.31
0.1	0.12	NA	0.03	0.15	-0.14	0.03	-0.93	-1.40	-0.67
0.2	NA	NA	NA	-0.06	-0.50	-0.18	-1.49	-2.56	-1.18

Table B.4: Pure heaving results for -0.4 ≤ $\bar{a}_f$ ≤ 0 Single-sided (continue on next page)

$\bar{a}_f$	x_{fc} = 0.0								
	η			$\bar{C}_t$			$\bar{C}_l$		
	NACA0012	NACA6302	S1020	NACA0012	NACA6302	S1020	NACA0012	NACA6302	S1020
0.0	0.20	0.01	0.16	0.28	0.01	0.20	-0.12	-0.37	0.31
-0.1	0.14	NA	0.10	0.19	0.10	0.13	-1.1	-1.29	-0.63
-0.2	0.04	NA	0.02	0.05	-0.30	0.03	-2.05	-2.04	-1.26
$\bar{a}_f$	x_{fc} = 0.5								
	η			$\bar{C}_t$			$\bar{C}_l$		
	NACA0012	NACA6302	S1020	NACA0012	NACA6302	S1020	NACA0012	NACA6302	S1020
0.0	0.20	0.01	0.16	0.28	0.01	0.20	-0.12	-0.37	0.31
-0.1	0.17	0.00	0.17	0.21	0.00	0.21	-0.35	0.46	0.12
-0.2	0.05	SD	0.07	0.05	SD	0.08	-0.36	SD	-0.40
$\bar{a}_f$	x_{fc} = 1.0								
	η			$\bar{C}_t$			$\bar{C}_l$		

	NACA0012	NACA6302	S1020	NACA0012	NACA6302	S1020	NACA0012	NACA6302	S1020
0.0	0.20	0.01	0.16	0.28	0.01	0.20	-0.12	-0.37	0.31
-0.1	0.14	NA	0.14	0.18	-0.01	0.19	0.69	0.90	1.00
-0.2	NA	NA	0.02	-0.05	-0.24	0.03	1.47	1.85	1.55

Table B.5: ME configuration results for $0 \leq \bar{a}_f \leq 0.4$ (continue on next page)

$\bar{a}_f$	x_{fc} = **0.0**								
	η			$\bar{C}_t$			$\bar{C}_l$		
	NACA0012	NACA6302	S1020	NACA0012	NACA6302	S1020	NACA0012	NACA6302	S1020
0.0	0.61	0.54	0.57	0.50	0.51	0.55	0.0	0.25	0.51
0.1	0.34	0.37	0.30	0.12	0.16	0.13	0.03	0.48	0.55
0.2	NA	NA	NA	-0.10	-0.14	-0.18	-0.04	0.56	0.53
$\bar{a}_f$	x_{fc} = 0.5								
	η			$\bar{C}_t$			$\bar{C}_l$		
	NACA0012	NACA6302	S1020	NACA0012	NACA6302	S1020	NACA0012	NACA6302	S1020
0.0	0.61	0.54	0.57	0.50	0.51	0.55	0.0	0.25	0.51
0.1	0.20	0.17	0.06	0.10	0.11	0.03	-0.03	0.40	0.45
0.2	NA	SD	NA	-0.29	SD	-0.37	-0.05	SD	0.36
$\bar{a}_f$	x_{fc} = 1.0								
	η			$\bar{C}_t$			$\bar{C}_l$		

	NACA0012	NACA6302	S1020	NACA0012	NACA6302	S1020	NACA0012	NACA6302	S1020
0.0	0.61	0.54	0.57	0.50	0.51	0.55	0.0	0.25	0.51
0.1	0.49	0.39	0.44	0.40	0.37	0.40	0.01	0.29	0.47
0.2	0.32	0.21	0.32	0.35	0.23	0.34	-0.11	0.18	0.29

Table B.6: ME configuration results for -0.4 ≤ $\bar{a}_f$ ≤ 0 (continue on next page)

$\bar{a}_f$	x_{fc} = 0.0								
	η			$\bar{C}_t$			$\bar{C}_l$		
	NACA0012	NACA6302	S1020	NACA0012	NACA6302	S1020	NACA0012	NACA6302	S1020
0.0	0.61	0.54	0.57	0.50	0.51	0.55	0.0	0.25	0.51
-0.1	0.56	0.49	0.49	0.55	0.54	0.52	0.02	0.32	0.54
-0.2	0.51	0.42	0.44	0.69	0.61	0.63	-0.25	0.06	0.61
-0.3	0.45	0.33	0.39	0.81	0.66	0.67	0.26	-0.27	0.23
-0.4	0.38	0.26	0.32	0.91	0.62	0.72	-0.19	0.01	0.17
-0.5	0.32	ND	0.23	0.89	ND	0.58	-0.76	ND	0.22
-0.6	ND	ND	0.15	ND	ND	0.53	ND	ND	0.26
$\bar{a}_f$	x_{fc} = 0.5								
	η			$\bar{C}_t$			$\bar{C}_l$		
	NACA0012	NACA6302	S1020	NACA0012	NACA6302	S1020	NACA0012	NACA6302	S1020
0.0	0.61	0.54	0.57	0.50	0.51	0.55	0.0	0.25	0.51

-0.1	0.49	0.56	0.49	0.49	0.58	0.55	0.07	0.60	0.22
-0.2	0.41	0.53	0.40	0.49	0.61	0.53	-0.03	0.51	0.45
$\bar{a}_f$				x_{fc} = 1.0					
		η			$\bar{C}_t$			$\bar{C}_l$	
	NACA0012	NACA6302	S1020	NACA0012	NACA6302	S1020	NACA0012	NACA6302	S1020
0.0	0.61	0.54	0.57	0.50	0.51	0.55	0.0	0.25	0.51
-0.1	0.48	0.55	0.51	0.27	0.35	0.34	-0.08	0.54	0.36
-0.2	0.40	0.49	0.45	0.16	0.24	0.23	0.07	0.51	0.50
-0.3	0.08	0.16	0.17	0.02	0.05	0.06	0.01	0.35	0.32
-0.4	ND	NA	ND	ND	-0.26	ND	ND	0.08	ND

Table B.7: ME configuration results for -0.4 ≤ $\bar{a}_f$ ≤ 0.4 Single-sided (continue on next page)

$\bar{a}_f$	x_{fc} = 0.0								
	η			$\bar{C}_t$			$\bar{C}_l$		
	NACA0012	NACA6302	S1020	NACA0012	NACA6302	S1020	NACA0012	NACA6302	S1020
-0.2	0.42	ND	ND	0.35	ND	ND	-1.23	ND	ND
-0.1	0.51	ND	ND	0.35	ND	ND	-0.63	ND	ND
0.0	0.61	0.54	0.57	0.50	0.51	0.55	0.0	0.25	0.51
0.1	0.50	0.51	0.41	0.33	0.40	0.33	0.71	1.13	1.11
0.2	0.41	0.39	0.30	0.34	0.35	0.30	1.31	1.92	1.86
0.3	0.28	0.20	0.17	0.29	0.22	0.17	1.71	2.52	2.31
0.4	0.06	NA	0.02	0.08	-0.27	0.03	2.48	3.16	3.21
$\bar{a}_f$	x_{fc} = 0.5								
	η			$\bar{C}_t$			$\bar{C}_l$		
	NACA0012	NACA6302	S1020	NACA0012	NACA6302	S1020	NACA0012	NACA6302	S1020
-0.2	0.13	ND	0.07	0.10	ND	0.08	-0.77	ND	-0.40

-0.1	0.4	ND	0.17	0.31	ND	0.21	-0.54	ND	0.11
0.0	0.61	0.54	0.57	0.50	0.51	0.55	0.0	0.25	0.51
0.1	0.39	0.32	0.25	0.28	0.28	0.22	0.42	0.67	0.68
0.2	0.14	0.00	NA	0.12	0.00	-0.10	0.89	0.42	1.11
0.3	SD	SD	ND	SD	SD	ND	SD	SD	ND
$\bar{a}_f$				x_{fc} = 1.0					
		η			$\bar{C}_t$			$\bar{C}_l$	
	NACA0012	NACA6302	S1020	NACA0012	NACA6302	S1020	NACA0012	NACA6302	S1020
-0.4	NA	ND	NA	-0.28	ND	-0.13	1.36	ND	1.77
-0.3	0.06	0.00	0.15	0.05	0.00	0.14	1.07	1.80	1.70
-0.2	0.28	0.29	0.36	0.22	0.24	0.29	0.88	1.39	1.29
-0.1	0.48	0.52	0.51	0.35	0.40	0.38	0.46	0.91	0.86
0.0	0.61	0.54	0.57	0.50	0.51	0.55	0.0	0.25	0.51
0.1	0.48	ND	ND	0.36	ND	ND	-0.42	ND	ND
0.2	0.20	ND	ND	0.14	ND	ND	-1.0	ND	ND

Table B.8: ME (20°) configuration results for $0 \leq \bar{a}_f \leq 0.4$ (continue on next page)

$\bar{a}_f$	x_{fc} = 0.0								
	η			$\bar{C}_t$			$\bar{C}_l$		
	NACA0012	NACA6302	S1020	NACA0012	NACA6302	S1020	NACA0012	NACA6302	S1020
0.0	0.50	0.39	0.43	0.60	0.47	0.45	-0.08	0.08	0.26
0.1	0.51	0.44	0.43	0.38	0.40	0.36	-0.13	0.40	0.41
0.2	0.43	0.38	0.3	0.19	0.22	0.17	-0.01	0.42	0.53
0.3	NA	NA	NA	-0.09	-0.03	-0.09	0.00	0.52	0.55
$\bar{a}_f$	x_{fc} = 0.5								
	η			$\bar{C}_t$			$\bar{C}_l$		
	NACA0012	NACA6302	S1020	NACA0012	NACA6302	S1020	NACA0012	NACA6302	S1020
0.0	0.50	0.39	0.43	0.6	0.47	0.45	-0.08	0.08	0.26
0.1	0.17	0.11	0.16	0.16	0.12	0.15	0.08	0.19	0.36
0.2	NA	NA	NA	-0.20	-0.07	-0.22	-0.07	-0.06	0.08
$\bar{a}_f$	x_{fc} = 1.0								

	η			$\bar{C}_t$			$\bar{C}_l$		
	NACA0012	NACA6302	S1020	NACA0012	NACA6302	S1020	NACA0012	NACA6302	S1020
0.0	0.50	0.39	0.43	0.6	0.47	0.45	-0.08	0.08	0.26
0.1	0.31	0.23	0.30	0.38	0.32	0.37	0.00	0.18	0.20
0.2	0.13	0.07	0.14	0.19	0.12	0.21	0.01	0.23	0.29

Table B.9: ME (20°) configuration results for $-0.4 \leq \bar{a}_f \leq 0$ (continue on next page)

$\bar{a}_f$	x_{fc} = 0.0								
	η			$\bar{C}_t$			$\bar{C}_l$		
	NACA0012	NACA6302	S1020	NACA0012	NACA6302	S1020	NACA0012	NACA6302	S1020
0.0	0.50	0.39	0.43	0.6	0.47	0.45	-0.08	0.08	0.26
-0.1	0.43	0.32	0.37	0.59	0.49	0.53	-0.12	-0.09	0.33
-0.2	0.36	0.24	0.31	0.64	0.46	0.55	-0.07	-0.33	0.13
-0.3	0.28	0.16	0.24	0.66	0.39	0.58	0.12	-0.42	0.27
-0.4	0.20	ND	0.16	0.59	ND	0.46	-0.31	ND	-0.03
-0.5	0.11	ND	ND	0.35	ND	ND	-0.23	ND	ND
$\bar{a}_f$	x_{fc} = 0.5								
	η			$\bar{C}_t$			$\bar{C}_l$		
	NACA0012	NACA6302	S1020	NACA0012	NACA6302	S1020	NACA0012	NACA6302	S1020
0.0	0.50	0.39	0.43	0.6	0.47	0.45	-0.08	0.08	0.26
-0.1	0.47	0.48	0.44	0.70	0.69	0.62	0.02	0.39	0.47

-0.2	0.37	0.47	0.36	0.63	0.71	0.62	0.26	0.66	0.21
-0.3	SD	SD	SD	SD	SD	SD	SD	SD	SD
$\bar{a}_f$				x_{fc} = 1.0					
		η			$\bar{C}_t$			$\bar{C}_l$	
	NACA0012	NACA6302	S1020	NACA0012	NACA6302	S1020	NACA0012	NACA6302	S1020
0.0	0.50	0.39	0.43	0.6	0.47	0.45	-0.08	0.08	0.26
-0.1	0.57	0.52	0.37	0.5	0.53	0.53	0.01	0.31	0.28
-0.2	0.56	0.60	0.30	0.44	0.51	0.56	0.07	0.50	0.04
-0.3	0.59	0.66	0.58	0.37	0.43	0.44	0.03	0.41	0.22
-0.4	0.46	0.62	0.46	0.19	0.28	0.23	0.02	0.28	0.31

Table B.10: ME (20^o) configuration results for $-0.4 \leq \bar{a}_f \leq 0.4$ Single-sided (continue on next page)

$\bar{a}_f$	x_{fc} = 0.0								
	η			$\bar{C}_t$			$\bar{C}_l$		
	NACA0012	NACA6302	S1020	NACA0012	NACA6302	S1020	NACA0012	NACA6302	S1020
0.0	0.50	0.39	0.43	0.6	0.47	0.45	-0.08	0.08	0.26
0.1	0.44	0.36	0.42	0.48	0.44	0.50	0.75	0.86	1.12
0.2	0.32	0.28	0.35	0.39	0.39	0.44	1.32	1.80	1.67
0.3	0.18	0.06	0.20	0.29	0.09	0.28	2.23	2.77	2.40
0.4	NA	NA	0.08	-0.06	-0.13	0.16	2.92	3.38	3.31
$\bar{a}_f$	x_{fc} = 0.5								
	η			$\bar{C}_t$			$\bar{C}_l$		
	NACA0012	NACA6302	S1020	NACA0012	NACA6302	S1020	NACA0012	NACA6302	S1020
0.0	0.50	0.39	0.43	0.6	0.47	0.45	-0.08	0.08	0.26
0.1	0.36	0.27	0.22	0.41	0.33	0.26	0.49	0.60	0.67
0.2	0.18	0.05	NA	0.21	0.05	-0.06	0.92	0.24	0.86

$\bar{a}_f$	x_{fc} = 1.0								
	η			$\bar{C}_t$			$\bar{C}_l$		
	NACA0012	NACA6302	S1020	NACA0012	NACA6302	S1020	NACA0012	NACA6302	S1020
-0.4	NA	SD	NA	-0.18	SD	-0.10	1.39	SD	1.78
-0.3	0.07	SD	0.10	0.08	SD	0.13	1.19	SD	1.70
-0.2	0.23	0.19	0.29	0.27	0.25	0.33	0.94	1.57	1.26
-0.1	0.39	0.38	0.42	0.43	0.38	0.45	0.54	0.98	1.07
0.0	0.50	0.39	0.43	0.6	0.47	0.45	-0.08	0.08	0.26
0.1	0.39	ND	ND	0.43	ND	ND	-0.54	ND	ND
0.2	0.25	ND	ND	0.29	ND	ND	-0.81	ND	ND

Table B.11: MT configuration results for $0 \leq \bar{a}_f \leq 0.4$ (continue on next page)

$\bar{a}_f$	x_{fc} = 0.0								
	η			$\bar{C}_t$			$\bar{C}_l$		
	NACA0012	NACA6302	S1020	NACA0012	NACA6302	S1020	NACA0012	NACA6302	S1020
0.0	0.25	0.21	0.26	2.50	2.10	2.33	0.41	0.30	1.35
0.1	0.25	0.21	0.24	2.58	2.23	2.54	0.34	0.68	1.70
0.2	0.21	0.18	0.20	2.36	2.41	2.35	-0.55	1.09	1.26
0.3	0.15	0.15	0.15	2.39	2.25	2.13	0.10	1.42	1.60
0.4	0.10	0.10	0.09	1.62	1.84	1.43	-1.21	1.24	3.24
0.5	ND	ND	0.05	ND	ND	0.97	ND	ND	2.52
$\bar{a}_f$	x_{fc} = 0.5								
	η			$\bar{C}_t$			$\bar{C}_l$		
	NACA0012	NACA6302	S1020	NACA0012	NACA6302	S1020	NACA0012	NACA6302	S1020
0.0	0.25	0.21	0.26	2.50	2.10	2.33	0.41	0.30	1.35
0.1	0.20	SD	0.17	1.50	SD	1.65	0.47	SD	2.85

0.2	0.07	ND	0.05	0.48	ND	0.50	1.06	ND	2.72
0.3	SD	ND	SD	SD	ND	SD	SD	ND	SD

$\bar{a}_f$	x_{fc} = 1.0								
	η			$\bar{C}_t$			$\bar{C}_l$		
	NACA0012	NACA6302	S1020	NACA0012	NACA6302	S1020	NACA0012	NACA6302	S1020
0.0	0.25	0.21	0.26	2.50	2.10	2.33	0.41	0.30	1.35
0.1	0.20	SD	0.20	2.08	SD	2.07	1.52	SD	1.00
0.2	SD	ND	SD	SD	ND	SD	SD	ND	SD

Table B.12: MT configuration results for $-0.4 \leq \bar{a}_f \leq 0$ (continue on next page)

$\bar{a}_f$	x_{fc} = 0.0								
	η			$\bar{C}_t$			$\bar{C}_l$		
	NACA0012	NACA6302	S1020	NACA0012	NACA6302	S1020	NACA0012	NACA6302	S1020
0.0	0.25	0.21	0.26	2.50	2.10	2.33	0.41	0.30	1.35
-0.1	0.25	SD	0.25	2.30	SD	2.23	0.31	SD	2.16
-0.2	0.20	ND	0.19	1.83	ND	1.68	0.60	ND	1.08
$\bar{a}_f$	x_{fc} = 0.5								
	η			$\bar{C}_t$			$\bar{C}_l$		
	NACA0012	NACA6302	S1020	NACA0012	NACA6302	S1020	NACA0012	NACA6302	S1020
0.0	0.25	0.21	0.26	2.50	2.10	2.33	0.41	0.30	1.35
-0.1	0.29	0.24	0.27	2.62	2.26	2.68	0.74	0.15	1.60
-0.2	0.25	0.24	0.26	2.51	2.18	2.35	-0.33	0.31	1.11
$\bar{a}_f$	x_{fc} = 1.0								
	η			$\bar{C}_t$			$\bar{C}_l$		

	NACA0012	NACA6302	S1020	NACA0012	NACA6302	S1020	NACA0012	NACA6302	S1020
0.0	0.25	0.21	0.26	2.50	2.10	2.33	0.41	0.30	1.35
-0.1	0.28	0.27	0.28	2.52	2.39	2.48	0.23	0.47	1.88
-0.2	0.28	0.28	0.27	2.18	2.49	2.30	0.16	1.36	1.92
-0.3	0.29	0.28	0.25	2.11	2.30	1.86	0.52	1.34	1.30
-0.4	0.21	SD	0.23	1.61	SD	1.66	0.18	SD	1.41

Table B.13: MT configuration results for -0.4 ≤ $\bar{a}_f$ ≤ 0.4 Single-sided (continue on next page)

$\bar{a}_f$	x_{fc} = 0.0								
	η			$\bar{C}_t$			$\bar{C}_l$		
	NACA0012	NACA6302	S1020	NACA0012	NACA6302	S1020	NACA0012	NACA6302	S1020
0.0	0.25	0.21	0.26	2.50	2.10	2.33	0.41	0.30	1.35
0.1	0.25	SD	0.24	2.44	SD	2.40	1.08	SD	2.41
0.2	SD	ND	0.23	SD	ND	2.39	SD	ND	3.86
0.3	ND	ND	SD	ND	ND	SD	ND	ND	SD
$\bar{a}_f$	x_{fc} = 0.5								
	η			$\bar{C}_t$			$\bar{C}_l$		
	NACA0012	NACA6302	S1020	NACA0012	NACA6302	S1020	NACA0012	NACA6302	S1020
-0.2	0.24	ND	ND	1.91	ND	ND	-2.06	ND	ND
-0.1	0.25	ND	ND	2.20	ND	ND	-0.54	ND	ND
0.0	0.25	0.21	0.26	2.50	2.10	2.33	0.41	0.30	1.35
0.1	0.22	SD	0.24	1.89	SD	2.06	1.90	SD	2.66

0.2	SD	ND	0.20	SD	ND	1.42	SD	ND	2.37
0.3	ND	ND	SD	ND	ND	SD	ND	ND	SD
$\bar{a}_f$				x_{fc} = 1.0					
		η			$\bar{C}_t$			$\bar{C}_l$	
	NACA0012	NACA6302	S1020	NACA0012	NACA6302	S1020	NACA0012	NACA6302	S1020
-0.4	0.14	ND	SD	1.41	ND	SD	3.62	ND	SD
-0.3	0.14	ND	0.14	1.40	ND	1.52	3.49	ND	4.61
-0.2	0.18	ND	0.20	1.64	ND	2.05	2.50	ND	4.11
-0.1	0.24	SD	0.24	2.22	SD	2.37	1.72	SD	2.58
0.0	0.25	0.21	0.26	2.50	2.10	2.33	0.41	0.30	1.35
0.1	0.24	ND	ND	2.27	ND	ND	-1.22	ND	ND
0.2	0.18	ND	ND	1.69	ND	ND	-2.48	ND	ND

Table B.14: ML configuration results for $0 \leq \bar{a}_f \leq 0.4$

$\bar{a}_f$	x_{fc} = **0.0**					
	η		$\bar{C}_t$		$\bar{C}_l$	
	NACA6302	S1020	NACA6302	S1020	NACA6302	S1020
0.0	0.21	0.20	1.78	1.63	1.72	1.93
0.1	0.18	0.15	2.47	2.12	1.23	0.98
0.2	0.11	0.10	2.53	2.36	-0.33	1.89
0.3	SD	0.11	SD	3.57	SD	1.65
0.4	ND	0.04	SD	1.92	SD	2.31
$\bar{a}_f$	x_{fc} = 0.5					
	η		$\bar{C}_t$		$\bar{C}_l$	
	NACA6302	S1020	NACA6302	S1020	NACA6302	S1020
0.0	0.21	0.20	1.78	1.63	1.72	1.93
0.1	0.17	0.17	1.95	1.95	1.91	1.91
0.2	SD	SD	SD	SD	SD	SD
$\bar{a}_f$	x_{fc} = 1.0					
	η		$\bar{C}_t$		$\bar{C}_l$	
	NACA6302	S1020	NACA6302	S1020	NACA6302	S1020
0.0	0.21	0.20	1.78	1.63	1.72	1.93
0.1	SD	0.17	SD	1.40	SD	1.52
0.2	ND	0.13	ND	1.04	ND	1.12

Table B.15: ML configuration results for $-0.4 \leq \bar{a}_f \leq 0$

$\bar{a}_f$	x_{fc} = **0.0**					
	η		$\bar{C}_t$		$\bar{C}_l$	
	NACA6302	S1020	NACA6302	S1020	NACA6302	S1020
0.0	0.21	0.20	1.78	1.63	1.72	1.93
-0.1	0.23	0.26	1.16	1.22	0.86	1.93
-0.2	0.19	0.26	0.50	0.74	0.17	1.62
-0.3	0.05	0.18	0.11	0.39	0.10	1.29
-0.4	ND	0.05	ND	0.13	ND	1.81
$\bar{a}_f$	x_{fc} = 0.5					
	η		$\bar{C}_t$		$\bar{C}_l$	
	NACA6302	S1020	NACA6302	S1020	NACA6302	S1020
0.0	0.21	0.20	1.78	1.63	1.72	1.93
-0.1	0.25	0.23	1.43	1.31	0.33	1.28
-0.2	SD	0.22	SD	0.67	SD	0.41
$\bar{a}_f$	x_{fc} = 1.0					
	η		$\bar{C}_t$		$\bar{C}_l$	
	NACA6302	S1020	NACA6302	S1020	NACA6302	S1020
0.0	0.21	0.20	1.78	1.63	1.72	1.93
-0.1	0.20	0.17	1.75	1.40	1.39	1.53
-0.2	0.16	0.13	1.22	1.04	0.58	1.12

Table B.16: ML configuration results for -0.4 ≤ $\bar{a}_f$ ≤ 0.4 Single-sided

$\bar{a}_f$	x_{fc} = 0.0					
	η		$\bar{C}_t$		$\bar{C}_l$	
	NACA6302	S1020	NACA6302	S1020	NACA6302	S1020
0.0	0.21	0.20	1.78	1.63	1.72	1.93
0.1	0.22	0.22	2.03	1.94	0.57	1.67
0.2	SD	SD	SD	SD	SD	SD
$\bar{a}_f$	x_{fc} = 0.5					
	η		$\bar{C}_t$		$\bar{C}_l$	
	NACA6302	S1020	NACA6302	S1020	NACA6302	S1020
0.0	0.21	0.20	1.78	1.63	1.72	1.93
0.1	0.20	0.23	1.65	1.83	1.35	3.13
0.2	0.22	SD	1.63	SD	2.68	SD
0.3	SD	ND	SD	ND	SD	ND
$\bar{a}_f$	x_{fc} = 1.0					
	η		$\bar{C}_t$		$\bar{C}_l$	
	NACA6302	S1020	NACA6302	S1020	N6302	S1020
0.0	0.21	0.20	1.78	1.63	1.72	1.93
-0.1	SD	0.21	SD	1.72	SD	3.57
-0.2	ND	0.19	ND	1.69	ND	4.38
-0.3	ND	SD	ND	SD	ND	SD

C Instructions to Execute Codes

C.1 UVLM User Instructions

The UVLM program runs under windows XP. It can be installed by clicking on the Setup1.7.1.exe file[§§§§§]. The program can be run by clicking on the UVLMTest 1.7.1. A data file "xxxxxxx.dat" (for example HPlate.dat) is used to define the flapping motions. It is a text file and the user can modify it to define the wing size, curvature and flapping motions. A number of sample files can be found in the subdirectory of the program in "Test_Cases". The GUI of the UVLM program is shown in Figure C.1.

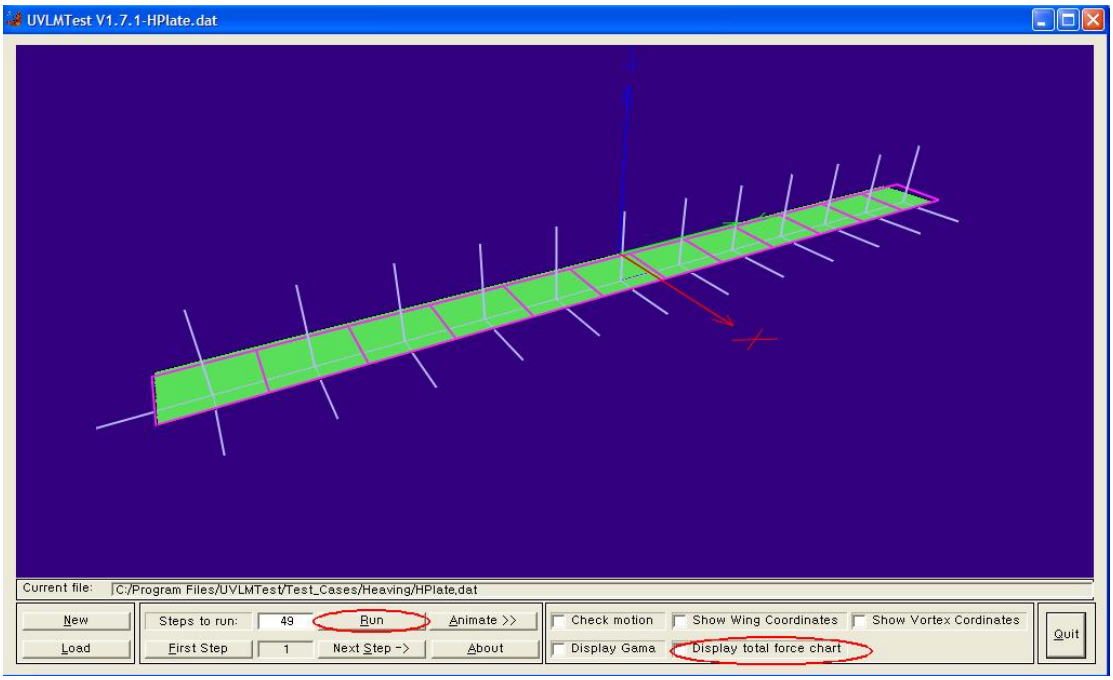

Figure C.1: GUI of the UVLM program

By clicking on the "Run" button (circled), the program will start running. When the program has completed, click on "Display total force chart" (circled) to obtain the forces and torque

[§§§§§] Note that in some cases, the user might need to install Compaq Visual Fortran due to missing dll files.

generated, as shown in Figure C.2.

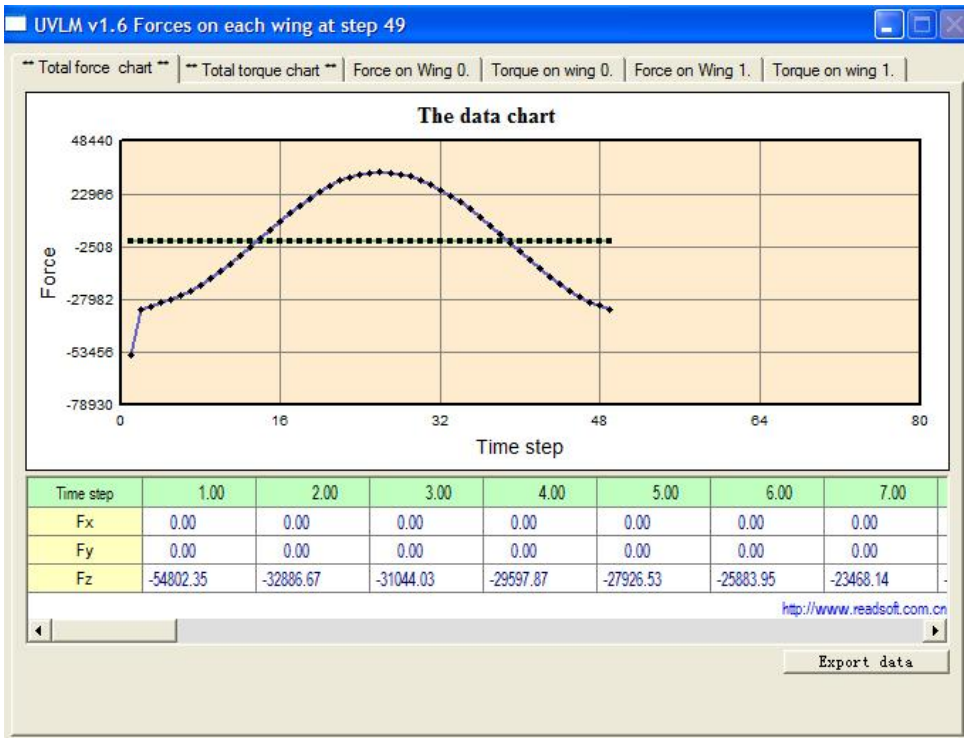

Figure C.2: Total force chart of the UVLM program

C.2 SCNSS User Instructions

C.2.1 Compilation

The source files of the SCNSS code with and without morphing both have the same names. However, the content of some of the files are different. They are global.F, grid.f90, flux_area.f90, bc.f90, bc_impl.f90, bc_semi.f90, set_matrix.f90, inter_step.f90, mom_disz.f90, poisson.f90, petsc_sub.F, cell_data.f90, fractional.f90 and ns2d_c.f90. The library files are tecio64.a and linux64.a and PETSc (Balay et al., 2003). PETSc is a library of linear solvers. The user has to download and compile the library before it can be used (http://www-unix.mcs.anl.gov/petsc/petsc-as/index.html). The makefile also has to be slightly modified due to installation directory difference. The code is compiled using make –f makefile_scnss. The same procedure is used for IBCNSS codes as well. It is recommended that the user use the precompiled a.out which is statically linked in the respective directories.

C.2.2 Execution

The a.out is executed on the atlas3 server, which is one of the fastest clusters in SVU. The command is:

bsub -a mvapich –o log -q linux64 -m "multicore" mpirun.lsf ./a.out $1 $2 … $12

where log is the logging file and $1 to $12 are the input variables.

The usual practice is to first run the code with $12 equal to a large negative value. After the first run, one can estimate the number of time steps required for approximately one period of flapping. Thereafter, the second run is carried out with $12 known.

C.2.2.1 Without Morphing

The filename for the grid used is gridgen.grd. The code is executed using

a.out $1 $2 $3 $4 $5 $6 $7 $8 $9 $10 $11 $12 where $1 to $12 refers to the input variables given in Table C.1.

Table C.1: Input variables for SCNSS without morphing (continue on next page)

Input	Variables represented
$1	= 1 Fresh start = 0 Continue from last stop
$2	= 0 Not used
$3	h_0
$4	f
$5	$-\theta_0$
$6	ϕ
$7	ψ
$8	= 0 Not used
$9	c_{rot}

$10	CFL number
$11	Time steps required if no generation of vorticity diagrams required or starting time step for generation of vorticity diagrams
$12	Time steps required, with generation of vorticity diagrams[*****], negative value if no vorticity diagram required

C.2.2.2 With Morphing

In this case, the grid's filename is still the same. However the input variables are different. The code is executed using a.out $1 $2 $3 $4 $5 $6 $7 $8 $9 $12 where $1 to $12 refers to the input variables given in Table C.2.

Table C.2: Input variables for SCNSS with morphing (continue on next page)

Input	**Variables represented**
$1	= 1 Fresh start = 0 Continue from last stopping time step
$2	= 1 Run with pure heaving configuration = 2 Run with ME configuration = 3 Run with ME(20^o) configuration = 4 Run with MT configuration = 5 Run with ML configuration
$3	x_{fc}
$4	$\bar{a}_f$ [††††††]

[******] The difference between $12 and $11 is slightly more than the time steps required to obtain one flapping cycle. This will ensure the vorticity diagrams generated cover one flapping cycle.

[††††††] Currently $4 to $7 are all equal to $\bar{a}_f$. It is meant for further revision of the program.

$5	$\overline{a}_f$
$6	$\overline{a}_f$
$7	$\overline{a}_f$
$8	= 90.0 (fixed in this study)
$9	= 3 (normal flexing) = 4 (single-sided flexing)
$10	CFL number
$11	Time steps required if no generation of vorticity diagrams required or starting time step for generation of vorticity diagrams
$12	Time steps required, with generation of vorticity diagrams, negative value if no vorticity diagram required

C.2.3 Output

The output files and their descriptions are given in Table C.3. The coef.txt is to be imported into Microsoft excel file SCNSS.xls. The user has to input the correct flapping configurations and starting time (obtainable from time.txt). One also has to ensure that the plot represents integer number of periods so that the efficiency can be calculated correctly.

Table C.3: Output files for SCNSS (continue on next page)

Output	**Description**
coef.txt	Contains data about lift, drag and moment coefficient. To be imported into Microsoft excel file SCNSS.xls
time.txt	Starting time and other values
time_m.txt	Instantaneous time and time steps
config.txt	Flapping configurations

node_value.txt	Binary file of the node velocity values
uv_value.txt	Binary file of the cell center velocity values
p_value.txt	Binary file of the cell center pressure values
vel_f_mn_value.txt	Binary file of the face center grid velocity values
vel_f_value.txt	Binary file of the face center velocity values
xy_value.txt	Binary file of the x/y coordinates values
node_v.plt	Tecplot output of the flapping airfoil at the instance the code stops
node01-30.plt	Tecplot output of the flapping airfoil from time step = $11 to $12 for Table C.1. Used for vorticity diagrams

Table C.4: Description for time.txt

Column	Description
1	Time elapsed
2	Starting time
3	Total time steps
4	Average outflow velocity
5	Number of grid point in x direction
6	Number of grid point in y direction
7-14	Miscellaneous values, used to resume calculation

Table C.5: Description for time_m.txt

Column	Description
1	Time elapsed
2	Current time step
3	Average outflow velocity

C.2.3.1 Without Morphing

Table C.6: Description for config.txt (without morphing)

Column	Description
1	Not used
2	h_0
3	f
4	$-\theta_0$
5	ϕ
6	ψ
7	Not used currently
8	c_{rot}
9	CFL number
10	Interval between time steps at writing each vorticity diagram file
11	Time steps required if no generation of vorticity diagrams required or starting time step for generation of vorticity diagrams
12	Time steps required, with generation of vorticity diagrams, negative value if no vorticity diagram required

C.2.3.2 With Morphing

Table C.7: Description for config.txt (with morphing) (continue on next page)

Column	Description
1	Not used
2	h_0
3	f
4	$-\theta_0$
5	ϕ
6	x_{fc}

7	$\overline{a}_f$
8	$\overline{a}_f$
9	$\overline{a}_f$
10	$\overline{a}_f$
11	ψ_f
12	CFL number
13	Time steps required if no generation of vorticity diagrams required or starting time step for generation of vorticity diagrams
14	Time steps required, with generation of vorticity diagrams, negative value if no vorticity diagram required

C.3 IBCNSS User Instructions

C.3.1 Compilation

The source files of the IBCNSS code for 1 or 2 airfoils in tandem both have the same names. However, the content of some of the files are different. The source files of the code are global.F, grid.f90, flux_area.f90, bc.f90, bc_impl.f90, bc_semi.f90, set_matrix.f90, inter_step.f90, mom_disz.f90, poisson.f90, airfoil.f90, hypre.f90, cell_data.f90, fractional.f90 and ns2d_c.f90. The library file is tecio64.a.

The code is compiled using make –f makefile_ibcnss. Similar, the user is encouraged to use the a.out in the IBCNSS directory.

C.3.2 Execution

The a.out is executed on the atlas3 mcore parallel or atlas4 quad_parallel server since it is

meant to run on more than 1 processor. The airfoils or body shapes are determined by body.txt and body2.txt for tandem arrangements. body.txt and body2.txt are ASCII files which contains the numbers of pts and the body coordinates.

C.3.2.1 For 1 Airfoil

The code is executed using a.out $1 $2 $3 $4 $5 $6 $7 $8 $9 $10 where $1 to $10 refers to the input variables given in Table C.8.

Table C.8: Input variables for IBCNSS for 1 airfoil

Input	Variables represented
$1	= 1 Fresh start = 0 Continue from last stopping time step
$2	Grid number, in x direction, in multiples of 60
$3	Grid number, in y direction, in multiples of 36
$4	h_0
$5	f
$6	$-\theta_0$
$7	ϕ
$8	CFL number
$9	Time steps required if no generation of vorticity diagrams required or starting time step for generation of vorticity diagrams
$10	Time steps required, with generation of vorticity diagrams, negative value if no vorticity diagram required

C.3.2.2 For 2 Airfoils in Tandem

The code is executed using a.out $1 $2 $3 $4 $5 $6 $7 $8 $9 $10 where $1 to $10 refers to the input variables given in Table C.9.

Table C.9: Input variables for IBCNSS for 2 airfoils in tandem

Input	Variables represented
$1	= 1 Fresh start = 0 Continue from last stopping time step
$2	= 4 Used for grids with $d_{12} \leq 2.5$ = 7 Used for grids with $d_{12} > 2.5$
$3	Grid number, in x direction, in multiples of 110 if $2 = 4, 132 if $2 = 7
$4	Grid number, in y direction, in multiples of 70
$5	= 1 Run with ME configuration = 2 Run with MT configuration = 3 Run with ML configuration
$6	d_{12}
$7	ϕ_{12}
$8	CFL number
$9	Time steps required if no generation of vorticity diagrams required or starting time step for generation of vorticity diagrams
$10	Time steps required, with generation of vorticity diagrams, negative value if no vorticity diagram required

C.3.3 Output

The output files and their descriptions are given in Table C.10. The coef3.txt is to be imported into Microsoft excel file IBCNSS.xls. The user has to input the correct flapping configurations and starting time. One also has to ensure that the plot represents integer number of periods so that the efficiency can be calculated correctly.

Table C.10: Output files for IBCNSS

Output	Description
coef3.txt	Contains data about lift, drag and moment coefficient. To be imported into Microsoft excel file IBCNSS.xls
time.txt	Starting time and other values
time2.txt	Starting time and other values
time_m.txt	Instantaneous time and time steps
config.txt	Flapping configurations
uv_value.txt	Binary file of the cell center velocity values
p_value.txt	Binary file of the cell center pressure values
body_pts.txt	Binary file of the fore airfoil instantaneous coordinates
body_pts2.txt	Binary file of the aft airfoil instantaneous coordinates
node01-20.plt	Tecplot output of the flapping airfoil from time step = $9 to $10 for Table C.8. Used for vorticity diagrams

Table C.11: Description for time.txt

Column	Description
1	Time elapsed
2	Starting time
3	Total time steps
4	Average outflow velocity
5	Number of grid point in x direction
6	Number of grid point in y direction
7-14	Miscellaneous values, used to resume calculation

Table C.12: Description for time2.txt

Column	Description
1-7	Miscellaneous values, used to resume calculation

Table C.13: Description for time_m.txt

Column	Description
1	Time elapsed
2	Current time step
3	Average outflow velocity

Table C.14: Description for config.txt

Column	Description
1	Not used
2	h_0
3	f
4	$-\theta_0$
5	ϕ
6	ψ
7	c_{rot}
8	d_{12}
9	ϕ_{12}
10	CFL number
11	Interval between time steps at writing each vorticity diagram file
12	Time steps required if no generation of vorticity diagrams required or starting time step for generation of vorticity diagrams
13	Time steps required, with generation of vorticity diagrams, negative value if no vorticity diagram required